DEVELOPMENT OF ADVANCED STRUCTURES FOR OPTICAL FIBER LASERS AND SENSORS

PHD. DISSERTATION BY SERGIO ROTA RODRIGO
SUPERVISOR: PROF. DR. MANUEL LÓPEZ-AMO SAINZ
PAMPLONA, 2015

upna Universidad Pública de Navarra Nafarroako Unibertsitate Publikoa

upna Universidad Pública de Navarra Nafarroako Unibertsitate Publik

RECONOCIMIENTOS

Este trabajo se ha llevado a cabo gracias a las aportaciones económicas recibidas de los siguientes organismos y proyectos:

- Universidad Pública de Navarra mediante la ayuda de investigación predoctoral, la ayuda para movilidad y las ayudas complementarias a tesis doctorales.

- Secretaria de Estado de Investigación, Desarrollo e Innovación, Ministerio de Economía y Competitividad de España a través del programa de Formación del Personal Investigador y asociado al proyecto de investigación TEC2010-20224-C02-01.

- Proyecto de investigación TEC2013-47264-C2-2-R a través del Fondo Europeo de Desarrollo Regional (FEDER).

- Acción Europea COST- TD1001: Novel and Reliable Optical Fibre Sensor Systems for Future Security and Safety Applications (OFSeSa)

- Proyecto INTERREG SUDOE Project "ECOAL-MGT - Ecological Management of Coal Waste Piles, SOE3/P2/P714".

- Ministerio de Economía y Competitividad de España a través del Proyecto campus de excelencia-Iberus (Innocampus).

- Grupo de investigación Comunicaciones Ópticas y Aplicaciones Electrónicas de la Universidad Pública de Navarra mediante la financiación de material y participación en congresos.

upna Universidad Pública de Navarra Nafarroako Unibertsitate Publikoa

AGRADECIMIENTOS

En estas líneas me gustaría agradecer a todos aquellos que han formado parte del camino de esta tesis, a los que lo han hecho posible, y a los que al margen de la universidad han formado parte de mi vida a lo largo de estos años.

En primer lugar, quiero mostrar mi más sincero agradecimiento a mi director de tesis, Manuel López-Amo Sainz. Antes incluso de empezar en la universidad, ya tenía en mente que quería dedicarme a la investigación, me fascinaba la idea de enfrentarme a retos nuevos y trabajar en un laboratorio. Gracias a la confianza que depositaste en mí, estoy cumpliendo mi sueño. Quiero darte las gracias por tu disponibilidad, tu confianza, por tener siempre en consideración cualquier idea que se te planteara (por muy descabellada que pareciese), por tu paciencia y por supuesto, gracias por compartir tus conocimientos conmigo y el resto de compañeros.

También quiero dar las gracias a los compañeros de laboratorio y del grupo, Mikel, Rosana, Dani, Javi, Santi, Montse, Cesar, Aitor, Mikel y Alayn... por estar siempre disponibles, por su ayuda en los malos momentos, y por crear ese ambiente de trabajo tan formidable. Gracias también al resto de compañeros de la universidad, José Mari, Alfonso, Paola, Santi, Pablo y Javier, con los que he compartido también muy buenos ratos a lo largo de estos años de tesis. En especial quiero agradecer a Ana Pinto, por su apoyo, su conocimiento, las risas, los buenos momentos, y los malos (que también nos hacen aprender). Se te ha echado de menos en esta recta final. También a Rosana Pérez por su ayuda, su paciencia infinita, esos cafés mañaneros "afortunados" y sobre todo por el apoyo durante la OFS de Santander.

A lo largo de la tesis he tenido la oportunidad de realizar dos estancias en otros centros de investigación y trabajar en colaboración con otras universidades. Por eso quiero agradecer en primer lugar a la

upna Universidad Pública de Navarra Nafarroako Unibertsitate Publikoa

Universidad de Cantabria, donde realice la primera de mis estancias. Gracias al Prof. José Miguel López Higuera por darme la oportunidad de investigar con su fantástico grupo. Gracias a todo el Grupo de Ingeniería Fotónica por aceptarme como uno más del grupo y en especial a Marian y Luis por su dirección y apoyo.

Also I would like to thank Prof. José Luis Santos and Dr. Orlando Frazão from INESC Porto, for their warm welcome in their group during my short-term mission (Muito obrigado). It was a pleasure to work in your fantastic group. I cannot forget Luisa, thanks for your help and for your good humor.

También quiero agradecer las colaboraciones realizadas con el Prof. Miguel Gonzalez Herraez y Prof. Oscar Esteban de la Universidad de Alcalá.

Por supuesto al margen de la universidad, quiero agradecer a mis amigos que también me han apoyado y ayudado durante estos años; Miguel Ángel, Amalia, Cesar, Mónica, Javi, Rubén, Lorena, Meri, Maialen, Alessandro y la cuadrilla de Tudelanas. A mi prima Sara por parte de piano, con la cual he compartido mucho durante este tiempo (La música nos hace libres). Agradecer a Ana Bravo por los buenos momentos, las risas, la oportunidad de disfrutar de una experiencia "canteril" genial, y por supuesto por la magnífica edición de esta tesis. Agradezco a Groman123 por la foto de la portada (https://www.flickr.com/photos/pkirtz/16271584131/).

También quiero agradecer profundamente a Mikel Bravo, gracias por estar a mi lado a lo largo de esta tesis, tanto en el ámbito académico como fuera de él. Si no me equivoco la Wii nos unió, y desde entonces nuestros caminos han ido paralelos hasta el punto de que tú ya eres Doctor, de lo cual me sentí y me siento muy orgulloso. He disfrutado tremendamente trabajando contigo, de las birras científicas, de las barbacoas y de nuestras numerosas excursiones improvisadas. Ah, por cierto, gracias por aguantar mi síndrome de "tema-hopping".

Finalmente, quiero agradecer y dedicar esta tesis a toda mi familia. Vuestro apoyo, no solo a lo largo de la tesis, sino durante toda la vida, ha sido determinante para poder llegar hasta aquí. A mis padres Casi y Alberto les debo todo, gracias por el gran esfuerzo que habéis hecho para darme la oportunidad de seguir estudiando, gracias por saber escuchar cualquier cosa que tuviera que contaros, gracias por el apoyo, pero sobre todo por ser como sois. A mi hermana Maite y mi cuñado Roberto, gracias por todo el apoyo, consejos, cenas y buenos momentos. Quiero expresar mi más profundo agradecimiento a Mariano Jiménez, porque ha estado siempre ahí, mucho antes incluso de que yo lo supiera. Sin tu apoyo incondicional esta tesis tampoco hubiera sido posible. No me olvido de Pili, ambos me habéis hecho sentir siempre como en casa. Gracias por dejar la luz siempre encendida. Finalmente, sin duda quiero darle las gracias a mi sobrino Roberto Jr., gracias por esas sonrisas que me regalas, que me transportan a la infancia y que me hacen tan feliz.

RESUMEN

Desde la irrupción de la fibra óptica en las telecomunicaciones, han surgido multitud de desarrollos basados en sus propiedades. Así, en las últimas décadas, la rápida evolución de los sistemas basados en fibra óptica, así como la aparición en el mercado de dispositivos como los amplificadores ópticos, los láseres de semiconductor de alta potencia, y otros elementos, ha hecho avanzar considerablemente la investigación en este campo. Además de la utilización de la fibra óptica en telecomunicaciones, han surgido nuevas aplicaciones, generando nuevas familias de dispositivos. Dos de ellas particularmente interesantes, son los láseres de fibra óptica y los sensores de fibra óptica. Ambas familias pueden combinarse de manera que sensores y redes de sensores de fibra óptica pueden interrogarse por medio de láseres de fibra óptica. En este marco de investigación se centra esta tesis, donde se han desarrollado estructuras avanzadas de fibra óptica para láseres y sensores. El objetivo ha sido mejorar las propiedades de los láseres de fibra, sensores y sus sistemas de monitorización, así como abordar los diferentes problemas que éstos presentan actualmente. Los retos encontrados, así como los objetivos de cada sistema, varían en función del tipo de sistema desarrollado. De esta forma, la primera parte de este trabajo ha sido dedicada al desarrollo de láseres de fibra óptica, buscando mejorar sus propiedades en términos de estabilidad, relación señal ruido, modos longitudinales, múltiples líneas de emisión y anchura de las mismas. Se han abordado diferentes tipos de configuraciones clásicas de láseres en anillo y de cavidad lineal. También se han realizado estudios de láseres de cavidad distribuida mediante dispersión Rayleigh (random). Estos láseres han suscitado gran interés en los últimos años dado que no presentan modos longitudinales. Por otro lado en el ámbito de la monitorización de sensores, se han desarrollado transductores ópticos basados en fibras micro-estructuradas, aprovechando las ventajas que éstas presentan en comparación con las fibras ópticas estándar. Finalmente se han desarrollado diferentes configuraciones de sistemas sensores con el objetivo de contribuir a la mejora de alguno de sus parámetros, como su alcance, capacidad de multiplexación, sensibilidad, rango dinámico y estabilidad de los sistemas sensores.

upna Universidad Pública de Navarra Nafarroako Unibertsitate Publikoa

ABSTRACT

Optical fiber technology as well as its rapidly evolution, has attracted the scientific community attention to develop lasers, fiber optic transducers and sensor networks. In this regard, the appearance in the last decades of commercial devices such as optical amplifiers, semiconductor high power lasers and others, has contributed to the rise of this technology. In this framework, a contribution to the improvement of the performance of fiber lasers and fiber optic sensors is presented in this PhD. work, taking into account their main merits and addressing their principal challenges. The challenges as well as the objectives addressed in each design vary depending on the application. In this way, the first part of the thesis has been dedicated to the development of optical fiber lasers. And it is focused on improving their properties in terms of stability, signal noise ratio, longitudinal modes, multiwavelength emission and bandwidth of the emission lines. Different classical configurations based on ring and linear cavity lasers have been addressed. Also, random cavity lasers, which have attracted great interest in recent years due to their longitudinal modeless behavior, have been studied. On the other hand, in the field of sensor monitoring, optical transducers based on micro-structured fibers have been developed, exploiting their advantages in comparison with standard optical fibers. Finally different optical sensor networks have been developed, whose main goal have been the improvement of features such as monitoring distance, multiplexing skill, sensitivity, dynamic range and stability.

upna Universidad Pública de Navarra Nafarroako Unibertsitate Publikoa

LIST OF FIGURES

FIGURE 2.1 Energy diagram for the Er^{3+} ion into silica glass fiber medium. Light amplification by stimulated emission from E_2 to E_1 is also shown. Dashed arrow indicates radiationless transitions (energy emission by lattice vibrations).

FIGURE 2.2 Typical scheme of an erbium doped fiber amplifier.

FIGURE 2.3 Schematic of the quantum mechanical process that takes place during Raman scattering.

FIGURE 2.4 Effect of a saturating signal on the gain curve depending on the type of atomic transition spectral broadening. (a) Homogeneous broadening, (b) inhomogeneous broadening.

FIGURE 2.5 Schematic of a linear cavity fiber laser.

FIGURE 2.6 Schematic of a unidirectional ring cavity fiber laser.

FIGURE 2.7 Laser intensity distribution and inverted population density within a fiber laser due to spatial hole burning.

FIGURE 2.8 Schematic diagram of the Raman gain (red line) and laser generated power (blue line) distributions in a random distributed feedback fiber laser.

FIGURE 2.9 Schematic diagrams of the (a) forward-pumped, (b) backward-pumped and (c) single-arm RDFB laser configurations.

FIGURE 2.10 Cavity resonance modes for a multi-longitudinal mode operated fiber laser.

FIGURE 2.11 Schematic of the self-heterodyne method.

FIGURE 2.12 Conceptual block diagram of a general optical sensor system.

FIGURE 2.13 Multiplexing modulation formats: a) WDM, b) TDM, c) FDM, d) CM and e) PDM.

FIGURE 2.14 Operation principle of a fiber Bragg grating.

FIGURE 2.15 Operation principle of a phase shift fiber Bragg grating.

FIGURE 2.16 Drawing of the cross section of (a) standard fiber, (b) Solid-core MOF, (c) Suspended-solid-core MOF and (d) Hollow-core MOF. Colors: Blue-silica, black-doped silica,white-air.

FIGURE 2.17 Microscopic picture of the (a) Hi-Bi MOF developed in [184] and (b) the PM-1550-01 from NKT [186].

FIGURE 2.18 Microscopic pictures of (a) a standard fiber and (b) a suspended core MOF.

FIGURE 2.19 Schematic of a multimode interferometer.
FIGURE 2.20 Schematic of a Hi-Bi inline polarimetric interferometer structure.
FIGURE 2.21 Simulated interference spectrum for a Hi-Bi inline polarimetric interferometer.
FIGURE 2.22 Schematic diagram of a Hi-Bi fiber loop mirror structure.
FIGURE 2.23 Interferometer spectra of a 3m Hi-Bi fiber loop mirror, (red) measured and (black dotted) simulated.
FIGURE 2.24 Schematic of a FORR structure, formed by using a 2x2 coupler.
FIGURE 2.25 Simulated spectrum of a FORR transmission response.
FIGURE 3.1 (a) Schematic diagram of the proposed dual-wavelength erbium doped fiber ring laser configuration; (b) Heterodyne detection system.
FIGURE 3.2 Measured output optical spectrum of the proposed dual-wavelength EDFRL configuration for a pump power of 70 mW.
FIGURE 3.3 Output optical spectrum measured by the ESA for the dual-wavelength EDFRL configuration, when the tunable laser was tuned for the first (a) and second (b) wavelength laser emission.
FIGURE 3.4 (a) OSA and (b) ESA spectrum when the output power imbalance between both emission lines was 9.23 dB.
FIGURE 3.5 Output power fluctuation for the emission line centered at 1547 nm when the laser worked in SLM and MLM operation regimes.
FIGURE 3.6 Schematic diagram of the proposed dual-wavelength EDFRL configuration. EDFA: Erbium-doped fiber amplifier. VA: Variable attenuator.
FIGURE 3.7 Simulated structure of the employed PSFBGs. (a) The phase shift was stronger for the m=-1 order of the SFBG. (b) Comparison of the simulated and measured spectra obtained with the m=-1 order.
FIGURE 3.8 Optical output spectrum of the EDFRL measured at OSA.
FIGURE 3.9 Output spectrum measured by the ESA at (a) λ_1=1562.8 nm, and (b) λ_2=1550.5 nm.
FIGURE 3.10 Frequency instability at (a) λ_1 and (b) λ_2 measured with Max-Hold mode in ESA for 1 hour.
FIGURE 3.11 Spectrum of the emission line of λ_1 (a) and λ_2 (b) measured at ESA with the self-heterodyne detection method.
FIGURE 3.12 Optical output spectra at BOSA for λ_1 (a) without PSFBG operating in multi longitudinal mode, and (b) with PSFBG operating in single longitudinal mode.
FIGURE 3.13 (a) Instability and output power of the EDFRL vs the EDFA output power. (b) Output power fluctuations of λ_1 and λ_2 for an EDFA output power of 130 mW.
FIGURE 3.14 Measured transmission spectra of the (a) Sagnac loop mirror and the OADMs response, and (b) the Sagnac loop mirror and the MUX-DMUX response.

FIGURE 3.15 Experimental scheme for the proposed tunable four-wavelength erbium doped fiber ring laser configuration based on optical Add-Drop multiplexers and a Sagnac loop mirror.
FIGURE 3.16 Experimental scheme for the proposed tunable four-wavelength EDFRL configuration based on MUX-DMUX and a Sagnac loop mirror.
FIGURE 3.17 Shift of the output spectra of the four-wavelength Add-Drop EDFRL proposed by adjusting the tunable filter at channel 41.
FIGURE 3.18 (a) Shift of the output spectra of the four-wavelength EDFRL proposed by adjusting the tunable filter at channel 35, measured by the BOSA. (b) Spectrum at channel 31 measured by the OSA.
FIGURE 3.19 Output power fluctuation for each emission line with the four channel laser outputs in operation.
FIGURE 3.20 Output optical spectrum measured by the ESA for the channel 31, (a) at single-wavelength operation and (b) at dual-wavelength operation with channel 47.
FIGURE 3.21 (a) Schematic of the self-heterodyne detection. (b) Spectrum of each emission line measured at ESA with the self-heterodyne detection method.
FIGURE 3.22 One FBG was detuned (dashed line) in terms of the other (dotted line). The overlapped spectrum (solid line) gave rise to a filter narrower than both individual FBGs.
FIGURE 3.23 Employed setup during the fabrication process. The DBR fiber laser structure is also shown: two uniform FBGs of 9 mm length were inscribed into Er-doped fiber with a distance between them of 40 mm.
FIGURE 3.24 SLM operation measured at 25ºC. The laser signal was beaten with a TLS source obtaining a single peak.
FIGURE 3.25 (a) Linewidth of 4.5 kHz (3dB) measured using self-heterodyne detection with a modulation frequency of 1GHz. (b) Wavelength stability (62.2MHz) of both orthogonal polarization modes measured during 10 minutes.
FIGURE 3.26 (a) Measured OSNR for a 26dBm pump power and (b) output power stability measured along 1 hour.
FIGURE 3.27 (a) Emitted wavelength displacement during the temperature sweep and (b) the two orthogonal polarization modes at the extreme temperatures (0ºC and 100ºC).
FIGURE 3.28 (a) Emitted wavelength displacement during the strain sweep. (b) The two orthogonal polarization modes are depicted in both extremes.
FIGURE 3.29 Schematic diagram of the proposed single-wavelength RDFB laser.
FIGURE 3.30 Reflected and transmitted spectra of the FBG and PS-FBG respectively, measured at BOSA
FIGURE 3.31 Optical spectrum of the generated emission line.

FIGURE 3.32 Line-width variation with Raman pump power for different coupling ratios.
FIGURE 3.33 Peak power of the emission line vs Raman pump power for different coupling ratios.
FIGURE 3.34 Laser's electrical self-beating signal for different spans/resolutions (black) and the detector's noise level (red).
FIGURE 3.35 Schematic diagram of the proposed multi-wavelength RDFB laser.
FIGURE 3.36 Spectra of the four emission lines measured at the BOSA with a 0.08 pm resolution.
FIGURE 3.37 Output power fluctuations of the four emission lines during 15 minutes
FIGURE 3.38 Experimental set-up of: (a) the hybrid ring-random fiber laser; (b) the ring fiber laser; and (c) random fiber laser. Black arrow symbol: optical isolator. Blue arrows: Random laser feedback. Green arrows: Ring laser contributions.
FIGURE 3.39 (a) Experimental demonstration of laser condition through the evolution the output power versus pump power. (b) Evolution of the output power versus pump power presenting the output power with a linear scale where the differences of threshold power and efficiency among the proposed fiber lasers are evident.
FIGURE 3.40 Output power fluctuations of the three laser configurations versus time
FIGURE 3.41 Spectra for the 3 fiber laser configurations using normalized output power and normalized wavelength to show the differences among them in terms of OSNR and full width at half maximum.
FIGURE 3.42 (a) Longitudinal modes generated in the hybrid ring-random fiber laser shown by the electrical spectrum analyzer. (b) Study of the beat modes in the case of the random fiber laser resulting in a modeless spectrum, characteristic of random fiber lasers.
FIGURE 3.43 Schematic set-up for the hybrid random-ring fiber laser in order to demonstrated that this laser was composed of the contribution of the ring fiber laser and the random fiber laser.
FIGURE 3.44 Study of the (a) electrical and (b) optical spectra in order to demonstrate that the hybrid random-ring fiber laser was not just a conventional ring cavity fiber Raman laser with some impact of Rayleigh scattering but it was really composed of the contribution of the ring fiber laser and the random fiber laser.
FIGURE 3.45 Position of the electro-optical modulator in the three fiber lasers in order to modulate their signals: (a) hybrid ring-random fiber laser; (b) ring fiber laser and (c) random fiber laser.
FIGURE 3.46 Original modulation signal and time domain lasers behavior when 500 MHz square signal internally modulated the signals of the different proposed fiber lasers.

FIGURE 4.1 (a) Schematic of the experimental setup used to characterize the Hi-Bi MOF sensing head and (b) optical microscopic picture of the Hi-Bi MOF cross-section.
FIGURE 4.2 Reflected spectrum of the Hi-Bi MOF interferometer when no external force is induced on the sensing head.
FIGURE 4.3 Interferometer spectra obtained for different polarization controller positions.
FIGURE 4.4 Experimental results (solid line) and theoretical simulations (dash line) of the reflected output signal for three different strain induced variations.
FIGURE 4.5 Experimental setup for strain measurement with an interferometric in-reflection Hi-Bi MOF sensing head.
FIGURE 4.6 Measured optical power variation with strain of the Hi-Bi MOF sensing head.
FIGURE 4.7 (a) Schematic of the strain sensor system. (b) Microscopy photograph of the Suspended Core MOF cross-section.
FIGURE 4.8 Variations of the optical output spectrum at different strain values for sensor L=5mm (a) and L=20mm (b) with a d=0.5m.
FIGURE 4.9 Wavelength dependence with strain for sensor L=5mm (black) and L=20mm (red).
FIGURE 4.10 Sensor´s sensitivity characterization according to the sensor length (L) and the stage lengths (d).
FIGURE 4.11 Characterization of the wavelength shift with temperature for the 5mm (red) and 75mm (black) sensor length.
FIGURE 4.12 (a) Schematic of the strain sensor system and (b) microscopy photograph of the suspended core MOF cross-section (bottom).
FIGURE 4.13 (a) Optical transmission spectra of the sensor when no external force is applied at room temperature (dark line), and low pass filtering with processing software (red line). (b) Fast Fourier transform of the optical transmission spectra.
FIGURE 4.14 (a) Characterization of the wavelength shift with strain, and (b) spectral evolution of the multimode interference with strain.
FIGURE 4.15 (a) Characterization of the wavelength shift with temperature, and (b) evolution of the spectra with temperature.
FIGURE 4.16 Setup of the bend sensor showing the angle stepper.
FIGURE 4.17 (a) Evolution of the low-frequency interferogram with angle, and (b) characterization of the wavelength shift with curvature.
FIGURE 4.18 Characterization of the wavelength shift of the high-frequency interferogram with curvature.
FIGURE 5.1 Schematic depiction of the ultra-long fiber Bragg grating sensor system.
FIGURE 5.2 Basic design of the tunable laser.

FIGURE 5.3 Spectrum of the reflected signal from the four remotely multiplexed FBGs for $P_{pum\text{-}Raman}$=0.72 W, $P_{tunable\text{-}laser}$=10.68 dBm and $OSA_{resolution}$= 0.1 nm. Amplified spontaneous emission at 200 km for a $P_{pum\text{-}Raman}$=0.85 W.
FIGURE 5.4 Spectrum of the tunable laser after 250 km length transmission for a
FIGURE 5.5 $P_{tunable\text{-}laser}$=10.68 dBm and $OSA_{resolution}$= 0.01 nm.Evolution of laser power vs. Raman pump laser.
FIGURE 5.6 Spectrum of the reflected signal from the remotely multiplexed four FBG.
FIGURE 5.7 $P_{pum\text{-}Raman}$=1.3W, $P_{tunable\text{-}laser}$=11dBm and $OSA_{resolution}$= 0.1nm.
FIGURE 5.8 Wavelength shift of the heated up FBG.
FIGURE 5.9 Spectrum of the reflected signal from the four FBG using the OSA sweep option of high sensitivity. $P_{pum\text{-}Raman}$=1.3 W, $P_{tunable\text{-}laser}$=11 dBm and $OSA_{resolution}$= 0.1 nm.
FIGURE 5.10 Experimental setup of the proposed switchable EDFRL system for temperature sensors multiplexing, where λi and λi' are the FBGs and the PSFBGs, respectively.
FIGURE 5.11 Simulated and measured reflection spectra for the phase shift of the SFBG first order.
FIGURE 5.12 Schematic representation of the experimental setup for the sensors temperature test.
FIGURE 5.13 (a) Optical output spectrum at 24°C measured at BOSA and (b) electrical output spectrum at 24°C measured at ESA.
FIGURE 5.14 (a) Beat frequency dependence with time at different temperatures. (b) Average beat frequency shift dependence with temperature.
FIGURE 5.15 Theoretical beat frequency shift dependence with temperature for different reference temperatures.
FIGURE 5.16 Switching time from B1 to B4 output (solid line) and from B4 to B1 output (dotted line).
FIGURE 5.17 Experimental setup configuration for the EDFRL remote sensing system.
FIGURE 5.18 Schematic of the high-strain bending intensity sensor.
FIGURE 5.19 (a) Output spectra of the high-strain sensor for different strain values and, (b) output power evolution with the strain.
FIGURE 5.20 (a) Output spectra of the low-strain sensor for different strain values and, (b) output wavelength evolution with the strain.
FIGURE 5.21 Switching time from B1 to B2 output (solid line) and from B2 to B1 output (dotted line).
FIGURE 5.22 Proposed single-longitudinal-mode four-wavelength fiber laser for sensors applications.
FIGURE 5.23 Output spectrum response of the MEDFRL (a)measured at OSA and (b) measured at BOSA.
FIGURE 5.24 Output optical spectrum measured by the ESA for the channel 47.
FIGURE 5.25 Spectrum of emission line measured at ESA with the self-heterodyne
X detection method for channel 35.

FIGURE 5.26 Wavelength shift as a function of temperature change.
FIGURE 5.27 Output spectrum response of the MEDFRL with the sensors located at 10 km of distance, measured at OSA.
FIGURE 5.28 Compound fiber-based ring resonator.
FIGURE 5.29 Experimental and simulated normalized spectra of the resonator for E_{01} (a), and E_{02} (b).
FIGURE 5.30 Experimental setup of the TLS interrogation method.
FIGURE 5.31 Output power fluctuations of the TLS interrogation method.
FIGURE 5.32 Experimental setup of the EDFRL interrogation method.
FIGURE 5.33 Output power fluctuations of the EDFRL interrogation method.
FIGURE 5.34 Experimental setup of the EDFRL sensor system.
FIGURE 5.35 Output power response against the voltage applied to VA located in position A (dash), position B (continuous) and position B without FORR (dash-dotted).
FIGURE 5.36 Output power instability of the structure against the voltage applied to VA.
FIGURE 5.37 Output power response against the voltage applied to a VA for two different coupling ratios of the upper coupler.
FIGURE 5.38 Experimental setup of EDFRLs for the displacement sensor interrogation system and, schematic of the displacement sensor based on bending.
FIGURE 5.39 Output power response versus the displacement applied to the sensor, when located in position A (dotted) and B (continuous).
FIGURE 5.40 Optical spectrum of the multi longitudinal mode EDFRL and the filter transmission (inset) measured with a BOSA.
FIGURE 5.41 Output power response depending on the sensor displacement in position A (dotted) and B (continuous).
FIGURE 5.42 Optical spectrum of the single longitudinal mode EDFRL and the filter transmission (inset) measured with a BOSA.
FIGURE 5.43 Output power response depending on the sensor displacement measured at position A (dotted) and at position B (continuous).
FIGURE 5.44 Experimental setup of the micro-bending random fiber laser sensor system.
FIGURE 5.45 Output power response depending on the sensor displacement in positions A (dotted) and B (continuous).

LIST OF TABLES

TABLE 2.1 Main types of optical amplifiers.
TABLE 2.2 Comparison of the main characteristics of EDFA and Raman amplifiers.
TABLE 2.3 General classification of fiber-optic sensors.
TABLE 2.4 State of the art in remote fiber optic point sensor systems.
TABLE 2.5 Fiber Bragg grating sensors interrogation types.
TABLE 3.1 Main properties of the EDFRL presented in section 3.1.
TABLE 4.1 Values for strain and temperature resolutions under simultaneous measurement obtained considering other fiber optic sensing layouts.
TABLE 5.1 Critical parameters comparison of the different sensor configurations.

ACRONYMS

ASE	Amplified Spontaneous Emission
ASS	Amplified Spontaneous Scattering
AWG	Arrayed Waveguide Gratings
BFL	Brillouin Fiber Laser
BOSA	Brillouin Optical Spectrum Analyzer
BW	Band Width
CCD	Charge Coupled Device
CI	Confidence Interval
CL	Confidence Level
CM	Coherence Multiplexing
CW	Continuous Wave
DCF	Dispersion Compensating Fiber
DMUX	Demultiplexer
DWDM	Dense Wavelength Division Multiplexing
EDF	Erbium Doped Fiber
EDFA	Erbium Doped Fiber Amplifier
EDFL	Erbium Doped Fiber Laser
EDFRL	Erbium Doped Fiber Ring Laser
EDWA	Erbium Doped Waveguide Amplifier
EOM	Electro-Optical Modulator
ESA	Electrical Spectrum Analyzer
FBG	Fiber Bragg Grating
FDM	Frequency Division Multiplexing
FFT	Fast Fourier Transform
FLM	Fiber Loop Mirror
FORR	Fiber Optical Ring Resonator
FPF	Fabry-Perot Filter
FRA	Fiber Raman Amplifier
FWHM	Full-Width at Half Maximum
FWM	Four Wave Mixing
HI-BI	High Birefringence

ITU	International Telecommunication Union
LPG	Long Period Grating
MEDFRL	Multiwavelength Erbium Doped Fiber Ring Laser
MMF	Multi-Mode Fiber
MOF	Microstructure Optical Fiber
MUX	Multiplexor
MWFL	Multi Wavelength Fiber Laser
OA	Optical Amplifier
OADM	Optical Add-Drop Multiplexer
OBR	Optical Backscattering Reflectometer
OC	Optical Coupler
OPA	Optical Parametric Amplifier
OPD	Optical Patch Difference
OSA	Optical Spectrum Analyzer
OSNR	Optical Signal to Noise Ratio
OTDR	Optical Time Domain Reflectometer
PBG	Photonic Band Gap
PC	Polarization Controller
PCF	Photonic Crystal Fiber
PDM	Polarization Division Multiplexing
PSFBG	Phase Shift Fiber Bragg Grating
RBS	Rayleigh Back-Scattering
RDFB	Random Distributed Feed-Back
RFL	Raman Fiber Laser
RIN	Relative Intensity Noise
SFBG	Sampled Fiber Bragg Grating
SHB	Spatial Hole Burning
SLM	Single Longitudinal Mode
SMF	Single Mode Fiber
SOA	Semiconductor Optical Amplifier
SRS	Stimulated Raman Scattering
TDM	Time Division Multiplexing
TEC	Thermo Electrical Cooler
TIR	Total Internal Reflection
TLS	Tunable Laser Source
VA	Variable Attenuator
WDM	Wavelength Division Multiplexing

INDEX OF CONTENTS

RECONOCIMIENTOS V

AGRADECIMIENTOS VII

RESUMEN XI

ABSTRACT XIII

LIST OF FIGURES XV

LIST OF TABLES XXIII

ACRONIMS XXV

INDEX OF CONTENTS XXVII

1. INTRODUCTION 1

1.1. Motivation and objectives 3

1.2. Thesis outline 5

2. OVERVIEW OF THE BASIC TECHNOLOGIES EMPLOYED 9

2.1. Introduction 11

2.2. Optical amplifiers 12

2.2.1. Types of optical amplifiers 12
2.2.2. Erbium doped fiber amplifiers 14
2.2.3. Fiber Raman amplifiers 16

2.3. Optical fiber lasers 18

upna Universidad Pública de Navarra Nafarroako Unibertsitate Publikoa

2.3.1. Merits of fiber lasers 19
2.3.2. Optical fiber lasers depending on the gain medium 20
2.3.2.1. Erbium doped fiber lasers 20
2.3.2.2. Raman fiber lasers 21
2.3.2.3. Line shapes 23
2.3.3. Fiber optic laser cavities 24
2.3.3.1. Linear cavity fiber lasers 24
2.3.3.2. Ring cavity fiber lasers 26
2.3.3.3. Spatial hole burning 27
2.3.3.4. Random distributed feedback fiber lasers 28
2.3.4. Single longitudinal mode fiber lasers 30
2.3.5. Multiwavelength fiber lasers 32
2.4. Optical fiber sensors 34
2.4.1. Merits of fiber sensors 35
2.4.2. Multiplexing and remote sensing 36
2.4.3. Fiber Bragg gratings 39
2.4.4. Microstructured and photonic crystal fibers 43
2.4.4.1. PCF/MOF geometry and guidance mechanisms 43
2.4.4.2. Modal characteristics 45
2.4.4.3. Birefringence 46
2.4.4.4. Temperature dependence 47
2.4.4.5. Young modulus 48
2.4.5. Interferometric and polarimetric sensors 49
2.4.5.1. Multimode interferometer 50
2.4.5.2. Hi-Bi inline polarimetric interferometer 50
2.4.5.3. Hi-Bi fiber loop mirror 52
2.4.5.4. Fiber optic ring resonator 54
2.5. Conclusions 55
2.6. References 55
3. OPTICAL FIBER LASERS 77
3.1. Erbium-doped fiber ring lasers 81
3.1.1. Low noise dual-wavelength EDFRL in single-longitudinal-mode operation 81

3.1.2. Dual-Wavelength Single-Longitudinal Mode EDFRL using Phase-Shift Bragg Gratings 86
3.1.3. EDFRLs based on Add-Drops and MUX-DMUX 92
3.1.4. Comparison of the developed EDFRLs 101
3.2. Single-longitudinal mode linear cavity laser based on a very narrow filtering technique 102
3.3. Random distributed feedback fiber lasers 108
3.3.1. Narrow-linewidth single-wavelength RDFB fiber laser 108
3.3.2. Narrow-linewidth multi-wavelength RDFB fiber laser 113
3.3.3. RDFB vs Ring fiber lasers 116
3.4. Conclusions 127
3.5. References 129

4. OPTICAL FIBER TRANSDUCERS 135

4.1. Hi-Bi MOF in reflection strain sensor 139
4.2. Control of the strain sensitivity of a MOF sensor 144
4.3. Multimodal interferometer based on a suspended core MOF for simultaneous measurement of physical parameters 147
4.4. Conclusions 153
4.5. References 154

5. OPTICAL FIBER SENSOR SYSTEMS 159

5.1. Remote 250Km FBG sensor 163
5.2. Switchable erbium doped fiber ring laser system for temperature sensors multiplexing 169
5.3. Switchable fiber optic laser system for high and low-strain fiber optic sensors remote multiplexing 174
5.4. Multi-wavelength fiber laser in single-longitudinal mode operation based on DWDMs for sensing applications 178
5.5. Compound lasing fiber optic ring resonators for sensor sensitivity enhancement 183

5.6. Conclusions 196
5.7. References 199

6. CONCLUSIONS AND OPEN RESEARCH LINES 205

6.1. Conclusions 207
6.2. Conclusiones 211
6.3. Open research lines 215

APENDIX: LIST OF PUBLICATIONS RELATED TO THE THESIS 217

CHAPTER I

INTRODUCTION

upna Universidad Pública de Navarra
Nafarroako Unibertsitate Publikoa

CHAPTER I

1.1 MOTIVATION AND OBJETIVES

Optical fiber technology as well as its rapidly evolution, has attracted the scientific community attention to develop lasers, fiber optic transducers and sensor networks. In this regard, the appearance in the last decades of commercial devices such as optical amplifiers, semiconductor high power lasers and others, has contributed to the rise of this technology.

Optical fiber lasers present good features such as simplicity, compactness, reliability, low intensity noise, low insertion loss and high compatibility with other optical components. These properties make them an attractive alternative for telecommunications, sensors monitoring, signal process and microwave signal generation. In this framework, the study and improvement of optical fiber lasers have been one of the motivations of this PhD. work. Different cavity structures, wavelength selection methods and amplification configurations for optical fiber lasers have been experimentally demonstrated. The aim of these developments was to contribute to the improvement of certain parameters that are important in the fields of telecommunications and sensor monitoring, such as stability, output power, optical signal to noise ratio, and the single longitudinal mode operation. The lasers devel-

CHAPTER I

oped here work in the C-band of telecommunications, due to the large number of equipment available for such wavelengths.

Optical fibers also offer efficient solutions for sensing. Fiber optic sensors present appealing characteristics that make them very attractive when compared with conventional electric sensors such as immunity to electromagnetic interferences, ability to work in harsh environments, small size and finally, multiplexing and remote monitoring capability.

Photonic crystal fibers and microstructured fibers are a kind of optical fibers that present a diversity of new and improved features beyond what standard fibers can offer. Due to their unique geometric structure, they present special properties and capacities that lead to an outstanding potential as sensors. Because of this, one of the motivations for this PhD work has been the use of microstructured fibers as optical transducers for improving the measurement of physical parameters such as temperature, strain and curvature.

Finally, the last objective of this thesis has been the development of fiber sensor systems, based on optical fiber lasers and focused on covering main aspects such as remote monitoring, multiplexing capability, integration of sensors of different nature and stability and sensitivity enhancement.

1.2 THESIS OUTLINE

This PhD. work has been structured into 6 chapters organized as follow:

After chapter 1 (this one), chapter 2 shows a brief introduction of the most important technologies in the fiber optic field that have been employed for the development of this thesis. Many of the developed structures are based on optical amplification, being this the first point presented in this chapter. Next, the fundamental aspects of fiber lasers are shown. This section begins with a summary of the fiber laser merits. Hereafter, a detailed classification of fiber lasers according to their gain medium and their cavity design is presented. Finally, other relevant aspects such as single-longitudinal mode (SLM) operation and multi-wavelength fiber lasers are addressed. The last section of chapter 2 covers the fundamental aspects of fiber sensors. This section begins with their classification and an introduction of their merits. Next, multiplexing and remote sensing concepts are shown. Hereafter, the main properties of fiber Bragg gratings (FBGs) and microstructured fibers (MOFs) for sensing are presented. To conclude the section, a brief introduction of the interferometric and polarimetric sensors used in this thesis, is shown.

Chapter 3 is devoted to the development of different configurations of fiber lasers. The aim of this chapter is to contribute to the improvement of the fiber lasers main parameters such as optical signal to noise ratio (OSNR) and output power stability. Single longitudinal mode operation with narrow emission lines bandwidths is also pursued. The multiwavelength operation and the independent control of the loss of each emission line are also taken into account. In this regard, section 3.1 presents four new configurations of multiwavelength erbium-doped fiber ring lasers (EDFRL), by using different methods for the selection of the emission lines such as FBGs, FBGs in combination with PSFBGs, Add-Drops and MUX-DMUX devices. Section 3.2 is dedicated to the development of a linear cavity laser, by using a narrow filtering technique based on the spectral overlapping of two uniform FBGs in order to achieve the SLM regime. The last section of chapter 3 is dedicated to random distributed feedback lasers. A configuration for sub-gigahertz line-width for the first time in RDFB lasers is proposed and experimental demonstrated, by using a narrow filtering technique based on a combination of FBGs with PSFBGs. Next, the configuration is extended for a multiwavelength laser with four narrow emission lines. Finally, to conclude this chapter a comparative study between a random, a ring and a hybrid ring-random cavity is performed.

Chapter 4 is fully dedicated to the development of transducers based on microstructured optical fibers for sensor systems. The main goal of this chapter has

been to exploit MOF's features in comparison with standard fibers. MOFs present a low Young modulus which provides high sensitivities to strain. Also, the wide possibility on their cross section design allows the fabrication of high-birefringence (Hi-Bi) MOFs for polarimetric sensors. Finally, Hi-Bi MOFs fabricated with a single material, present low temperature dependence. Based on these characteristics, three different MOF sensor systems are shown in this chapter.

Chapter 5 presents different optical fiber sensor systems which have been designed to cover main aspects such as, remote monitoring, multiplexing, integration of different kind of transducers, instability and sensitivity enhancement. Section 5.1 presents two remote (200 Km and 250 Km) sensors multiplexing systems based on FBGs. Afterward, a fiber laser sensor system for temperature measurements is presented. This system is based on the detection in the electrical domain of the resulting beat signal of two different SLM laser lines, which are generated by an EDFRL. Next, section 5.3 presents a 50 Km long switchable EDFRL system for sensors remote multiplexing. This system allows the integration of different interrogation methods, based on wavelength or amplitude detection. Afterward, a novel multi-wavelength ring laser configuration for sensing applications by means of a DWDM and four FBGs is experimentally demonstrated. The last part of chapter 5 is dedicated to present a new fiber laser system for enhancing fiber-optic intensity sensor measurements, based on a resonant ring cavity. The main advantage of this method is its ability to increase the dynamic range of an intensity sensor up to 15 dB, while keeping good stability values. This concept is tested for a displacement sensor based on fiber optic bendings. A study of different topologies (3 based on an EDFRL with different filters and another one based on a random fiber laser) is also carried out.

The main conclusions of this PhD. work and the open research lines are reported in chapter 6.

Finally, author´s publications list concerning the Ph.D. work is attached as an appendix.

CHAPTER II

OVERVIEW OF THE BASIC TECHNOLOGIES EMPLOYED

upna Universidad Pública de Navarra Nafarroako Unibertsitate Publikoa

CHAPTER II

2.1. INTRODUCTION

This chapter is mainly dedicated to introduce briefly the most important technologies in the fiber optic field that have been employed in chapters 3, 4 and 5. Because this overview is far from complete, an extensive bibliography about the actual state of the art is also provided.

Most part of the structures developed along this Ph.D. work are based on optical amplification, therefore this is the first point presented in this chapter. Next the fundamental aspects of fiber lasers (merits, classification, cavity designs, single longitudinal mode operation and multiwavelength fiber lasers) are also provided. Finally, fundamental aspects of fiber sensors (merits, classification, multiplexing, remote monitoring, fiber Bragg gratings technology, photonic crystal and micro structured fibers, and interferometric sensors) are shown as well.

2.2 OPTICAL AMPLIFIERS

An optical amplifier can be defined as a device that increases the power of an optical signal directly in the optical domain. The physical phenomenon responsible for amplification is stimulated emission, introduced by Albert Einstein [1]. Unlike spontaneous emission, the photons generated by the stimulated emission process present the same characteristics as the stimulating photons, which make the former indistinguishable from the last ones. This way, a light beam can be amplified when crossing a material medium where stimulated emission is stronger than absorption. In order to achieve this condition, the atoms of the material medium used in a fiber optic amplifier must be excited by what is called pump energy, part of which gets transferred to the amplifier light beam [2].

The development of the first amplifiers in single mode optical fibers dates back to the second half of the 1980s [3, 4]. This development opened the possibility of substituting the opto-electronic regenerators of communications networks, by optical amplifiers. Thus after the demonstration of fiber-optic amplifiers a lot of effort was made to rapidly achieve commercial devices.

The performance of optical amplifiers keeps improving by increasing their bandwidth, gain, spectral response flatness, output power and reducing noise figures. In addition, new types of amplifiers are becoming commercially available, not only for telecommunication amplification purposes, but also for a wide variety of optical processing tasks such as fiber lasers generation and sensors interrogation.

2.2.1 TYPES OF OPTICAL AMPLIFIERS

Optical amplifiers (OA) can be classified depending on different parameters. Table 2.1. shows this classification for the main types of optical amplifiers. Firstly, according to the amplifying material, amplifiers can be differentiated in optical fiber amplifiers (rare earth doped fiber, Raman and Brillouin) or semiconductor optical amplifiers (SOA). These last ones present advantages as their small size and their ability to be integrated in a substrate along with light sources, detectors and other optical waveguide type devices. However, their major drawbacks are their difficult connection to optical fibers, higher noise levels, and polarization dependence, in comparison with optical fiber amplifiers.

OPTICAL AMPLIFIERS			
Amplifying medium	Optical fiber		Semiconductor
Operating mechanism	Stimulated emission	Stimulated scattering	Stimulated emission
Main utilized families of OA	Er^{3+} (EDFA) Other rare earth	Raman Brillouin	SOA (Fabry-Perot) (Travelling wave)

TABLE 2.1. Main types of optical amplifiers.

Regarding to the operating mechanism we can distinguish between the stimulated emission on which are based rare earth doped amplifiers and SOAs, and stimulated scattering in the cases of Raman and Brillouin amplifiers. For the first group, the stimulated emission is achieved by using special doping ions into the fiber cores as in EDFAs. In semiconductor amplifiers, two amplifying structures have been used: initially Fabry-Perot cavities and nowadays, the travelling wave configuration. On the other hand, Raman and Brillouin amplifiers are based on stimulated scattering along standard fibers.

Less utilized optical amplification mechanisms are also possible, such as parametric interactions (OPAs) [5]. This family of amplifiers is based on the four-wave mixing (FWM) nonlinear process and it was reported for the first time by Stolen in 1975 [6].

Finally, it should be mentioned that planar waveguide amplifiers such as EDWAs [7-9] and Er doped Lithium Niobate waveguides [10, 11] have been also developed offering reduced dimensions but lower gains that their fiber counterparts.

The election of the amplification type will depend on the application to cover. For the lasers and sensors developed in this Ph.D. work, erbium doped and Raman amplifiers have been employed. Both amplifications methods are explained in detail below, but first Table 2.2 shows their typical characteristics.

PROPERTY	EDFA	RAMAN
Amplification band	1530-1560 nm	Depends on the pump wavelength
Gain BW	30 nm	25 nm per pump
Noise figure	3-5 dB	5-6 dB (lumped) Better with distributed amplification
Gain	25-40 dB (weak signal operation)	10-40 dB
Pump wavelength	980 or 1480 nm	100 nm (13 THz) shorter than amplified signal
Pump power	20-200 mW	0.35-5 W
Saturation power	10-20 dBm	10-25 dBm
Direction	Bidirectional	Bidirectional

TABLE 2.2. Comparison of the main characteristics of EDFA and Raman amplifiers.

2.2.2 ERBIUM DOPED FIBER AMPLIFIERS

An erbium doped fiber amplifier is an optical amplifier that consists of a fiber whose core has been doped during the manufacturing process with Er^{3+} ions. By pumping them at a suitable wavelength, optical gain is provided through population inversion and stimulated emission. Erbium is a rare-earth and it is important to note that there are others rare-earth utilized amplifiers whose main differences are the gain operation band and the energy levels system [12]. In this regard, EDFAs are the most commonly used amplifiers because they present an operation band in the 1.53 μm to 1.55 μm wavelength range, which corresponds to the C-band. This band is used nowadays for communications because of the low loss exhibited by silica fibers on these wavelengths.

The principle of operation (Figure 2.1) is based on getting the population inversion of the Er^{3+} ions at the E_2 energy level (0.80 eV). The energy difference from level E_1 to level E_2 corresponds to the 1550 nm band. Different transitions can be used to pump an EDFA. The different energy levels, E_3 (0.84 eV), E_4 (1.27 eV) and E_5 (1.54 eV) can be reached by pumping at 1.48 μm, 0.98 μm and 0.81 μm respectively. However the most efficient pump corresponds with 0.98 μm. The pump at 0.81 μm generates not only transitions from E_1 to E_5 but also, transitions from E_2 to a higher order energy level that not contributes to the amplification and therefore reduces the efficiency of the pump power. On the other hand, pumping at 1.48 μm requires longer fibers and higher powers than pumping at 0.98 μm because its wavelength corresponds with the tail of the EDFA's absorption band [13].

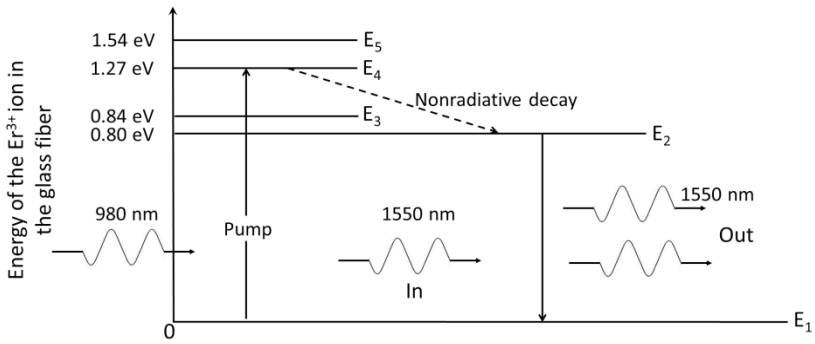

FIGURE 2.1. Energy diagram for the Er^{3+} ion into silica glass fiber medium. Light amplification by stimulated emission from E_2 to E_1 is also shown. Dashed arrow indicates radiationless transitions (energy emission by lattice vibrations).

By pumping at 0.98 μm, as it is shown in Figure 2.1, a transition from E_1 to E_4 is obtained. The electrons decay rapidly from this level to E_2, which has a long lifetime of about 10ms. This decay involves energy losses by radiationless transitions (phonon emissions) and is very rapid. The accumulation of electrons at E_2 leads to a population inversion between E_2 and E_1, and give rise to stimulated transitions of electrons from E_2 to E_1. Therefore, when the signal to be amplified at 1.55 μm cross the gain medium, and the population inversion condition is fulfilled, the input signal stimulates transitions of electrons from E_2 to E_1 achieving the amplification. It is important to note that in order to achieve light amplification, the stimulated emission must exceed the absorption or otherwise, the input photons will be absorbed to reach E_2.

Some of the electrons at E_2 will decay spontaneously from E_2 to E_1 which will give rise to unwanted noise in the amplified light signal (ASE). Further, if the erbium doped fiber is not pumped, it will act as an attenuator absorbing the 1.55 μm input signal increasing the population of the E_2 level which could be returned back to E_1 by spontaneous emission with a random behavior.

A typical scheme for a doped fiber amplifier is depicted in Figure 2.2. Light emitted by the pump lasers is coupled to the fiber through wavelength multiplexers which mixes the pump and the signal to be amplified.

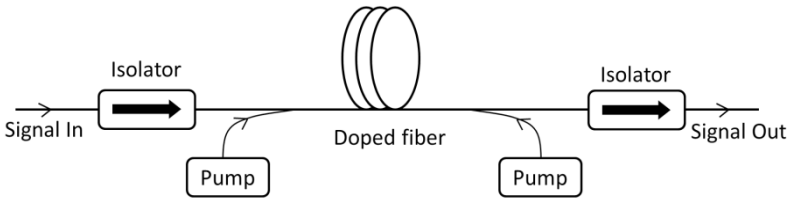

FIGURE 2.2. Typical scheme of an erbium doped fiber amplifier.

The pumping scheme can be bidirectional or unidirectional. In the latter case, there are two options, co-propagating pump if the pump and the signal have the same directions and counter-propagating if they have opposite directions. While counter- propagating pumping is usually more efficient in terms of providing gain than co-propagating one, this last configuration yields lower noise power [2]. Therefore, the optimum pumping scheme must be chosen for each particular situation.

2.2.3 FIBER RAMAN AMPLIFIERS

Fiber Raman amplifiers (FRA) are based on the stimulated Raman scattering (SRS), a nonlinear effect that occurs in optical fibers. During Raman scattering, light incident on a medium is converted to a lower frequency. A pump photon υ_p excites a molecule up to a virtual level (nonresonant state). The molecule quickly decays to a lower energy level emitting a signal photon υ_s in the process (Figure 2.3). The difference in energy between the pump and signal photons is dissipated by the molecular vibrations of the host material. These vibrational levels determine the frequency shift and shape of the Raman gain curve. The frequency difference between the pump and the signal photon ($\Omega = \upsilon_p - \upsilon_s$)is called the Stokes shift, and in standard transmission fibers with a Ge-doped core, the peak of this frequency shift is about 13.2 THz (~100 nm @ 1.5μm) and has a full-width at half maximum (FWHM) close to 6 THz [13, 14].

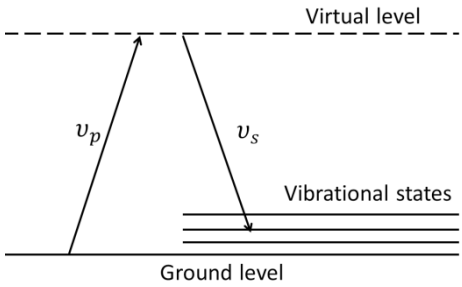

FIGURE 2.3 Schematic of the quantum mechanical process that takes place during Raman scattering.

SRS presents the following fundamental properties that must be taken into account to design a FRA [15-17]:

Firstly, the Raman gain is determined by the Stokes shift. Therefore, by choosing properly the pump wavelength, it could be achieved amplification almost at any wavelength. This spectral flexibility of Raman amplification allows to tailor the gain spectrum by combining multiple pump wavelengths to give an overall flat profile.

Secondly, Raman gain can be obtained regardless of the relative propagation direction of pump and signal. Consequently, Raman amplification can be achieved by forward, backward or bidirectional pumping with respect to the signal. Forward pump provides better performance from the noise viewpoint since the signal experiences amplification before decaying, but suffers from elevated nonlinear effects due to higher optical power levels. On the other hand, backward pump reduces the presence of nonlinear effects and also minimizes the transfer of relative intensity noise (RIN) from the pump laser to the signal [14]. Finally, bidirectional pumping offers the best option at the cost of an extra pump.

Thirdly, Raman amplifiers present a relatively poor pump absorption efficiency in comparison with other amplifiers such EDFAs. Therefore, they require longer fibers in order to achieve the same gain, about tens of kilometers in the case of single-mode fibers (SMFs). However, this distance can be reduced by using fibers with a smaller core, such as dispersion compensated fibers, accomplishing the amplification using few kilometers of these fibers [18].

Finally, in Raman amplifiers there are two main noise sources, amplified spontaneous scattering (ASS) and Rayleigh backscattering (RBS). The ASS is due to the amplification of spontaneously scattered photons, which is an unavoidable

by-product of gain in all optical amplifiers. It is bidirectional, has a random polarization and fills a broad bandwidth. RBS makes a marked contribution to the amplifiers total noise. This noise comes from the scattered light due to the local microscopic material inhomogeneities. The scattered light, as also happens to the input signal, is amplified along the fiber by the Raman effect, increasing the overall noise and, depending on the pump power level, may even generate a double Rayleigh backscattering. This last effect is the operation principle of random lasers, which are explained in section 2.3.3.4.

2.3 OPTICAL FIBER LASERS

A basic fiber laser scheme requires of two key elements, a gain material that provides amplification and an optical cavity that traps the light creating a positive feedback. Therefore, a fiber laser can be achieved by inserting an optical fiber amplifier in a cavity designed to provide optical feedback. In this case, the lasing condition is reached when the total gain in the cavity overcomes the total cavity loss.

The first fiber laser was demonstrated by E. Snitzer as early as 1961, by using a neodymium-doped glass fiber [19]. During the next years, other pioneering works were published [20, 21]. In 1970s Stone et al. realized the first silica-based fiber lasers [22, 23]. In 1980s the arrival of practical rare-earth based fiber amplifiers allowed the development of new fiber lasers based on these materials [24]. The initial emphasis was focused in neodymium (Nd) due to its high efficiency. However, thereafter Er doped fiber lasers would become as the best option. The first erbium doped fiber laser was developed in 1986 by Mears et al. [25]. Since that time, Er doped fiber lasers have received much attention from fiber-optical telecommunications, because, as was seen before, the ions of Er doped fibers have a radiative transition around 1.55 μm corresponding with the lowest loss transmission window in silica fiber [26].

On the other hand, Raman fiber lasers were demonstrated in the 1970s [27]. However, due to the high power pumps requirements of Raman amplification, practical lasers based on this technology appeared in the mid-nineties when high-power lasers became available.

2.3.1 MERITS OF FIBER LASERS

Fiber lasers have been thoroughly investigated in the last years allowing the development of commercial devices. This technology presents many advantages over other laser types. It is natural to contrast different kind of lasers, in particular when they are used in overlapping application areas. In this regard, fiber laser technology presents good features such as simplicity, compactness and reliability among others, which make them an attractive alternative for industrial applications. Some of the merits of fiber lasers are [26]:

High pump intensity: Since glass fiber cores can be made having only a few microns in diameter, the small mode field diameter of the waveguided pump light yields a much higher pump power density in a fiber laser than in a bulk device, and therefore a reduced lasing threshold. This feature is particularly important in three-level systems.

Signal and pump light waveguiding: The excellent mode overlap between the signal and pump light and the guaranteed parallelism between the two light beams allows efficient laser operation.

Independence of pump spot size and gain medium length: In a bulk gain medium, since the pump beam is divergent, there is a relationship between the optimum gain medium length and the pump spot size. However, for a fiber laser, the two parameters are independent. This added a degree of freedom which allows the doping density to be kept sufficiently low to avoid unwanted ion-ion interactions like cooperative up-conversion. The possibility of using an arbitrarily long gain medium allows us to utilize the weak pump absorption lines to excite the lasing transition. This can be of practical importance if that weak pump band were to coincide with the wavelength of commercially available laser diodes. It also permits the use of weak radiative transitions, as in the case of the L-Band erbium-doped fiber amplifiers.

Compact gain medium: In optical fibers the gain medium can be arbitrarily long, yet compact. High quality silica fiber can be coiled to small bend radii (about 10 mm) and can be packaged in many different ways.

Heat dissipation: The small diameter of the fiber allows a good heat dissipation, thus greatly reducing the occurrence of heat-related problems like thermal lensing, thermal gradient-induced stresses and reduced fluorescence at high temperature.

Beam quality: A single mode optical fiber will provide a diffraction limited beam up to very high output powers.

Robustness: An all-fiber laser cavity is much more robust to mechanical perturbations than a free-space laser. Also, there is no need for further optical alignment once every component is spliced.

Easy design: There are many possible laser cavity designs and configurations, which are less cumbersome and more stable than their bull optics counterparts.

However, on the other hand, fiber laser technology presents different challenges regarding to nonlinear effects, instability, requirements of equalization control in multiwavelength lasers and single longitudinal mode operation. These problems will be addressed in this Ph.D. work.

2.3.2 OPTICAL FIBER LASERS DEPENDING ON THE GAIN MEDIUM

Optical fiber lasers can be achieved by using one of the amplification processes presented before, being the most important families: Erbium doped fiber lasers (EDFL), Raman fiber lasers (RFL), Brillouin fiber lasers (BFL) and SOA based fiber lasers. Also, there are fiber lasers based on hybrid gains such as Brillouin/Erbium [28, 29], Raman/Brillouin [30, 31] and Raman/Erbium [32, 33] fiber lasers. Along this work different fiber EDFLs and RFLs have been developed, and their principal features are presented below

2.3.2.1 ERBIUM DOPED FIBER LASERS

Erbium doped fiber lasers (EDFLs) have become an essential reference within the family of fiber lasers. Their applications extend from sensing to telecommunications fields: dense wavelength-division multiplexing [34], fiber optic sensors interrogation [35], optical signal processing [36], sensor network multiplexing schemes [37], optical spectroscopy [38] and soliton sources [39] among others. Rare earth doped fiber lasers can operate in several wavelengths regions.

As seen before, the high interest in the 1.55 μm region prompted the development of commercial EDFAs for communications and their uses for developing EDFL. However, this kind of devices is optimized for communications and only is allowed the control of the pump power. In this regard the use of different sections and types of EDFs allows the control of different design parameters in the EDFLs development, which are described below.

Firstly, the doped fiber length is an important factor that affects to the laser threshold, slope efficiency and wavelength. Unpumped fiber acts as a strong ab-

sorber at the laser wavelength, so low pumped doped fiber sections at the end of the amplifier increase the threshold. Therefore there is a trade-off between the fiber length and the available pump power. The length of the fiber also affects to the laser wavelength. This is due to the non-flat response of EDF. If the fiber is too long, the farthest fiber end from the pump source strongly absorbs the signal, mainly at the short wavelengths side of the gain spectrum where absorption is stronger. Finally, the length affects to the number of longitudinal modes in the laser, been this number higher when the length is increased. This last point is explained in detail in section 2.3.3.

Secondly, the concentration of Er in the fiber is another factor to be taken into account. There are studies showing that for a high concentration of Er the threshold is increased, raising also the pump power requirements and reducing the efficiency [12]. However, on the other hand, with a high concentration of Er, the length of the doped fiber can be shorten significantly, and as it is mentioned before, this fact allows the reduction of the number of longitudinal modes in the laser.

Another aspect is the pump wavelength. As it was seen in section 2.2.2, EDF can be pumped at different wavelengths, but the most used are 0.98 μm and 1.48 μm. The 0.98 μm pump is more effective. However, pumping at 1.48 μm offers the possibility of using high power laser diodes. In practice, both have been used to develop EDFLs with excellent performances [37, 40-42].

Finally, the selection method of the operation wavelength is an important factor in the EDFL design. Among the different optical filtering mechanisms, the most widespread are Mach-Zehnder filters [26], arrayed waveguide gratings (AWG) [43], Fabry-Perot filter (FPF) [44, 45], Sagnac loop mirror [46], high-birefringence fiber filter [47] and fiber Bragg gratings (FBG) [37, 41]. Each type of filter has its own good features and disadvantages as well, but the last group is the preferred. EDFL with FBGs can be tuned continuously while exhibiting a narrow line width. Along chapter 3 different EDFL with many of these filter mechanism are presented.

EDFLs present different challenges regarding to the stability and the multiwavelength operation. Two of the main reasons for this: the homogeneous broadened gain and longitudinal modes of the laser cavity will be explained in sections 2.3.2.3 and 2.3.4 respectively.

2.3.2.2 RAMAN FIBER LASERS

Raman fiber lasers (RFL) exploit stimulated Raman scattering effect to overcome the fiber loss and to create a positive feedback at the shifted Stokes frequen-

cies using the transmission fiber itself. A typical RFL consist of a fiber resonator in which SRS shifts the spectrum of the radiation from pump (or combination of pumps) propagating along the fiber, to lower frequency (≈13 THz) Stokes components. This new wavelength can be partially trapped into the laser cavity with the help of FBGs or other wavelength selective methods [48].

RFLs have been thoroughly investigated and have been proposed for their utilization in different fields due to their properties [48-50]. Their capability of multiwavelength operation makes them attractive continuous wave (CW) sources in applications such as long distance remote sensing [51, 52], optical tomography or super continuum generation [53, 54].

There are three main parameters to be taken into account in the design of a RFL: the pump source, the fiber wherein is generated the Raman effect and the wavelength selection method.

Firstly, regarding to the pump source, there are also three main requirements that it must fulfill in order to optimize the RFL performance: it should be unpolarized due to the polarization dependence of the Raman gain; it should be able to pump hundreds of milliwatts due to the relative low gain coefficient of the Raman gain; finally, the spectrum of a particular pump should be relatively broad, a few nanometers, in order to avoid the onset of Brillouin scattering [55].

Also, in reference to the pump source, is important to remark that, as seen in section 2.2.3, Raman gain can be achieved at any wavelength as long as the pump wavelength is properly chosen. Therefore, multiple pumps can be used to broad and flatten the RFL spectrum. However when different pumps are used, is important to take into account that, for a flattened spectrum, it will be necessary higher pump powers for shorter wavelengths, because all pumps interacts through SRS along the fiber and some power is transferred to longer wavelengths pumps within the amplifiers [56].

Secondly, we have to consider the gain medium. As seen in section 2.2.3, in Raman amplification the fiber acts as the gain medium. The properties of the fiber can determinate the behavior of the RFL. Therefore, the choice for a RFL is based on five key points: to increase the gain coefficient, to reduce the effective area, to decrease the fiber loss, to reduce the splice loss, and the kind and quantity of dopant used [57].

Thirdly, different techniques have been used to provide feedback and select the emission wavelengths. Ring and linear cavities have been demonstrated utilizing different filtering structures, most of them similar to those used in EDFLs: Fabry-Perot filters [58], Sagnac filters [59] , fiber loop mirrors [60] and FBGs [37]. Howev-

er, nowadays there is another configuration based on random cavities, which has a growing interest because of this kind of RFL not presents longitudinal modes [61, 62]. This point will be analyzed in section 2.3.3.4.

Finally, unlike EDFAs, stimulated Raman effect presents an inhomogeneous broadened gain, which improves the fiber laser stability at room temperature [37]. This point is discussed in detail in the next section.

2.3.2.3 LINE SHAPES

Measurements of spontaneous transitions show line shapes with measurable width, which indicates a source of line broadening. There are two separate conditions that will lead to line broadening. In the first, the atoms are all assumed to be identical, so the energy difference between the two levels is the same for all atoms. This leads to homogeneous line broadening. In the second alternative, inhomogeneous line broadening, the atoms are assumed to be in slightly different environments, so the energy difference between their two states is not all the same [63].

Both cases are depicted in Figure 2.4, where the red and black lines represent the unsaturated and saturated gain curves respectively.

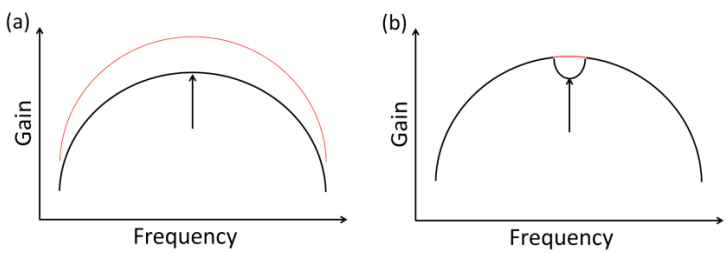

FIGURE 2.4. Effect of a saturating signal on the gain curve depending on the type of atomic transition spectral broadening. (a) Homogeneous broadening, (b) inhomogeneous broadening.

As seen, in a homogeneous gain medium gain is saturated uniformly over all frequencies. However, in an inhomogeneous medium, the gain is not saturated evenly for all frequencies. The saturation occurs mostly for the channels around the saturating signal. Thus, it is possible to have a strong gain at certain frequencies even under strong saturation.

Many phenomena determine the linewidth of an atomic transition. For free ions, the intrinsic linewidth broadening is related to the lifetime of the levels (*i*,*j*) involved in the transition by [26]:

$$\Delta\omega_a(i,j) = \frac{1}{\tau_i} - \frac{1}{\tau_j} \qquad (2.1)$$

Where $\tau_k = \tau_{R,k} + \tau_{NR,k}$ is the level lifetime, $\tau_{R,k}$ is the radiative lifetime and $\tau_{NR,k}$ is the non-radiative lifetime. When ions are incorporated into a glass matrix, the high frequency lattice vibrations generate phonon broadening. For solid-state lasers the phonon broadening is the dominant effect.

Regarding to the two gain media used in this work for fiber lasers development, it is well known that EDF is a homogeneous gain medium at room temperature; whose homogeneous linewidth exceeds 10 nm. This fact leads to strong mode competition and unstable lasing, thus it is difficult to obtain stable multiwavelength EDFL [64-67]. On the other hand, Raman amplification is characterized by its inhomogeneous broadening. This reduces considerably the modes competition and therefore allows to obtain more stable fiber lasers than EDFL ones.

2.3.3 FIBER OPTIC LASER CAVITIES

The most used configurations to design the cavity of fiber lasers are: Fabry-Perot (or linear cavity) and ring cavity. As can be seen next, both cavities present similar features, but the most important is their resonant behavior, which results in design challenges due to the limitations that impose longitudinal modes. However, recently a third type of cavity based on distributed random mirrors has attracted much interest due to its properties, concretely the absence of longitudinal modes. In this section, these three fiber laser cavities and their main properties are presented.

2.3.3.1 LINEAR CAVITY FIBER LASERS

In a linear cavity fiber laser, the gain medium is placed between two high-reflecting mirrors. Figure 2.5 shows a schematic of a linear cavity fiber laser by using two identical FBGs as mirrors.

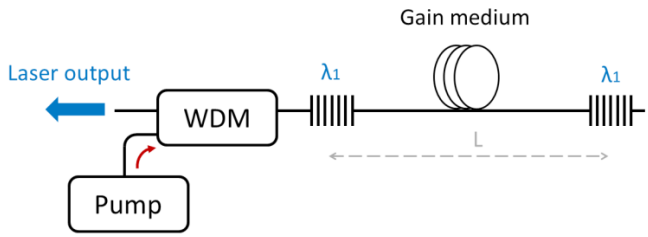

FIGURE 2.5. Schematic of a linear cavity fiber laser.

In these kinds of cavities, the light oscillates backwards and forward. The output mirror transmits a constant fraction of the light, reflecting the rest back into the cavity. This fact is important since it allows the laser to reach the equilibrium state. Thus, the power levels both inside and outside the laser become constant.

This reflective configuration generates a resonant condition that depends on the fiber length. The waves reflected from the end mirrors interfere constructively and destructively generating strongly amplification or canceling the laser output, respectively. The following equation defines the resonance separation of the longitudinal modes generated in a linear cavity fiber laser:

$$\Delta\lambda = \frac{\lambda^2}{n \cdot 2L} \qquad (2.2)$$

Where λ is the operation wavelength of the laser, *n* is the refractive index of the fiber and *L* the length of the cavity. The maximum number of modes of one emission line is limited by the bandwidth of the reflectors, and can be calculated by using:

$$N = \frac{FWHM_{reflector}}{\Delta\lambda} \qquad (2.3)$$

Where *N* is the number of longitudinal modes into an emission line of the laser, and FWHM is the full-width at half maximum of the reflector.

Linear cavities are ideal for compact single-longitudinal mode fiber lasers due to their short length, in the order of centimeters. This fact in combination with the development of high concentration EDF, makes it possible to achieve short cavities with high output powers [68, 69].

2.3.3.2 RING CAVITY FIBER LASERS

In a ring cavity fiber laser, the gain medium is placed inside the ring. Figure 2.6 shows a schematic of a fiber ring without mirrors. Ring cavities can obtain laser emission without a mirror. There are different methods to select a particular lasing wavelength in these lasers. The most extended method is the use of FBGs in reflection, nowadays in combination with circulators. This configuration not only allows the wavelength selection but also the ASE filtering, improving the OSNR of the fiber laser [41]. Other techniques are based on different interferometric filters: Fabry-Perot [70], Mach-Zehnder [71], Sagnac [72], polarimetrics [73] and others. These last kinds of filters are usually used for multiwavelength lasers generation with equally spaced emission lines. However, they present the problem of the difficult equalization of the individual wavelengths and the amplitudes of the emission lines are defined by the shape of the gain spectrum.

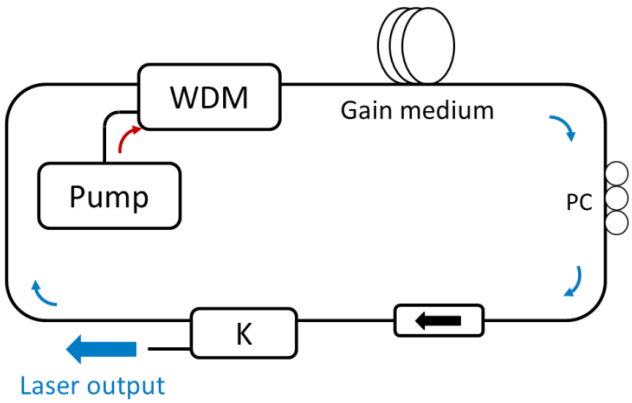

FIGURE 2.6. Schematic of a unidirectional ring cavity fiber laser.

Usually ring cavities use the gain provided by the gain medium more efficiently in comparison with linear cavities [26]. In a ring cavity, the light can do round trips in both directions. Therefore, is often necessary to ensure unidirectional laser operation through the insertion of isolators or optical circulators. These optical components avoid the spatial hole burning effect, presented in next section. Theoretically, a polarization controller is also needed for conventional doped fiber that does not preserve polarization. However, some works have demonstrated that the polarization control has reduced influence on the multiwavelength regime [74].

As in linear cavities, ring configurations also generate a resonant condition that depends on the fiber length. Specifically, the separation of their longitudinal modes is twice the achieved using the same cavity length in linear cavities, and it is defined as:

$$\Delta\lambda = \frac{\lambda^2}{n \cdot L} \qquad (2.4)$$

2.3.3.3 SPATIAL HOLE BURNING

At this point, it is important to introduce a concept that affects directly lasers based on resonant cavities. Spatial hole burning (SHB) is responsible for shaping the population inversion of the gain medium in standing-wave laser cavities [75]. The SHB process is shown in Figure 2.7.

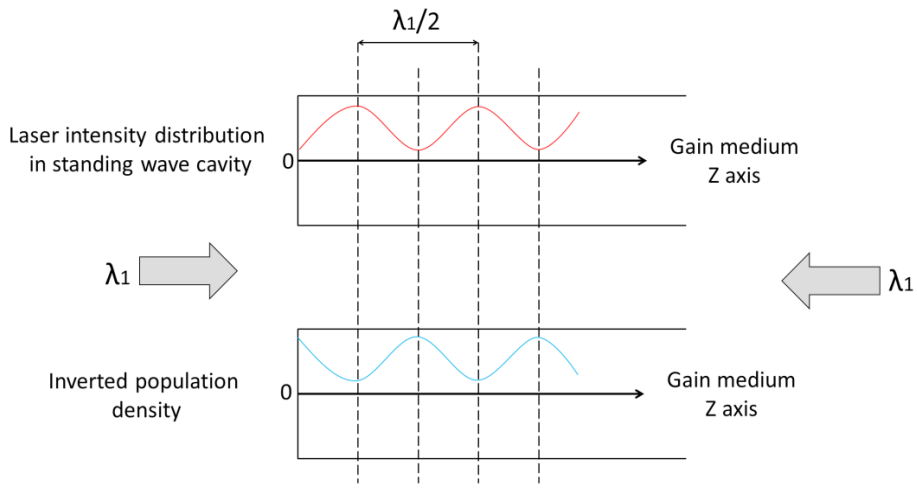

FIGURE 2.7. Laser intensity distribution and inverted population density within a fiber laser due to spatial hole burning.

When two waves at λ_1 travel counter-propagated along the gain medium, they will produce an interference called standing-wave, whose period is half the wavelength (red line in Figure 2.7).This process generates periodic minima of signal intensity along the gain medium and therefore, at those minimum points there are not stimulated emission. As can be seen, the inverted population distribution

has a periodical profile that is π radians out of phase with the laser intensity profile within the gain medium. Such a spatial distribution leads to wasted gain [76].

2.3.3.4 RANDOM DISTRIBUTED FEEDBACK FIBER LASERS

Random distributed feedback (RDFB) fiber lasers have been the subject of intense theoretical and experimental studies [61]. Random lasers are characterized by open-cavities or mirror-less-cavities. This means that, unlike conventional fiber lasers, their principle of operation relies on distributed scattering events along the fiber cavity.

Figure 2.8 shows a basic RDFB fiber laser setup where standard single mode fiber is pumped from Z=0 towards both ends of each laser´s arm [77]. As seen before, optical fibers present material inhomogeneities due to the fiber's fabrication process. Owing to these inhomogeneities, Rayleigh scattering occurs and the backscattered light is amplified by the SRS effect in each point along the fiber. These amplified Rayleigh backscattering contributions also generate double backscattering events along the cavity. All these random events produced inside the cavity generate, when the gain overcomes the losses, the random distributed feedback lasing process.

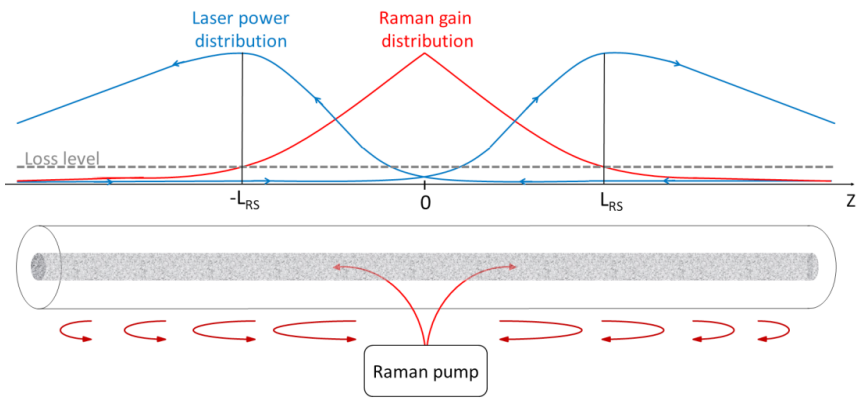

FIGURE 2.8. Schematic diagram of the Raman gain (red line) and laser generated power (blue line) distributions in a random distributed feedback fiber laser.

There are three different basic configurations of the RDFB fiber lasers, which are shown in Figure 2.9. The first one is the forward-pumped configuration (Figure 2.9 (a)). In this configuration the pump power is co-propagated along with the lasing power towards the output. It can be formed by two fiber arms of length *L*. Alternatively, one of the arms can be substituted by a mirror placed at *Z*=0. The second case corresponds to a backward-pumped configuration (Figure 2.9 (b)). In this case the pump is counter-propagated to the fiber laser output. Its equivalent configuration also consist of a mirror placed at *Z*=0. Finally, the last configuration is a single-arm RDFB laser without any reflector (Figure 2.9 (c)), thus the laser is operated only by the RDFB.

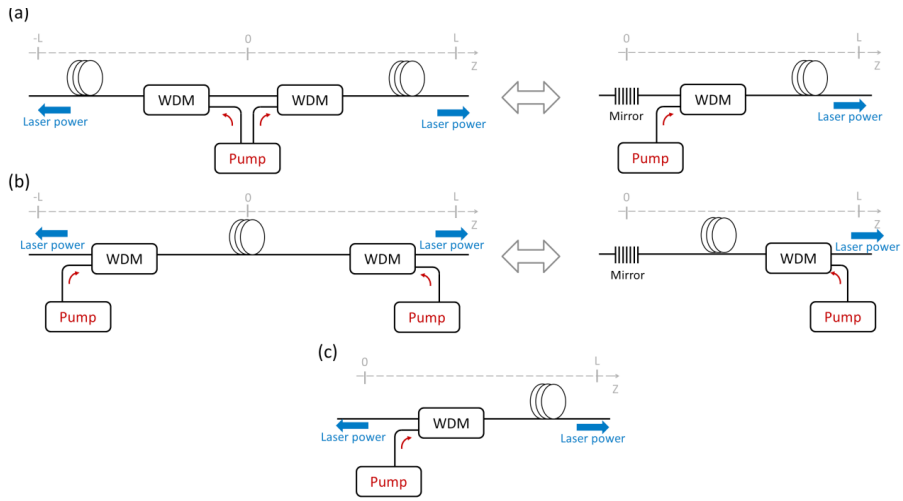

FIGURE 2.9. Schematic diagrams of the (a) forward-pumped, (b) backward-pumped and (c) single-arm RDFB laser configurations.

The fiber length required for lasing based on the RDFB can be estimated as follows [77]. Neglecting the pump depletion due to Stokes wave generation, the longitudinal distribution of the Raman gain $g_R P_P(Z)$ is defined by the pump power attenuation:

$$P_P(z) = P_0 \exp[-\alpha_P |z|] \qquad (2.5)$$

where $\alpha_P \approx 0.057\ km^{-1}$. Thus, the length of the amplification region estimated through the gain/loss balance condition, $g_R P_P(L_{RS}) = \alpha$, is:

$$L_{RS} = \frac{\ln(g_R P_0/\alpha)}{\alpha_P} \qquad (2.6)$$

The threshold condition, for each arm of the RDFB laser, in the long length limit $L \gg 2L_{RS}$ is defined by:

$$P_0 = \frac{\alpha}{g_r}\left(1 + \ln\left(\frac{g_r P_{th}}{\alpha}\right)\right) + \frac{\alpha_P}{2g_R}\ln\left(\frac{1}{\varepsilon}\sqrt{\frac{\alpha\alpha_P}{\pi}}\right) \approx 0.8\ W \qquad (2.7)$$

The most remarkable property of RDFB lasers in comparison with the cavities presented before is their absence of longitudinal modes. Random lasers have infinite distributed cavities along the fiber, achieving a continuous emission line as wide as the optical gain spectrum permits. This property avoids the mode competition improving the stability of the laser, and also allows the modulation of random fiber lasers without the mode-locking problems of the conventional fiber lasers configurations [18].

2.3.4 SINGLE LONGITUDINAL MODE FIBER LASERS

Single longitudinal mod (SLM) fiber lasers have recently attracted great interest because they can be potentially applied in dense wavelength division multiplexed (DWDM) communications, fiber sensing systems, high resolution spectroscopy, microwave generation and other fields.

As it was seen in the previous sections, fiber lasers based on resonant cavities presents longitudinal modes. Figure 2.10 shows the output spectrum of a multi-longitudinal mode operation fiber laser. As can be seen, the number of the laser modes is determined by the gain bandwidth, or by the filter bandwidth used for the emission line selection, as for example when using an FBG as a reflector.

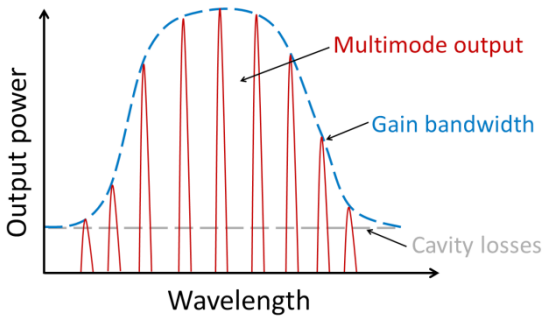

FIGURE 2.10 Cavity resonance modes for a multi-longitudinal mode operated fiber laser.

Longitudinal modes have high impact in the gain medium. In the case of homogeneous broadening, the waves associated with different modes within the same gain region are all competing for the gain. Each mode is attempting to grow towards reaching its saturation intensity by stimulating more emission into its wavelength. While the modes reach the saturation intensity, the gain curve begins to decrease. This process generates power and wavelength instabilities in the laser. On the other hand, for the case of inhomogeneous broadening, different longitudinal modes can operate somewhat independently if their natural linewidths do not overlap, since they are not competing for the same upper laser level species.

Along the last years different SLM fiber lasers have been demonstrated by using different techniques. In [78, 79] the SLM operation is guaranteed by using unpumped EDF as a saturable-absorber element. Another extended way is by using a multi-ring cavity configuration [80, 81] in which each ring cavity has different lengths and therefore different longitudinal modes separation. This way the resultant cavity modes are limited by multiplying the transfer functions of the rings. Also the SLM operation can be achieved through the use of narrow filters, such as for example a fiber Bragg grating Fabry-Perot structure [82].

The measurement of the SLM operation can be achieved in diverse ways; by using a high resolution optical spectrum analyzer [41], by beating the laser itself and detecting the presence of the beating modes in an electrical spectrum analyzer (ESA) [83] or by beating the laser with an external SLM or a laser without modes, detecting a single peak at ESA [84].

The SLM condition contributes not only to improve the stability of the laser but also to reduce the bandwidth of the emission line. For the measurement of the band-width (BW) of the SLM operated lasers developed in this thesis, we used a self-heterodyne method. This method is based on the use of part or the laser output itself as the local oscillator signal. Figure 2.11 shows the principle of the self-heterodyne method [85]. The laser output is divided into two paths by using a 3 dB coupler. The light through the upper branch is delayed by time τ_d using a single mode fiber. The signal in the bottom branch is modulated by a frequency f_S by using an optical modulator. The throughputs of both branches are mixed by using a 3 dB coupler and measured at an ESA.

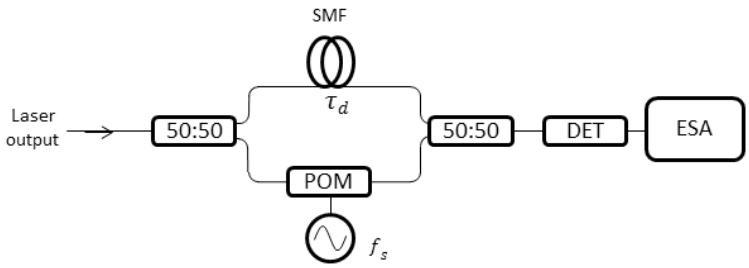

FIGURE 2.11. Schematic of the self-heterodyne method.

Once the spectrum has been detected, the next step is to fit it in order to determine if it shows a Lorentzian or a Gaussian shape. This point is very important because the measured bandwidth at ESA corresponds with twice the original value when the spectrum is Lorentzian, and $\sqrt{2}$ times the original when it is Gaussian.

2.3.5 MULTIWAVELENGTH FIBER LASERS

The term multiwavelength fiber lasers (MWFL) are used to denote lasers which simultaneously generate more than one coherent emission wavelength in a single cavity. MWFLs have attracted much attention in recent years, mainly because of their advantages and applications. Optical communication and sensing systems need multi-channel signals with high OSNRs and narrow bandwidth, in order to compensate the transmission loss and signal distortion in the transmission line.

MWFL have been widely studied, having been reported a number of structures by using different gain mediums [84, 86, 87] and through the use of different topologies for achieving the multiple lasing lines. As in the previous presented sections

about fiber lasers, the main techniques for the wavelength selection in MWFL are also based on the use of FBGs [84] , Sagnac loops [88], long-period fiber gratings [89] or other filtering techniques [86]. More recently, with the development of photonic crystal fibers, MWFLs based on this technology have been also reported: through the use of PCFs in a Sagnac configuration [90], or by entering the PCF into a ring cavity [91], or including a nonlinear PCF in combination with FBGs or with other selective filters [92].

As it was seen before, the stability of fiber lasers is especially important in telecommunications [34] and sensing applications [93]. Therefore much attention has been dedicated to laser output fluctuations in the development of the different fiber lasers and sensor systems presented in this thesis. For this reason, it is important to define the parameters used for their measurement. The instability is defined as the output power or wavelength variations for a given interval of time and a specific confidence level (*CL*), that is the probability value associated with a confidence interval, given as a percentage [94]. The confidence interval (*CI*) is the estimated range of values where the parameter of interest is included.

Depending on the *CL*, the confidence interval (CI_p) of the output power or the signal wavelength (CI_w) is defined. As a consequence, the instability of the output power and the signal wavelength is calculated within the corresponding *CI*. The CI_x, where *x* is *p* or *w* for the output power or the signal wavelength, respectively, is defined as:

$$CI_x = (Y_{cx} - FU_x, Y_{cx} + FU_x) \qquad (2.8)$$

Where Y_{cx} is the average of the output power or signal wavelength, U_x is the standard deviation, and *F* is the uncertainty factor that shows the *CL*.

As it was mentioned before, SLM condition in fiber lasers is extremely important for some applications. In this regard, MWFL presents an interesting property in order to achieve this condition. Previous works demonstrated that a SLM condition can be achieved by annihilating the mode competition when two emission lines are presented in a laser with similar power levels, due to the interaction of the seed light produced from one channel to the other and vice versa. In other words, one channel works as an auxiliary laser to the other [41, 95]. This point makes more important the control of the power of the emission lines and therefore the possibility of their equalization, a key point which has been taken into account in the development of the lasers presented in this Ph.D. work.

2.4 OPTICAL FIBER SENSORS

An optical fiber sensor may be defined as a device in which a parameter to measure (physical, chemical, biological or others), introduces modifications or modulations in some of the characteristics of light in an optical system [96]. The basic block of an optical sensor system is shown in Figure 2.12. The optoelectronic unit usually consists of a laser source whose signal is launched using an optical fiber towards the optical transducer. This element interacts with the parameter to measure, and experiments a change of one or several optical parameters: intensity, phase, wavelength or polarization. These changes are detected in the optoelectronic unit by a detector and then, measured.

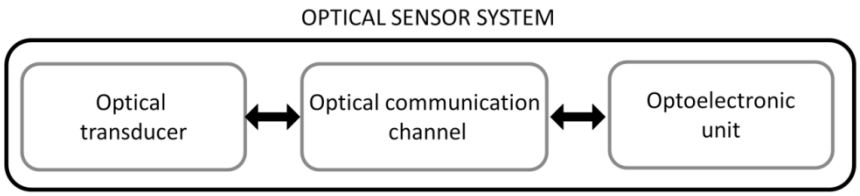

FIGURE 2.12. Conceptual block diagram of a general optical sensor system.

Optical fiber sensors can be classified depending on different parameters; the domain of the magnitude to be measured, the nature of the optical transduction process, the measurand modulation and finally, the spatial distribution of the measurand. This generic classification is presented in Table 2.3. A deep state of the art of each fiber-optic sensor type can be found in [96].

OPTICAL FIBER SENSORS			
Magnitude domain	Transduction nature	Measurand modulation	Measurand spatial distribution
Mechanical Thermal Electromagnetic Radiation Chemical Flow, turbulence Biomedical	Intrinsic Extrinsic	Intensity Phase Wavelength Polarization	Point Distributed Quasi-distributed

TABLE 2.3. General classification of fiber-optic sensors.

2.4.1 MERITS OF FIBER SENSORS

Optical fiber sensors have been thoroughly investigated in the last decades allowing the development of new sensor transducers, networks and interrogation techniques, in research as well as in commercial field. Some of the merits of optical fiber sensors are [97]:

Dielectric material: Optical fiber sensors are usually comprised exclusively of dielectric materials which are in general chemically inert. This fact confers them electrical and chemical passivity that, along with the nature of the optical signal used in the interrogation process, makes them high interesting for applications with harsh environments such as corrosive, electromagnetic or with risk of explosion.

Small size: Given the sizes and nature of optical fibers, small and lightweight sensors can be fabricated, facilitating their integration with almost all applications.

Sensor quality: Their sensitivity, dynamic range and resolution can potentially be much greater than conventional sensors. These parameters can be improved by using interferometric techniques.

High fusion point: Optical fiber sensors can withstand relatively high temperatures thanks to the high fusion point of the optical fiber. Using special coatings it is possible to make optical transducers that can work adequately at very high temperature ranges.

Remote monitoring: The low loss of optical fibers and their full compatibility with the fiber transducers, allows the remote monitoring of fiber sensors, at tens of kilometers. This means that the optical interrogation system can be installed far from a hostile environment in which the sensor is placed.

Multiplexing: Due to the good features of optical fibers and in combination with different techniques, optical fiber sensors can be multiplexed in order to reduce the number of active elements needed and therefore, achieving a more cost-effective system.

Biocompatibility: Due to this property of optical fiber sensors, in combination with the possibility of making small and simple interfaces between the sensor and the measurement point, makes them very suitable for detection of biomedical variables.

However, on the other hand, optical fiber sensors sometimes present different challenges such as undesired effects generated by the interrogation method,

nonlinearities of the fiber, noise levels, complex handling of the transducers, the influence of undesired measurand variable on the desired variable, and the cost of the system.

2.4.2 MULTIPLEXING AND REMOTE SENSING

Multiplexing is defined as the simultaneous transmission of two or more information channels along a common path [98]. As it was seen before, a fiber sensor system includes three main parts or subsystems: the sensing elements or transducers, the optical fiber channel and the optoelectronic unit. Among these three subsystems, the optoelectronic one is the most expensive and therefore, by increasing the number of sensors in the system, the cost per sensing element decreases. Another significant point that may justify the cost of the optoelectronic unit is the possibility of using it for remote sensor monitoring. This fact in combination with a suitable multiplexing method allows the use of one optoelectronic unit for interrogating several sensors located at hundreds of kilometers.

The design of sensor systems with multiplexing and remote monitoring abilities requires of many passive and actives elements as couplers, switches, optical amplifiers and filters. These elements come from the fiber-optic telecommunications field. Therefore, this fact has helped to a fast growing of the multiplexing and remote sensor systems.

With regard to multiplexing, a variety of multiplexing techniques based on different modulation formats have been developed: Wavelength Division Multiplexing (WDM), Time Division Multiplexing (TDM), Frequency Division Multiplexing (FDM), Coherence Multiplexing (CM) and Polarization Division Multiplexing (PDM) [99]. Figure 2.13 shows these multiplexing methods.

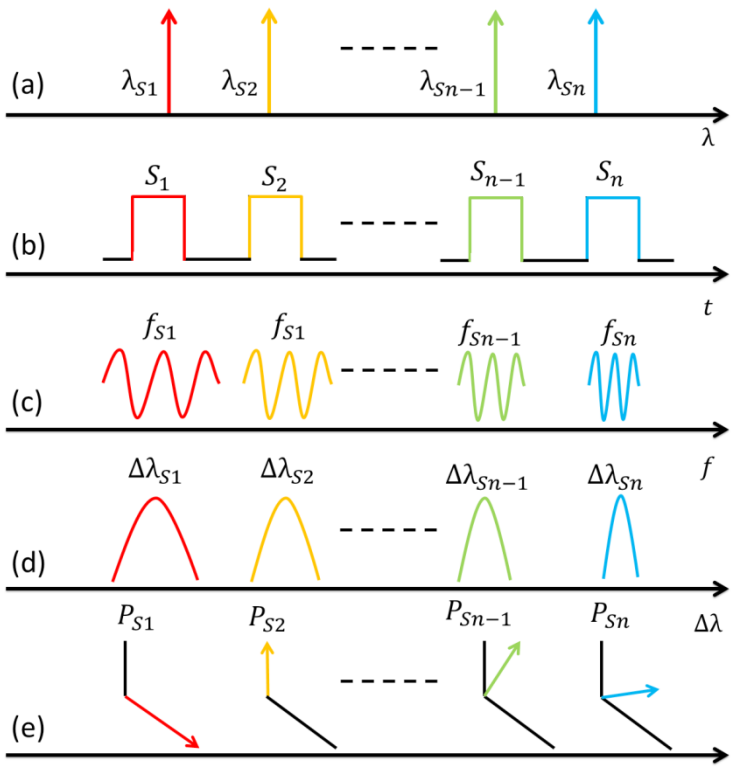

FIGURE 2.13. Multiplexing modulation formats: a) WDM, b) TDM, c) FDM, d) CM and e) PDM.

Wavelength Division Multiplexing

This technique is based on the principle of that each sensor in the network modulates an assigned wavelength band independently of the remaining sensors on the network. The interrogation of a WDM sensor network could be achieved by using a tunable laser [100], a broadband source [101, 102], or even, by using some sensors as "sensing mirrors" which contributes to develop a multiwavelength fiber laser that actuates as "self-interrogator" [51, 103].

Time Division Multiplexing

TDM networks are based on the assignment of a different time slot for each sensor. The typical TDM systems achieve this by using a pulsed source. This way, using optical delay elements (fiber coils), the modulated signal by the sensor is detected in the different slot times [104, 105].

This technology presents the advantage that only a common source and detector are needed. However, they precise a pulsed source (or an external modulator), a wide-band detector and also delay elements.

Frequency Division Multiplexing

FDM topologies use a different sub-carrier frequency of the light for each transducer [106].The issue of source-induced optical coherent noise can be reduced in FDM networks by using multiple sources.

Coherence Multiplexing

This technique is able to multiplex several interferometric sensors onto a single fiber by using the coherence properties of a short coherence length light source. In a CM network, each sensor presents an optical path difference (OPD) which is within the coherence length of the source. The interrogation of the sensing network is carried out scanning the OPD of each sensor in the receiver interferometer [107].

Polarization Division Multiplexing

PDM is based on the assignment of a polarization state to each sensor. The major problems of this technique are the polarization changes that occur continuously in standard fibers and cross-polarization modulation. Consequently it is necessary the use of maintaining polarization elements in the network.

On the other hand, as stated before, remote sensing is another important merit in fiber optic multiplexing sensor systems. In general, the main idea behind the concept of remote sensing is the continuous monitoring of structures from a central station located tens or hundreds of kilometers away from the field, allowing the central station to be far from hostile environments where sensors are placed. The major challenge is to achieve the maximum network distance without the necessity of electrical power feeds in the remote locations. In this regard, the limiting factors are not only the attenuation of the fiber but also the noise generated by the Rayleigh scattering and the broadening of the source due to the SBS [108].

In Table 2.4 a state of the art of remote discrete fiber optic sensor systems, for distances higher than 50 Km, is presented. The contributions related to this thesis are also included in bold.

YEAR/ REF.	NETWORK LENGTH	LASER SOURCE/ AMPLIFICATION TYPE	SENSORS MULTIPLEXED	OSNR
2005/[51]	50 km	Raman	2	50 dB
2007/[109]	120 km	External laser source/ No amplification	1	24 dB
2008/[110]	230 km	EDFA	1	4 dB
2010/[111]	100 km	Raman+EDFA	1	30 dB
2011/[112]	100 km	Raman+Brillouin	4	30 dB
2011/[113]	155 km	Raman+EDFA +Brillouin	2	10 dB
2011/[114]	**200 km**	**Raman**	**4**	**22 dB**
2011/[114]	**250 km**	**Raman**	**4**	**8 dB**
2011/[115]	253 km	OTDR/ No amplification	1	3 dB
2012/[116]	50 km	OTDR/ EDFA	2	25 dB
2012/[117]	150 km	Raman	3	1.5 dB
2013/[118]	75 km	Raman+EDFA	6	30 dB
2013/[119]	50 km	FBG Interrogator/ Raman	7	10 dB
2013/[120]	50 km	Raman	1	---
2013/[121]	**50 km**	**EDFA**	**2**	**46 dB**
2013/[103]	200 km	Raman	11	10 dB
2014/[122]	100 km	OTDR/ No ampflication	1	23 dB
2014/[123]	100 km	EDFA	4	25 dB
2014/[124]	50 km	EDFA+Raman	11	20 dB
2015/[125]	100 km	Raman	2	30 dB

TABLE 2.4. State of the art in remote fiber optic point sensor systems.

2.4.3 FIBER BRAGG GRATINGS

A fiber Bragg grating is an optical filter based on a periodic perturbation of the refractive index along a fiber length. FBGs have been thoroughly used as sensor elements for physical and chemical measurements [126] and can be used as narrowband filters/reflectors in fiber lasers. Figure 2.14 shows the working principle of the FBG.

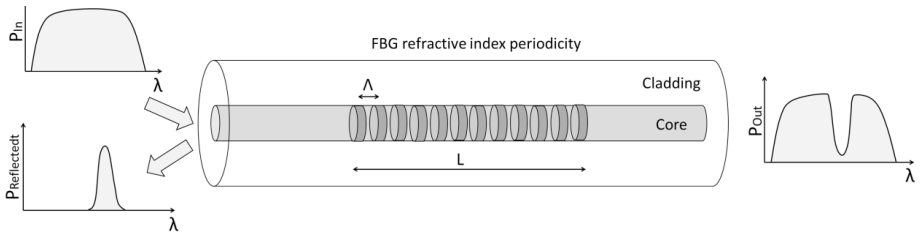

FIGURE 2.14. Operation principle of a fiber Bragg grating.

FBGs present a resonance frequency which is defined by

$$\lambda_B = 2n_{eff}\Lambda \qquad (2.9)$$

where n_{eff} is the effective refractive index of the fiber core and Λ is the pitch, or period of the refractive index modulation. When the incident light match with λ_B, an amount of light proportional to the FBG reflectivity is reflected and the rest is transmitted.

A variation of FBGs, that also have been used along this thesis, are the phase shift fiber Bragg gratings (PSFBGs). These elements present a phase shift in the periodic perturbation of the refractive index, generating a narrow band pass at the central wavelength (Figure 2.15) [127].

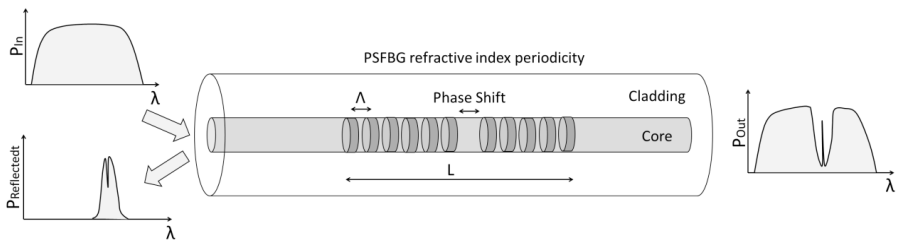

FIGURE 2.15. Operation principle of a phase shift fiber Bragg grating.

The central wavelength of the FBGs and PSFBGs are defined by Equation 2.9. As can be seen, it depends on n_{eff} and Λ, parameters which are susceptible to temperature and strain changes. Therefore, the FBG/PSFBG wavelength experiments a shift according to these physical parameters.

When longitudinal strain is applied to FBGs or PSFBGs, these components experiment an expansion of the grating pitch and axial compression of the fiber. This

also induces modifications of the refractive index due to photoelastics effects. The relative wavelength shift, $\Delta\lambda_B$, for an applied longitudinal strain $\Delta\varepsilon$ is given by

$$\Delta\lambda_B = \lambda_B(1-\rho_\alpha)\Delta\varepsilon \qquad (2.10)$$

Where p_α is an effective optical-strain constant defined as:

$$\rho_\alpha = \frac{{n_{eff}}^2}{2}[\rho_{12} - \nu(\rho_{11}+\rho_{12})] \qquad (2.11)$$

Where p_{11} and p_{12} are the components of the strain-optic tensor, and ν is the Poisson's ratio. For a typical optical fiber p_{11}=0.113 ε^{-1}, p_{12}=0.252 ε^{-1},ν =0.16, and n_{eff} =1.482 [126].

The normalized strain response at constant temperature is found to be [102]

$$\frac{1}{\lambda_B}\frac{\Delta\lambda_B}{\Delta\varepsilon} = 0.78\cdot 10^{-6}\ \mu\varepsilon^{-1} \qquad (2.12)$$

With regard to the temperature effect, this occurs principally through the effect on the induced refractive index change. However, the thermal expansion affects also to the Bragg pitch. The relative wavelength shift, $\Delta\lambda_B$, for an applied temperature change of ΔT, is given by:

$$\Delta\lambda_B = \lambda_B(\alpha-\xi)\Delta T \qquad (2.13)$$

Where α and ξ are the thermal expansion and the thermo-optic coefficients, respectively. For a standard fiber these coefficients are approximately $\alpha = 0.55\cdot 10^{-6}$ °C^{-1} and $\xi = 8.6\cdot 10^{-6}$ °C^{-1} [126].

The normalized temperature response at constant strain is found to be [102]:

$$\frac{1}{\lambda_B}\frac{\Delta\lambda_B}{\Delta T} = 6.67\cdot 10^{-6}\ °C^{-1} \qquad (2.14)$$

Thus fiber Bragg gratings present a resonance which changes with physical parameters such as temperature and strain. Therefore, this property makes FBGs interesting transducers for sensing.

There are different techniques for the interrogation of sensors based on FBGs, showed in Table 2.5. They can be grouped in two main families, passive and active detection schemes. Passive techniques are based on the detection of wavelength or amplitude variations due to the measurand, by using conventional spectrometers, which are widely used in laboratories. However, high precision optical spectrum analyzers are unsuitable for real sensor systems due to their high cost, large size and slow scanning speed.

The election of the interrogation method depends on several factors such as precision, sensitivity, sampling frequency, number of sensors being multiplexed, range of the measurement, and the cost of the interrogation system. In this regard, active detection has been used to improve these parameters, by using tracking, scanning or modulating techniques. However, is important to highlight that these improvements require more complex systems.

SCHEME TYPES	TECHNOLOGIES	REFERENCES
Passive detection scheme	Linearly wavelength-dependent device	[128-130]
	CCD spectrometer	[102, 131]
	Power detection	[132, 133]
	Identical chirped-grating pair	[134]
Active detection scheme	Fabry-Perot filter	[101, 135]
	Mach-Zehnder interferometer	[136, 137]
	Fiber Fourier transform spectrometer	[138, 139]
	Tunable filter	[124, 140, 141]
	Matched FBG pair	[142, 143]
	Michelson interferometer	[144]
	LPG pair interferometer	[145]

TABLE 2.5. Fiber Bragg grating sensors interrogation types.

2.4.4 MICROSTRUCTURED AND PHOTONIC CRYSTAL FIBERS

The development of optical fiber sensors experienced a substantial change with the appearance of photonic crystal fibers (PCFs) in 1996 [146]. PCF geometry is characterized by a periodic array of air holes running along the entire length of the fiber, which surround a solid or hollow core. Microstructured optical fibers (MOFs) fulfill this geometrical characteristic, however PCFs are those that also satisfy a photonic band gap (PBG) light guidance condition [147].

MOF configuration provides unprecedented properties for sensing in comparison with standard fibers: the possibility of light guiding in a hollow core; the filling of the holes with gases or liquids, improvement of the strain sensitivity, temperature insensitive sensors [148], and other advantages which are described in the following sections.

Due to their versatility, MOF sensors have been used to measure a wide variety of physical and chemical parameters: bend/curvature [149-152]; strain/displacement [153-155]; temperature [156, 157]; simultaneous strain/temperature [158-161];electric field [162, 163]; magnetic field [164, 165]; pressure [166, 167]; torsion [168, 169]; refractive index [170, 171]; vibration[172]; DNA [173]; humidity[174, 175]; and gases [176-178].

2.4.4.1 PCF/MOF GEOMETRY AND GUIDANCE MECHANISMS

Standard fibers are based on a doped solid-core enclosed by a solid-cladding (Figure 2.16 (a)). This configuration generates a refractive index difference between the core and the cladding that allows the light guidance. Microstructured optical fiber's geometry consists of a solid or hollow core, enclosed by an array of air holes running along the entire length of the fiber. Therefore, MOFs can be divided in two families based on their geometry: solid-core and hollow-core. Solid-core MOFs present a solid-core that can be surrounded by a periodic array of microscopic air-holes (Figure 2.16 (b)) or by a configuration of big holes obtaining a suspended-core MOF (Figure 2.16 (c)). On the other hand, hollow-core microstructured fibers present an air-hole as core, which is enclosed by a microstructured air-hole cladding (Figure 2.16 (d)).

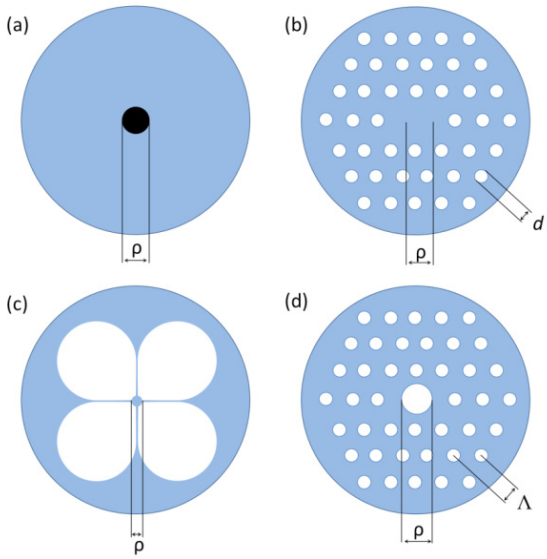

FIGURE 2.16. Drawing of the cross section of (a) standard fiber, (b) Solid-core MOF, (c) Suspended-solid-core MOF and (d) Hollow-core MOF. Colors: Blue-silica, black-doped silica, white-air.

There are three parameters to take into account in the design of a MOF; the diameter of the core (ρ), the diameter of the air-holes in the cladding (*d*) and the distance between the center of two consecutive air holes, or pitch (Λ). These three physical parameters in combination with the choice of the refractive index, make the fabrication of MOFs more flexible than standard fibers. There are four different guidance mechanisms depending on the MOFs geometry and core/cladding materials [179]:

- Index-guiding – guides in a solid-core through modified total internal reflection (TIR)
- Hollow-core – guides through PBG effect in a hollow-core
- All-solid PBG - guides by PBG anti-resonant effect in a solid-core
- Hybrid – guidance through simultaneous PBG and TIR

The following sections are focused on solid-core MOFs because these fibers have been used for the development of the MOFs sensors of this Ph.D. work.

2.4.4.2 MODAL CHARACTERISTICS

The modal behavior of standard step-index fibers is often described by the normalized frequency or V-parameter:

$$V_{standard\ fiber}(\lambda) = \frac{2\pi}{\lambda} a \sqrt{n_{co}^2 - n_{cl}^2} \qquad (2.15)$$

Where a is the core radius and, n_{co} and n_{cl} are the refractive index of the core and cladding, respectively. The V-parameter determines the cutoff condition and the number of modes supported by a fiber [180]. For a single mode fiber, V must be less than 2.405.

In solid-core MOFs the core refractive index is greater than the average index of the cladding, consequently the fiber guides via total internal reflection as in standard fibers. Therefore, there are guided modes characterized by a propagation constant β available to light in the core but not in the cladding [181]:

$$\beta_{FSM} < \beta < kn_{co} \qquad (2.16)$$

Where β_{FSM} is the propagation constant of the fundamental space-filling mode, $k = 2\pi/\lambda$ is the wavenumber and n_{co} is the refractive index of the fiber core. FSM is defined as the fundamental mode of the infinite MOF cladding if the core is absent, therefore β_{FSM} represents the maximum β allowed by the cladding. The lower limit for β in a step-index fibers is kn_{cl}, in the same way for a MOF:

$$\beta_{FSM} = kn_{cl(MOF)} \qquad (2.17)$$

Consequently in solid-core MOFs the TIR guidance mechanism depends on the nature of the core and the air-holes arrangement. Thus, the V-parameter for these fibers is defined as [181, 182]:

$$V_{Solid\ core}(\lambda) = \frac{2\pi}{\lambda} \Lambda \sqrt{n_{co}^2 - n_{cl(MOF)}^2} \qquad (2.18)$$

Where Λ is the fiber pitch and $n_{cl(MOF)}$, is the cladding effective refractive index defined as in equation 2.17.

However, for the case of a suspended-core MOF, due to its structure, the core can be considered as a micro-fiber enclosed by air. This way, the V-parameter can be approximated using the same equation as for standard fibers (Equation 2.15), taking into account that n_{co} and n_{cl} are, the refractive index of the core and the holes, respectively, or by using simulation software.

The choice of the V in the design of a MOF, not only determines its single-mode or multimode behavior, but also their confinement in the core. The modes confinement has special relevance in gas sensors, where an interaction between the core and the gases introduced in the cladding holes is needed.

Also, it can be seen that MOFs present a higher number of degrees of freedom in the design process than standard fibers.

2.4.4.3 BIREFRINGENCE

In an ideal fiber, all polarization components should propagate at the same velocity. However, real fibers exhibit considerable variations in the shape of their core along the fiber length. These imperfections of the fiber make a different velocity propagation of the orthogonally polarized fiber modes and consequently, the polarization at the fiber output is unpredictable. In order to avoid the random birefringence in a fiber, the solution was the use of highly birefringent fibers, which introduce deliberately linear or circular birefringence into the fiber [180].

The degree of modal birefringence is defined by

$$B = |n_x - n_y| \qquad (2.19)$$

where n_x and n_y are the refractive index of the orthogonally polarized fiber modes. Birefringence generates a phase lag between the orthogonally polarized modes. The beat length is defined as the distance along which the polarization rotates 360 degrees or, in other words, given a phase difference between the two eigenmodes, the distance along which the two eigenmodes come into the same phase difference [183].

$$L_b = \frac{\lambda}{|n_x - n_y|} = \frac{\lambda}{B} \qquad (2.20)$$

In standard OFs, birefringence can be accomplished by modifying the shape of the refractive index profile making the core elliptical, or by doping the cladding material which surrounds the core as in bow-tie or Panda OFs [183] with beat lengths around 4 mm at 1550 nm. Birefringence in microstructured optical fibers is obtained through the asymmetry of the core, due to the distribution of the air holes that enclose it. The first Hi-Bi MOF was presented in 2000 [184], where the birefringence was obtained by a regular array of air holes of two sizes surrounding the solid core, with a twofold rotational symmetry (Figure 2.17 (a)). This fiber presented a L_b=0.4 mm at 1540 nm, which is shorter than standard birefringent fibers.

Another design of Hi-Bi MOF was proposed in 2001 [185]. This fiber was used for the sensor transducer presented in chapter 4, in its commercial version PM-1550-01 from NKT Photonics [186]. In this MOF birefringence was introduced by enlarging two of the central air-holes (Figure 2.17 (b)), providing a L_b=3.65 mm at 1550 nm.

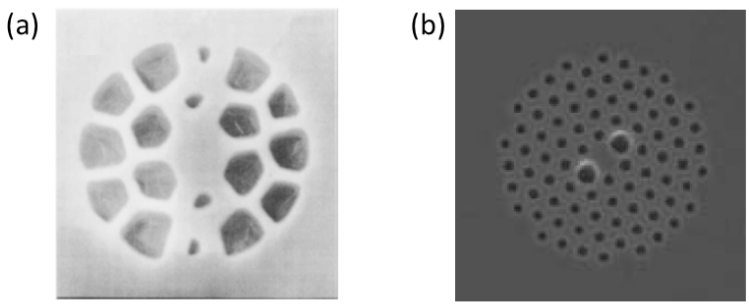

FIGURE 2.17. Microscopic picture of the (a) Hi-Bi MOF developed in [184] and (b) the PM-1550-01 from NKT [186].

2.4.4.4 TEMPERATURE DEPENDENCE

Microstructured optical fibers present another interesting feature in comparison with standard fibers: a lower sensitivity to temperature variations. The low temperature sensitivity characteristic is a direct consequence of their fabrication using a single material. Conventional optical fibers contain two different materials with different thermal (thermal expansion coefficient) and mechanical properties (Young's modulus and Poisson's ratio), which will generate high thermal stress when the fiber is subjected to temperature variations. However MOFs are made of a single material and therefore, present absence of thermal stress.

Temperature effect is remarkable in birefringent fibers, where the different materials of these fibers (bow-tie, elliptical core, or Panda) generate a core non-uniform deformation with temperature changes and consequently, a change in the birefringence of the fundamental mode. Therefore, in strain sensors based on birefringence interference, temperature changes affect significantly to strain measurements. On the other hand Hi-Bi MOFs are made of a single material and present absence of thermal stress showing a negligible effect in strain measurements [187].

2.4.4.5 YOUNG MODULUS

The elastic modulus describes the resistance of a material to being deformed elastically, when an external force is applied. The Young modulus (E) is a specific elastic modulus that is given when the external force is a tensile stress along one axis and the opposing forces are applied along that axis [188]. This is the case of fiber strain sensors, where a tensile stress is applied along Z axis generating an extensional strain in the same axis.

The Young modulus is defined by:

$$E = \frac{\sigma}{\varepsilon} = \frac{F}{A\varepsilon} \qquad (2.21)$$

Where σ and ε are the tensile stress and the extensional strain, respectively. F is the force applied and A the cross-section area through which the force is applied.

In chapter 4 are presented two optical fiber transducers based on suspended core MOFs spliced between SMFs. Therefore, the relation of the Young modulus between both kinds of fibers is an important parameter to take into account. Figure 2.18 shows two fibers with the same external diameter (D_0), one standard SMF, and a suspended core MOF.

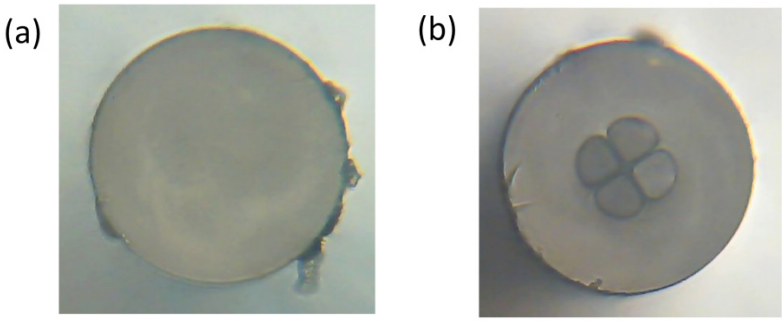

FIGURE 2.18 Microscopic pictures of (a) a standard fiber and (b) a suspended core MOF.

The relation between a standard fiber and a suspended core MOF, with same external diameters, are given by:

$$A_{MOF} = A_{SF} - A_{Holes} \qquad (2.22)$$

$$E_{MOF} = E_{SF}\frac{A_{MOF}}{A_{SF}} \qquad (2.23)$$

Where A_{MOF} and E_{MOF} are the silica area and the Young modulus of the MOF, respectively. A_{Holes} is the integration of the total holes area of the MOF. And finally, A_{SF} and E_{SF} are the area and the Young modulus of the standard fiber, respectively. From this relation can be concluded that the MOF presents a lower Young modulus.

2.4.5 INTERFEROMETRIC AND POLARIMETRIC SENSORS

Optical fiber interferometers have been thoroughly investigated for precision metrology. An interferometer converts a phase change to an intensity change. When two or more optical coherent signals with a phase difference are combined, the result is an intensity signal with a periodical response. Therefore, if the phase difference is generated by the parameter to be measured, it can be monitored. A polarimetric sensor in a single-mode fiber can be regarded as an interferometer in which the phase difference is generated by the two polarization eigenmodes in the fiber [189, 190].

There are different interferometers that can be classified depending on the method used to generate the phase difference and therefore, to measure the different physical or chemical parameters. The main interferometers used for the development of this thesis are presented below.

2.4.5.1 MULTIMODE INTERFEROMETER

Multimode interferometers are based on the different propagation constants of the modes in a multimode fiber (MMF). Figure 2.19 shows a basic schematic of a multimode sensor based on a SMF-MMF-SMF transition.

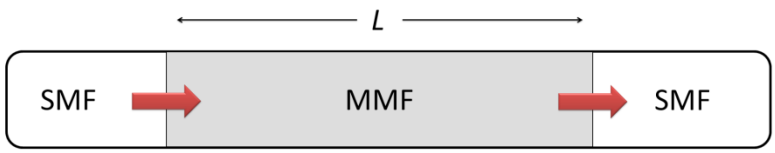

FIGURE 2.19. Schematic of a multimode interferometer.

When the light is coupled from the SMF into the MMF, high-order eigenmodes of the MMF are excited. The number of guided modes in the MMF can be approximated by using the V-parameter presented in the section 2.4.4.2. Each excited mode is propagated along the MMF with different propagation constant and therefore, acquires a phase difference along their propagation along the MMF. The interference of the modes generates a fringe pattern that depends on: the wavelength, the number of excited modes and their propagation constants, and the length of the MMF [191].

The multimode interference have been extensively used with standard multimode fibers for the measurement of curvature [192], strain and temperature [191], refractive index [193] and simultaneous parameter measurements [194]. The appearance of microstructured optical fibers, has also allowed the development of multimode MOFs and therefore, the use of multimode interferometers based on this technology [149, 153].

2.4.5.2 HI-BI INLINE POLARIMETRIC INTERFEROMETER

A high birefringence inline interferometer is based on the phase difference generated between the two orthogonal axes (fast and slow) of a birefringent fiber,

which causes a variation of the optical path length with the polarization state. Figure 2.20 shows the schematic of a Hi-Bi inline polarimetric interferometer. It is important to note that in order to use the interference between the two orthogonal states it is necessary to add an extra element that processes the interference, such as a coupler or, in the case of Figure 2.20, a linear polarizer. This is because usual detectors respond to the power of the radiation rather than its electric field strength [189].

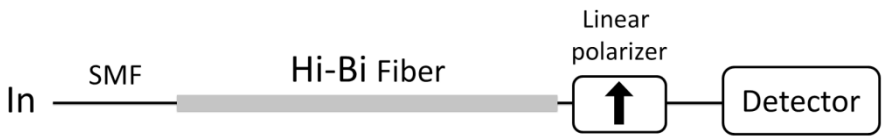

FIGURE 2.20. Schematic of a Hi-Bi inline polarimetric interferometer structure.

As stated before, the transmission characteristics of a high birefringent interferometer depends on the phase difference between the two orthogonal axes of the fiber, generating a sinusoidal transmission spectrum that can be modeled by [195]:

$$T(\lambda) = \left[\cos\left(2\pi\frac{L \cdot b}{\lambda} - \emptyset\right)\right]^2 \qquad (2.24)$$

Where λ is the operating wavelength and, *L* and *b* are the length and the birefringence of the Hi-bi fiber, respectively. Therefore, as can be seen, the output spectrum presents a dependence with *L* and *b*. This fact allows the measurement of different physical parameters such as strain or temperature, which affects directly to these terms. Figure 2.21 shows the simulated interference spectrum for a Hi-bi inline configuration with *L*= 0.2 m, *b*=4.25x10^{-4} @1550 nm and ∅=0.

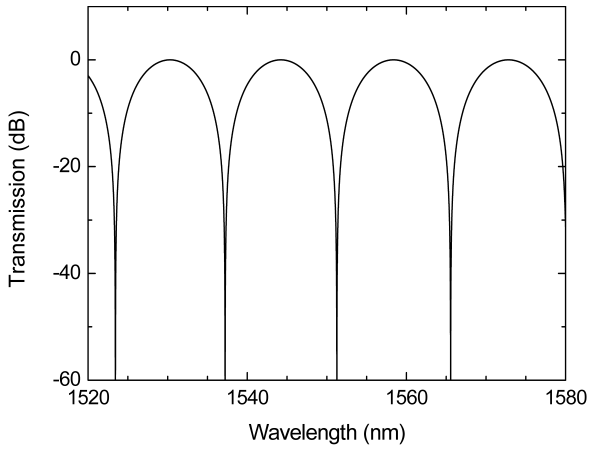

FIGURE 2.21. Simulated interference spectrum for a Hi-Bi inline polarimetric interferometer.

2.4.5.3 HI-BI FIBER LOOP MIRROR

A Hi-Bi fiber loop mirror (FLM) is also a polarimetric interferometer. This device is based on a Sagnac configuration, as it can be seen in Figure 2.22, and includes a Hi-Bi fiber inside the ring.

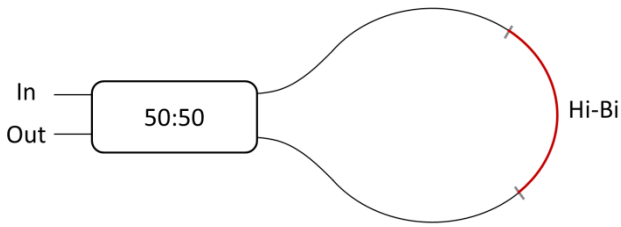

FIGURE 2.22. Schematic diagram of a Hi-Bi fiber loop mirror structure.

In a FLM the input light is equally splitted by the coupler to form two signals that travel counter-propagated along the loop. If the Hi-Bi fiber is not considered, light coupled across the coupler suffers a $\pi/2$ phase lag with respect to light traveling straight through. Therefore the transmitted intensity in the output port is the sum of a clockwise field of arbitrary phase $\emptyset$ and an anticlockwise field of relative phase $\emptyset - \pi$, both of equal amplitude. This results in a zero transmitted inten-

sity and by conservation of energy all input light is reflected back along the input port. However, if a Hi-Bi fiber is introduced in the loop, its birefringence causes a variation of the optical path length with polarization angle. Therefore, when both signals are recombined at the coupler, an interference pattern is generated which is wavelength dependent [196, 197]. The transmission spectrum of the Hi-Bi FLM ($T(\lambda)$) and its wavelength spacing ($\Delta\lambda$) between two maxima (or minima) can be described as:

$$T(\lambda) = \left[\cos\left(\frac{2\pi}{\lambda} 2L \cdot b\right)\right]^2 \qquad (2.25)$$

$$\Delta\lambda = \frac{\lambda^2}{2L \cdot b} \qquad (2.26)$$

Where L and b are the length and the birefringence of the Hi-Bi fiber. Figure 2.23 shows the measured and simulated interference spectra for a Hi-bi fiber loop mirror configuration with L= 3 m and b= 4.25x10^{-4} @1550 nm.

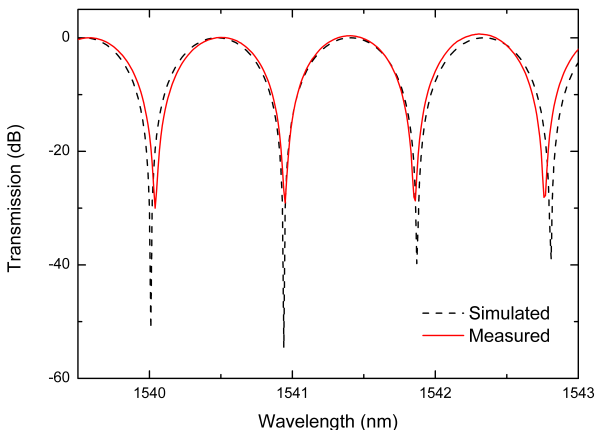

FIGURE 2.23. Interferometer spectra of a 3m Hi-Bi fiber loop mirror, (red) measured and (black dotted) simulated.

It is important to note that this structure has been previously used as a sensor in different works [197-199]. However, in this Ph.D. work, the Hi-Bi FLM has been used as a filter for the development of multiwavelength fiber lasers which are presented in section 3.1.3.

2.4.5.4 FIBER OPTIC RING RESONATOR

A fiber optic ring resonator (FORR) is a configuration that use transverse coupling in order to achieve multiple circulations of power inside a mirrorless cavity. A schematic of a FORR formed by using a 2x2 coupler is shown in Figure 2.24.

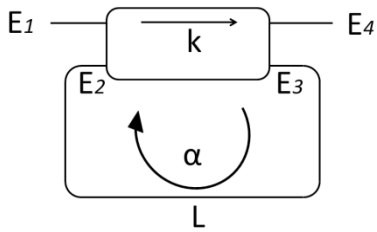

FIGURE 2.24. Schematic of a FORR structure, formed by using a 2x2 coupler.

When the light is introduced into the input (E_1), part of this light is coupled into the optical ring resonator (E_3) and travels along it. This process generates a phase difference between E_1 and E_2, which depends on the ring length (L). Therefore, an interferometric pattern is obtained at E_4, which is defined by the following expression [200]:

$$\frac{E_4}{E_1} = \frac{k\ exp\left(\frac{iwnL}{c}\right) - \alpha}{exp\left(\frac{iwnL}{c}\right) - k\alpha} \qquad (2.27)$$

Where α and L are the loss and the length of the ring, respectively, and k is the coupling ratio. As can be seen, the FORR output spectrum depends on the length and loss of the ring. Therefore, these two parameters can be used for sensing, as is presented in previous works [201-203] and in the experimental results of this Ph.D. work in section 5.5. Figure 2.25 shows the transmission response spectrum for a FORR configuration with k=0.9 L= 1 m and α=0.9.

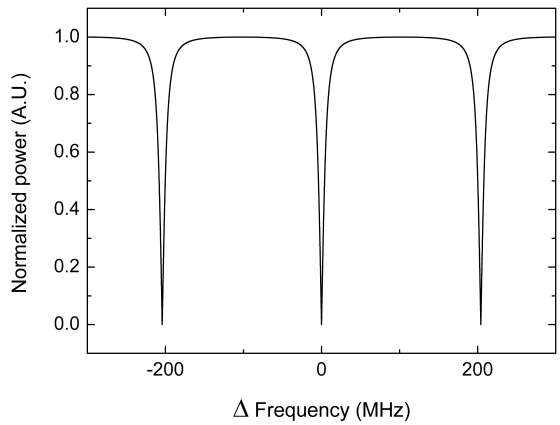

FIGURE 2.25. Simulated spectrum of a FORR transmission response.

2.5 CONCLUSIONS

Throughout this chapter, the fundamental aspects of the main technological concepts used for the development of this thesis have been addressed. All these tools will be employed in the experimental sections presented in the following chapters.

2.6 REFERENCES

[1] A. Einstein, "Zur Quantentheorie der Strahlung," *Phys. Z.*, Vol. 18, pp. 121, 1917.

[2] M. A. Rebolledo and M. López-Amo, "Chapter 9, optical amplifiers," in *Handbook of Optical Fibre Sensing Technology*, John Wiley & Son Ed., J. M. López-Higuera, pp. 165-186, 2002.

[3] R. J. Mears, L. Reekie, I. M. Jauncey and D. N. Payne, "High-gain rare-earth-doped fiber amplifier at 1. 54 mu M.," in *Optical Fiber Communication*, 1987 OSA Technical Digest Series, paper WI2, pp. 167,1987.

[4] R. J. Mears, L. Reekie, I. M. Jauncey and D. N. Payne, "Low-noise erbium-doped fibre amplifier operating at 1. 54 mu m." *Electron. Lett.*, Vol. 23, Iss. 19, pp. 1026-1028, 1987.

[5] M. E. Marhic, P. A. Andrekson, P. Petropoulos, S. Radic, C. Peucheret and M. Jazayerifar, "Fiber optical parametric amplifiers in optical communication systems," *Laser and Photonics Reviews,* Vol. 9, Iss. 1, pp. 50-74, 2015.

[6] R. H. Stolen, "Phase-matched-stimulated four-photon mixing in silica-fiber waveguides," *IEEE J. Quant. Electron.,* Vol. 11, Iss. 3, pp. 100-103, 1975.

[7] M. Federighi, I. Massarek and P. F. Trwoga, "Optical amplification in thin optical waveguides with high er concentration," *IEEE Photonics Technology Letters,* Vol. 5, Iss. 2, pp. 227-229, 1993.

[8] C. Jiang and Q. Zeng, "Optimization of erbium-doped waveguide amplifier," *Optics and Laser Technology,* Vol. 36, Iss. 2, pp. 167-171, 2004.

[9] K. Ennser, S. Taccheo, T. Rogowski and J. Shmulovich, "Efficient erbium-doped waveguide amplifier insensitive to power fluctuations," *Optics Express,* Vol. 14, Iss. 22, pp. 10307-10312, 2006.

[10] R. Brinkmann, I. Baumann, M. Dinand, W. Sohler and H. Suche, "Erbium-doped single- and double-pass Ti:LiNbO3 waveguide amplifiers," *IEEE J. Quant. Electron.,* Vol. 30, Iss. 10, pp. 2356-2360, 1994.

[11] C.I. Huang and L. McCaughan, "980-nm-pumped Er-doped LiNbO3 waveguide amplifiers: A comparison with 1484-nm pumping," *IEEE Journal on Selected Topics in Quantum Electronics,* Vol. 2, Iss. 2, pp. 367-372, 1996.

[12] I. D. Miller, C. A. Millar, B. J. Ainslie, D. B. Mortimore and J. R. Armitage, "Rare-earth doped fibre lasers and amplifiers for optical communications," in *Proceedings of SPIE 0813* pp. 323-324, 1987.

[13] G. P. Agrawal, "Chapter 7, Loss management," in *Fiber-Optic Communication Systems: Fourth Edition,* John Wiley & Sons, 2011, .

[14] C. Headley and G. P. Agrawal, "Raman Amplification in Fiber Optical Communication Systems," in *Raman Amplification in Fiber Optical Communication Systems,* 2005.

[15] S. Namiki, K. Seo, N. Tsukiji and S. Shikii, "Challenges of Raman amplification," *Proc IEEE,* Vol. 94, No. 5, pp. 1024-1034, 2006.

[16] J. Bromage, "Raman Amplification for Fiber Communications Systems," *J. Lightwave Technol.,* Vol. 22, Iss. 1, pp. 79-93, 2004.

[17] M. N. Islam, "Raman amplifiers for telecommunications," *IEEE Journal on Selected Topics in Quantum Electronics,* Vol. 8, No. 3, pp. 548-559, 2002.

[18] M. Bravo, M. Fernandez-Vallejo and M. Lopez-Amo, "Internal modulation of a random fiber laser," *Opt. Lett.,* Vol. 38, pp. 1542-1544, 2013.

[19] E. Snitzer, "Optical maser action of Nd+3 in a barium crown glass," *Phys. Rev. Lett.,* Vol. 7, No. 12, pp. 444-446, 1961.

[20] N. E. Wolff and R. J. Pressley, "Optical maser action in an eu+3-containing organic matrix," *Appl. Phys. Lett.,* Vol. 2, pp. 152-154, 1963.

[21] J. Charles and E. Snitzer, "Amplification in a fiber laser," *Appl.Opt.,* Vol. 3, No. 10, pp. 1182, 1964.

[22] J. Stone and C. A. Burrus, "Neodymium-Doped fiber lasers: Room temperature CW operation with and injection laser pump," *Appl.Opt.,* Vol. 13, Iss. 6, pp. 1256, 1974.

[23] J. Stone and C. A. Burrus, "Neodymium-doped silica lasers in end-pumped fiber geometry," *Appl. Phys. Lett.,* Vol. 23, pp. 388-389, 1973.

[24] W. L. Barnes, S. B. Poole, J. E. Townsend, L. Reekie, D. J. Taylor and D. N. Payne, "Er3+-Yb3+ and Er3+ doped fiber lasers," *J. Lightwave Technol.,* Vol. 7, Iss. 10, pp. 1461-1465, 1989.

[25] R. J. Mears, L. Reekie, S. B. Poole and D. N. Payne, "Low-threshold tunable CW and Q-switched fibre laser operating at 1.55 μm," *Electron. Lett.,* Vol. 22, Iss. 3, pp. 159-160, 1986.

[26] A. Bellemare, "Continuous-wave silica-based erbium-doped fibre lasers," *Progress in Quantum Electronics,* Vol. 27, Iss. 4, pp. 211-266, 2003.

[27] K. O. Hill, B. S. Kawasaki and D. C. Johnson, "Low-threshold cw Raman laser," *Appl. Phys. Lett.,* Vol. 29, pp. 181-183, 1976.

[28] B. Li, X. Wei, X. Wang and K. K. H. Wong, "Single-longitudinal-mode brillouin/erbium fiber laser with high linewidth-reduction ratio," *IEEE Photonics Technology Letters,* Vol. 26, Iss. 23, pp. 2387-2390, 2014.

[29] Y. Yuan, Y. Yao, M. Yi, B. Guo and J. Tian, "Multiwavelength fiber laser employing a nonlinear Brillouin optical loop mirror: Experimental and numerical studies," *Optics Express,* Vol. 22, Iss. 13, pp. 15352-15363, 2014.

[30] G. Mamdoohi, A. R. Sarmani, M. H. Yaacob, M. Mokhtar and M. A. Mahdi, "Multi-wavelength Brillouin-Raman fiber laser utilizing enhanced nonlinear amplifying loop mirror design," *Optics Express,* Vol. 21, Iss. 26, pp. 31800-31808, 2013.

[31] M. Z. Zulkifli, H. Ahmad, J. M. Taib, F. D. Muhammad, K. Dimyati and S. W. Harun, "S-band multiwavelength Brillouin/Raman distributed Bragg reflector fiber lasers," *Appl. Opt.,* Vol. 52, Iss. 16, pp. 3753-3756, 2013.

[32] M. R. Shirazi and M. Biglary, "Multiple wavelength generation using a compacted hybrid raman / bi-EDF amplifier," in *EPJ Web of Conferences*,Vol. 48, No. 22, 2013, .

[33] H. Lin and Y. W. Wang, "Erbium-doped fiber-ring-laser-based supercontinnum source using nonlinear polarization-rotation and stimulated Raman scattering," *IEEE Photonics Technology Letters,* Vol. 24, Iss. 4, pp. 324-326, 2012.

[34] A. Bellemare, M. Karásek, M. Rochette, S. LaRochelle and M. Têtu, "Room temperature multifrequency erbium-doped fiber lasers anchored on the ITU frequency grid," *J. Lightwave Technol.,* Vol. 18, Iss. 16, pp. 825-831, 2000.

[35] N. Haramoni, A. S. Paterno, A. Goedtel, G. R. Soares, J. C. C. Silva and H. J. Kalinowski, "Hybrid wavelength-time-domain interrogation system for multiplexed fiber Bragg sensors using a strain-tuned erbium-doped fiber laser," *IEEE Sensors Journal,* Vol. 8, Iss. 7, pp. 1061-1066, 2008.

[36] X. Feng, C. Lu, H. Y. Tam and P. K. A. Wai, "Reconfigurable microwave photonic filter using multiwavelength erbium-doped fiber laser," *IEEE Photonics Technology Letters,* Vol. 19, Iss. 17, pp. 1334-1336, 2007.

[37] M. Fernández-Vallejo, S. Diaz, R. A. Pérez-Herrera, R. Unzu, M. A. Quiniela, J. M. López-Higuera and M. López-Amo, "Comparison of the stability of ring resonator structures for multiwavelength fiber lasers using raman or Er-Doped fiber amplification," *IEEE J. Quant. Electron.,* Vol. 45, Iss.12, pp. 1551-1557, 2009.

[38] J. Cousin, P. Masselin, W. Chen, D. Boucher, S. Kassi, D. Romanini and P. Szriftgiser, "Application of a continuous-wave tunable erbium-doped fiber laser to molecular spectroscopy in the near infrared," *Appl. Phy. B,* Vol. 83, Iss. 2, pp. 261-266, 2006.

[39] Y. T. Lin and G. R. Lin, "Dual-stage soliton compression of a self-started additive pulse mode-locked erbium-doped fiber laser for 48 fs pulse generation," *Opt. Lett.,* Vol. 31, Iss. 10, pp. 1382-1384, 2006.

[40] R. Parvizi, S. W. Harun, N. S. Shahabuddin, Z. Yusoff and H. Ahmad, "Multiwavelength bismuth-based erbium-doped fiber laser based on four-wave

mixing effect in photonic crystal fiber," *Opt. Laser Technol.,* Vol. 42, Iss. 8, pp. 1250-1252, 2010.

[41] M. A. Quintela, R. A. Perez-Herrera, I. Canales, M. Fernández-Vallejo, M. Lopez-Amo and J. M. López-Higuera, "Stabilization of dual-wavelength erbium-doped fiber ring lasers by single-mode operation," *IEEE Photonics Technology Letters,* Vol. 22, Iss. 6, pp. 368-370, 2010.

[42] D. Saez-Rodriguez, J. L. Cruz, A. Diez, Y. O. Barmenkov and M. V. Andres, "Q-switch all-fiber laser pulsed by high order modes," *IEEE Photonics Technology Letters,* Vol. 25, Iss. 11, pp. 1058-1061, 2013.

[43] Y. G. Han, T. V. A. Tran and S. B. Lee, "Wavelength-spacing tunable multiwavelength erbium-doped fiber laser based on four-wave mixing of dispersion-shifted fiber," *Opt. Lett.,* Vol. 31, Iss. 6, pp. 697-699, 2006.

[44] S. Pan, C. Lou and Y. Gao, "Multiwavelength erbium-doped fiber laser based on inhomogeneous loss mechanism by use of a highly nonlinear fiber and a Fabry-Perot filter," *Optics Express,* Vol. 14, Iss. 3, pp. 1113-1118, 2006.

[45] X. Feng, H. Y. Tam and P. K. A. Wai, "Stable and uniform multiwavelength erbium-doped fiber laser using nonlinear polarization rotation," *Optics Express,* Vol. 14, Iss. 18, pp. 8205-8210, 2006.

[46] X. He, D. N. Wang and C. R. Liao, "Tunable and switchable dual-wavelength single-longitudinal-mode erbium-doped fiber lasers," *J. Lightwave Technol.,* Vol. 29, Iss. 6, pp. 842-849, 2011.

[47] Z. Zhang, L. Zhan, K. Xu, J. Wu, Y. Xia and J. Lin, "Multiwavelength fiber laser with fine adjustment, based on nonlinear polarization rotation and birefringence fiber filter," *Opt. Lett.,* Vol. 33, Iss. 4, pp. 324-326, 2008.

[48] V. Karalekas, J. D. Ania-Castañón, P. Harper, S. A. Babin, E. V. Podivilov and S. K. Turitsyn, "Impact of nonlinear spectral broadening in ultra-long Raman fibre lasers," *Optics Express,* Vol. 15, Iss. 25, pp. 16690-16695, 2007.

[49] E. M. Dianov, M. V. Grekov, I. A. Bufetov, S. A. Vasiliev, O. I. Medvedkov, V. G. Plotnichenko, V. V. Koltashev, A. V. Belov, M. M. Bubnov, S. L. Semjonov and A. M. Prokhorov, "CW high power 1.24μm and 1.48μm Raman lasers based on low loss phosphosilicate fibre," *Electron. Lett.,* Vol. 33, Iss. 18, pp. 1542-1544, 1997.

[50] M. D. Mermelstein, C. Headley, J. C. Bouteiller, P. Steinvurzel, C. Horn, K. Feder and B. J. Eggleton, "Configurable three-wavelength Raman fiber laser for Raman amplification and dynamic gain flattening," *IEEE Photonics Technology Letters,* Vol. 13, Iss. 12, pp. 1286-1288, 2001.

[51] Y. G. Han, T. V. A. Tran, S. H. Kim and S. B. Lee, "Multiwavelength Raman-fiber-laser-based long-distance remote sensor for simultaneous measurement of strain and temperature," *Opt. Lett.,* Vol. 30, Iss. 11, pp. 1282-1284, 2005.

[52] P. C. Peng, H. Y. Tseng and S. Chi, "Long-Distance FBG Sensor System Using a Linear-Cavity Fiber Raman Laser Scheme," *IEEE Photonics Technology Letters,* Vol. 16, Iss. 2, pp. 575-577, 2004.

[53] J. H. Lee, J. Kim, Y. G. Han, S. H. Kim and S. B. Lee, "Investigation of Raman fiber laser temperature probe based on fiber Bragg gratings for long-distance remote sensing applications," *Optics Express,* Vol. 12, Iss. 8, pp. 1747-1752, 2004.

[54] A. K. Abeeluck, C. Headley and C. G. Jørgensen, "High-power supercontinuum generation in highly nonlinear, dispersion-shifted fibers by use of a continuous-wave Raman fiber laser," *Opt. Lett.,* Vol. 29, Iss. 18, pp. 2163-2165, 2004.

[55] K. Rottwitt, "Chapter 3, distributed raman ampflifiers," in *Raman Amplification in Fiber Optical Communication Systems*, C. Headley and G. P. Agrawal, Eds. Elsevier Inc., pp. 103-163, 2005.

[56] G. P. Agrawal, "Chapter 2, theory of raman amplifiers," in *Raman Amplification in Fiber Optical Communication Systems*, C. Headley and G. P. Agrawal, Eds. Elsevier, pp. 33-102, 2005.

[57] C. Headley, M. D. Mermelstein and J. -. Bouteiller, "Chapter 11, raman fiber lasers," in *Raman Amplifiers for Telecommunications 2*, M. N. Islam, Ed. Springer, pp. 353-382, 2003.

[58] N. S. Kim, X. Zou and K. Lewis, "CW depolarized multiwavelength raman fiber ring laser with over 58 channels and 50 GHz channel spacing," in *Conference on Optical Fiber Communication, Technical Digest Series,* pp. 640-642, 2002.

[59] C. S. Kim, R. M. Sova and J. U. Kang, "Tunable multi-wavelength all-fiber Raman source using fiber Sagnac loop filter," *Opt. Commun.,* Vol. 218, Iss.4-6, pp. 291-295, 2003.

[60] X. Dong, P. Shum, N. Q. Ngo and C. C. Chan, "Multiwavelength Raman fiber laser with a continuously-tunable spacing," *Optics Express,* Vol. 14, Iss. 8, pp. 3288-3293, 2006.

[61] S. K. Turitsyn, S. A. Babin, D. V. Churkin, I. D. Vatnik, M. Nikulin and E. V. Podivilov, "Random distributed feedback fibre lasers," *Physics Reports,* Vol. 542, Iss. 2, pp. 133-193, 2014.

[62] V. DeMiguel-Soto, M. Bravo and M. Lopez-Amo, "Fully switchable multiwavelength fiber laser assisted by a random mirror," *Opt. Lett.,* Vol. 39, Iss.7, pp. 2020-2023, 2014.

[63] J. Simmons and K. S. Potter, "Chapter 6: Optical gain and lasers," in *Optical Materials*, Academic Press, pp. 273, 1999.

[64] E. Desurvire, J. L. Zyskind and J. R. Simpson, "Spectral gain hole-burning at 1.53 μm in erbium-doped fiber amplifiers," *IEEE Photonics Technology Letters,* Vol. 2, pp. 246-248, 1990.

[65] J. L. Zyskind, E. Desurvire, J. W. Sulhoff and D. J. Di Giovanni, "Determination of homogeneous linewidth by spectral gain hole-burning in an erbium-doped fiber amplifier with GeO2:SiO2 core," *IEEE Photonics Technology Letters,* Vol. 2, Iss. 12, pp. 869-871, 1990.

[66] S. Yamashita and K. Hotate, "Multiwavelength erbium-doped fibre laser using intracavity etalon and cooled by liquid nitrogen," *Electron. Lett.,* Vol. 32, Iss. 14, pp. 1298-1299, 1996.

[67] C.L. Zhao, X. Yang, J. H. Ng, X. Dong, X. Guo, X. Wang, X. Zhou and C. Lu, "Switchable dual-wavelength erbium-doped fiber-ring lasers using a fiber Bragg grating in high-birefringence fiber," *Microwave Opt Technol Lett,* Vol. 41, Iss. 1, pp. 73-75, 2004.

[68] R. A. Perez-Herrera, S. Chen, W. Zhao, T. Sun, K. T. V. Grattan and M. López-Amo, "Stability performance of short cavity Er-doped fiber lasers," *Opt. Commun.,* Vol. 283, Iss. 6, pp. 1067-1070, 2010.

[69] Y. Shen, Y. Qiu, B. Wu, W. Zhao, S. Chen, T. Sun and K. T. V. Grattan, "Short cavity single frequency fiber laser for in-situ sensing applications over a wide temperature range," *Optics Express,* Vol. 15, Iss. 2, pp. 363-370, 2007.

[70] J. Masson, R. St-Gelais, A. Poulin and Y.A. Peter, "Tunable fiber laser using a MEMS-based in plane fabry-pérot filter," *IEEE J. Quant. Electron.,* Vol. 46, Iss. 9, pp. 1313-1319, 2010.

[71] F. Wang, E. M. Xu, J. J. Dong and X. L. Zhang, "A tunable and switchable single-longitudinal-mode dual-wavelength fiber laser incorporating a reconfigurable dual-pass Mach-Zehnder interferometer and its application in microwave generation," *Opt. Commun.,* Vol. 284, pp. 2337-2340, 2011.

[72] A. González-García, O. Pottiez, R. Grajales-Coutiño, B. Ibarra-Escamilla and E. A. Kuzin, "Switchable and tuneable multi-wavelength Er-doped fibre ring laser using Sagnac filters," *Laser Physics,* Vol. 20, Iss. 3, pp. 720-725, 2010.

[73] H. Lin, "Waveband-tunable multiwavelength erbium-doped fiber laser," *Appl. Opt.,* Vol. 49, Iss. 14, pp. 2653-2657, 2010.

[74] A. Gusarov and F. Liegeois, "Experimental study of a tunable fiber ring laser stability," *Opt. Commun.,* Vol. 234, Iss. 1-6, pp. 391-397, 2004.

[75] J. J. Zayhowski, "Limits imposed by spatial hole burning on the single-mode operation of standing-wave laser cavitites," *Optics Express,* Vol. 15, Iss. 8, pp. 431-433, 1990.

[76] C. L. Tang, H. Statz and G. Demars, "Spectral output and spiking behavior of solid-state lasers," *J. Appl. Phys.,* Vol. 34, pp. 2289-2295, 1963.

[77] S. K. Turitsyn, S. A. Babin, A. E. El-Taher, P. Harper, D. V. Churkin, S. I. Kablukov, J. D. Ania-Castãón, V. Karalekas and E. V. Podivilov, "Random distributed feedback fibre laser," *Nature Photonics,* Vol. 4, pp. 231-235, 2010.

[78] J. Zhao, C. Zhang, C. Miao and H. Gu, "Switchable narrow linewidth single-longitudinal mode erbium fiber laser by using saturable-absorber filter and cavity loss control," *Opt. Commun.,* Vol. 331, pp. 229-234, 2014.

[79] T. Sun, Y. Guo, J. Huo and D. Hu, "Stable single longitudinal mode fiber ring laser based on polarization maintaining erbium doped fiber," *Optik,* Vol. 125, Iss. 11, pp. 2487-2490, 2014.

[80] S. Feng, Q. Mao, Y. Tian, Y. Ma, W. Li and L. Wei, "Widely tunable single longitudinal mode fiber laser with cascaded fiber-ring secondary cavity," *IEEE Photonics Technology Letters,* Vol. 25, Iss. 4, pp. 323-326, 2013.

[81] S. Pan, Z. Xiaofan and L. Caiyun, "Switchable single-longitudinal-mode dual-wavelength erbium-doped fiber ring laser incorporating a semiconductor optical amplifier," *Opt. Lett.,* Vol. 33, Iss. 8, pp. 764-766, 2008.

[82] J. L. Zhou, L. Xia, X. P. Cheng, X. P. Dong and P. Shum, "Photonic generation of tunable microwave signals by beating a dual-wavelength single longitudinal mode fiber ring laser," *Appl. Phy. B,* Vol. 91, Iss. 1, pp. 99-103, 2008.

[83] Y. L. Yu, S. K. Liaw, W. C. Hsu, M. H. Shih and N. K. Chen, "Single longitudinal mode Ytterbium doped fiber lasers with large proposed tuning range," *Opt. Quant. Electron.,* Vol. 47, Iss. 2, pp. 131-137, 2014.

[84] R. A. Perez-Herrera, A. Ullan, D. Leandro, M. Fernandez-Vallejo, M. A. Quintela, A. Loayssa, J. M. Lopez-Higuera and M. Lopez-Amo, "L-band multiwavelength single-longitudinal mode fiber laser for sensing applications," *J. Lightwave Technol.,* Vol. 30, Iss. 8, pp. 1173-1177, 2012.

[85] T. Okoshi, K. Kikuchi and A. Nakayama, "Novel method for high resolution measurement of laser output spectrum," *Electron. Lett.,* Vol. 16, Iss. 16, pp. 630-631, 1980.

[86] D. S. Moon and Y. Chung, "Multi-wavelength fiber ring laser based on a sampled chirped fiber Bragg grating with a hybrid gain medium," *Opt. Commun.,* Vol. 285, Iss. 7, pp. 1908-1910, 2012.

[87] Y. G. Han, "A long-distance remote sensing technique using a multiwavelength Raman fiber laser based on fiber bragg gratings embedded in a quartz tube," *IEEE Sensors Journal,* Vol. 11, Iss. 5, pp. 1152-1156, 2011.

[88] T. Wang, X. Miao, X. Zhou and S. Qian, "Tunable multiwavelength fiber laser based on a double Sagnac HiBi fiber loop," *Appl. Opt.,* Vol. 51, Iss. 10, pp. C111-C116, 2012.

[89] Y. G. Han, C. S. Kim, J. U. Kang, U. C. Paek and Y. Chung, "Multiwavelength Raman fiber-ring laser based on tunable cascaded long-period fiber gratings," *IEEE Photonics Technology Letters,* Vol. 15, Iss. 3, pp. 383-385, 2003.

[90] D. Chen, "Stable multi-wavelength erbium-doped fiber laser based on a photonic crystal fiber Sagnac loop filter," *Laser Physics Letters,* Vol. 4, Iss. 6, pp. 437-439, 2007.

[91] D. Chen and L. Shen, "Switchable and tunable Erbium-doped fiber ring laser incorporating a birefringent and highly nonlinear photonic crystal fiber," *Laser Physics Letters,* Vol. 4, pp. 368-370, 2007.

[92] X. Liu, X. Zhou, X. Tang, J. Ng, J. Hao, T. Y. Chai, E. Leong and C. Lu, "Switchable and tunable multiwavelength erbium-doped fiber laser with fiber Bragg gratings and photonic crystal fiber," *IEEE Photonics Technology Letters,* Vol. 17, Iss. 8, pp. 1626-1628, 2005.

[93] S. Diaz, S. Abad and M. Lopez-Amo, "Fiber-optic sensor active networking with distributed erbium-doped fiber and Raman amplification," *Laser and Photonics Reviews,* Vol. 2, Iss. 6, pp. 480-497, 2008.

[94] *http://www.stats.gla.ac.uk/steps/glossary/confidence_intervals.html*.

[95] J. Sun and L. Huang, "Single-longitudinal-mode fiber ring laser using internal lasing injection and self-injection feedback," *Optical Engineering,* Vol. 46, Iss. 7, 2007.

[96] J. M. López-Higuera, "Introduction to fibre optic sensing thecnology," in *Handbook of Optical Fiber Sensing Technology,* López-Higuera,J.M. ed. John Wiley & Sons, 2002.

[97] J. M. Lopez-Higuera, "Chapter 1, Introduction to fibre optic sensing technology," in *Handbook of Optical Fibre Sensing Technology,* J. M. Lopez-Higuera, Ed. John Wiley & Sons, 2002.

[98] M. Lopez-Amo and J. M. Lopez-Higuera, "Chapter 6, Multiplexing techniques for FBG sensors," in *Fiber Bragg Graitngs Sensors: Research Advancements, Industrial Applications and Market Explotation,* Benthan science publishers, 2010, .

[99] J. M. Senior, S. E. Moss and S. D. Cusworth, "Multiplexing techniques for noninterferometric optical point-sensor networks: A review," *Fiber and Integrated Optics,* Vol. 17, pp. 3-20, 1998.

[100] Y. Zhao and Y. Liao, "Discrimination methods and demodulation techniques for fiber Bragg grating sensors," *Optics and Lasers in Engineering,* Vol. 41, Iss. 1, pp. 1-18, 1, 2004.

[101] A. D. Kersey, T. A. Berkoff and W. W. Morey, "Multiplexed fiber Bragg grating strain-sensor system with a fiber Fabry-Perot wavelength filter," *Opt. Lett.,* Vol. 18, Iss. 16, pp. 1370-1372, 1993.

[102] A. D. Kersey, M. A. Davis, H. J. Patrick, M. LeBlanc, K. P. Koo, C. G. Askins, M. A. Putnam and E. J. Friebele, "Fiber grating sensors," *J. Lightwave Technol.,* Vol. 15, Iss. 8, pp. 1442-1462, 1997.

[103] M. Fernandez-Vallejo, M. Bravo and M. Lopez-Amo, "Ultra-long laser systems for remote fiber Bragg gratings arrays interrogation," *IEEE Photonics Technology Letters,* Vol. 25, Iss. 14, pp. 1362-1364, 2013.

[104] M. Bravo and M. López-Amo, "Remote-time division multiplexing of bending sensors using a broadband light source," *Journal of Sensors,* Vol. 2012, No. 154586, 6 pages, 2012.

[105] O. C. Akkaya, M. J. F. Digonnet, G. S. Kino and O. Solgaard, "Time-division-multiplexed interferometric sensor arrays," *J. Lightwave Technol.,* Vol. 31, Iss. 16, pp. 3001-3008, 2013.

[106] S. Kojima and T. Numai, "Theoretical analysis of modified repeated unequally spaced frequency allocations in FDM lightwave transmission systems," *J. Lightwave Technol.,* Vol. 24, Iss. 7, pp. 2786-2797, 2006.

[107] X. Zhou, K. Iiyama and K. Hayashi, "Detection scheme of coherence-multiplexed sensor signals using an optical loop with a frequency shifter: sensitivity enhancement," *IEEE Photonics Technology Letters,* Vol. 6, Iss. 6, pp. 767-769, 1994.

[108] R. B. Jenkins, R. M. Sova and R. I. Joseph, "Steady-state noise analysis of spontaneous and stimulated Brillouin scattering in optical fibers," *J. Lightwave Technol.,* Vol. 25, Iss. 3, pp. 763-770, 2007.

[109] T. Saitoh, K. Nakamura, Y. Takahashi, H. Iida, Y. Iki and K. Miyagi, "Ultralong-distance fiber Bragg grating sensor system," *IEEE Photonics Technology Letters,* Vol. 19, Iss. 20, pp. 1616-1618, 2007.

[110] T. Saitoh, K. Nakamura, Y. Takahashi, H. Iida, Y. Iki and K. Miyagi, "Ultralong-distance (230 km) FBG sensor system," in *Proceedings of SPIE* 7004, 19th International Conference on Optical Fibre Sensors (OFS-19), 70046C, 2008 .

[111] J. Hu, Z. Chen, X. Yang, J. Ng and C. Yu, "100-km long distance fiber bragg grating sensor system based on erbium-doped fiber and raman amplification," *IEEE Photonics Technology Letters,* Vol. 22, Iss. 19, pp. 1422-1424, 2010.

[112] M. Fernandez-Vallejo, D. Leandro, A. Loayssa and M. Lopez-Amo, "Fiber bragg grating interrogation technique for remote sensing (100km) using a hybrid brillouin-raman fiber laser," in *Proceedings of SPIE 7753,* 21th International Conference on Optical Fiber Sensors (OFS-21), 77867l, 2011.

[113] D. Leandro, A. Ullan, A. Loayssa, J. M. López-Higuera and M. López-Amo, "Remote (155 km) fiber bragg grating interrogation technique combining Raman, Brillouin, and erbium gain in a fiber laser," *IEEE Photonics Technology Letters,* Vol. 23, Iss. 10, pp. 621-623, 2011.

[114] M. Fernandez-Vallejo, S. Rota-Rodrigo and M. Lopez-Amo, "Remote (250 km) fiber Bragg grating multiplexing system," *Sensors,* Vol. 11, Iss. 9, pp. 8711-8720, 2011.

[115] M. Bravo, J. M. Baptista, J. L. Santos, M. Lopez-Amo and O. Frazão, "Ultralong 250 km remote sensor system based on a fiber loop mirror interrogated by an optical time-domain reflectometer," *Opt. Lett.,* Vol. 36, Iss. 20, pp. 4059-4061, 2011.

[116] M. Bravo, M. Fernández Vallejo and M. Lopez-Amo, "Hybrid OTDR-fiber laser system for remote sensor multiplexing," *IEEE Sensors Journal,* Vol. 12, Iss. 1, pp. 174-178, 2012.

[117] J. Hu, Z. Chen and C. Yu, "150 km long distance FBG temperature and vibration sensor system based on stimulated raman amplification," *Journal of Lightwave Technology,* Vol. 30, Iss. 8, pp. 1237-1243, 2012.

[118] M. Bravo, M. Fernández-Vallejo, M. Echapare, M. López-Amo, J. Kobelke and K. Schuster, "Multiplexing of six micro-displacement suspended-core Sagnac interferometer sensors with a Raman-Erbium fiber laser," *Optics Express,* Vol. 21, Iss. 3, pp. 2971-2977, 2013.

[119] M. Bravo, M. A. Erro, J. M. Algueta, S. Diaz and M. Lopez-Amo, "Remote fiber optic switch powered by light for robust interrogation of fiber Bragg grating sensor networks," *Measurement Science and Technology,* Vol. 24, No. 9, 4 pages, 2013.

[120] T. V. N. Coelho, J. P. Carvalho, M. J. Pontes, J. L. Santos and A. Guerreiro, "A remote long-period grating sensor with electrical interrogation assisted by Raman amplification," *Opt. Laser Technol.,* Vol. 47, pp. 107-113, 2013.

[121] S. Rota-Rodrigo, L. Rodríguez-Cobo, M. A. Quintela, J. M. López-Higuera and M. López-Amo, "Switchable fiber optic laser system for high and low-strain fiber optic sensors remote multiplexing," in *Proceedings of SPIE 8794,* Fifth European Workshop on Optical Fibre Sensors (EWOFS 2013), 87943U, 2013.

[122] J. Yuan, C. Zhao, M. Ye, J. Kang, Z. Zhang and S. Jin, "A Fresnel reflection-based optical fiber sensor system for remote refractive index measurement using an OTDR," *Photonic Sensors,* Vol. 4, Iss. 1, pp. 48-52, 2014.

[123] M. Bravo, A. Candiani, A. Cucinotta, S. Selleri, M. Lopez-Amo, J. Kobelke and K. Schuster, "Remote PCF-based sensors multiplexing by using optical add-drop multiplexers," *Opt. Laser Technol.,* Vol. 57, pp. 9-11, 2014.

[124] M. Bravo, V. De Miguel-Soto, A. Ortigosa and M. Lopez-Amo, "Fully switchable multi-wavelength fiber laser based interrogator system for remote and versatile fiber optic sensors multiplexing structures," in *Proceedings of SPIE 9157*- 23dn Conference on Optical Fiber Sensors (OFS-23), 91576P, 2014 .

[125] D. Leandro, R. A. Perez-Herrera, I. Iturri and M. Lopez-Amo, "Experimental study of the SLM behavior and remote sensing applications of a multi-

wavelength fiber laser topology based on DWDMs," *Appl. Phy. B,* Vol. 118, Iss. 3, pp. 497-503, 2015.

[126] A. Othonos, "Fiber Bragg gratings," *Rev. Sci. Instrum.,* Vol. 68, No. 12, pp. 4309-4341, 1997.

[127] G. P. Agrawal and S. Radic, "Phase-shifted fiber Bragg gratings and their application for wavelength demultiplexing," *IEEE Photonics Technology Letters,* Vol. 6, Iss. 8, pp. 995-997, 1994.

[128] S. M. Melle, K. Liu and R. M. Measures, "A passive wavelength demodulation system for guided-wave Bragg grating sensors," *IEEE Photonics Technology Letters,* Vol. 4, Iss. 5, pp. 516-518, 1992.

[129] A. B. L. Ribeiro, L. A. Ferreira, M. Tsvetkov and J. L. Santos, "All-fibre interrogation technique for fibre Bragg sensors using a biconical fibre filter," *Electron. Lett.,* Vol. 32, No. 4, pp. 382-383, 1996.

[130] M. A. Davis and A. D. Kersey, "All-fibre Bragg grating strain-sensor demodulation technique using a wavelength division coupler," *Electron. Lett.,* Vol. 30, Iss. 1, pp. 75-77, 1994.

[131] Y. Hu, S. Chen, L. Zhang and I. Bennion, "Multiplexing Bragg gratings using combined wavelength and spatial division techniques with digital resolution enhancement," *Electron. Lett.,* Vol. 33, Iss. 23, pp. 1973-1975, 1997.

[132] V. Grubsky and J. Feinberg, "Long-period fiber gratings with variable coupling for real-time sensing applications," *Opt. Lett.,* Vol. 25, No. 4, pp. 203-205, 2000.

[133] S. Kim, J. Kwon, S. Kim and B. Lee, "Temperature-independent strain sensor using a chirped grating partially embedded in a glass tube," *IEEE Photonics Technology Letters,* Vol. 12, Iss. 6, pp. 678-680, 2000.

[134] R. W. Fallon, L. Zhang, A. Gloag and I. Bennion, "Identical broadband chirped grating interrogation technique for temperature and strain sensing," *Electron. Lett.,* Vol. 33, Iss. 8, pp. 705-707, 1997.

[135] Y. Ma, C. Wang, Y. Yang, S. Yan and J. Li, "High resolution and wide scale fiber Bragg grating sensor interrogation system," *Opt. Laser Technol.,* Vol. 50, pp. 107-111, 2013.

[136] H. J. Park and M. Song, "Fiber grating sensor interrogation using a double-pass Mach-Zehnder interferometer," *IEEE Photonics Technology Letters,* Vol. 20, Iss. 22, pp. 1833-1835, 2008.

[137] S. J. Choi, W. Mao and J. K. Pan, "Novel RF interrogation of a fiber Bragg grating sensor using bidirectional modulation of a Mach-Zehnder electro-optical modulator," *Sensors,* Vol. 13, Iss. 7, pp. 8403-8411, 2013.

[138] M. A. Davis and A. D. Kersey, "Application of a fiber Fourier transform spectrometer to the detection of wavelength-encoded signals from Bragg grating sensors," *J. Lightwave Technol.,* Vol. 13, Iss. 7, pp. 1289-1295, 1995.

[139] K. B. Rochford and S. D. Dyer, "Demultiplexing of interferometrically interrogated fiber Bragg grating sensors using Hilbert transform processing," *J. Lightwave Technol.,* Vol. 17, Iss. 5, pp. 831-836, 1999.

[140] M. Volanthen, H. Geiger, M. G. Xu and J. P. Dakin, "Simultaneous monitoring of multiple fibre gratings with a single acousto-optic tunable filter," *Electron. Lett.,* Vol. 32, Iss.13, pp. 1228-1229, 1996.

[141] H. Geiger, M. G. Xu, N. C. Eaton and J. P. Dakin, "Electronic tracking system for multiplexed fibre grating sensors," *Electron. Lett.,* Vol. 31, Iss. 12, pp. 1006-1007, 1995.

[142] D. A. Jackson, A. B. L. Ribeiro, L. Reekie and J. L. Archambault, "Simple multiplexing scheme for a fiber-optic grating sensor network," *Opt. Lett.,* Vol. 18, Iss. 14, pp. 1192-1194, 1993.

[143] S. C. Kang, S. Y. Kim, S. B. Lee, S. W. Kwon, S. S. Choi and B. Lee, "Temperature-independent strain sensor system using a tilted fiber bragg grating demodulator," *IEEE Photonics Technology Letters,* Vol. 10, Iss. 10, pp. 1461-1463, 1998.

[144] Y. J. Rao, D. A. Jackson, L. Zhang and I. Bennion, "Dual-cavity interferometric wavelength-shift detection for in-fiber Bragg grating sensors," *Opt. Lett.,* Vol. 21, Iss. 19, pp. 1556-1558, 1996.

[145] J. Jung, Y. W. Lee and B. Lee, "High-resolution interrogation technique for fiber bragg grating strain sensor using long period grating pair and EDF," in *Proceedings of SPIE 4185* - 14th International Conference on Optical Fiber Sensors (OFS-14), pp. 114-117, 2000.

[146] J. C. Knight, T. A. Birks, P. S. J. Russell and D. M. Atkin, "All-silica single-mode optical fiber with photonic crystal cladding," *Opt. Lett.,* Vol. 21, Iss. 19, pp. 1547-1549, 1996.

[147] P. S. J. Russell, "Photonic-crystal fibers," *J. Lightwave Technol.,* Vol. 24, No. 12, pp. 4729-4749, 2006.

[148] A. M. R. Pinto and M. Lopez-Amo, "Photonic crystal fibers for sensing applications," *Journal of Sensors,* Vol. 2012, Article ID 598178, 2012.

[149] S. Liu, N. Liu, M. Hou, J. Guo, Z. Li and P. Lu, "Direction-independent fiber inclinometer based on simplified hollow core photonic crystal fiber," *Opt. Lett.,* Vol. 38, Iss. 4, pp. 449-451, 2013.

[150] B. Kim, T. H. Kim, L. Cui and Y. Chung, "Twin core photonic crystal fiber for in-line Mach-Zehnder interferometric sensing applications," *Optics Express,* Vol. 17, Iss. 18, pp. 15502-15507, 2009.

[151] H. P. Gong, C. C. Chan, P. Zu, L. H. Chen and X. Y. Dong, "Curvature measurement by using low-birefringence photonic crystal fiber based Sagnac loop," *Opt. Commun.,* Vol. 283, Iss. 16, pp. 3142-3144, 2010.

[152] W. C. Wong, C. C. Chan, H. Gong and K. C. Leong, "Mach-Zehnder photonic crystal interferometer in cavity ring-down loop for curvature measurement," Vol. 23, Iss. 12, pp. 795-797, 2011.

[153] M. Bravo, A. M. R. Pinto, M. Lopez-Amo, J. Kobelke and K. Schuster, "High precision micro-displacement fiber sensor through a suspended-core Sagnac interferometer," *Opt. Lett.,* Vol. 37, Iss. 2, pp. 202-204, 2012.

[154] R. M. André, S. O. Silva, M. Becker, K. Schuster, M. Rothardt, H. Bartelt, M. B. Marques and O. Frazão, "Strain sensitivity enhancement in suspended core fiber tapers," *Photonic Sensors,* Vol. 3, Iss. 2, pp. 118-123, 2013.

[155] K. Karim Qureshi, Z. Liu, H. Y. Tam and M. Fahad Zia, "A strain sensor based on in-line fiber Mach-Zehnder interferometer in twin-core photonic crystal fiber," *Opt. Commun.,* Vol. 309, pp. 68-70, 2013.

[156] W. Qian, C. L. Zhao, S. He, X. Dong, S. Zhang, Z. Zhang, S. Jin, J. Guo and H. Wei, "High-sensitivity temperature sensor based on an alcohol-filled photonic crystal fiber loop mirror," *Opt. Lett.,* Vol. 36, Iss. 9, pp. 1548-1550, 2011.

[157] R. Wang, J. Yao, Y. Miao, Y. Lu, D. Xu, N. Luan, M. Musideke, L. Duan and C. Hao, "A reflective photonic crystal fiber temperature sensor probe based on infiltration with liquid mixtures," *Sensors,* Vol. 13, Iss. 6, pp. 7916-7925, 2013.

[158] B. Dong, J. Hao, C. Y. Liaw, B. Lin and S. C. Tjin, "Simultaneous strain and temperature measurement using a compact photonic crystal fiber intermodal interferometer and a fiber Bragg grating," *Appl. Opt.,* Vol. 49, Iss. 32, pp. 6232-6235, 2010.

[159] T. Li, X. Dong, C. C. Chan, L. Hu and W. Qian, "Simultaneous strain and temperature measurement based on a photonic crystal fiber modal-interference interacting with a long period fiber grating," *Opt. Commun.,* Vol. 285, Iss. 24, pp. 4874-4877, 2012.

[160] R. A. Perez-Herrera, R. M. André, S. F. Silva, M. Becker, K. Schuster, J. Kobelke, M. Lopez-Amo, J. L. Santos and O. Frazao, "Simultaneous measurement of strain and temperature based on clover microstructured fiber loop mirror," in *Proceedings of SPIE 8421,* 22nd International Conference on Optical Fiber Sensors (OFS-22), 84216W, 2012, .

[161] R. M. André, M. B. Marques, P. Roy and O. Frazão, "Fiber loop mirror using a small core microstructured fiber for strain and temperature discrimination," *IEEE Photonics Technology Letters,* Vol. 22, Iss. 15, pp. 1120-1122, 2010.

[162] S. Mathews, G. Farrell and Y. Semenova, "Liquid crystal infiltrated photonic crystal fibers for electric field intensity measurements," *Appl. Opt.,* Vol. 50, Iss. 17, pp. 2628-2635, 2011.

[163] S. Mathews, G. Farrell and Y. Semenova, "Directional electric field sensitivity of a liquid crystal infiltrated photonic crystal fiber," *IEEE Photonics Technology Letters,* Vol. 23, Iss. 7, pp. 408-410, 2011.

[164] Y. K. Chamorovskiy, N. I. Starostin, M. V. Ryabko, A. I. Sazonov, S. K. Morshnev, V. P. Gubin, I. L. Vorob'ev and S. A. Nikitov, "Miniature microstructured fiber coil with high magneto-optical sensitivity," *Opt. Commun.,* Vol. 282, Iss. 23, pp. 4618-4621, 2009.

[165] H. V. Thakur, S. M. Nalawade, S. Gupta, R. Kitture and S. N. Kale, "Photonic crystal fiber injected with Fe3O4 nanofluid for magnetic field detection," *Applied Physics Letters,* Vol. 99, Iss. 16, pp. 161101-161101-3, 2011.

[166] T. Martynkien, G. Statkiewicz-Barabach, J. Olszewski, J. Wojcik, P. Mergo, T. Geernaert, C. Sonnenfeld, A. Anuszkiewicz, M. K. Szczurowski, K. Tarnowski, M. Makara, K. Skorupski, J. Klimek, K. Poturaj, W. Urbanczyk, T. Nasilowski, F. Berghmans and H. Thienpont, "Highly birefringent microstructured fibers with enhanced sensitivity to hydrostatic pressure," *Optics Express,* Vol. 18, Iss. 14, pp. 15113-15121, 2010.

[167] H. Y. Fu, C. Wu, M. L. V. Tse, L. Zhang, K. C. D. Cheng, H. Y. Tam, B. O. Guan and C. Lu, "High pressure sensor based on photonic crystal fiber for downhole application," *Appl. Opt.,* Vol. 49, Iss. 14, pp. 2639-2643, 2010.

[168] D. E. Ceballos-Herrera, I. Torres-Gómez, A. Martínez-Ríos, L. García and J. J. Sanchez-Mondragon, "Torsion Sensing Characteristics of Mechanically Induced Long-Period Holey Fiber Gratings," *Sensors Journal, IEEE,* Vol. 10, Iss. 7, pp. 1200-1205, 2010.

[169] M. S. Ferreira, J. L. Santos, P. Mergo and O. Frazão, "Torsion sensor based on a figure-of-eight cavity fibre laser," *Laser Physics Letters,* Vol. 10, No. 4, 2013.

[170] M. Smietana, D. Brabant, W. J. Bock, P. Mikulic and T. Eftimov, "Refractive-index sensing with inline core-cladding intermodal interferometer based on silicon nitride nano-coated photonic crystal fiber," *J. Lightwave Technol.,* Vol. 30, Iss. 8, pp. 1185-1189, 2012.

[171] F. Shi, J. Wang, Y. Zhang, Y. Xia and L. Zhao, "Refractive index sensor based on S-tapered photonic crystal fiber," *IEEE Photonics Technology Letters,* Vol. 25, Iss. 4, pp. 344-347, 2013.

[172] H. V. Thakur, S. M. Nalawade, Y. Saxena and K. T. V. Grattan, "All-fiber embedded PM-PCF vibration sensor for Structural Health Monitoring of composite," *Sensors and Actuators A: Physical,* Vol. 167, Iss. 2, pp. 204-212, 6, 2011.

[173] N. Burani and J. Lægsgaard, "Perturbative modeling of Bragg-grating-based biosensors in photonic-crystal fibers," *J. Opt. Soc. Am. B,* Vol. 22, Iss. 11, pp. 2487-2493, 2005.

[174] J. Mathew, Y. Semenova, G. Rajan and G. Farrell, "Humidity sensor based on photonic crystal fibre interferometer," *Electron. Lett.,* Vol. 46, Iss. 19, pp. 1341-1343, 2010.

[175] T. Li, X. Dong, C. C. Chan, K. Ni, S. Zhang and P. P. Shum, "Humidity sensor with a PVA-coated photonic crystal fiber interferometer," *IEEE Sensors Journal,* Vol. 13, Iss. 6, pp. 2214-2216, 2013.

[176] T. Ritari, J. Tuominen, H. Ludvigsen, J. C. Petersen, T. Sørensen, T. P. Hansen and H. R. Simonsen, "Gas sensing using air-guiding photonic bandgap fibers," *Optics Express,* Vol. 12, Iss. 17, pp. 4080-4087, 2004.

[177] G. Yan, A. P. Zhang, G. Ma, B. Wang, B. Kim, J. Im, S. He and Y. Chung, "Fiber-optic acetylene gas sensor based on microstructured optical fiber bragg gratings," *IEEE Photonics Technology Letters,* Vol. 23, Iss. 21, pp. 1588-1590, 2011.

[178] S. H. Kassani, J. Park, Y. Jung, J. Kobelke and K. Oh, "Fast response in-line gas sensor using C-type fiber and Ge-doped ring defect photonic crystal fiber," *Optics Express,* Vol. 21, Iss. 12, pp. 14074-14083, 2013.

[179] S. Arismar Cerqueira, "Recent progress and novel applications of photonic crystal fibers," *Reports on Progress in Physics,* Vol. 73, No. 2, 2010.

[180] G. Agrawal, "Nonlinear Fiber Optics," *Nonlinear Fiber Optics,* 2012.

[181] T. A. Birks, J. C. Knight and P. S. J. Russell, "Endlessly single-mode photonic crystal fiber," *Opt. Lett.,* Vol. 22, Iss. 13, pp. 961-963, 1997.

[182] N. A. Mortensen, J. R. Folkenberg, M. D. Nielsen and K. P. Hansen, "Modal cutoff and the V parameter in photonic crystal fibers," *Opt. Lett.,* Vol. 28, Iss. 20, pp. 1879-1881, 2003.

[183] A. Rogers, *Polarization in Optical Fibers*. Artech House, 2008.

[184] A. Ortigosa-Blanch, J. C. Knight, W. J. Wadsworth, J. Arriaga, B. J. Mangan, T. A. Birks and P. S. J. Russell, "Highly birefringent photonic crystal fibers," *Opt. Lett.,* Vol. 25, Iss. 18, pp. 1325-1327, 2000.

[185] K. Suzuki, H. Kubota, S. Kawanishi, M. Tanaka and M. Fujita, "Optical properties of a low-loss polarization-maintaining photonic crystal fiber," *Optics Express,* Vol. 9, No. 13, pp. 676-680, 2001.

[186] *http://nktphotonics.com/files/files/PM-1550-01.pdf*.

[187] D. H. Kim and J. U. Kang, "Analysis of temperature-dependent birefringence of a polarization-maintaining photonic crystal fiber," *Optical Engineering,* Vol. 46, Iss. 7, 2007.

[188] L. Euler, *The Rational Mechanics of Flexible Or Elastic Bodies 1638 - 1788*. Birkhäuser Basel, 1960.

[189] J. D. C. Jones, "Chapter 12, interferometry and polarimetry for optical sensing," in *Hand Book of Optical Fiber Sensing Technology*, J. M. Lopez-Higuera, Ed. John Wiley & Sons, 2002, pp. 227-245.

[190] A. Rogers, "Chapter 6, polarimetric optical-fiber sensing," in *Polarization in Optical Fibers,* B. Culshaw and A. Rogers, Eds. Artech house, 2008, pp. 193-224.

[191] S. M. Tripathi, A. Kumar, R. K. Varshney, Y. B. P. Kumar, E. Marin and J. P. Meunier, "Strain and temperature sensing characteristics of single-mode-multimode-single-mode structures," *J. Lightwave Technol.,* Vol. 27, Iss. 13, pp. 2348-2356, 2009.

[192] Y. Gong, T. Zhao, Y. J. Rao and Y. Wu, "All-fiber curvature sensor based on multimode interference," *IEEE Photonics Technology Letters,* Vol. 23, Iss. 11, pp. 679-681, 2011.

[193] Q. Wu, Y. Semenova, P. Wang and G. Farrell, "High sensitivity SMS fiber structure based refractometer - Analysis and experiment," *Optics Express,* Vol. 19, Iss. 9, pp. 7937-7944, 2011.

[194] Q. Wu, A. M. Hatta, P. Wang, Y. Semenova and G. Farrell, "Use of a bent single SMS fiber structure for simultaneous measurement of displacement and temperature sensing," *IEEE Photonics Technology Letters,* Vol. 23, Iss. 2, pp. 130-132, 2011.

[195] Y. G. Han, "Temperature-insensitive strain measurement using a birefringent interferometer based on a polarization-maintaining photonic crystal fiber," *Appl. Phy. B,* Vol. 95, Iss. 2, pp. 383-387, 2009.

[196] D. B. Mortimore, "Fiber loop reflectors." *J. Lightwave Technol.,* Vol. 6, Iss. 7, pp. 1217-1224, 1988.

[197] W. Qian, C. L. Zhao, X. Dong and W. Jin, "Intensity measurement based temperature-independent strain sensor using a highly birefringent photonic crystal fiber loop mirror," *Opt. Commun.,* Vol. 283, Iss. 24, pp. 5250-5254, 2010.

[198] H. Zhang, B. Liu, Z. Wang, J. Luo, S. Wang, C. Jia and X. Ma, "Temperature-insensitive displacement sensor based on high-birefringence photonic crystal fiber loop mirror," *Optica Applicata,* Vol. 40, No.1, pp. 209-217, 2010.

[199] O. Frazao, J. M. Baptista and J. L. Santos, "Temperature-independent strain sensor based on a hi-bi photonic crystal fiber loop mirror," *IEEE Sensors Journal,* Vol. 7, Iss. 10, pp. 1453-1455, 2007.

[200] M. Bravo, X. Angulo-Vinuesa, S. Martin-Lopez, M. Lopez-Amo and M. Gonzalez-Herraez, "Slow-light and enhanced sensitivity in a displacement sensor using a lossy fiber-based ring resonator," *J. Lightwave Technol.,* Vol. 31, Iss. 23, pp. 3752-3757, 2013.

[201] C. Yu, Y. Zhang, X. Zhang, K. Wang, C. Yao, P. Yuan and Y. Guan, "Nested fiber ring resonator enhanced Mach-Zehnder interferometer for temperature sensing," *Appl. Opt.,* Vol. 51, Iss. 36, pp. 8873-8876, 2012.

[202] L. Zhang, P. Lu, L. Chen, C. Huang, D. Liu and S. Jiang, "Optical fiber strain sensor using fiber resonator based on frequency comb Vernier spectroscopy," *Opt. Lett.,* Vol. 37, Iss. 13, pp. 2622-2624, 2012.

[203] Y. Guo and X. Fan, "Optofluidics in bio-chemical analysis," in *Progress in Biomedical Optics and Imaging - Proceedings of SPIE 8212,* 82120C, 2012.

CHAPTER II

OPTICAL FIBER LASERS

upna Universidad Pública de Navarra
Nafarroako Unibertsitate Publikoa

CHAPTER III

INTRODUCTION

Optical fiber lasers have attracted considerable interest in recent years, not only for telecommunications applications, but also for instrument testing, optical signal processing and fiber sensors systems. This technology present a variety of advantages such as a simple structure, high power, low intensity noise, low insertion loss, multiwavelength operation and high compatibility with other optical components [1-3].

As seen in chapter 2, optical fiber lasers can be classified in two main groups depending on the gain medium and on the cavity design. Firstly, depending on the gain medium, it can be achieved fiber lasers based on; erbium doped fiber amplifiers (EDFA) [4-6], semiconductor optical amplifiers (SOAs) [7] or Raman amplifiers [8-10]. On the other hand, depending on the fiber laser cavity design, optical fiber ring lasers [11, 12], optical fiber lasers based on linear cavities [4] and random fiber lasers [9, 13], can be achieved.

Throughout this chapter, different configurations of fiber lasers, sorted according to their cavity design, are presented. The aim of these designs is focused on the improvement of parameters such as output power, optical signal to noise ratio, stabil-

CHAPTER III

ity and the achievement of single longitudinal mode operation.

Section 3.1 presents four multiwavelength erbium doped fiber ring laser (MEDFRLs) configurations. The first one is based on a double FBG reflection for each wavelength in order to improve the OSNR and to allow the independent control of the loss of each emission line. The second laser is designed using a combination of FBG and PSFBGs in order to achieve a SLM laser. Finally, a comparison of two MEDFRLs based on Add-drops and MUX-DMUX technologies, is presented.

Section 3.2 shows the experimental study of an erbium doped fiber laser based on a linear cavity. A narrow filtering technique based on the spectral overlapping of two uniform FBGs is used in order to achieve SLM operation. The laser is tested exhibiting SLM operation even with temperature and strain variations.

Section 3.3 presents a study of a single-wavelength and a multi-wavelength random DFB fiber laser with sub-gigahertz line-widths for the first time to our knowledge. Both laser topologies are designed using a combination of FBG and PSFBGs in order to achieve the narrowest linewidths up to the date.

Also, this section includes an experimental comparison of three fiber laser structures, a hybrid ring-random laser, a purely ring laser and a random fiber laser, with the same Raman gain medium, in order to establish the main pros and cons of each basic scheme. Several aspects are taken into account in the study such output power, lasing threshold, slope efficiency, power fluctuations and the longitudinal modes. Also, the possible utilization of these fiber lasers in digital modulated optical communication systems is studied.

Finally section 3.4 summarizes the chapter's main conclusions.

3.1 ERBIUM-DOPED FIBER RING LASERS

3.1.1 LOW NOISE DUAL-WAVELENGTH EDFRL IN SINGLE-LONGITUDINAL-MODE OPERATION

As it has been mentioned in the introduction, multiwavelength EDFRLs have attracted considerable interest not only for telecommunications but also for sensing systems. The use of a dual-wavelength fiber laser for sensor interrogation is a technique which can improve the accuracy of interferometric sensor measurements as it is shown in [14].

Erbium-doped fiber ring lasers output are susceptible to power instabilities. These instabilities might degrade the performance characteristics of a communication system or a sensor multiplexing network based on a laser interrogation scheme. The optimization of the ring laser configuration can improve considerably the stability of these lasers. In this regard, the independent control of the loss of each emission line contributes to reduce the laser instability and also to obtain SLM operation, when intensity equalization of the emission lines is achieved [12].

In this section, a stable dual-wavelength EDFRL that operates in SLM condition is experimentally proposed and demonstrated. This laser increases the optical signal to noise ratio due to the low noise configuration. Besides, the topology allows an independent control of the loss of each emission line improving the laser stability and achieving a SLM operation laser.

Description of the laser

The experimental setup of the proposed dual-wavelength erbium-doped fiber ring laser is shown in Figure 3.1 (a). The designed laser consisted of an amplifying fiber ring cavity wherein a double reflection for each wavelength was used. For this purpose, it was utilized a four port circulator and two reflecting elements (a FBG and a tunable FBG) for each wavelength. The non-tunable FBGs were connected at port 2 of the circulator, because their bandwidths were narrower than the tunable FBGs, so most part of the amplified spontaneous emission was filtered at first reflection. The two FBG sets were centered at 1547 nm and 1550 nm respectively, having the first FBGs a full-width at half maximum (FWHM) of 0.19 nm and 0.165 nm; a reflectivity of 99% and 98.3% and an extinction ratio of 33 dB and 35.3 dB, in this order. The tunable FBGs had a FWHM of 0.609 nm

and 0.390 nm, a reflectivity of 98.9% and 99.7% and an extinction ratio of 30 dB and 26.9 dB, respectively. In order to achieve an independent control of the system´s equalization, the order of connection of the tunable FBGs were inverted at the port number 3 of the circulator, the λ'1 wavelength was tuned at 1547 nm and λ'2 to 1550 nm, this way the variable attenuator 1 (VA1) controlled the gain at λ2 and at the same mode the (VA2) only affected to λ1. In particular, in order to achieve power equalization of both channels the attenuation of VA1 was set to 0.86 dB, while the loss induced by VA2 were fixed to 0.15dB.

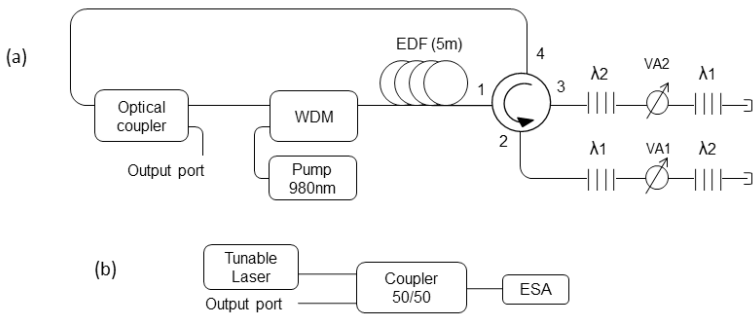

FIGURE 3.1. (a) Schematic diagram of the proposed dual-wavelength erbium doped fiber ring laser configuration; (b) Heterodyne detection system.

The gain of the fiber laser was provided by a 5 m-long highly Erbium-doped fiber (EDF, Er-30 by Liekki, with an absorption of 30 dB/m at λ=1530 nm). A 980/1550 nm wavelength-division multiplexer was used to introduce the 70 mW of optical pump power from a 980 nm laser diode. The laser output was extracted from the cavity using a 70:30 fiber coupler, being the 70% exit the output of the laser.

The circulator guided both emission lines inside the ring cavity and served also as an isolator in our lasing structure ensuring the unidirectional circulation of the light, and avoiding the undesired spatial hole-burning effect. All the free terminations were immersed in refractive-index-matching gel to avoid undesirable reflections.

The laser output was monitored by an optical spectrum analyzer (OSA, Q8384 of Advantest) with a highest spectral resolution of 0.01 nm. The single-longitudinal-mode operation was verified by a heterodyne detection system, which is depicted in Figure 3.1 (b). Each lasing wavelength from our fiber laser was combined with a commercial tunable laser source (TLS, Agilent 8464B) using a 3 dB

coupler. This TLS had a linewidth of 100 KHz and its wavelength was placed close to the fiber laser emission wavelengths. Thus the beating signal was observed by means of an ESA (Rohde & Schwarz FSP), whose resolution bandwidth can be as good as 1 Hz.

Experimental results

Figure 3.2 displays the output spectra of the proposed dual-wavelength EDF fiber ring laser corresponding to the reflection bands of both FBGs when pump power was 70 mW. The measured power of both channels was around -10 dBm, which it was more than 65 dB higher than the ASE noise floor. An interesting conclusion to be drawn from Figure 3.2 is that the proposed scheme was a very low noise topology because the ASE was filtered twice, this being a crucial advantage over some previously reported lasers in the literature [12, 14-17] .

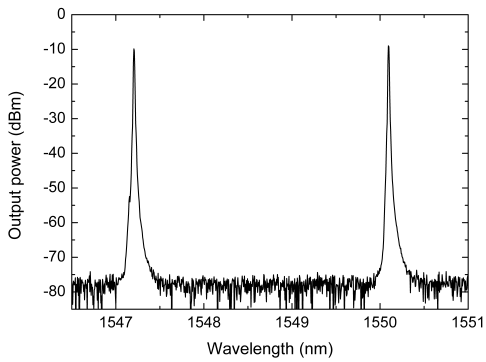

FIGURE 3.2. Measured output optical spectrum of the proposed dual-wavelength EDFRL configuration for a pump power of 70 mW.

A good stability and single-longitudinal-mode operation are desired requirements for EDF lasers used in demanding applications. Before looking at the stability of the output power laser, let us consider first the SLM operation.

As it has been explained in section 2.3.3, fiber ring lasers usually support a vast number of spaced longitudinal modes, which can be calculated using equation 2.3. Therefore, taking into account the corresponding values of FWHM and λ for each FBG, provided previously, and that: n=1.5; L=17 m; the calculated number of modes for each emission line were 2024 and 1757 respectively, centered at 1547 nm and 1550 nm.

However, when both lasing wavelengths were oscillating simultaneously with similar output powers by using the VAs to adjust the cavity loss, the laser presented a SLM operation behavior as it is shown in Figure 3.3. To corroborate it, we calculated the mode spacing for each wavelength region, which were $\Delta\lambda_1 = 9.385 \times 10^{-5}$ nm and $\Delta\lambda_1 = 9.421 \times 10^{-5}$ nm. Figure 3.3 shows a bandwidth of 3GHz (or 2.4×10^{-2} nm, so the observed bandwidth was around 25 times higher than the mode spacing between longitudinal modes, thus we can conclude that indeed the dual wavelength EDF laser worked in single mode operation. The picture presents the results of the heterodyne detection system measured by the ESA with a resolution of 100 KHz: the beating between the tunable laser source and both emission lines when the tunable laser source was tuned close to the first emission line (Figure 3.3 (a)) and the second (Figure 3.3 (b)). As aforementioned, Figures 3.3 (a) and (b) only can show the ESA spectrum for one of the wavelengths laser emission because the wavelength difference between both emission lines was around 3 nm, while the bandwidth of Figure 3.3 was 2 orders of magnitude lower and the mode spacing was approximately 5 orders lower.

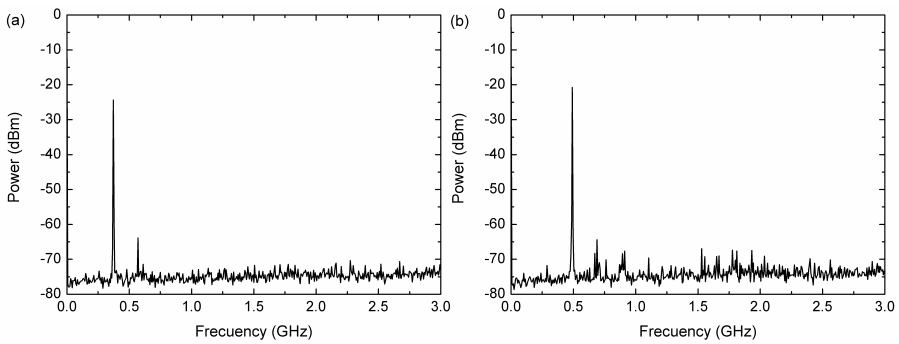

FIGURE 3.3. Output optical spectrum measured by the ESA for the dual-wavelength EDFRL configuration, when the tunable laser was tuned for the first (a) and second (b) wavelength laser emission.

In ref. [12]an SLM fiber ring laser was achieved by annihilating the mode competition with an auxiliary lasing wavelength. This process was explained by the interaction of the seed light produced from one channel to the other and vice versa. One channel worked as auxiliary lasing to the other and the channels´ multiple-longitudinal-mode oscillation were suppressed.

The output power imbalance between both lasing wavelengths had a direct influence in the mode of operation. Figure 3.4(a) shows the laser output spectrum for an equalization with a power difference between emission lines of 9.23 dB, at this point it can be seen that the laser did not fulfill the SLM operation regime (Figure 3.4 (b)).

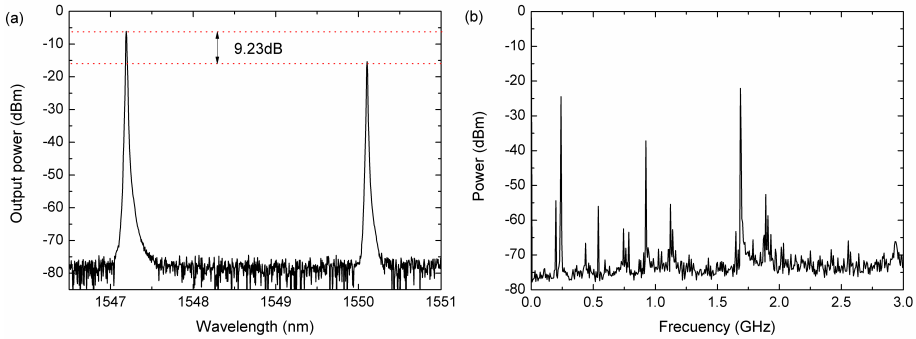

FIGURE 3.4. (a) OSA and (b) ESA spectrum when the output power imbalance between both emission lines was 9.23 dB.

The measurements were repeated at different pump power from 28 mW to 150 mW. In all cases, a SLM operation in both channels was achieved when the two lasing wavelengths are oscillating simultaneously with similar output powers by using the VAs to adjust the cavity loss. The pump power chosen was 70 mW in order to work further than the pumping threshold needed to obtain laser emission.

To determinate the instability of the system the output power of the EDFL was also measured during a period of 10 minutes at room temperature. The measured data were stored each 15 seconds and a CL of 90 % was considered. Figure 3.5 shows the power fluctuation for the emission line of 1547 nm when the laser worked in SLM and MLM operation. The instability was 1.08 and 0.67 dB for the emission lines centered at 1550 nm and 1547 nm respectively in SLM. Unsurprisingly, the reduction of the number of longitudinal modes inside the cavity till the SLM operation had an outstanding positive effect in the output power variations, as it is shown in Figure 3.5. Power fluctuations of the emission line centered at 1547 nm vary from 1.52 dB, when the laser operation was a multiple longitudinal mode one, to 0.67 dB when it worked in SLM operation regime.

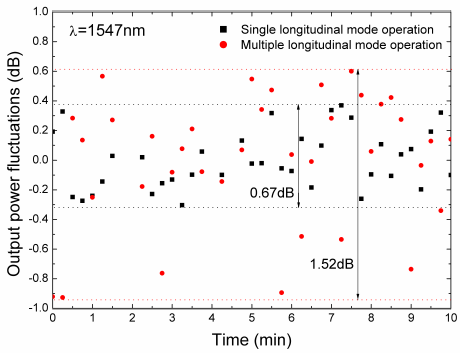

FIGURE 3.5. Output power fluctuation for the emission line centered at 1547 nm when the laser worked in SLM and MLM operation regimes.

3.1.2 DUAL-WAVELENGTH SINGLE-LONGITUDINAL MODE EDFRL USING PHASE-SHIFT BRAGG GRATINGS

As it has been seen in the previous section, SLM behavior can be achieved by equalization; when the powers of the lasing channels are similar. However, there is another way to ensure a stable SLM behavior in an EDFRL, which is based on filtering. EDFRL usually has a long cavity, which leads to the generation of a large number of densely spaced longitudinal modes. Therefore, an ultra-narrow bandwidth mode selection mechanism can be incorporated to ensure SLM operation.

In this section, a stable dual-wavelength EDFRL that operates in SLM regime is experimentally proposed and demonstrated. The laser topology is based on the serial connection of the FBGs using optical circulators. Ultra-narrow bandwidth phase-shifted FBGs are incorporated into the laser cavity. With them, we experimentally demonstrate the SLM operation for the lasing wavelengths in all circumstances, achieving high power stability and a remarkable OSNR.

Description of the laser

Figure 3.6 shows the experimental setup of the proposed dual-wavelength laser structure. This was a FBGs serial configuration based on circulators which included a phase shift fiber Bragg grating (PSFBG) in each arm in order to reduce the linewidth of the lasing wavelengths by obtaining the single longitudinal mode operation; and consequently, to improve the stability.

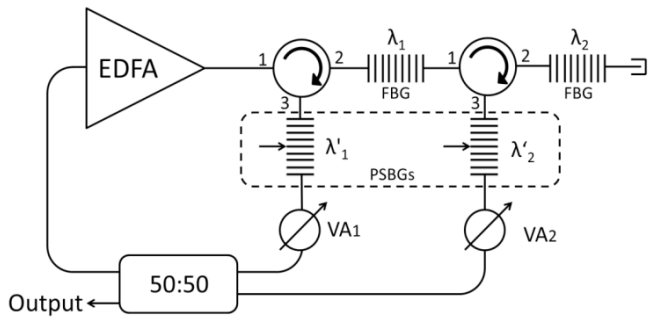

FIGURE 3.6. Schematic diagram of the proposed dual-wavelength EDFRL configuration. EDFA: Erbium-doped fiber amplifier. VA: Variable attenuator.

The wavelength selection was carried out by a combination of FBGs and PSFBGs. The FBGs were used as wavelength selective mirrors by using circulators and their purpose was the coarse wavelength selection in each arm. These FBGs were centered at 1562.8 nm (λ1) and 1550.5 nm (λ2) showing a reflectivity above 90% and a corresponding full-width at half-maximum of 0.120 and 0.125 nm respectively. Afterwards, the PSFBGs actuated as fine transmission filters with a FWHM of around 2 pm for both PSFBGs.

Based on [18], any phase shift can be obtained by changing the sampled period of a Sampled Fiber Bragg Grating (SFBG) [19]. For this application, two PSFBGs were written into a standard telecommunication optical fiber using the phase mask technique with a continuous laser emitting at 244 nm. The sampling effect was generated by opening and closing the laser shutter at preset locations. The total length of the PSFBGs was $L \approx 24$ mm, with a sampling period of $P=1.5$ mm. An increment in the sampling period P with a scale factor of F=1.5 located at the center of the grating created an equivalent pi-phase shift in the first order of the SFBG. The chosen scale factor was slightly modified to maximize the pi-shift on the m=-1 order, as can be noticed in Figure 3.7 (a). The measured phase-shifted SFBG was compared to its simulated response in Figure. 3.7 (b). All the SFBG spectra were calculated using the T-matrix method [20]. Two identical PSFBGs were manufactured, being their central wavelengths 1550.5 and 1562.8 nm respectively, and fabricated just by changing the phase mask.

The utilized gain medium was a commercial erbium-doped fiber amplifier (EDFA FIBERAMP-BT 17 by Photonetics). This device had an internal isolator, which ensures the unidirectional operation of the multi-wavelength laser and therefore avoids the spatial hole-burning.

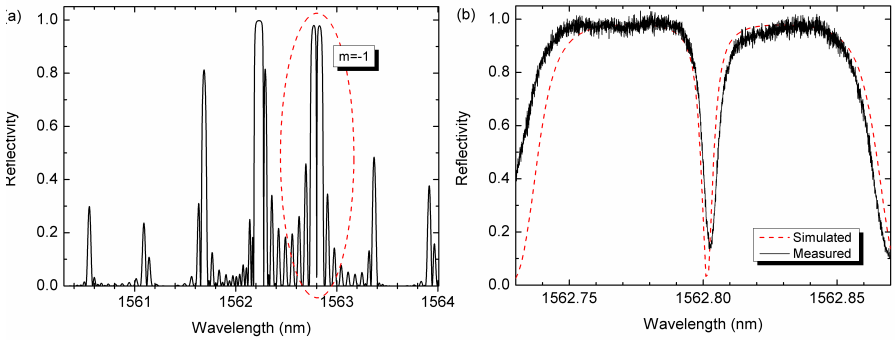

FIGURE 3.7. Simulated structure of the employed PSFBGs. (a) The phase shift was stronger for the m=-1 order of the SFBG. (b) Comparison of the simulated and measured spectra obtained with the m=-1 order.

A 2x2 coupler with a coupling ratio of 50/50 was used to combine both wavelengths, redirecting the 50% of the power to the EDFA and extracting the other 50% to the laser output. An advantage of this topology was the individual control of the loss for each wavelength by connecting variable attenuators between the 50/50 coupler and each PSFBG.

Experimental results

Figure 3.8 shows the output spectrum of the EDFRL for an EDFA output power of 130 mW measured with an optical spectrum analyzer (HP-70952B) which offered a resolution of 0.1 nm and a sensitivity of -60 dBm. As can be appreciated, two lasing channels were obtained with an optical output power close to 0 dBm and an OSNR higher than 55 dB. For the equalization of the system, the variable attenuator values were 1.38 dB and 0 dB for VA1 and VA2, respectively.

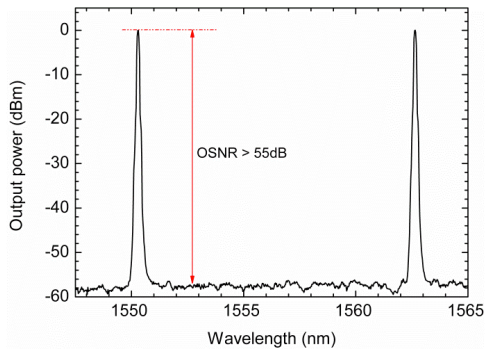

FIGURE 3.8. Optical output spectrum of the EDFRL measured at OSA.

In order to analyze the longitudinal-mode operation of the laser, a series of measurements were carried out using an ESA with a resolution of 100 KHz (Rohde & Schwarz FSP) in combination with a photo detector (New Focus 1544-B). For this purpose, the EDFRL output was beaten with a TLS with a BW of 100 KHz (Agilent 8464B) using a 50:50 coupler.

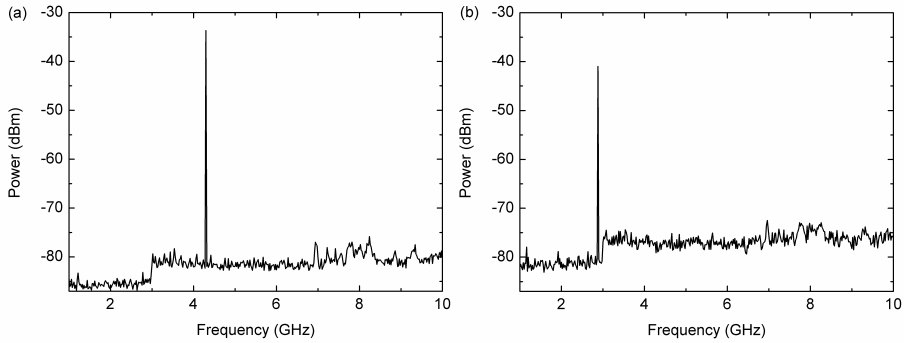

FIGURE 3.9. Output spectrum measured by the ESA at (a) λ1=1562.8 nm, and (b) λ2=1550.5 nm.

Figure 3.9 shows only one beat peak for each wavelength laser output, thus both emission lines were operating in the single-longitudinal-mode regime. Also to determine the wavelength instability of the laser a measurement of one hour for each wavelength at room temperature, using the max-hold mode at ESA, was carried out. The wavelength instability corresponds to the difference between the higher and the lowest frequency. As can be shown at figure 3.10, a maximum instability of 320 MHz (≈2.56 pm) and 896 MHz (≈7.16 pm) for λ1 and λ2 respectively were retrieved, being these results better than the 15 pm and 10 pm obtained in [11] and [16] respectively.

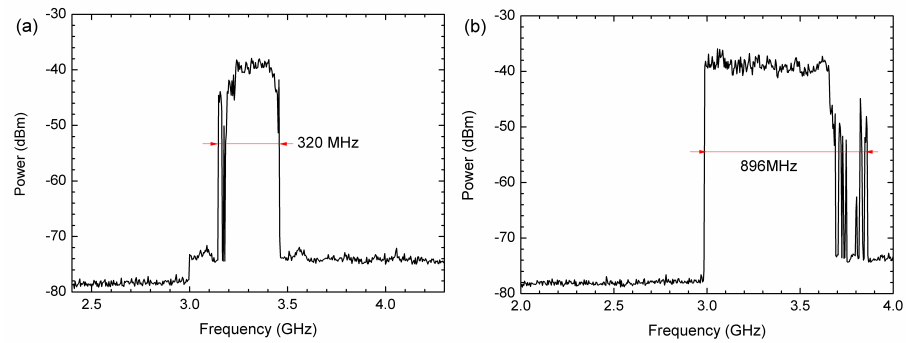

FIGURE 3.10. Frequency instability at (a) λ1 and (b) λ2 measured with Max-Hold mode in ESA for 1 hour.

The emission lines band widths were also measured using the self-heterodyne method described in section 2.3.4, by beating the MEDFRL output delayed by 100 Km of SMF, with the same MEDFRL output modulated by a phase optical modulator (POM, Avanex IM10-P) in combination with a RF generator (Rohde & Schwarz SMT02) at 1GHz MHz. A tunable filter was used to select the channel to be measured. Because the spectrum presented a Gaussian shape, this spectrum was $\sqrt{2} \cdot BW$, so as is shown in Figure 3.11 the BWs were around 11 KHz and 13 KHz corresponding with λ1 and λ2 respectively.

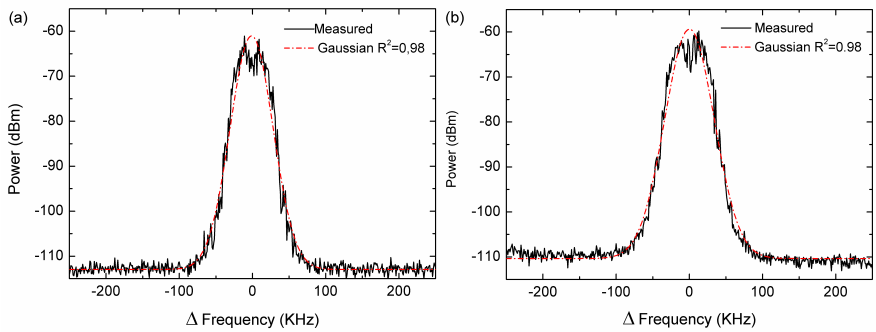

FIGURE 3.11. Spectrum of the emission line of λ1 (a) and λ2 (b) measured at ESA with the self-heterodyne detection method.

In the previous section we saw how to obtain a SLM fiber ring laser through the power equalization of two emission lines. Also, as mentioned before, in [12] a SLM fiber ring laser was achieved by annihilating the mode competition with an auxiliary lasing. Taking these results into consideration, we checked if our laser showed the same behavior due to some interaction between the seed light produced from one channel to the other and vice versa. Thus, a study with only one wavelength was carried out. The experiment consisted in analyzing the behavior of the PSFBG in the system. In order to simplify the characterization process, a high resolution Brillouin optical spectrum analyzer (BOSA-C Aragon Photonics) with a resolution of 0.08 pm was employed to measure the λ1 spectrum with and without the corresponding PSFBG. Figure 3.12 shows that the laser operated in SLM regime for a unique wavelength due to the PSFBG, and discarding the effect presented at [12].Therefore the SLM operation was explained due to the combination of the thinness of the PSFBG's spectrum with the EDFA's gain within the ring.

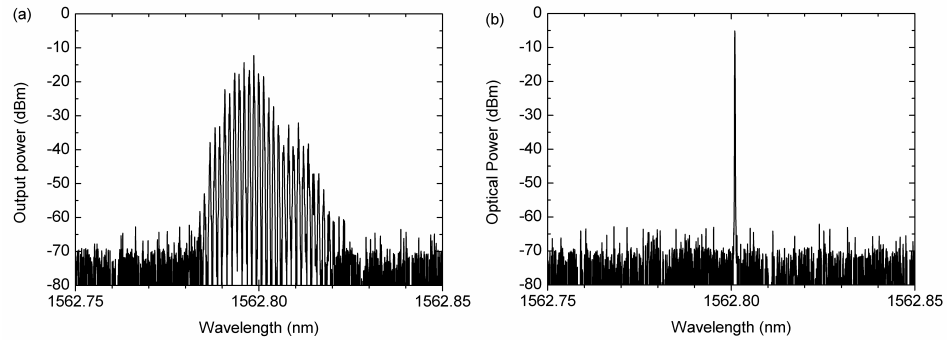

FIGURE 3.12. Optical output spectra at BOSA for λ1 (a) without PSFBG operating in multi longitudinal mode, and (b) with PSFBG operating in single longitudinal mode.

Finally, a study of the instability and output power of the EDFRL versus the EDFA output power was also performed. The EDFRL was tested for 6 different values of EDFA output powers when the two wavelengths were simultaneously excited. Each measurement was carried out at room temperature during 1 hour with an acquisition time of 10 seconds and a confidence level of 90%. Figure 3.13 (a) shows that when the laser output power was increased the instability was reduced directly following the EDFA output power. The laser operated in single-longitudinal for all the tested values. The laser output power was improved and the instability was reduced as the EDFA output power increased. However, for powers exceeding 130 mw, the laser output power did not improve and the instability was worsened. Therefore, the optimal power level for the EDFA output power was 130 mW. At this point, instabilities of 0.35 dB and 0.2 dB were measured for λ1 and λ2, respectively. Figure 3.13 (b) shows the fluctuation of the output power for both channels in this case.

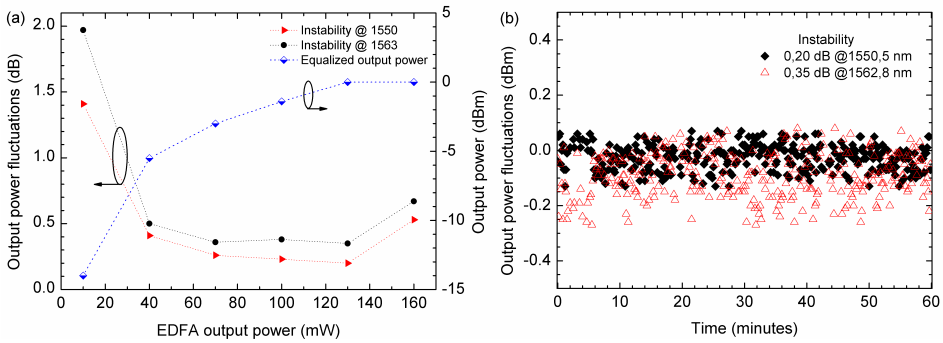

FIGURE 3.13. (a) Instability and output power of the EDFRL vs the EDFA output power. (b) Output power fluctuations of λ1 and λ2 for an EDFA output power of 130 mW.

3.1.3 EDFRLS BASED ON ADD-DROPS AND MUX-DMUX

The combination of dense wavelength-division multiplexing (DWDM) and erbium-doped fiber amplifiers can take full advantage of the C-band fiber telecommunications bandwidth and increases the capacity and transmission distance of optical fiber links [21, 22]. In this regard, standard optical wavelength multiplexers (MUX-DMUX) and optical add-drop multiplexers (OADMs) will play a critical role in enabling greater connectivity and flexibility in DWDM networks. OADMs and MUX are devices that give simultaneous access to the wavelength channels in WDM communication systems [23, 24]. Their widespread use has increased their commercial applications, reducing significantly their cost in recent years.

The main goal of this section is the development of two EDFRL based on these devices in order to exploit their flexibility and compatibility for WDM communication systems. However, in the same way as in the previous EDFRL presented in this chapter, parameters such as OSNR, SLM operation and instability are considered in their development.

Add-Drop and MUX-DMUX response

Figure 3.14 (a) and Figure 3.14 (b) show the measured spectral response of the OADMs and the Mux, respectively. These elements presented a flat response with a bandwidth per channel of about 1nm, which was a problem for achieve a stable laser in both, wavelength and output power. For this reason, the proposed solution was the use of a Sagnac loop mirror as additional comb filter, based on a Hi-Bi MOF.

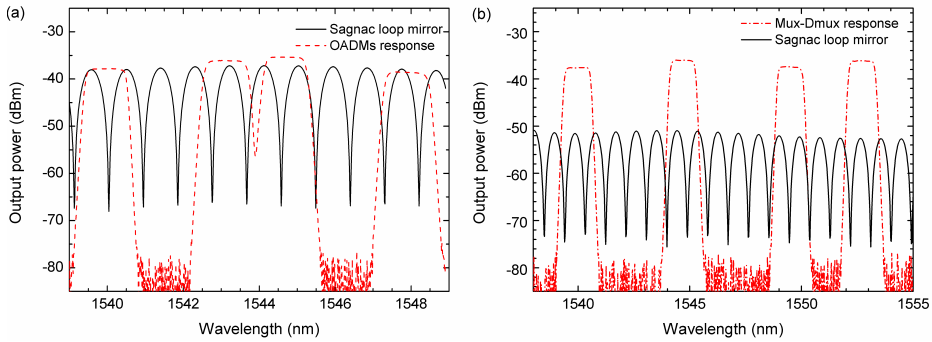

FIGURE 3.14. Measured transmission spectra of the (a) Sagnac loop mirror and the OADMs response, and (b) the sagnac loop mirror and the MUX-DMUX response.

Experimental studies were carried out in order to find the proper length of Hi-Bi MOF in the Sagnac loop mirror and consequently optimize the tunable capability of the proposed laser. It was observed that the proper length of the HI-BI PCF for this application was ~3 meters. In Figure 3.14 can be seen the measured transmission spectra of the 3 m Hi-Bi MOF Sagnac loop mirror and the OADM/MUX responses, taken individually while illuminating each of them with a broadband light source.

Description of the laser

Figures 3.15 and 3.16 illustrate the experimental setups of the proposed tunable multiwavelength fiber ring lasers. Both were constructed using a commercial EDFA (EFA-P21 from MPB) as gain medium and a Sagnac loop mirror as comb filter. The Sagnac interferometer was formed by a 3 dB optical coupler (OC), a polarization controller (PC) and one section of highly birefringent microstructured fiber. This Hi-Bi MOF (PM-1550-01 of NKT Photonics) presented a beat length lower than 4 mm and a temperature coefficient measured to be 30 times lower than that of a conventional polarization maintaining fiber. The temperature sensitivity for this fiber was measured to be 0.29 pm/°C [25] , leading to no further power variations due to temperature variations. The splices between the Hi-Bi MOF and the SMF were made by the use of a conventional fusion splicer with parameters particularly studied for this particular splice, based on [26], allowing high reproducibility.

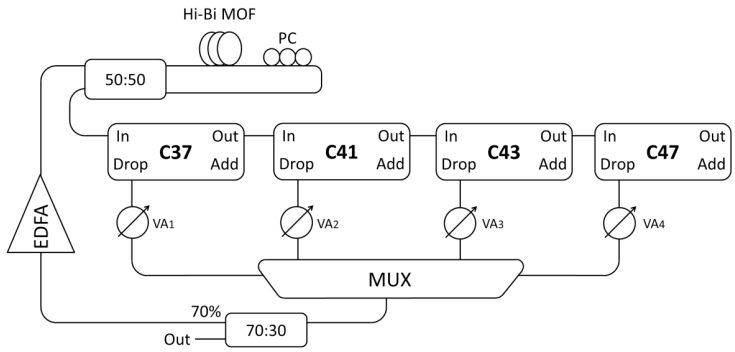

FIGURE 3.15. Experimental scheme for the proposed tunable four-wavelength erbium doped fiber ring laser configuration based on optical Add-Drop multiplexers and a Sagnac loop mirror.

For the first EDFRL (Figure 3.15), four OADMs were used to direct the signal inside the ring into four different branches, ensuring unidirectional operation and therefore avoiding the spatial hole-burning effect. Each branch was composed of an OADM and an optical variable attenuator.

As mentioned before, one of the major problems in multiwavelength EDFRL is the correctly adjusting of the cavity loss on each wavelength in order to achieve oscillation of the system in all the desired channels. As it is well known, the oscillation threshold power for each wavelength is different due to the non-flat shape of the erbium fiber gain profile. The use of this topology enables the required individual loss control for each wavelength in order to ease the power equalization.

The Sagnac loop mirror output signal was filtered by the array of OADMs. The ITU channels selected by these OADMs were C37, C41, C43 and C47 corresponding with the wavelength values of 1547.72 nm, 1544.53 nm, 1542.94 nm and 1539.77 nm, respectively. After being equalized, these four signals were collected by means of: (a) a 4×2 optical coupler and (b) an optical multiplexer into their ITU channels. A comparison between these two different options for collecting the four arm signals was carried out. As expected, the output power levels obtained for the configuration with a 4×2 optical coupler was about 6 dB lower than the one using the multiplexer.

For the proposed configuration, the optimum coupling ratio for this structure was found to be 30%-70%. This coupling ratio enabled the extraction of 30% of the laser's output power into the analyzer.

On the other hand, for the second EDFRL (Figure 3.16) the MOF Sagnac interferometer and a couple of thin-film wavelength division multiplexer/demutilplexers (DWDM 200G 4Ch from AFOP) were used as comb filter.

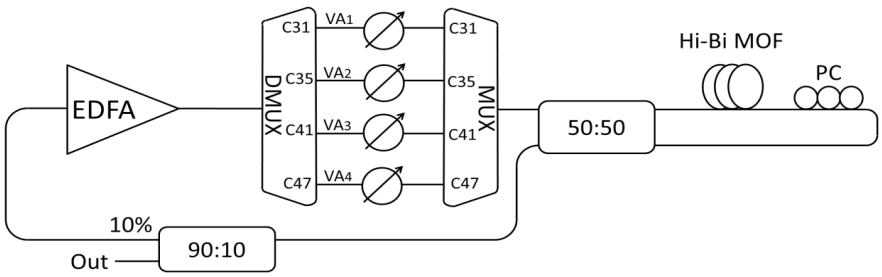

FIGURE 3.16. Experimental scheme for the proposed tunable four-wavelength EDFRL configuration based on MUX-DMUX and a Sagnac loop mirror.

The MUX-DMUX setup was used to select the interference signal from the Sagnac loop mirror in order to obtain laser emitted wavelengths only at the ITU wavelength channels. This structure also filtered the out-of-band amplified spontaneous emission noise generated by EDFA improving its amplification efficiency.

The ITU channels selected by these MUX were C31, C35, C41 and C47 corresponding to the wavelength values of 1552.52 nm, 1549.32 nm, 1544.53 nm and 1539.77 nm respectively. With this configuration the number of the laser wavelengths could be increased by replacing the MUX-DMUX by another with more channels.

In the same way as in the EDFRL based on Add-drops (Figure 3.15), this configuration also presented the individual control of the loss of each channel by including variable attenuators between the MUX and the DMUX.

In this case we used a 90:10 coupler enabling the extraction of the 90% laser power from the ring to the analyzer, being the other 10% redirected to the erbium doped amplifier. The EDFA had an internal isolator ensuring the unidirectional operation of the multi-wavelength laser and therefore avoiding the spatial hole-burning.

Experimental results

The first step was the comparison of both EDFRLs in terms of OSNR, output power and instability.

As can be seen in Figure 3.14, the combination of the Add-Drops or the MUX-DMUX with the Sagnac loop mirror generated two peaks per each channel, only one of them acquiring the laser condition. This fact allowed the selection between two wavelength emission lines, by using a tunable filter.

For the Add-Drop EDFRL, a tunable filter of 0.8 nm bandwidth was located at the output port of one of the OADMs (channel C41) in order to select a specific wavelength emission line. Figure 3.17 shows two possible outputs (measured using OSA Q8384 from Advantest) of the four-wavelength EDFRLs, generated by a fine-tuning of the filter placed at the output port of channel C41. These four laser lines could be easily tuned by inserting tunable filters at the output port of the others channels, in the same way as it was done for the channel C41.

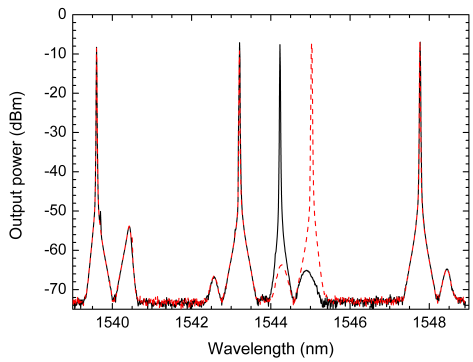

FIGURE 3.17. Shift of the output spectra of the four-wavelength Add-Drop EDFRL proposed by adjusting the tunable filter at channel 41.

The output power of each one of the four output channels is ~-7.5 dBm and, for every channel, the signal output power was more than 65 dB higher than the ASE noise floor, although low amplitude residual side-lobes corresponding to non-excited wavelengths inside the multiplexers bands can be observed.

The output power instability was tested during a period of 10 minutes. The measured data were stored each 10 seconds and a CL of 90% was considered. It was observed, that at room temperature the peak powers averaged presented a variation between 1.8 dB and 2.3 dB for different lasing wavelengths.

We repeated the process for the MUX-DMUX EDFRL. Figure 3.18 (a) shows two possible four-wavelength EDFLs with the tunable filter of 0.8 nm bandwidth located at channel 35 and placed between the MUX and DMUX. The measurement was carried out using a BOSA (OPT100 from Aragon Photonics) with a resolution of 0.08 pm.

In order to determine the OSNR an additional measurement was made using the OSA, because this device had more sensitivity than the BOSA, and revealed an OSNR > 65 dB for all channels. Figure 3.18 (b) shows the measured spectrum at channel 31.

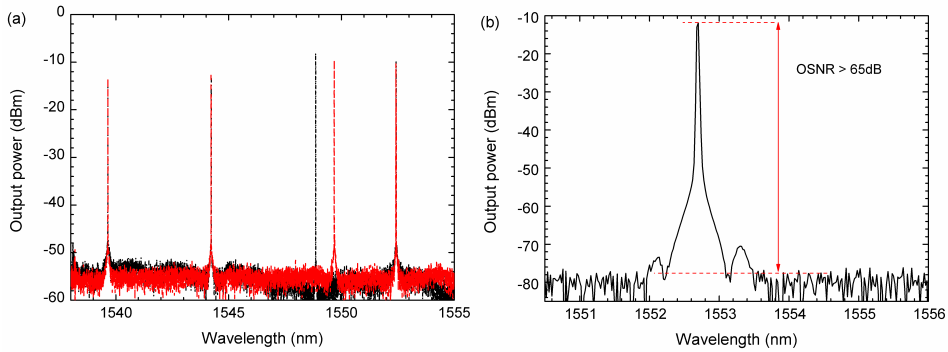

FIGURE 3.18. (A) Shift of the output spectra of the four-wavelength EDFRL proposed by adjusting the tunable filter at channel 35, measured by the BOSA. (b) Spectrum at channel 31 measured by the OSA.

To determinate the instability of the system the output power of the EDFL was also measured during a period of 10 minutes with an acquisition time of 10 s and a CL of 90%, at room temperature. Figure 3.19 shows the output power fluctuation for each emission line. The best instability was 0.82 dB and corresponds with the channel 47. The rest of the measured values were 0.93 dB, 0.95 dB and 0.97 dB, corresponding with the channels 41, 35 and 31, respectively.

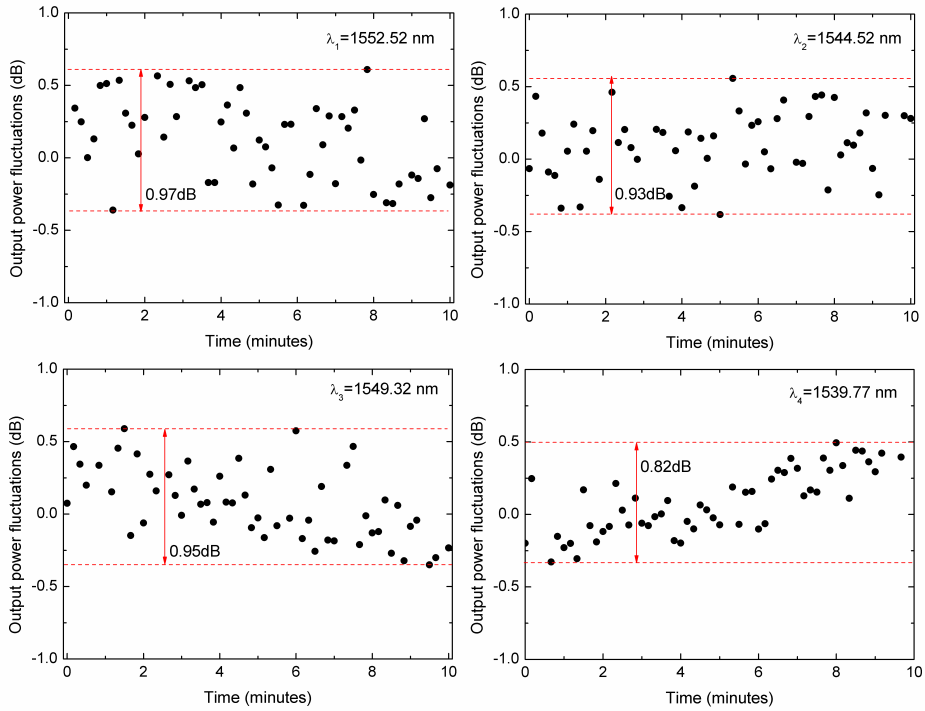

FIGURE 3.19. Output power fluctuation for each emission line with the four channel laser outputs in operation.

To summarize, both EDFRLs presented an OSNR > 65 dB, and output powers between -7.5 and -10 dBm. However, the EDFRL based on MUX-DMUX presented a considerable stability improvement. This was the reason why we selected the MUX-DMUX laser for a further study, which is presented below.

A single-longitudinal-mode operation is required from MEDFRL in some specific applications. The number of longitudinal modes and the space between them was calculated. Taking into account: n=1.5; L=34 m; $FWHM_{Sagnac}$=0.46 nm and the corresponding values of λ for each channel provided previously; 9897, 9838, 9779 and 9737 were the calculated number of modes inside the emission lines centered at 1539.6 nm, 1544.2 nm, 1548.8 nm and 1552.2 nm, respectively.

However, Figure 3.18 (a) shows the measurement of the four-laser emission in single-longitudinal-mode operation. As seem previously, in [12] an SLM fiber ring laser was achieved by annihilating the mode competition with an auxiliary lasing. In order to confirm this effect in this new structure we studied the measured modes from the channel 31 using an ESA with a resolution of 100 KHz (Rohde &

Schwarz FSP) in combination with a photodetector (New Focus 1544-B). For this purpose the MEDFRL output was beaten with a tunable laser source with a BW of 100 KHz (Agilent 8464B) using a 50:50 coupler. The measures were done in two situations. At first, only channel 31 was emitted. This situation corresponds to a multi-longitudinal-mode behavior as it is shown in Figure 3.20 (a). However when another channel was introduced into the system, each emitted wavelength starts operating in a single-longitudinal mode regime, Figure 3.20 (b). From this, one can infer that because of the interaction of the seed light produced from one channel to the other and vice versa, the multiple-longitudinal-mode oscillation inside each channel was suppressed, and thus the mode competition was reduced.

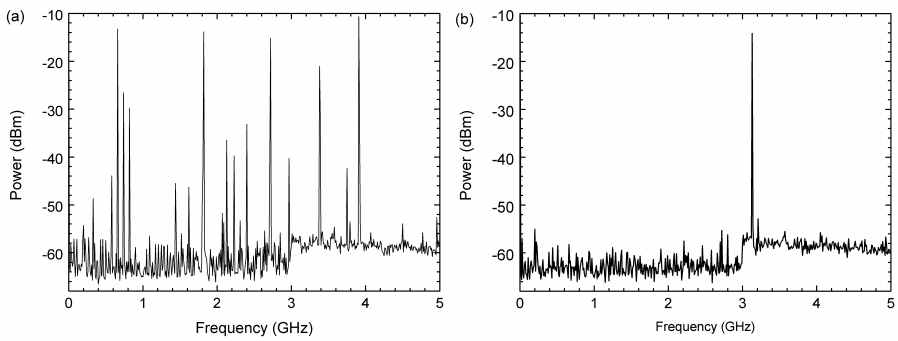

FIGURE 3.20. Output optical spectrum measured by the ESA for the channel 31, (a) at single-wavelength operation and (b) at dual-wavelength operation with channel 47.

Also the wavelength instability was measured for all emission lines. For this purpose the MEDFRL output was beaten with the TLS and captured at ESA showing an instability of 36.7 pm, 34.6 pm, 31.1 pm and 33.9 pm for channels 47, 41, 35 and 31 respectively.

Finally, in order to determine the emission lines bandwidth, a series of measurements using the self-heterodyne method described in section 2.3.4, were carried out. Figure 3.21 (a) shows the detection schematic based on the beating of the MEDFRL output, delayed by 20 Km of single mode fiber (SMF), with the same MEDFRL output modulated by a phase optical modulator (POM, Avanex IM10-P) in combination with a RF generator (Rohde & Schwarz SMT02) at 200 MHz. A tunable filter was used to isolate the channel to be measured. Figure 3.21 (b) shows the spectrum at ESA with a resolution of 1 KHz. Because the spectrum presented a Gaussian shape, this spectrum was $\sqrt{2} \cdot BW$, so the BW at channel 47 was 4.2

KHz. The rest of the measured values were, 3.5 KHz, 3.5 KHz and 4.3 KHz, corresponding with the channels 41, 35 and 31, respectively.

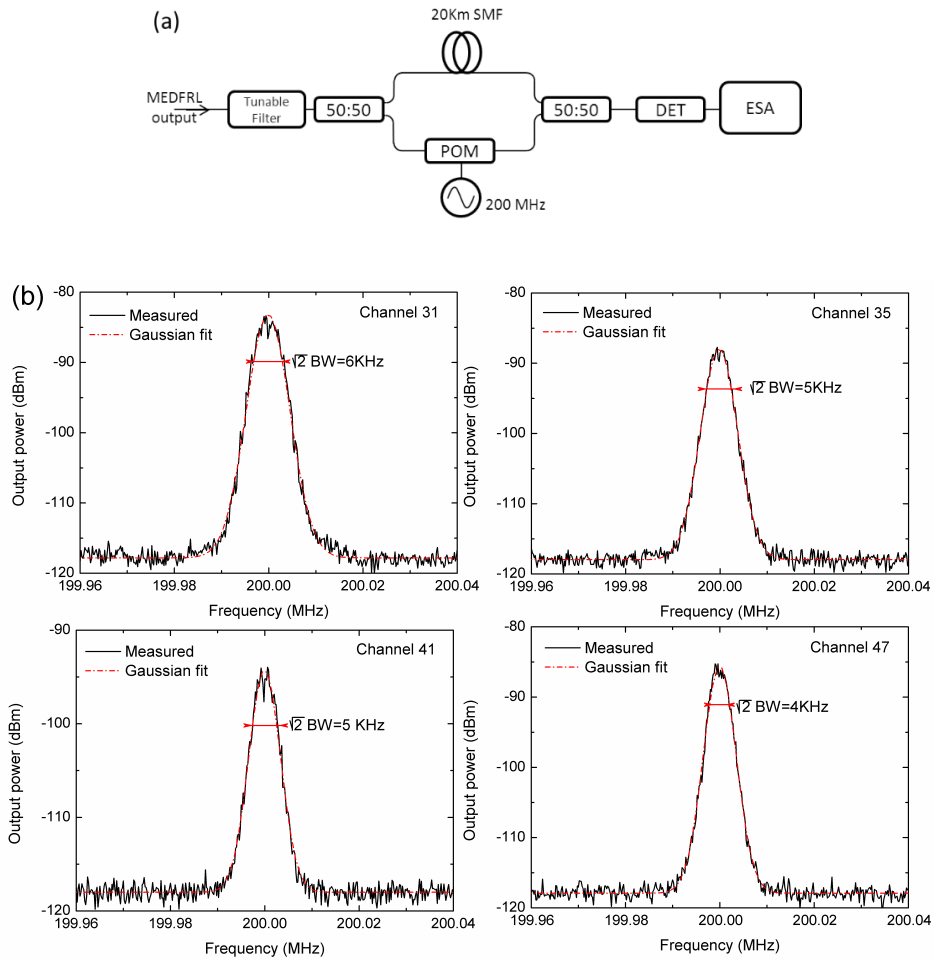

FIGURE 3.21. (a) Schematic of the self-heterodyne detection. (b) Spectrum of each emission line measured at ESA with the self-heterodyne detection method.

3.1.4 COMPARISON OF THE DEVELOPED EDFRLS

The aim of section 3.1 has been the demonstration of four new configurations of multiwavelength erbium doped fiber ring lasers. Much attention has been paid to the most crucial parameters such as output power, optical signal to noise ratio, instability, bandwidth, the independent control of loss and their operation in a single longitudinal mode regime. Table 3.1 shows a comparison of these parameters for the four EDFRL configurations.

EDFRL TECHNOLOGY	FBGS PAIRS (3.1.1)	FBGS+PSFBGS (3.1.2)	ADD-DROP (3.1.3)	MUX-DMUX (3.1.3)
Output power	-10 dBm	0 dBm	-7.5 dBm	-10 dBm
OSNR	›65 dB	›55 dB	›65 dB	›65 dB
SLM operation	Yes	Yes	---	Yes
Instability	‹1.08 dB	‹0.4 dB	‹2.3 dB	‹1 dB
Bandwidth	---	‹13 KHz	---	‹4.3 KHz
Number of wavelengths	2	2	4	4
Scalable	Yes	Yes	Yes	Yes
Independent control of the loss	Yes	Yes	Yes	Yes

Table 3.1. Main properties of the EDFRL presented in section 3.1.

The output power of the developed EDFRLs varies in the range of -10 dBm to 0 dBm, corresponding the last to the laser based on the combination of FBGs with PSFBGs (section 3.1.2). These variations are due to three main factors, the EDFA used for each laser, the loss of the passive elements in each configuration and finally, the wavelength of the emission lines which is directly related to the gain of the EDFA at these wavelengths.

One of the goals in this section has been to achieve high OSNRs and, as can be seen in Table 3.1, this objective has been successfully accomplished with values higher than 65 dB for three of the presented lasers, and $>$ 55 dB for the other one.

Regarding to the SLM operation, this condition has been demonstrated for 3 of the lasers. In two of them (sections 3.1.1 and 3.1.3), the SLM condition has been achieved by the equalization of the emission lines of the laser as in [12]. However,

in the laser of section 3.1.2, this behavior has been achieved by using PSFBG's as a thin filter, allowing the SLM condition without needing equalization.

Finally, another key point of the EDFRL is the instability. As introduced in chapter 2 erbium doped fiber amplifiers presents a homogeneous broadening. However, as can be seen in table 3.1, low instabilities < 1 dB, even reaching < 0.4 dB for the EDFRL based on FBGs in combination with PSFBGs (section 3.1.2) have been achieved.

3.2 SINGLE-LONGITUDINAL MODE LINEAR CAVITY LASER BASED ON A VERY NARROW FILTERING TECHNIQUE

In the previous chapter, different configurations of EDFRLs which improve the OSNR, instability, and also ensure a SLM operation have been experimentally demonstrated. The aim of this chapter is focused on the development of a SLM laser based on a linear cavity, maintaining comparable results as in EDFRLs, and simplifying the setup for applications that require a small size laser.

The laser is based on a very narrow filtering technique through the spectral overlap of two uniform FBGs. The spectral overlapping of odd FBGs has been already applied [27, 28] but, this is the first time that two uniform FBGs are combined to reduce the final bandwidth of the achieved filter. The proposed technique is employed to build a SLM linear laser. The proposed structure maintains the SLM operation even under strain and temperature variations.

Spectral overlapping principle

The filtering required for the SLM operation was obtained by combining two matched FBGs. The narrowing effect was produced by detuning one FBG, but keeping it partially overlapped with the other. In this way, the two filters were matched just when the wavelength of the optical signal was within the overlapped section, thus narrowing the whole spectral response. An example of the FBG detuning is depicted in Figure 3.22.

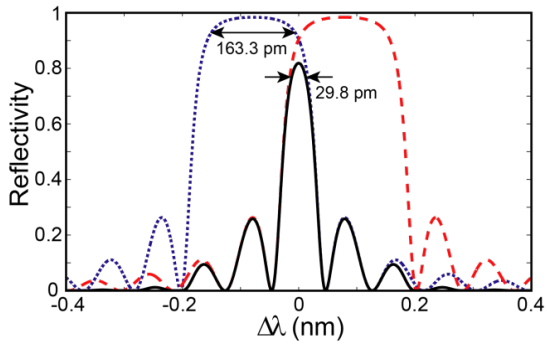

FIGURE 3.22. One FBG was detuned (dashed line) in terms of the other (dotted line). The overlapped spectrum (solid line) gave rise to a filter narrower than both individual FBGs.

In Figure 3.22, a simulation of the proposed spectral filter is shown. Two uniform FBGs having a length of L=9 mm with a 1 dB bandwidth (W_1dB) of 163.3 pm were detuned $\Delta\lambda$=156.4 pm obtaining an equivalent filter of W_1 dB=29.8 pm. Employing this structure, when the detuning increased (maintaining some spectral overlapping) the narrowing of the equivalent filter also improved. The main drawback of this scheme was the power drop due to the equivalent reflection reduction of the overlapped filter. This effect can be minimized by employing FBGs with a higher reflectivity (even being saturated) because their side slopes are steeper. Thus, maintaining the same bandwidth, a higher equivalent reflectivity can be achieved. This spectral filtering scheme can be applied to different fiber laser structures however, a trade-off between reflectivity (limited by the medium gain) and bandwidth (limited by the modal spacing) has to be reachable to get SLM operation. In this work, a proof-of-concept laser was manufactured by writing two uniform and spectrally displaced FBGs into an Er-doped fiber creating a DBR structure.

Laser manufacturing

The two matched FBGs were written into a commercial erbium doped fiber (Fibercore M12 which has an absorption ratio of 12 dB/m at 980 nm) using the phase mask technique with a continuous laser emitting at 244 nm. A small Gaussian apodizing function has been applied to reduce the secondary lobes of both FBGs. In comparison to the laser structures where two FBGs are spliced to the active fiber, the writing of the FBGs directly to the Er-doped fiber reduces the power loss (lower threshold power) and avoids mechanical weak points. Once the FBGs were written, one of them was post-exposed in order to drift its Bragg wavelength

and reduce the overlapping area, narrowing consequently the equivalent filter bandwidth. The achieved FBGs had a reflectivity of 99% with a FWHM bandwidth of 240 pm and the final wavelength drift is 180 pm.

During the FBGs post-exposition, the DBR fiber laser was pumped at 1480 nm to generate the laser emission. The laser signal was monitored by using a high resolution optical spectrum analyzer (BOSA-C from Aragon Photonics) to measure the behavior of the longitudinal modes. The FBG drift was stopped when the SLM behavior was confirmed at the BOSA. The proposed DBR structure is depicted in Figure 3.23.

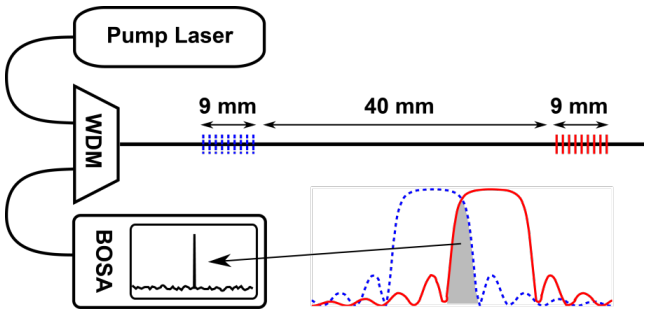

FIGURE 3.23. Employed setup during the fabrication process. The DBR fiber laser structure is also shown: two uniform FBGs of 9 mm length were inscribed into Er-doped fiber with a distance between them of 40 mm.

Experimental characterization

Since the wavelength selective effect was given by the equivalent filter bandwidth that results from the partial FBG's reflection bands overlapping, the wavelength of the obtained laser was centered at the Bragg wavelength of the equivalent filter. This value matched the upper and lower edges from the lower and upper FBG's bands respectively (1552.2 nm).

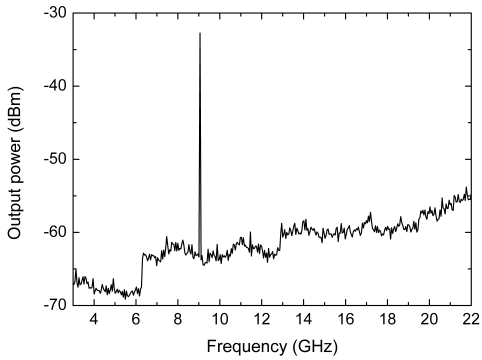

FIGURE 3.24. SLM operation measured at 25°C. The laser signal was beaten with a TLS source obtaining a single peak.

The SLM operation was verified with a heterodyne detection system. A polarization splitter was connected to the laser output to remove one of the orthogonal polarization modes. The measurements were performed using an optical converter (HP11982A) and an ESA (HP8592L). A single polarization mode of the lasing signal from the manufactured laser was combined with the signal of a TLS using a 3 dB coupler. The TLS (Agilent 8164B) had a FWHM of 100 kHz and its wavelength was placed close to the manufactured laser. In Figure 3.24, a single peak is shown proving the SLM operation of the tested device.

FWHM linewidth and wavelength stability

In order to measure the FWHM linewidth of the emitted wavelength, the self-heterodyne method described in section 2.3.4 was used. A phase modulator (Avanex IM10-P) was employed to perform a 1 GHz modulation. A 100 km reel of standard optical fiber was employed as a delay line. An EDFA (MPB-EFA-P18F) was introduced in the setup to amplify the delayed line. According to this method, the measured FWHM linewidth was the square root of two times the real linewidth, so this was less than 5 kHz as is shown in Figure 3.25 (a). This narrow linewidth indicated a stable SLM operation of the fiber laser, being this very important to achieve high resolution in sensing systems that depends on the linewidth and stability of the emitted laser wavelength.

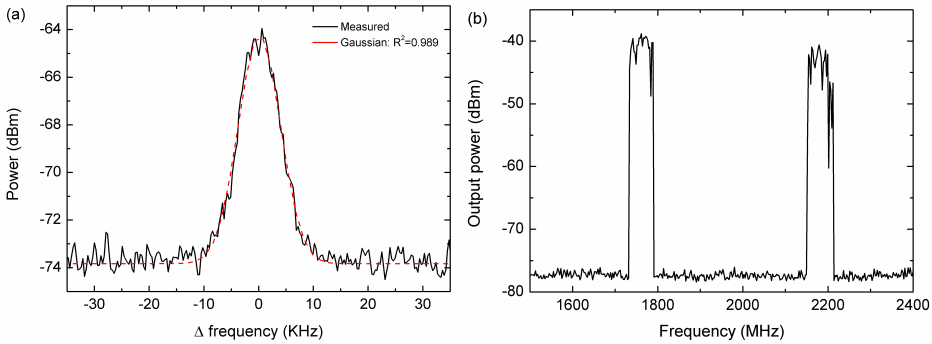

FIGURE 3.25. (a) Linewidth of 4.5 kHz (3dB) measured using self-heterodyne detection with a modulation frequency of 1GHz. (b) Wavelength stability (62.2MHz) of both orthogonal polarization modes measured during 10 minutes.

Figure 3.25 (b) also shows the wavelength stability measured using the heterodyne detection method (without the polarization splitter).The laser signal is mixed with the TLS and both polarization modes were held in the ESA during 10 minutes. The orthogonal polarization mode spacing of 400 MHz (3.2 pm) corresponded to the typical fiber birefringence. The higher wavelength drift of both polarization modes was under 65 MHz (0.52 pm).

OSNR and power stability

The output laser signal was connected directly to an OSA (HP70952B) to study the power behavior of the fabricated laser. Maintaining the emitted pump power at 26 dBm, the generated optical output power was monitored during 1 hour by using the OSA.

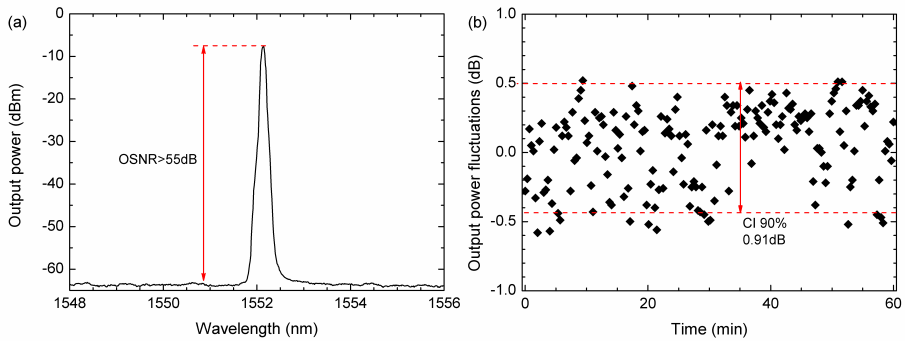

FIGURE 3.26. (a) Measured OSNR for a 26dBm pump power and (b) output power stability measured along 1 hour.

In Figure 3.26 (a), the output spectra of the proposed laser emitting at the Bragg wavelength of the equivalent filter is depicted (left), exhibiting an optical signal-to-noise ratio greater than 55 dB. The power stability measured each 20 seconds (Figure 3.26 (b)) is also depicted. The achieved stability was 0.91 dB with a 90% confidence interval, measuring along 1 hour.

Temperature response

As the laser wavelength was given by the spectral overlapping of the reflected bandwidths of the FBGs, the wavelength laser response should follow the FBG thermal response. A temperature sweep between 0 and 100 °C was performed while the laser wavelength was measured using the OSA.

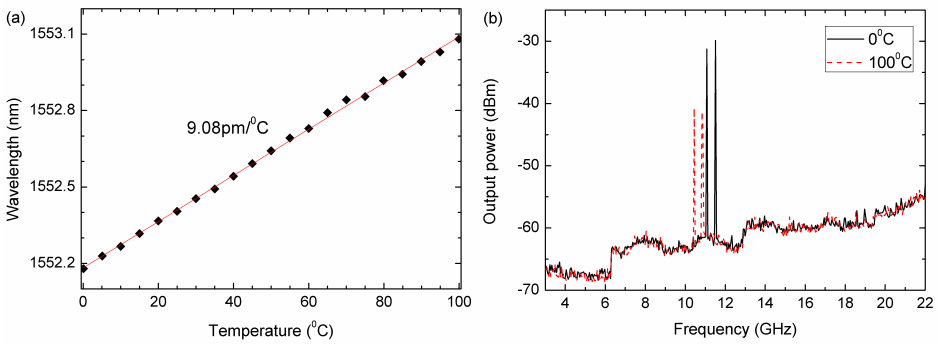

Figure 3.27. (a) Emitted wavelength displacement during the temperature sweep and (b) the two orthogonal polarization modes at the extreme temperatures (0°C and 100°C) (b).

The laser response to the temperature sweep is depicted in Figure 3.27 (a). The whole DBR structure behaved as their mirror FBGs, exhibiting linear response with a 0.9 nm drift within the 100°C sweep (similar to a FBG written into standard fiber). The SLM operation was also studied during the temperature sweep. The measurements associated with the sweep limits are depicted in Figure 3.27 (b). The same single modal behavior (polarization modes) could be observed in both temperature limits.

Strain response

The manufactured device was attached to a micrometric linear motor stage to perform a strain sweep. If the applied strain is the same for both FBGs, the laser properties should be maintained while the structure is being stretched.

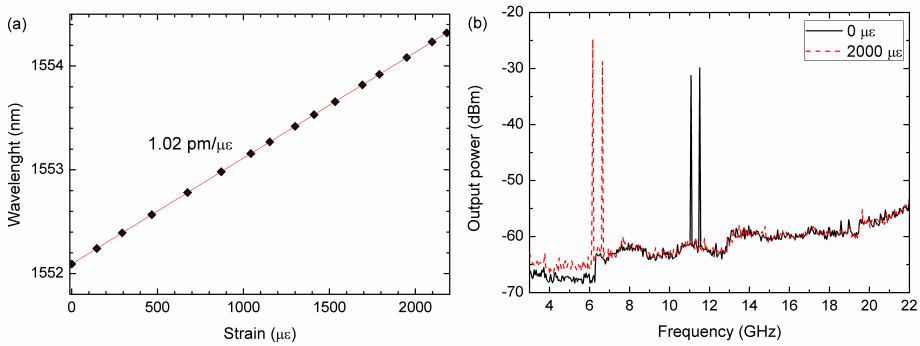

FIGURE 3.28. (a) Emitted wavelength displacement during the strain sweep. (b) The two orthogonal polarization modes are depicted in both extremes.

A strain sweep up to 2000 με was performed while the laser wavelength was measured obtaining a peak drift of 2.2 nm. These results are shown in Figure 3.28 (a) and they exhibited the same linear behavior as a single FBG. The SLM condition was also evaluated during the sweep using the heterodyne detection. Results are shown in Figure 3.28 (b) and the SLM was maintained for the highest achieved deformation.

3.3 RANDOM DISTRIBUTED FEEDBACK FIBER LASERS

3.3.1 NARROW-LINEWIDTH SINGLE-WAVELENGTH RDFB FIBER LASER

As stated before, random distributed feedback fiber lasers are characterized by their absence of longitudinal modes improving multiwavelength laser stability. This feature has led to increase the interest in this kind of cavity. However, the absence of longitudinal modes makes a challenge in order to achieve narrow emission lines.

Previous published works about narrow random lasers use Fabry Perot filters (FFP), Mach-Zehnder interferometers and diverse types of gratings to obtain emission lines with line-widths of tens of picometers [29-31]. Other studies also show that a RDFB fiber laser spectrum can be modified at will by using programmable filters [32] appropriately placed in order to avoid or enhance power redistribution between lines [33]. A direct conclusion of this customizability is that narrower RDFB fiber lasers could be easily achieved if more selective filtering devices are used. In this section we carried out an experimental study for a narrow RDFB laser depending on different parameters.

Description of the laser

The laser topology presented was based on a backward-pumped RDFB configuration, Figure 3.29. As it can be seen, a WDM was used to inject the pump laser (IPG RLD 3-1445) into the cavity formed by 50 km of standard single mode fiber. The SMF acted as the gain medium through the SRS effect and also, acted as distributed mirror providing a weak feedback along the fiber because of the Rayleigh scattering. The scattered light travelled back into the port 2 of an optical circulator which role, together with other components, was to filter the light and redirected it into the cavity. The design of this filtering mirror was the key point of this study, since depending on the setup particularly narrow band emission line could be attained.

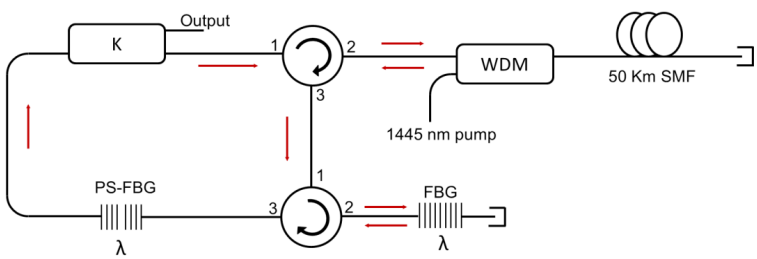

FIGURE 3.29. Schematic diagram of the proposed single-wavelength RDFB laser.

As in the EDFRL presented in section 3.1.2, the main purpose of this system was to obtain a laser by using the narrow central transmission peak of a phase shifted fiber Bragg grating, but this time by using a random cavity. To achieve this, the light was initially filtered by a FBG centered at λ=1545 nm (FWHM of 0.22 nm) which was properly connected to an optical circulator that allowed the FBG to

operate in reflection. The next component placed in the loop was a PS-FBG centered at λ (FWHM of 11 pm) in a serial configuration narrowing the emission line. In this manner, the resulting transmitted line of the loop was the combination of the reflected spectrum of the FBG and the PS-FBG response in transmission as depicted in Figure 3.30. Finally, an optical coupler was included in order to extract part of the signal as the output port.

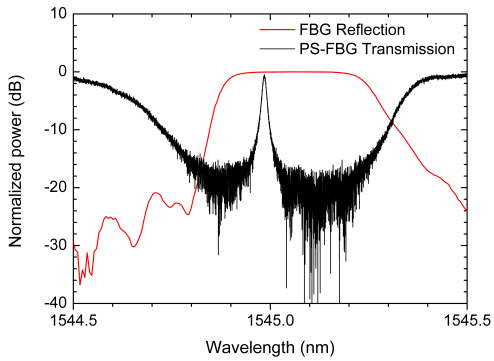

FIGURE 3.30. Reflected and transmitted spectra of the FBG and PS-FBG respectively, measured at BOSA.

Experimental results

In order to investigate the performance of the proposed setups, a series of experiments were carried out. Initially, the output emission line was analyzed by means of a BOSA (BOSA C by Aragon Photonics) with a resolution of 0.08 pm. As can be seen in Figure 3.31, the narrowest emission line obtained had a quasi-Lorentzian shape with a line-width at -3 dB of 3.2 pm, which was more than ten times narrower than other reported random lasers as far as we known [29-31]. This emission line corresponded to a pump power of 1.42 W and a coupling ratio of 70/30 with a 30% of the power re-inserted into the cavity.

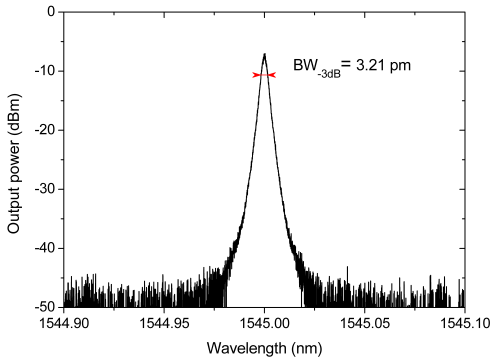

FIGURE 3.31. Optical spectrum of the generated emission line.

The dependence of the line-width on the pump power was also studied. With the aim of finding the optimal coupling ratio of the optical coupler placed in the loop, the experiment was repeated for different coupling values (Figure 3.32). The results showed that there was a clear increase of the line-width with the pump power, obtaining the narrowest possible line-width right above the lasing threshold in every case. Furthermore, as expected, the increase rate of the line-width with the pump power varied with the coupling ratio. After applying a linear fitting, the gradient increased from 14 to 22 pm/W as the re-injected power into the cavity increased from 10% to 90%.

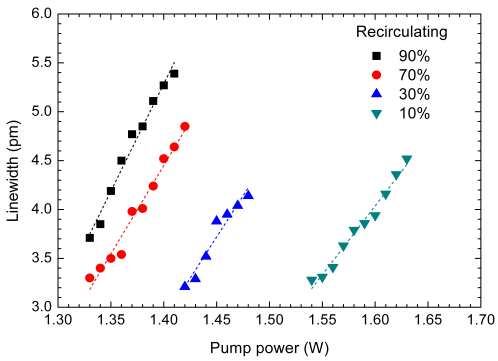

FIGURE 3.32. Line-width variation with Raman pump power for different coupling ratios.

The selected coupling ratio also implied a trade-off between lasing threshold and peak power as can be seen in Figure 3.33. The maximum peak power achieved was 1.2 dBm which corresponds to the case of a 10 % of re-inserted power with a pump power of 1.67 W. Since the output port of the laser was placed inside the loop mirror, the attained peak power values were smaller than in other random lasers, but were close to 0 dBm when the extracted power from the loop mirror gone beyond the 50 %. It is worth noticing that the results depicted in Figure 3.33 also proved that the studied emission line was a laser itself, clearly showing the lasing threshold for each different coupling ratio.

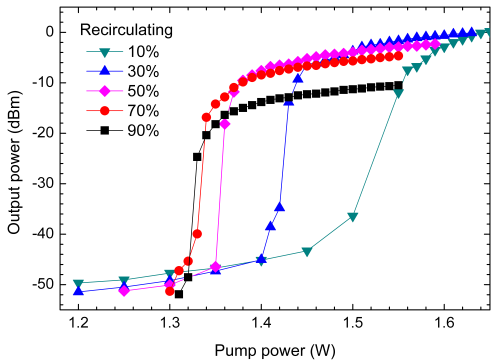

FIGURE 3.33. Peak power of the emission line vs Raman pump power for different coupling ratios.

As reported in studies before [9], one of the main properties of the random lasers is their longitudinal mode-less behavior due to the distributed reflection of the light along the fiber because of the Rayleigh scattering. In order to demonstrate the full random operation of the proposed laser, a test showing this mode-less operation was carried out. In this experiment, the output light was received by means of a photo-detector (Agilent 83440B) and measured at ESA (Rohde & Schwarz FSP30). The self-beating signal of the emission line can be clearly seen in Figure 3.34 with different spans (6 GHz, 90 kHz and 10 kHz) and resolution bandwidths (100 kHz, 300 Hz and 100 Hz respectively). There was no evidence of longitudinal mode beating, thus the random laser operation was verified.

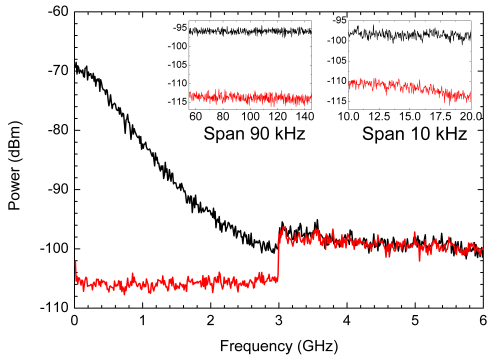

FIGURE 3.34. Laser's electrical self-beating signal for different spans/resolutions (black) and the detector's noise level (red).

3.3.2 NARROW-LINEWIDTH MULTI-WAVELENGTH RDFB FIBER LASER

RDFB fiber lasers present interesting properties for sensing applications as reported in [34-37] due to their good performance in terms of tunability and wavelength operation. Moreover, high power and wavelength stabilities together with narrow emission lines could give precise amplitude and wavelength-based measurements. Because of these, the main objective in this section is the development of a multiwavelength RDFB laser with narrow linewidths.

Description of the laser

As seen in the previous section, a narrow single wavelength RDFB laser can be achieved by using a filter combination of FBGs with PSFBGs. The objective of this work was to increase the number of emission lines, by using the same main scheme and maintaining the narrow bandwidth of the emission lines feature. In this regard, four pairs of PS-FBGs and FBGs corresponding to the wavelengths $\lambda 1$=1539.8 nm, $\lambda 2$=1545 nm, at $\lambda 3$=1549.6 nm and $\lambda 4$=1552.9 nm were utilized. A MUX/DMUX was used as it can be seen in Figure 3.35. The MUX/DMUX had four 200 GHz-wide channels (ITU channels C31, C35, C41 and C47) with insertion losses between 1.8 to 2.2 dB per channel. As in the laser presented in section 3.1.3, this configuration permitted the inclusion of variable attenuators in every branch to independently control the loss of each channel. The PS-FBGs were concatenated in a serial configuration with FWHMs of 14.5 pm, 11 pm, 19.2 pm and 29.9 pm at $\lambda 1$, $\lambda 2$, $\lambda 3$ and $\lambda 4$, in that order.

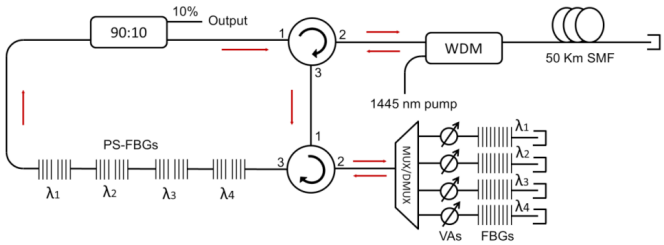

FIGURE 3.35. Schematic diagram of the proposed multi-wavelength RDFB laser.

The mode-less behavior of RDFB lasers implied that there was no mode-hopping or mode-competition. Consequently the wavelength and peak power instabilities of the multiwavelength RDFB laser are smaller than in other fiber lasers as in EDFLs. In order to exploit these advantages the setup reported in the previous section (see Figure 3.29) was adapted to a four-wavelength laser with narrow line-widths.

Experimental results

The spectrum of the four emission lines can be seen in Figure 3.36. Note that the wavelength axis was clipped in order to allow the line-widths to be properly displayed. A 90/10 coupler was used for the measurements, extracting just a 10% of the power through the output port. According with the study previously presented in section 3.3.1 (see Figures 3.32 and 3.33), for a 90% of recirculated power the values attained are lower than for other coupler ratios, however the necessary pump power for fulfill the laser condition was reduced.

The laser threshold for the multiwavelength RDFL laser was 1.47 W. At this operation point, the spectral line-widths of the four emission lines placed at the wavelengths 1539.8, 1545, 1549.6 and 1552.9 nm were 5.74, 5.04, 6.36 and 9.16 pm respectively. The difference between the line-widths was due to the different spectral response of the PS-FBGs, being this particularly evident in λ4.

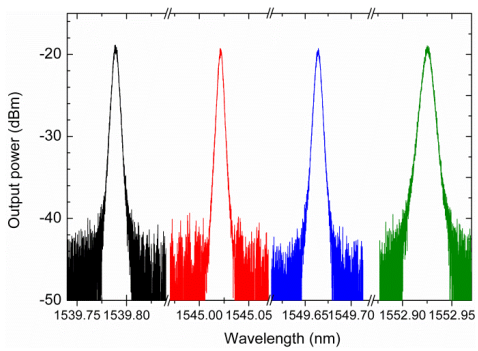

FIGURE 3.36. Spectra of the four emission lines measured at the BOSA with a 0.08 pm resolution.

The inhomogeneous behavior of the Raman gain permits the emission lines to be adjusted independently, in contrast for instance with EDFLs, where the variation of one emission line unavoidably affects the gain provided to the other lines. In Figure 3.36 the multi-wavelength laser was easily equalized by means of VAs to achieve identical peak power in each emission line. This lack of gain competition together with the absence of mode-hopping and mode-competition result in low power instability over time. Figure 3.37 shows the peak power fluctuations of the four emission lines every 10 seconds for 15 minutes. The instabilities attained for $\lambda 1$ to $\lambda 4$ are 0.04, 0.05, 0.06 and 0.07 dB respectively. These values are better than the obtained in section 3.1 and 3.2 with the EDFLs, however these last lasers present another features such as a better bandwidth, efficiency and OSNR. Therefore, there is a trade-off between these parameters, depending on the application requirements, which should be taken into account in the election of the fiber laser.

It is worth mentioning that power and wavelength stabilities were affected by temperature variations. Accordingly, these results may possibly be improved by better isolating the system.

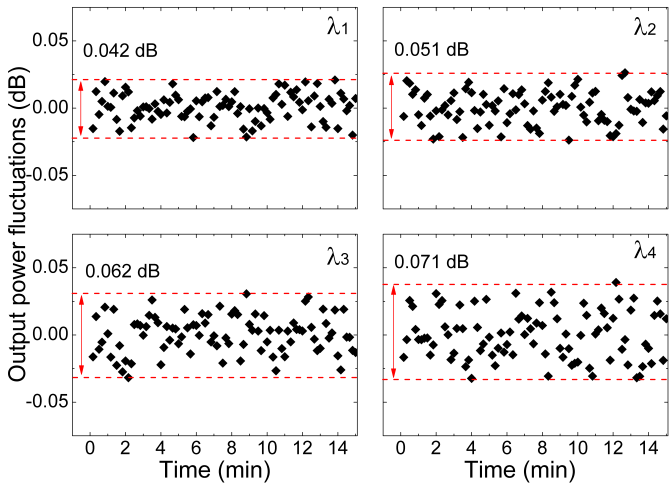

FIGURE 3.37. Output power fluctuations of the four emission lines during 15 minutes.

Finally, is important to point out that with this scheme extra emission lines could be generated by increasing the number of channels of the MUX/DMUX and including the corresponding pairs of FBGs and PSFBGs.

3.3.3 RDFB VS RING FIBER LASERS

In this section three fiber laser topologies are compared: the first one is based on a hybrid ring-random fiber laser; the second one is a ring fiber laser and the last one is a random mirror based fiber laser. Since the major goal of this section is the comparison of the behavior of the three basic fiber laser configurations, the proposed schemes are as simple as possible.

Description of the lasers

The three fiber lasers are depicted in Figure 3.38 and their characteristics are described below:

The following aspects were common to all topologies:

- A section of 2.4 km dispersion compensating fiber (DCF) was used to achieve greater Raman gain (greater than the achieved with standard single

mode fiber) per unit pump power. The Raman pump laser radiated at 1445 nm and could deliver up to 3 W. The pump power was launched to the system through a WDM.

- The wavelength selection was carried out by means of a FBGs centered at 1545 nm with 0.2 nm bandwidth and 95% reflectivity.
- All the free terminations of all systems were immersed in refractive-index-matching gel to avoid undesired reflections. This issue can be particularly critical in the random fiber laser.

The initial configuration, the ring-random fiber laser, shown in Figure 3.38 (a), was chosen in such a way the behavior of the hybrid scheme could be studied. Blue arrows point out the optical path followed by the random fiber laser contribution, while green arrow indicates the direction of the fiber ring laser. But, afterwards, it was also possible to study the individual contributions of each basic fiber laser that compose the hybrid fiber laser. The pure-ring laser structure (Figure 3.38 (b)) was obtained by adding an optical isolator to the previous structure and finally, the random fiber laser (Figure 3.38 (c)) consisted of the cavity section of the first structure wherein the random mirror was affecting the behavior of the hybrid configuration. The output of each laser (after the reflection in the FBG) was selected to reduce the effect of the noise in the optical signal to noise ratio.

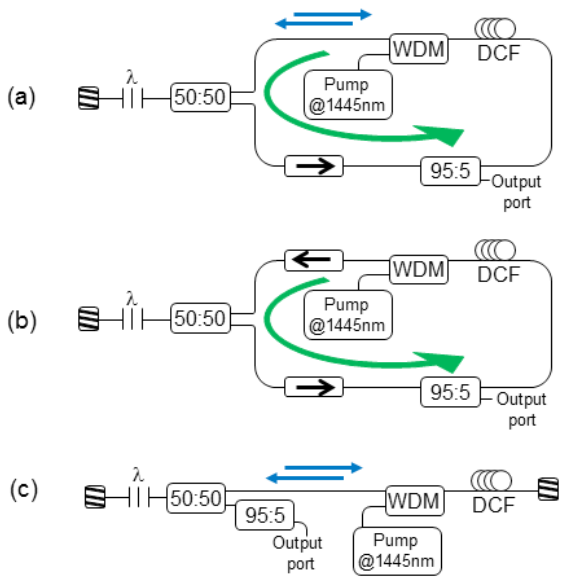

FIG. 3.38. Experimental set-up of: (a) the hybrid ring-random fiber laser; (b) the ring fiber laser; and (c) random fiber laser. Black arrow symbol: optical isolator. Blue arrows: Random laser feedback. Green arrows: Ring laser contributions.

HYBRID RING-RANDOM FIBER LASER

The first fiber laser was based on a hybrid ring-random fiber laser (Figure 3.38 (a)). On the one hand, the ring structure used the backward spontaneous Raman scattering in order to generate a counterclockwise fiber laser whose wavelength operation was determined by the FBG. The random fiber laser, on the other hand, created a linear cavity between the FBG and the DCF spool which worked as a distributed mirror, thus, this laser used the amplified Rayleigh scattering feedback through Raman effect. In conclusion, the output signal was composed of the contribution of two fiber lasers with different nature but operating at the same wavelength.

To extract a 5% of the laser output power from the ring, a 95% coupler was used and an optical spectrum analyzer was utilized to measure different parameters.

An optical isolator was also included between the optical couplers to ensure unidirectional operation of the ring laser avoiding spatial hole-burning effect. This

position of the isolator did not obstruct the random fiber laser behavior.

The scheme of the random fiber laser also included a 95% coupler which, at first sight, could seem is in excess. However, it was added to make the comparison study under the same conditions of loss in each of the three fiber laser structures.

Ring fiber laser

The second laser had a purely ring topology. As it can be seen in Figure 3.38 (a) and (b), both schemes were the same apart from an extra isolator located between the WDM and the 50 % coupler. This isolator avoided the generation of the random fiber laser because the power only could travel in the counterclockwise, thus, it was not possible to had feedback from the random mirror.

Random fiber laser

Figure 3.38 (c) depicts the schematic setup of the random fiber laser. This laser was based on a linear cavity formed by two different mirrors: the first one, the FBG which selected the emission wavelength and the second one, a distributed mirror created by the dispersion compensating fiber reel as it has been previously explained. It seems important to highlight that angled cleaves were used at the fiber end facets to eliminate reflections and to ensure that the feedback was only due to the randomly distributed scattering [38].

Experimental results

The main goal of this work was the comparison of the three basic configurations taking into account different aspects. Firstly, from the optical point of view, the parameters of interest were: output power, lasing threshold, slope efficiency, power fluctuations and finally, the analysis of the emitted lasing modes. And secondly, the applications of the fiber lasers in the optical communication field were also studied.

First of all, the output power evolution versus the Raman pump power launched to the system was measured using a power meter. The power progressions are shown in Figure 3.39 (a) and (b). Both figures show the same result with different scales in order to appreciate different aspects of the lasers outputs. One interesting parameter to analyze, from the results displayed on Figure 3.39 (a), is the pump power necessary to achieve the laser condition: at the beginning, the out-

put power increased with a low slope when the pump power was also increased, but, afterwards there was a great leap achieved with a small increment of pump power, thus the laser behavior was demonstrated. It is also observed from Figure 3.39 (a) and (b) that the threshold power of the hybrid ring-random laser was the lowest, around 390 mW; the purely ring laser threshold was around 500 mW and finally, the random mirror was the configuration which needed higher pump power, 650 mW, to reach the lasing operation.

Regarding the output power and slope efficiency, the ring scheme offered the better characteristics followed by the hybrid laser; being the random fiber laser the worst option taking into account this parameter.

In conclusion, the combination of the ring and the random cavity improved the laser threshold due to a more efficient use of the amplification. However, when the laser condition was achieved, a lower final output power, in comparison with the ring laser, was obtained because some of the Raman amplification was used to amplify the signal that travels in clockwise direction; that was finally lost at the isolator.

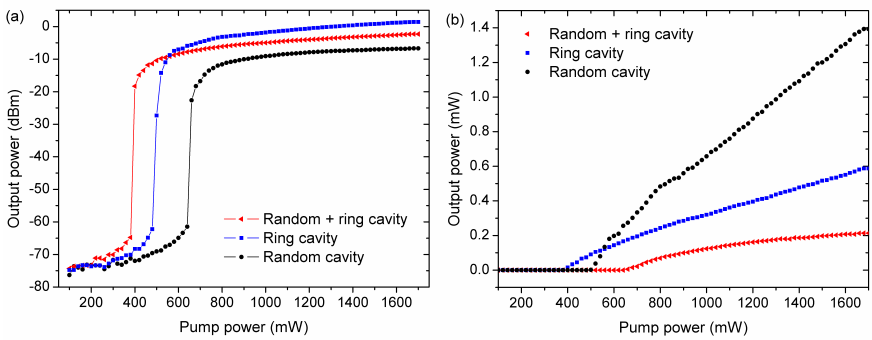

FIGURE 3.39. (a) Experimental demonstration of laser condition through the evolution the output power versus pump power. (b) Evolution of the output power versus pump power presenting the output power with a linear scale where the differences of threshold power and efficiency among the proposed fiber lasers are evident.

Fiber lasers are known to be susceptible to output power instabilities [9], particularly in multiwavelength fiber lasers but also, although to a lesser extent, in the case of single-emission lines. This issue is especially critical because these instabilities can degrade the performance characteristics of a telecommunication or sensor multiplexing network based on a laser interrogation scheme. Because

of it, the analysis of the output power fluctuations of the proposed lasers was required. Figure 3.40 shows the achieved measurements. It should be stressed that due to the non multiwavelength operation of the studied fiber lasers, the power fluctuations were lower than 0.1 dB in all the cases. The ring cavity offered the better stability, and the worst case came from the hybrid ring-random fiber laser. This fact may be due to the gain competition established among signals amplified from the random and ring cavities.

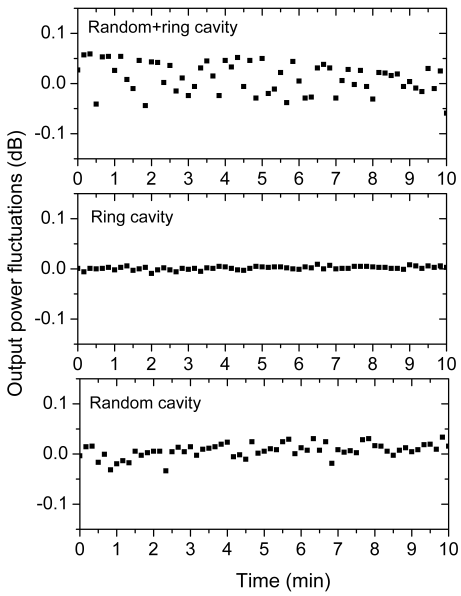

FIGURE 3.40. Output power fluctuations of the three laser configurations versus time.

The study of the longitudinal modes behavior in the cavity can be interesting in order to have a more complete understanding of the basic proposed schemes both in the extreme cases when the lasers are completely ring or random and in the hybrid ring-random laser.

The purely ring laser generates longitudinal modes which are evenly spaced according to the following equation:

$$\Delta f = c/nL \qquad (3.1)$$

where *c* is the speed of the light in vacuum, n is the refractive index of the fiber and *L* is the fiber length of the cavity. Thus, in the fiber ring laser the resonance longitudinal modes were spaced around 86.8 KHz. This distance was too low to be observed in our optical spectrum analyzers, consequently the longitudinal modes were detected in the electrical domain using an ESA. As many modes were generated in the cavity due to the long cavity length, the ESA showed the beat among the longitudinal modes by means of a heterodyne process.

Figure 3.41 shows the spectra for the three fiber lasers schemes. As can be seen, the purely ring fiber laser presented the narrowest FWHM. This fact demonstrated that the presence of random components contributed to broaden the emission line width, due to the Rayleigh scattering. On the other hand, Figure 3.41 also reveals an OSNR around 60 dB achieved for the three configurations.

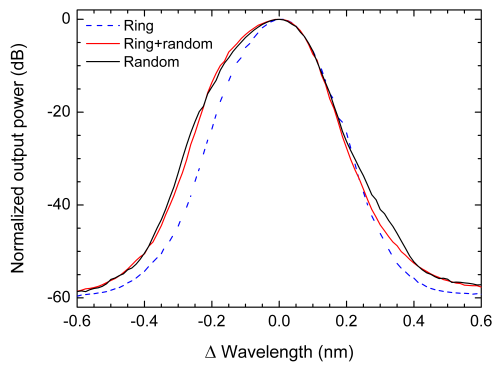

FIGURE 3.41. Spectra for the 3 fiber laser configurations using normalized output power and normalized wavelength to show the differences among them in terms of OSNR and full width at half maximum.

Figure 3.42 (a) presents the longitudinal modes beat of the hybrid ring-random fiber laser. When the Raman pump was 510 mW, it can be said that the cavity behavior was the one of a pure ring, because the random laser had a higher lasing threshold and its influence was negligible in the modal evolution. However, when the Raman pump was increased, the spectrum was affected by the random mirror effect. On the one hand, the ring had a main role and modes were generated at the same frequencies; but on the other hand, the random process had certain impact on the behavior: the longitudinal modes were wider and wider and, also, the noise floor increased.

A completely different situation can be seen in Figure 3.42 (b), where the study of the longitudinal modes of the pure random fiber laser is shown. In this case,

any longitudinal mode beat signal is observed in the picture in spite of the fact that the selected bandwidth was wide enough to address three beating modes. This modeless property is a unique characteristic of random fiber laser which is the main difference between ring fiber lasers and random fiber lasers. This study confirmed the different nature of the fiber lasers under study.

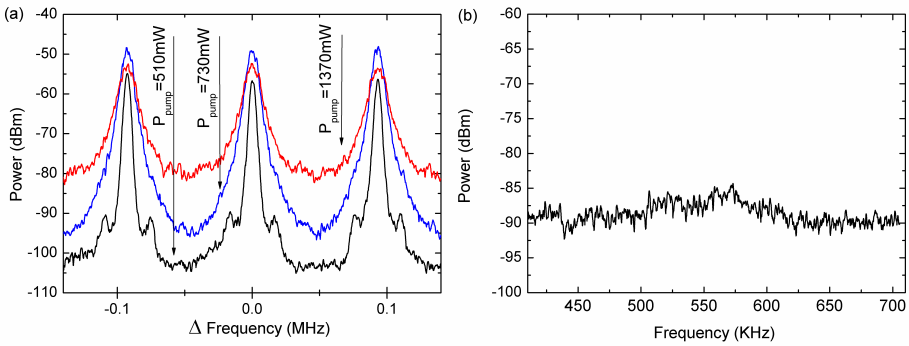

FIGURE 3.42. (a) Longitudinal modes generated in the hybrid ring-random fiber laser shown by the electrical spectrum analyzer. (b) Study of the beat modes in the case of the random fiber laser resulting in a modeless spectrum, characteristic of random fiber lasers.

For sake of completeness, it seems really important to demonstrate that the hybrid random-ring fiber laser was not just a conventional ring cavity fiber Raman laser with some impact of Rayleigh scattering but it was really composed of the contribution of two fiber lasers with different nature. Set-up shown in Figure 3.43 was used to carry out this demonstration; it was the same scheme of the hybrid random-ring fiber laser presented in Figure 3.38 (a) but taking into account both outputs of the 95% coupler.

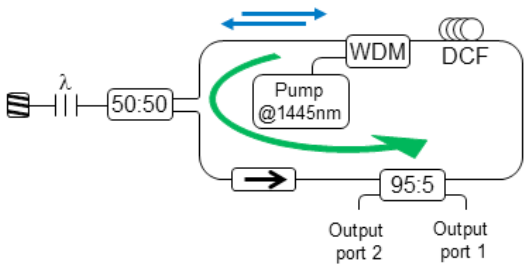

FIGURE 3.43. Schematic set-up for the hybrid random-ring fiber laser in order to demonstrated that this laser was composed of the contribution of the ring fiber laser and the random fiber laser.

Figure 3.44 (a) is the key of the demonstration; it shows the electrical spectra of both output ports simultaneously. On the one hand, output port 1 (depicted in green) shows the hybrid random-ring fiber laser output. Because of the ring component, the resonance longitudinal modes appeared equidistant, and their separation in the spectrum was inversely proportional to the laser length. However, on the other hand, in output port 2 (depicted in blue) there were no longitudinal modes but the power level was higher than the receptor noise (depicted in black). So, the modeless spectra corroborates that there was a random fiber laser in the cavity along with the ring fiber laser. To conclude, the optical spectrum of the output port 2 was also studied. Figure 3.44 (b) shows that there was also a laser emission in output port 2, which did not belong to the ring fiber laser because the ring fiber laser traveled in the opposite direction; thus, there was a random fiber laser in the cavity. In conclusion, hybrid fiber laser was composed of the contribution of the ring fiber laser and the random fiber laser and it was not just a conventional ring cavity fiber Raman laser with some impact of Rayleigh scattering.

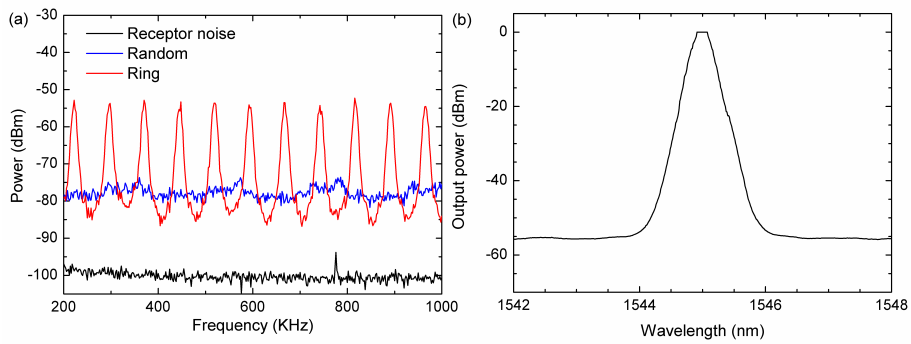

FIGURE 3.44. Study of the (a) electrical and (b) optical spectra in order to demonstrate that the hybrid random-ring fiber laser was not just a conventional ring cavity fiber Raman laser with some impact of Rayleigh scattering but it was really composed of the contribution of the ring fiber laser and the random fiber laser.

Finally, the last part of this experimental section was devoted to the possible applications of the fiber lasers in the optical communication field. To accomplish this task, light was internally modulated by a $LiNbO_3$ Mach-Zehnder EOM (Electro-Optical Modulator) with an extinction ratio of ~20 dB, and the signal selected to modulate the structure was a square shape one. In order to modulate internally the signal of both the ring and hybrid ring-random fiber laser, the electro-optical modulator was directly included in the scheme, as shown in Figure 3.45. Con-

versely, the random configuration was modified to modulate its signal because our electro-optical modulator is not a bidirectional component, so a 4 ports circulator was included in order to enable the back and forth path of the random signal.

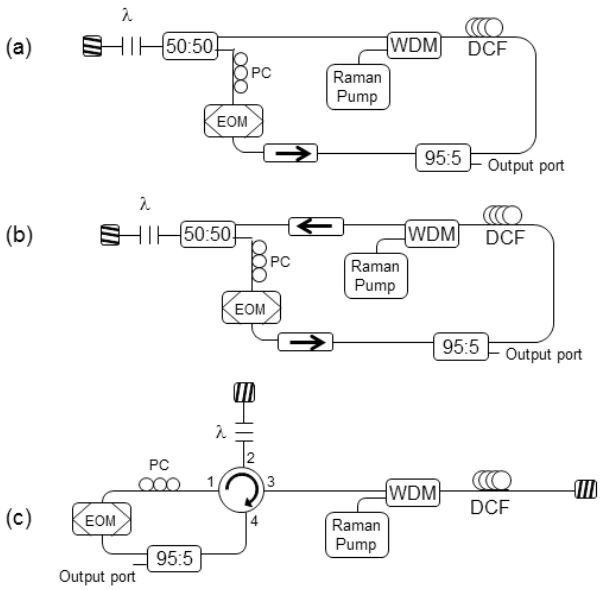

FIGURE 3.45. Position of the electro-optical modulator in the three fiber lasers in order to modulate their signals: (a) hybrid ring-random fiber laser; (b) ring fiber laser and (c) random fiber laser.

The frequency response characterization of a ring and a random cavity was demonstrated in [9], however here we present a time-domain comparison to analyze the modulation distortion of the three configurations. Thus, in the particular case of modulating with a frequency of 500 MHz, in the random fiber laser the signal was not distorted as can be seen in Figure 3.46; the same happens when the frequency was changed to 499 MHz or 501 MHz. This fact means these kinds of lasers are able to adapt their cavities without distortion to each selected frequency of modulation. However, ring fiber lasers or hybrid ring-random fiber lasers with the ring laser having a dominant role have a conventional behavior: the length of the cavity is a decisive parameter because of the fact that it determines the possible repetition rate if the laser is internally modulated. Taking into consideration this explanation, when one chooses a modulation frequency arbitrarily, the

signal is completely distorted as can be seen in Figure 3.46: the modulation was optimized when the frequency is 500 MHZ where the distortion is evident, but, this effect was more significant when the frequency was changed only 1 MHz up or down, in these cases the distortion was complete.

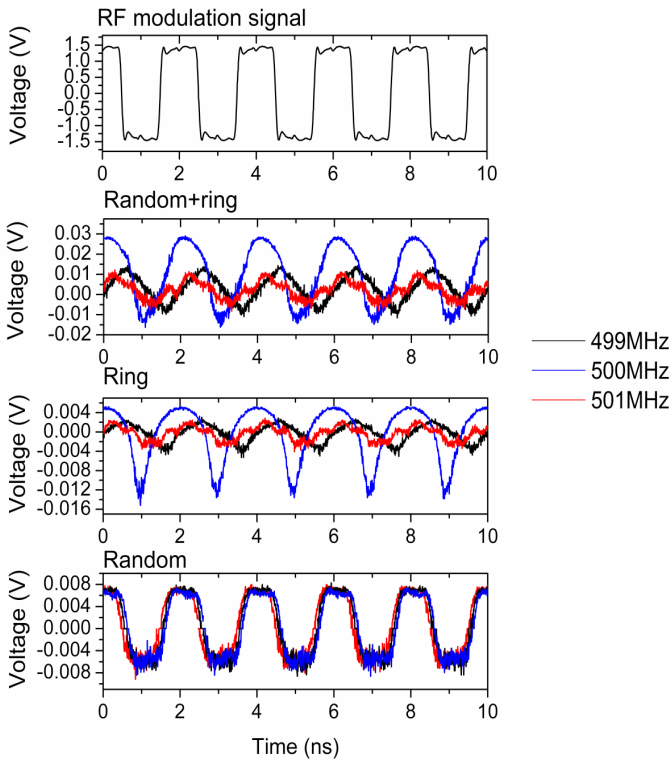

FIGURE 3.46. Original modulation signal and time domain lasers behavior when 500 MHz square signal internally modulated the signals of the different proposed fiber lasers.

3.4 CONCLUSIONS

In this chapter different laser configurations have been described and experimentally studied. The main groups that have been discussed and classified by their cavity design are: fiber ring lasers, linear cavity lasers and random lasers.

In the first part of this chapter (section 3.1) four new configurations of multiwavelength erbium doped fiber ring lasers has been presented. Much attention have been paid to the most crucial parameters such as output power, optical signal to noise ratio, instability, bandwidth, the independent control of loss and their operation in single longitudinal mode regime.

The first MEDFRL is based on ring resonators and employs fiber Bragg gratings to select the operation wavelengths. The topology of the laser has a significant influence in its performance: allowing an independent control of the loss and achieving a low noise configuration. As a result, it has been experimentally demonstrated that both emission lines work in a single-longitudinal-mode regime, showing an optical signal-to-noise ratio that is as high as 65 dB and a power stability which varies from 1.1 to 1.25 dB for both emission lines. In this laser, the SLM behavior has been achieved by equalization when the output powers of the lasing channels are similar. However, there is another way to ensure a stable SLM behavior in an EDFRL which is based on thin-filtering.

In the second MEDFRL a new configuration based on a combination of FBGs and PSFBGs have been experimentally demonstrated. Two single-longitudinal-mode wavelength laser emissions have been simultaneously obtained showing a power-instability lower than 0.35 dB, a FWHM linewidth lower than 3.5 KHz, an optical output close to 0 dBm and an OSNR higher than 55 dB. In addition, we achieve an independent control of the loss for each channel of the laser, thus improving the equalization process.

The last two MEDFRLs have been based on optical communications elements, MUX-DMUX and Add-Drops, in combination with a Hi-Bi-PCF Sagnac loop mirror. Four wavelength laser emissions have been obtained simultaneously showing power instabilities lower than 2.3 dB for the Add-Drops configuration and lower than 1 dB for the MUX-DMUX scheme. Both configurations show an OSNR higher than 65 dB. We have also demonstrated the possibility of switching two different wavelengths for each channel only by using a tunable filter. Besides this, we achieve an independent control of the loss for each channel of the laser, improving the equalization process. MUX/DMUXs and Add-drops are standard optical communication devices, thus the system is adapted to the ITU channels norma-

tive and, in addition, this device makes it possible to increment the number of lasers only by using another with more channels.

These results have originated the publications in references [39-42]

In section 3.2, a narrow filtering technique based on the spectral overlapping of two uniform FBGs has been proposed to achieve a SLM regime in a fiber laser. The two uniform FBGs are spectrally detuned during the fabrication process to reduce the equivalent filter bandwidth. In order to verify this proposed technique, a DBR fiber laser has been fabricated by directly inscribing the two spectral overlapping FBGs in a commercial erbium doped fiber. The total length of fiber laser, including the two FBGs, is 58 mm. This laser operates in robust SLM regime for different working conditions and in two orthogonal polarization modes. The FWHM is less than 5 kHz and the higher signal wavelength variation is under 65 MHz (0.52 pm). The OSNR is better than 55 dB and the power instability is lower than 0.91 dB for a pump power of 26 dBm. It has been also confirmed that the fiber laser maintains a SLM behavior over the whole temperature and strain range discussed.

From the experimental results, we can conclude that the proposed narrow filtering technique has provided a simple approach to achieve a stable SLM fiber laser where a precise control of the cavity length is not required. These fiber lasers can be particularly appealing for applications requiring high resolution and small size sensors.

These results have originated the publication in reference [43]

In sections 3.3.1 and 3.3.2, a single wavelength and a multiwavelength RDFB fiber laser schemes have been proposed and experimentally demonstrated. These lasers present sub-gigahertz line-widths for the first time in a random distributed feedback laser, to our knowledge. The gain has been provided by the Raman scattering effect along 50 km of single-mode fiber which also acts as a distributed mirror. The filtering process has been realized by fiber Bragg gratings placed in a loop mirror at the end of the cavity. In the first topology a single emission line has been attained with a line-width of 3.2 pm which improves significantly (approx. 10 times) any other published work up to date. A second scheme has been also presented for multi-wavelength operation where four narrow emission lines have been obtained with line-widths between 5 and 9 pm. This topology can be extended for a greater number of lines and presents a good versatility since the wavelength and peak power of each emission line can be independently adjusted.

Finally, in section 3.3.3 the behavior of three basic fiber lasers configurations have been experimentally evaluated in order to establish the main pros and

cons of each scheme. The first fiber laser is based on a hybrid ring-random fiber laser; the second one is a pure ring fiber laser and the last one is a random fiber laser. Several aspects have been taken into account in the study: from the optical point of view, and the possible applications of the fiber lasers in the optical communication field.

Summarizing, firstly, the combination of both kind of reflectors, ring and random, has a positive effect on the threshold power but a negative consequence in the output power and slope efficiency in comparison with the pure ring cavity. Secondly, the ring cavity offers the better stability. The worst case belongs to the hybrid ring-random fiber laser. Thirdly, the different nature of the basic fiber lasers has been evaluated through the study of the longitudinal modes: in the ring cavity fiber laser and in the hybrid ring-random fiber laser, the cavity generates longitudinal modes equally spaced; however, the random fiber laser is characterized by a modeless behavior. Finally, it has been demonstrated that the random fiber lasers are able to adapt their cavities to any frequency of internal modulation, in contrast with ring fiber laser or hybrid ring-random fiber lasers, whose repetition rate is completely determined by the length of the cavity.

These results have originated the publication in reference [44]

3.5 REFERENCES

[1] A. Bellemare, "Continuous-wave silica-based erbium-doped fibre lasers," *Progress in Quantum Electronics,* Vol. 27, Iss. 4, pp. 211-266, 2003.

[2] M. Fernández-Vallejo, S. Diaz, R. A. Pérez-Herrera, R. Unzu, M. A. Quiniela, J. M. López-Higuera and M. López-Amo, "Comparison of the stability of ring resonator structures for multiwavelength fiber lasers using raman or Er-Doped fiber amplification," *IEEE J. Quant. Electron.,* Vol. 45, Iss. 12, pp. 1551-1557, 2009.

[3] R. A. Perez-Herrera and M. López-Amo, "Fiber lasers for optical sensing applications," in *Advances in Sensors, Signals and Materials - 3rd WSEAS International Conference on Sensors and Signals, SENSING 10, 3rd WSEAS International Conference on Materials Science, MATERIALS'10,* 2010, pp. 125-129.

[4] R. A. Perez-Herrera, S. Chen, W. Zhao, T. Sun, K. T. V. Grattan and M. López-Amo, "Stability performance of short cavity Er-doped fiber lasers," *Opt. Commun.,* Vol. 283, Iss. 6, pp. 1067-1070, 2010.

[5] A. Bellemare, M. Karásek, M. Rochette, S. LaRochelle and M. Têtu, "Room temperature multifrequency erbium-doped fiber lasers anchored on the ITU frequency grid," *J. Lightwave Technol.,* Vol. 18, Iss. 6, pp. 825-831, 2000.

[6] C. A. Khansa, S. Bhattacharya and A. Prabhakar, "Multiwavelength Erbium doped fiber ring lasers," *Opt. Commun.,* Vol. 282, pp. 2380-2387, 2009.

[7] H. Ahmad, A. H. Sulaiman, S. Shahi and S. W. Harun, "SOA-based multi-wavelength laser using fiber Bragg gratings," *Laser Physics,* Vol. 19, Iss. 5, pp. 1002-1005, 2009.

[8] A. M. R. Pinto, O. Frazão, J. L. Santos and M. Lopez-Amo, "Multiwavelength fiber laser based on a photonic crystal fiber loop mirror with cooperative Rayleigh scattering," *Appl. Phy. B,* Vol. 99, Iss. 3, pp. 391-395, 2010.

[9] M. Bravo, M. Fernandez-Vallejo and M. Lopez-Amo, "Internal modulation of a random fiber laser," *Opt. Lett.,* Vol. 38, Iss. 9, pp. 1542-1544, 2013.

[10] G. Ning, P. Shum, J. Q. Zhou and L. Xia, "Multiwavelength Raman fiber laser inserting a sampled chirped fiber bragg grating," *Microwave Opt Technol Lett,* Vol. 49, Iss. 9, pp. 2242-2245, 2007.

[11] R. A. Pérez-Herrera, M. A. Quintela, M. Fernández-Vallejo, A. Quintela, M. López-Amo and J. M. López-Higuera, "Stability comparison of two ring resonator structures for multiwavelength fiber lasers using highly doped er-fibers," *J. Lightwave Technol.,* Vol. 27, Iss. 14, pp. 2563-2569, 2009.

[12] M. A. Quintela, R. A. Perez-Herrera, I. Canales, M. Fernández-Vallejo, M. Lopez-Amo and J. M. López-Higuera, "Stabilization of dual-wavelength erbium-doped fiber ring lasers by single-mode operation," *IEEE Photonics Technology Letters,* Vol. 22, Iss. 6, pp. 368-370, 2010.

[13] S. K. Turitsyn, S. A. Babin, D. V. Churkin, I. D. Vatnik, M. Nikulin and E. V. Podivilov, "Random distributed feedback fibre lasers," *Physics Reports,* Vol. 542, Iss. 2, pp. 133-193, 2014.

[14] A. M. R. Pinto, O. Frazão, J. L. Santos, M. Lopez-Amo, J. Kobelke and K. Schuster, "Interrogation of a suspended-core Fabry-Perot temperature sensor through a dual wavelength Raman fiber laser," *J. Lightwave Technol.,* Vol. 28, Iss. 21, pp. 3149-3155, 2010.

[15] S. Pan, Z. Xiaofan and L. Caiyun, "Switchable single-longitudinal-mode dual-wavelength erbium-doped fiber ring laser incorporating a semiconductor optical amplifier," *Opt. Lett.,* Vol. 33, Iss. 8, pp. 764-766, 2008.

[16] K. Zhang and J. U. Kang, "C-band wavelength-swept single-longitudinal-mode erbium-doped fiber ring laser," *Optics Express,* Vol. 16, Iss. 18, pp. 14173-14179, 2008.

[17] J. L. Zhou, L. Xia, X. P. Cheng, X. P. Dong and P. Shum, "Photonic generation of tunable microwave signals by beating a dual-wavelength single longitudinal mode fiber ring laser," *Appl. Phy. B,* Vol. 91, Iss. 1, pp. 99-103, 2008.

[18] Y. Dai, X. Chen, D. Jiang, S. Xie and C. Fan, "Equivalent phase shift in a fiber Bragg grating achieved by changing the sampling period," *IEEE Photonics Technology Letters,* Vol. 16, Iss. 10, pp. 2284-2286, 2004.

[19] B. J. Eggleton, P. A. Krug, L. Poladian and F. Ouellette, "Long periodic superstructure Bragg gratings in optical fibres," *Electron. Lett.,* Vol. 30, Iss. 19, pp. 1620-1622, 1994.

[20] R. Kashyap, *"Fiber Bragg Gratings",* Academic Press,1999.

[21] X. Zhou, G. Liang and T. Wang, "An optical add-drop multiplexer design based on fiber bragg gratings," in *ICEOE 2011 - 2011 International Conference on Electronics and Optoelectronics Proceedings,* Vol.2 , pp. 241-243, 2011.

[22] L. D. Garrett, M. H. Eiselt, J. M. Wiesenfeld, M. R. Young and R. W. Tkach, "Bidirectional ULH transmission of 160-Gb/s full-duplex capacity over 5000 km in a fully bidirectional recirculating loop," *IEEE Photonics Technology Letters,* Vol. 16, Iss. 7, pp. 1757-1759, 2004.

[23] K. Okamoto, K. Takiguchi and Y. Ohmori, "16-channel optical add/drop multiplexer using silica-based arrayed-waveguide gratings," *Electron. Lett.,* Vol. 31, Iss. 9, pp. 723-724, 1995.

[24] V. Kaman, X. Zheng, S. Yuan, J. Klingshirn, C. Pusarla, R. J. Helkey, O. Jerphagnon and J. E. Bowers, "A 32 × 10 Gb/s DWDM metropolitan network demonstration using wavelength-selective photonic cross-connects and narrow-band EDFAs," *IEEE Photonics Technology Letters,* Vol. 17, Iss. 9, pp. 1977-1979, 2005.

[25] C. Zhao, X. Yang, C. Lu, W. Jin and M. S. Demokan, "Temperature-insensitive interferometer using a highly birefringent photonic crystal fiber loop mirror," *IEEE Photonics Technology Letters,* Vol. 16, Iss. 11, pp. 2535-2537, 2004.

[26] O. Frazão, J. P. Carvalho and H. M. Salgado, "Low-loss splice in a microstructured fibre using a conventional fusion splicer," *Microwave Opt Technol Lett,* Vol. 46, Iss. 2, pp. 172-174, 2005.

[27] M. Ibsen, B. J. Eggleton, M. G. Sceats and F. Ouellette, "Broadly tunable DBR fibre laser using sampled fibre Bragg gratings," *Electron. Lett.,* Vol. 31, Iss. 1, pp. 37-38, 1995.

[28] X. He, X. Fang, C. Liao, D. N. Wang and J. Sun, "A tunable and switchable single-longitudinalmode dual-wavelength fiber laser with a simple linear cavity," *Optics Express,* Vol. 17, Iss. 24, pp. 21773-21781, 2009.

[29] S. Sugavanam, N. Tarasov, X. Shu and D. V. Churkin, "Narrow-band generation in random distributed feedback fiber laser," *Optics Express,* Vol. 21, Iss. 14, pp. 16466-16472, 2013.

[30] L. Wang, X. Dong, P. P. Shum and H. Su, "Tunable erbium-doped fiber laser based on random distributed feedback," *IEEE Photonics Journal,* Vol. 6, Iss. 5, 2014.

[31] Y. Y. Zhu, W. L. Zhang and Y. Jiang, "Tunable multi-wavelength fiber laser based on random rayleigh back-scattering," *IEEE Photonics Technology Letters,* Vol. 25, Iss. 16, pp. 1559-1561, 2013.

[32] V. DeMiguel-Soto, M. Bravo and M. Lopez-Amo, "Fully switchable multi-wavelength fiber laser assisted by a random mirror," *Opt. Lett.,* Vol. 39, Iss. 7, pp. 2020-2023, 2014.

[33] S. Sugavanam, Z. Yan, V. Kamynin, A. S. Kurkov, L. Zhang and D. V. Churkin, "Multiwavelength generation in a random distributed feedback fiber laser using an all fiber Lyot filter," *Optics Express,* Vol. 22, Iss. 3, pp. 2839-2844, 2014.

[34] Z. N. Wang, Y. J. Rao, H. Wu, P. Y. Li, Y. Jiang, X. H. Jia and W. L. Zhang, "Long-distance fiber-optic point-sensing systems based on random fiber lasers," *Optics Express,* Vol. 20, Iss. 16, pp. 17695-17700, 2012.

[35] M. Bravo, V. De Miguel-Soto, A. Ortigosa and M. Lopez-Amo, "Fully switchable multi-wavelength fiber laser based interrogator system for remote and versatile fiber optic sensors multiplexing structures," in *Proceedings of SPIE 9157,* 23rd International Conference on Optical Fibre Sensors (OFS-23), 91576P, 2014.

[36] A. M. R. Pinto, M. Lopez-Amo, J. Kobelke and K. Schuster, "Temperature Fiber laser sensor based on a hybrid cavity and a random mirror," *J. Lightwave Technol.,* Vol. 30, Iss. 8, pp. 1168-1172, 2012.

[37] X. H. Jia, Y. J. Rao, Z. N. Wang, W. L. Zhang, Y. Jiang, J. M. Zhu and Z. X. Yang, "Towards fully distributed amplification and high-performance long-range

distributed sensing based on random fiber laser," in *Proceedings of SPIE 8421,* 22nd International Conference on Optical Fiber Sensors (OFS-22), 842127, 2012, .

[38] A. M. R. Pinto, O. Frazão, J. L. Santos and M. López-Amo, "Multiwavelength Raman fiber lasers using Hi-Bi photonic crystal fiber loop mirrors combined with random cavities," *J. Lightwave Technol.,* Vol. 29, Iss. 10, pp. 1482-1488, 2011.

[39] S. Rota-Rodrigo, R. A. Perez-Herrera, M. Fernandez-Vallejo and M. López-Amo, "Low noise dual-wavelength erbium fiber laser in single-longitudinal-mode operation," *Appl. Phy. B,* Vol. 106, Iss. 3, pp. 563-567, 2012.

[40] S. Rota-Rodrigo, L. Rodriguez-Cobo, M. A. Quintela, J. M. Lopez-Higuera and M. Lopez-Amo, "Dual-wavelength single-longitudinal mode fiber laser using phase-shift bragg gratings," *IEEE Journal on Selected Topics in Quantum Electronics,* Vol. 20, Iss. 5, pp. 161-165, 2014.

[41] S. Rota-Rodrigo, R. A. Perez-Herrera, I. Ibañez, A. M. R. Pinto, M. Fernandez-Vallejo and M. Lopez-Amo, "Multiwavelength fiber ring laser based on optical add-drop multiplexers and a photonic crystal fiber Sagnac interferometer," *Opt. Laser Technol.,* Vol. 48, pp. 72-74, 2013.

[42] S. Rota-Rodrigo, I. Ibañez and M. López-Amo, "Multi-wavelength fiber laser in single-longitudinal mode operation using a photonic crystal fiber Sagnac interferometer," *Appl. Phy. B,* Vol. 110, Iss. 3, pp. 303-308, 2013.

[43] L. Rodriguez-Cobo, M. A. Quintela, S. Rota-Rodrigo, M. López-Amo and J. M. López-Higuera, "Single-longitudinal mode laser structure based on a very narrow filtering technique," *Optics Express,* Vol. 21, Iss. 8, pp. 10289-10294, 2013.

[44] M. Fernandez-Vallejo, S. Rota-Rodrigo and M. Lopez-Amo, "Comparative study of ring and random cavities for fiber lasers," *Appl. Opt.,* Vol. 53, Iss. 16, pp. 3501-3507, 2014.

CHAPTER IV

OPTICAL FIBER TRANSDUCERS

upna Universidad Pública de Navarra Nafarroako Unibertsitate Publikoa

CHAPTER IV

INTRODUCTION

Optical fiber sensors have been thoroughly investigated due to their competitive application in the monitoring and control of some physical and chemical parameters. As stated in chapter 2, a fiber optic sensor presents relevant advantages, such as its immunity to electromagnetic interference, small size, reliability, remote sensing ability and multiplexing capability.

The measure of physical parameters such as temperature, strain or curvature has grown significantly in importance for health monitoring of aerospace, marine or civil structures; and in fabrication processes, among others [1, 2].Throughout this chapter, different configurations of optical fiber sensors for monitoring these parameters are presented.

Section 4.1 presents a strain sensor based on a microstructured optical fiber (MOF). The sensor comprises a Hi-Bi MOF transducer to measure the reflected signal using interferometry. A deep experimental study of the sensing head´s polarization components is conducted utilizing an optical backscatter reflectometer, confirming the theoretical predictions. Using a more accessible set up, one of the Hi-Bi MOF polarization

signals is isolated allowing us to measure accurately strain variations.

Section 4.2 shows a microstructured optical fiber strain sensor. The sensor comprises a suspended core MOF between SMFs and is based on the multimodal interference generated in these transitions. A strain sensitivity study for different sensing heads and stage separation lengths is carried out. Also the sensing head is tested for curvature and temperature, showing in the first case that it is insensitive to curvature effects, and secondly, that for small sensor lengths it is insensitive to temperature variations.

Section 4.3 presents a multimodal interferometer based on a suspended core MOF for simultaneous strain and temperature measurements. The structure is also employed for angle measurements. The sensor comprises a 3mm suspended core MOF between SMFs and is based on the combination of two multimodal interferences with different frequency fringe patterns. The interferometric patterns show different sensitivity responses to strain and temperature. Through a low-pass frequency filtering of the detected spectrum, the wavelength shift of the two patterns can be measured allowing the discrimination of strain and temperature effects. The sensor is also characterized for simultaneous measurement of bend angle and temperature.

Finally section 4.4 summarizes the chapter's main conclusions.

4.1. HI-BI MOF IN REFLECTION STRAIN SENSOR

As it has been seen in section 2.4.4, microstructured optical fibers provide unprecedented properties for sensing in comparison with standard fibers. Concretely, the sensor presented in this section exploits two properties of a high-birefringent MOF: high sensitivity to strain and, a negligible sensitivity to temperature. In addition, the sensor is designed in reflection in order to make it more versatile for applications with a difficult access to the measurement zone.

Operation principle

The optical transducer presented in this section is based on the Hi-Bi MOF shown in Figure 4.1 (b). As seen before, when light is launched into a high birefringent fiber the difference in velocities between the two birefringent axes becomes in a phase difference in the waves, determined by the fiber beat length (L_B).

Since the sensing head works in reflection, the interferometric signal is proportional to twice the fiber length and its wavelength dependence can be expressed by (4.1), where l is the fiber length, A is the amplitude and ϕ is the total phase:

$$R(\lambda) = 10\log\left[A\cdot\cos\left(2\pi\cdot\frac{2l\cdot b}{\lambda}-\emptyset\right)\right]^2 \qquad (4.1)$$

The total phase is defined as $\phi=\phi 0+\Delta\phi$, where ϕ_0 is the initial phase and $\Delta\phi$ is the phase change induced by external perturbations. When strain is applied to the fiber, the phase variation will be given by:

$$\Delta\emptyset(\lambda) = \frac{2\pi}{\lambda}\cdot(\Delta b\cdot 2l + 2\Delta l\cdot b) \qquad (4.2)$$

Where Δl and Δb are the length and birefringence variations, respectively.

Sensing head characterization

The developed Hi-Bi MOF sensing head was obtained by splicing one end of 20.8 cm Hi-Bi MOF to a SMF (splice maximum loss of 2 dB) and cleaving the other end. The Hi-Bi MOF was a polarization maintaining MOF (PM-1550-01 from NKT Photonics) with a beat length of ~3.65 mm at 1550 nm and an attenuation of 1.0 dB/Km (cross section photograph can be seen in Figure 4.1 (b)). Figure 4.1 (a) presents

the characterization setup using an optical backscattering reflectometer (OBR), a linear polarizer, a polarization controller and the Hi-Bi MOF sensing head. The OBR used is fabricated by Luna Technologies and presents characteristics such as high spatial resolution (up to ~10 μm) for different measurable magnitudes, such as amplitude, polarization states and return loss in time and frequency domains.

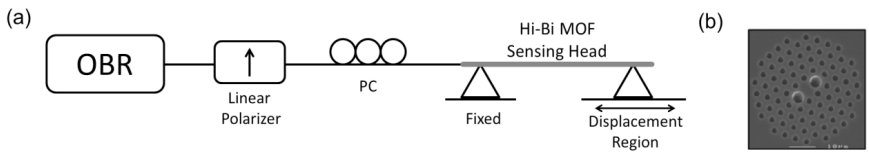

FIGURE 4.1. (a) Schematic of the experimental setup used to characterize the Hi-Bi MOF sensing head and (b) optical microscopic picture of the Hi-Bi MOF cross-section.

In the experimental setup depicted in Figure 4.1, the linear polarizer converted the polarization state of the light source into a linear one, while the polarization controller allowed to adjust the alignment angle with the MOF. When the light was propagated along the MOF, a phase shift was generated between the two birefringent axes due to its own birefringence. The reflected light passed again through the linear polarizer producing the interference between the delayed component signals. The interferometric signal obtained from the sensing head, when no external forces acted on it, is presented in Figure 4.2.

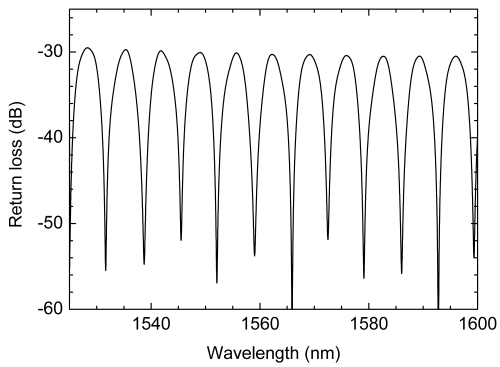

FIGURE 4.2. Reflected spectrum of the Hi-Bi MOF interferometer when no external force is induced on the sensing head.

Since the sensing head was based on a Hi-Bi MOF, it was sensitive to the angle between the input polarized light and the birefringent axes of the fiber. It was expected from theory, that if this angle was 0° or 90° there would be no interference signal, however if the angle was 45° both components should have the same optical input and the interference pattern shown a maximum. Figure 4.3 presents the interferometric spectra obtained for different angles between the input light and the birefringent axes. These results were obtained using the setup shown in Figure 4.1.

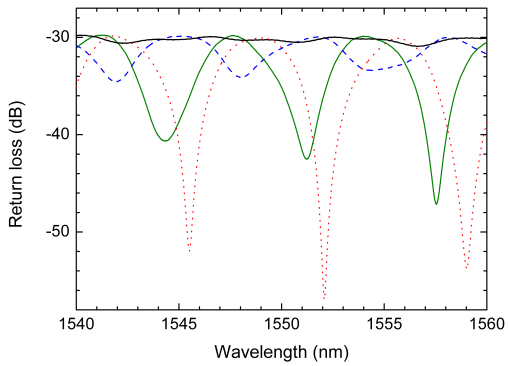

FIGURE 4.3. Interferometer spectra obtained for different polarization controller positions.

When strain variations were inflicted to the MOF sensing head, the output interference pattern (presented in Figure 4.3) should shift in wavelength. Figure 4.4 displays the experimental and theoretical results obtained for three different strain variations (0 με, 500 με and 1000 με). As it can be seen in Figure 4.4, the interferometric spectrum presented a wavelength shift when strain variations were forced into the sensing head, which was quite in agreement with the simulations presented. Based on this characterization, strain measurement could be achieved by monitoring the interference wavelength shift, which was proportional to strain variations.

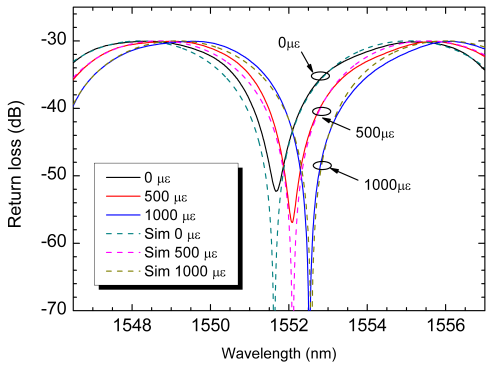

FIGURE 4.4. Experimental results (solid line) and theoretical simulations (dash line) of the reflected output signal for three different strain induced variations.

Sensor system and experimental results

After the characterization of the Hi-Bi MOF sensing head, its response to strain variations was measured through a more usual setup, which is presented in Figure 4.5. The experimental configuration consisted of a laser working at 1554 nm (Ando AQ8201-13), a circulator, a linear polarizer, a polarization controller, the Hi-Bi MOF sensing head, and an OSA with a maximum resolution of 10 pm. After passing through the circulator, the laser light was linearly polarized and the polarization angle optimized before reaching the Hi-Bi MOF sensing head. The interferometric reflected signal made another pass through the circulator before reaching the OSA.

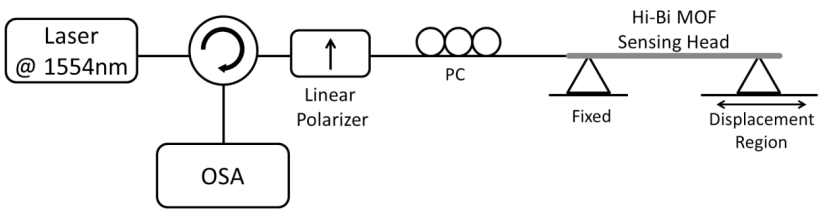

FIGURE 4.5. Experimental setup for strain measurement with an interferometric in-reflection Hi-Bi MOF sensing head.

When strain changes were enforced into the Hi-Bi MOF sensing head, its output signal shifted in wavelength (see Figure 4.4). Using the cost effective system illustrated in Figure 4.5, the sensing head interrogation was carried out by using

the laser, transforming the sensor system into an intensiometric one. Since its interrogation was made now at a fixed laser wavelength, the output signal due to strain changes presented power shifts. Since the Hi-Bi MOF sensing head was illuminated by the narrow band emitted laser signal, the output signal level corresponded only to the attenuated transmitted bandwidth of the laser. As so, if the laser wavelength was placed at an interferometric minimum, the output peak power was at its minimum value. On the contrary, if the emitted wavelength corresponded to an interferometric maximum, the output peak power reached its maximum value. This provided a visual sensation that the laser line was sweeping the interferometric signal, as the output peak power varied between a maximum and a minimum. The observed power shift with strain induced variations is depicted in Figure 4.6, using a stepper motor with increments of 22.2 με. The Hi-Bi MOF sensing head interference pattern may be divided in two different zones. The initial one shows a quadratic behavior. Afterwards, the second zone shows a linear one; being this last zone characterized by a sensitivity to strain variations of 7.96 dB/mε in an operative region of 1200 με. The breaking point of the sensor head was found to be close to 5000 με.

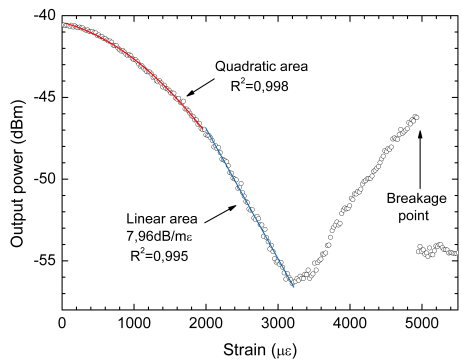

FIGURE 4.6. Measured optical power variation with strain of the Hi-Bi MOF sensing head.

The presented sensing head sensitivity to strain induced variations was higher than other developed structures based on this fiber. For instance, when using the Hi-Bi MOF as the sensing element in a fiber loop mirror a sensitivity to strain that varied from 2.7 dB/mε at 1530 nm to 3.2 dB/mε at 1545 nm was obtained [3]. This interferometric sensing head showed an appropriate response to strain variations, opening the possibility to obtain even better performance with a proper auto-referenced interrogation scheme such as a highly stable in-quadrature dual-

wavelength fiber laser [4]. Also, the use of this system in reflection is an attractive choice as a basic sensing element, since it is simple, compact and presents the ability for remote sensing and multiplexing.

4.2. CONTROL OF THE STRAIN SENSITIVITY OF A MOF SENSOR

The aim of this section is the optimization of a microstructured optical fiber sensor for strain measures. In this regard, a study of its sensitivity depending on the sensor length and its fixing points is conducted.

Description of the sensor system

The sensor was based on the multimode interference created by introducing a section of a suspended core MOF (Fabricated by the Institute of Photonic Technology, IPHT, Jena, Germany) between two SMFs, Figure 4.7. Our MOF presents a 3 μm core enclosed by four large holes and a multimode behavior. The SMF-MOF splices were done using a splice machine (Fitel S182PM) in manual mode, with an arc-power of 110 (splicer parameter) and an arc-duration of 750 ms.

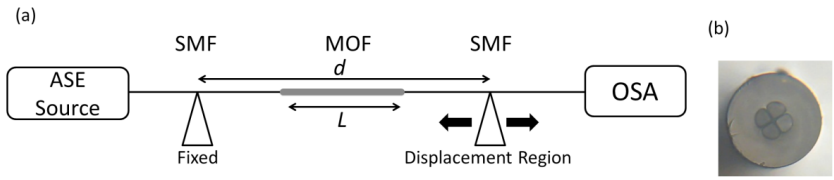

FIGURE 4.7. (a) Schematic of the strain sensor system. (b) Microscopy photograph of the Suspended Core MOF cross-section.

Experimental results

The characterization of the MOF sensing head response to strain variations was measured through the experimental setup presented in Figure 4.7 (a). The experimental configuration consisted of an EDFA (Fiberamp-BT 1400) as broadband source, the sensing head and an OSA (Advantest Q8384) with a maximum resolution of 10 pm. The fiber was fixed by two translation stages in order to apply strain by moving one of the stages while the other remains fixed. For this characterization, a series of measurements for three different stages separations, d=0.125 m, d= 0.25 m and d=0.50 m, and for different sensor lengths (L) was carried out.

Figure 4.8 shows the variations of the optical spectrum of the sensing head for two cases, a) L=5 mm with d=0.5 m and b) L=20 mm with d=0.5 m, for three different strain values. This figure also shows a linear behavior of both sensors with strain; however their sensitivities were different.

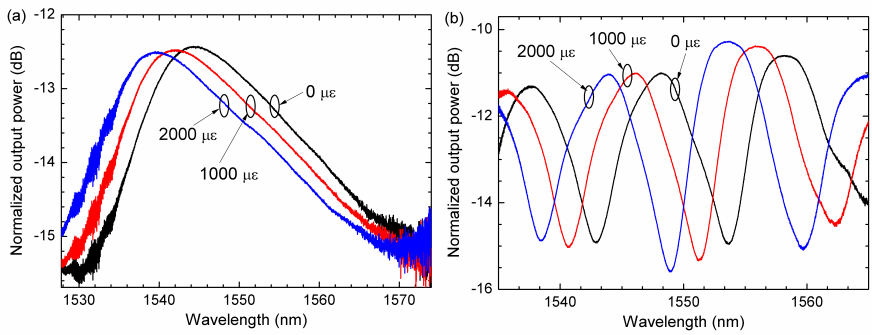

FIGURE 4.8. Variations of the optical output spectrum at different strain values for sensor L=5 mm (a) and L=20 mm (b) with a d=0.5 m.

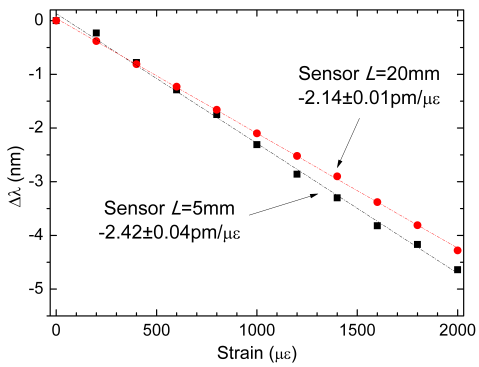

FIGURE 4.9. Wavelength dependence with strain for sensor L=5 mm (black) and L=20 mm (red).

Figure 4.9 shows the sensitivity of the sensing head depending on the sensor length (L) and the stage lengths (d). From these results there are two conclusions to be drawn. Firstly the sensitivity was increased with the stage lengths. This effect is justified by the fact that the Young module of the MOF was less than the SMF´s one, as stated in section 2.4.4.5. Taking this into account, for a constant sensor length L, when the stages length was increased, it was necessary a major displacement to obtain the same strain. Therefore, the MOF, which presented a

lower Young module than SMF, experienced a major elongation generating a major sensitivity in the sensing head.

Secondly, the sensitivity varied with the sensor length. In the case of the MOF, these variations were due to the combination of the different modes of the fiber at its output. When the light was coupled from the SMF to the MOF, few modes were excited, each one with a different propagation constant, that produced a phase delay between modes. In the transition from the MOF to the SMF the different modes were combined with its respective phase differences, generating the interference pattern. When a strain was applied to the sensor, an increment of the sensor length was produced and consequently, the modes experimented a different change in their phase.

These properties of the optical transducer provoked the changes in the sensing head sensitivity shown in Figure 4.10. The best values of strain sensitivity, -2.42 pm/με and -2.40 pm/με, were achieved for L=5 mm and L=75 mm sensor lengths, respectively, with a 50 cm stages´ separation.

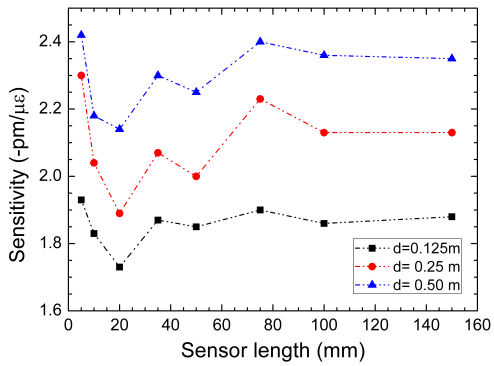

FIGURE 4.10. Sensor´s sensitivity characterization according to the sensor length (L) and the stage lengths (d).

Taking into account this strain characterization, a temperature study for 5 mm and 75 mm sensor lengths was carried out. Figure 4.11 shows that for the 75 mm sensor a sensitivity of 5.93 pm/°C was achieved. However, for the 5 mm sensor the temperature effect was negligible due to its short length.

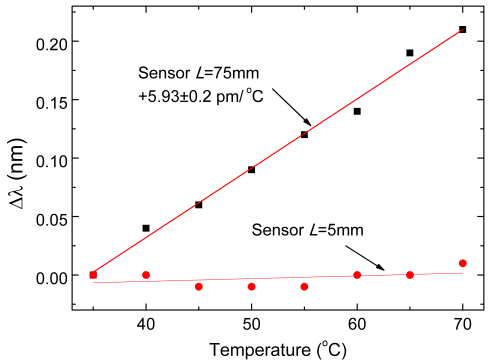

FIGURE 4.11. Characterization of the wavelength shift with temperature for the 5mm (red) and 75mm (black) sensor length.

Also, a curvature effect study was carried out showing that the behavior of the sensor remained constant for bending radii higher than 0.25 m.

4.3. MULTIMODAL INTERFEROMETER BASED ON A SUSPENDED CORE MOF FOR SIMULTANEOUS MEASUREMENT OF PHYSICAL PARAMETERS

As seen before, a MOF sensor can be used for strain, temperature or curvature monitoring. Usually, the sensor is used for monitoring just one of these parameters, and the simultaneous variations of other parameters could affect the measures. Therefore these kinds of sensors require the use of another element as a reference [5, 6]. In this regard, the possibility to isolate different physical parameters using the same sensing head allows the simultaneous measurement of different parameters. In this section, a sensor based on a suspended core MOF for simultaneous measurement of physical parameters is presented.

Description of the sensor system

The sensing principle derived from the analysis of the interferogram which resulted from the combination of two different multimodal interferometric patterns originated by introducing a 3 mm long suspended-core MOF (Fabricated by the Institute of Photonic Technology, IPHT, Jena, Germany) between two SMFs (see Figure 4.12). This MOF presented an asymmetric core with a ~ 2.4 μm diameter enclosed by three large holes, showing a multimode behavior. The shorter length of the sensor and its configuration in transmission made it more versatile than sensors based on a fiber loop mirror in which the length usually is in the order of centimeters [7, 8].

The SMF-MOF splices were done using a splice machine (Fitel S182PM) in manual mode, with an arc-power of 60 (splicer parameter) and an arc-duration of 650 ms.

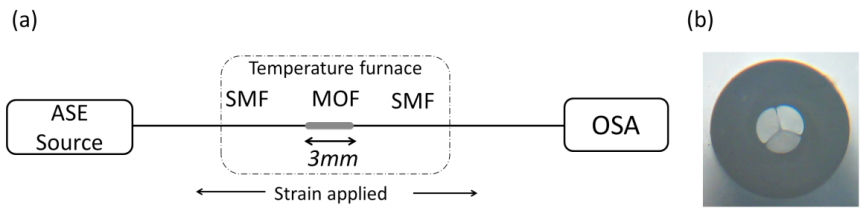

FIGURE 4.12. (a) Schematic of the strain sensor system and (b) microscopy photograph of the suspended core MOF cross-section (bottom).

The experimental configuration included an EDFA (Fiberamp-BT 1400) operating as a broadband optical source and an OSA (Advantest Q8384) with a maximum resolution of 10 pm. The fiber was fixed on two translation stages, separated 50 cm, in order to apply strain by moving one of the stages while the other remains fixed.

Figure 4.13 (a) shows the transmission spectrum of the sensing head (dark line). Two different frequency components were appreciated, associated to the high and low frequency fringe patterns. The low frequency one came from the birefringence generated by the asymmetric core of the MOF, while the high frequency pattern resulted from the interference of the modes propagated in the sensing head fiber, which showed a multimode behavior.

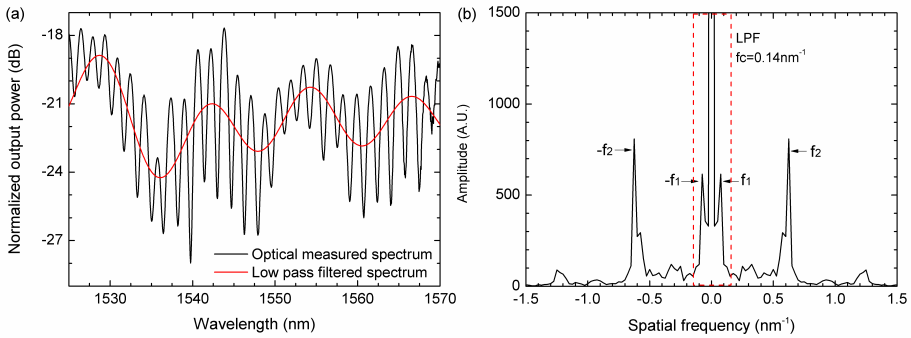

FIGURE 4.13. (a) Optical transmission spectra of the sensor when no external force is applied at room temperature (dark line), and low pass filtering with processing software (red line). (b) Fast Fourier transform of the optical transmission spectra.

Figure 4.13 (b) gives the fast Fourier transform (FFT) of the transmission spectrum shown in Figure 4.13 (a), evidencing the two frequency components, f1 and f2, which correspond to the low and high frequency fringe patterns, respectively. The low frequency component presented in Figure 4.13 (a) was obtained using a digital low-pass filter with a cut-off frequency of 0.14 nm^{-1}. The presence of two clearly periodic interferences, allowed the repeatability of the sensor in comparison with those based on a non-periodic interference [5, 7].

Simultaneous strain and temperature measurements

For the strain characterization of the sensing head a measurement from 0 to 2000 με with steps of 200 με was carried out. Figure 4.14 (a) shows the wavelength shift of each interference pattern. This characterization was carried out by tracking a maximum of the spectrum of each interference pattern. The low-frequency interferogram had a considerable higher sensitivity, -3.16 pm/με, in comparison with the +0.34 pm/με of the high-frequency one. Figure 4.14 (b) shows the evolution with strain of the low-frequency spectrum.

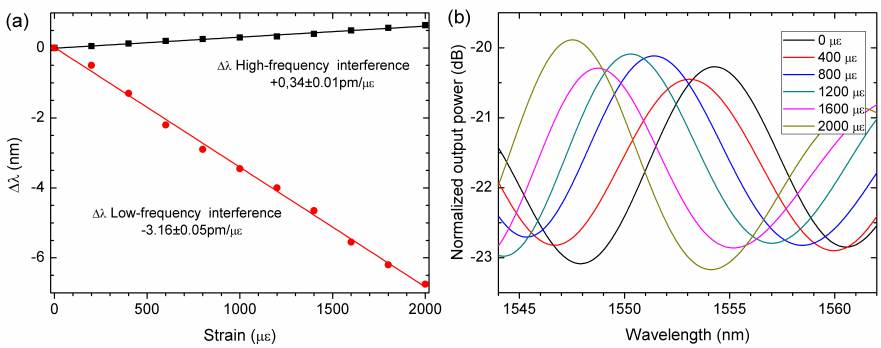

FIGURE 4.14. (a) Characterization of the wavelength shift with strain, and (b) spectral evolution of the multimode interference with strain.

Once the strain response was characterized, a temperature study was carried out. For this purpose, a measurement from 40°C to 70°C with steps of 5°C was conducted. Figure 4.15 (a) shows that in this case that the high-frequency interferogram had a higher sensitivity (25.30 pm/°C) compared with the low-frequency one (-6.01 pm/°C). The unfiltered spectral evolution with temperature variations is shown in Figure 4.15 (b).

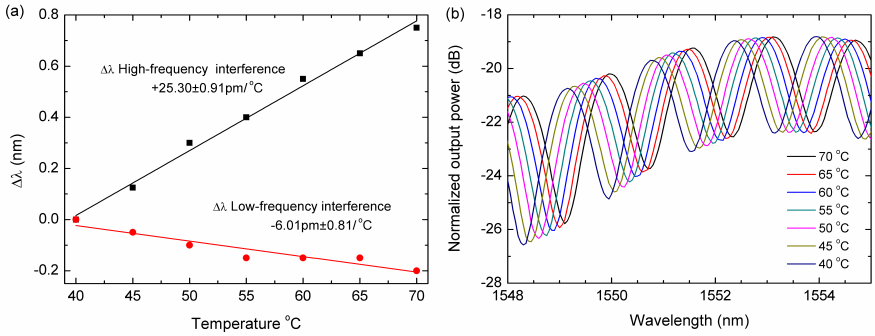

FIGURE 4.15. (a) Characterization of the wavelength shift with temperature, and (b) evolution of the spectra with temperature.

With the results obtained from the strain and temperature dependence of the two interferometric patterns, it can be written:

$$\Delta\lambda_{Low-freq} = -6.01 \cdot \Delta T - 3.16 \cdot \Delta\varepsilon \qquad (4.3)$$

$$\Delta\lambda_{High-freq} = 25.30 \cdot \Delta T + 0.34 \cdot \Delta\varepsilon \qquad (4.4)$$

where $\Delta\lambda_{low\text{-}freq}$ and $\Delta\lambda_{High\text{-}freq}$ are expressed in pm. These equations reveal that it is possible to discriminate the strain and temperature effects by rearranging them in the following way:

$$\begin{bmatrix}\Delta T \\ \Delta\epsilon\end{bmatrix} = \frac{1}{77.908} \cdot \begin{bmatrix}0.34 & 3.16 \\ -25.30 & -6.01\end{bmatrix} \begin{bmatrix}\Delta\lambda_{Low-freq} \\ \Delta\lambda_{High-freq}\end{bmatrix} \qquad (4.5)$$

The temperature and strain measurement based on this approach showed resolutions, δT and $\delta\varepsilon$, which were calculated using the method presented in [9], considering that the OSA has a spectral resolution of δ_{OSA}=10 pm. It turned out values of δT = 0.45°C and $\delta\varepsilon$ = 4.02 me, which compares favorably with values reported by other authors, as outlined in Table 4.1.

TECHNOLOGY	ΔE	ΔT	YEAR	REF.
Modal interferometer + FBG	9.1 με	0.27°C	2010	[5]
Modal interferometer + LPG	5.2 με	1.5°C	2012	[6]
Clover MOF Sagnac	11 με	2.0°C	2012	[7]
Hi-Bi PCF Sagnac	4.7 με	1.5°C	2010	[8]

TABLE 4.1. Values for strain and temperature resolutions under simultaneous measurement obtained considering other fiber optic sensing layouts.

Simultaneous angle and temperature measurements

The sensor was also characterized for bend angle (α) measurements. An angle stepper was used in the range of -90 deg to +90 deg with steps of 30 deg (Figure 4.16). The angle was measured with respect to the two fixed points of the fiber (Figure 4.16 in blue), with a separation of 7.5 cm.

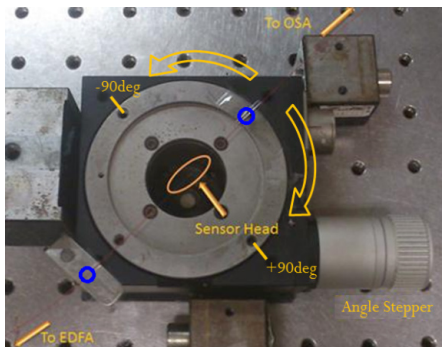

FIGURE 4.16. Setup of the bend sensor showing the angle stepper.

Figure 4.17 shows the evolution of the low-frequency spectral interferogram with the angle applied, indicating an appreciable change in wavelength and amplitude. In order to overcome in the measurement attenuation effects, it was decided to track the wavelength evolution, which is shown in Figure 4.17 (b). It can be observed that the sensor presented two regions with different sensitivities. This was attributed to the MOF asymmetric core and its birefringence. However, both regions revealed a linear behavior. The angular sensitivity of the sensor was dependent on the position of the fiber core with respect to the angle direction.

From the date shown in Figure 4.17 (b) , a sensitivity value of 5.67 pm/deg was derived for the range 0 to -90 deg, while for the range 0 to 90 deg, was 9.17 pm/deg.

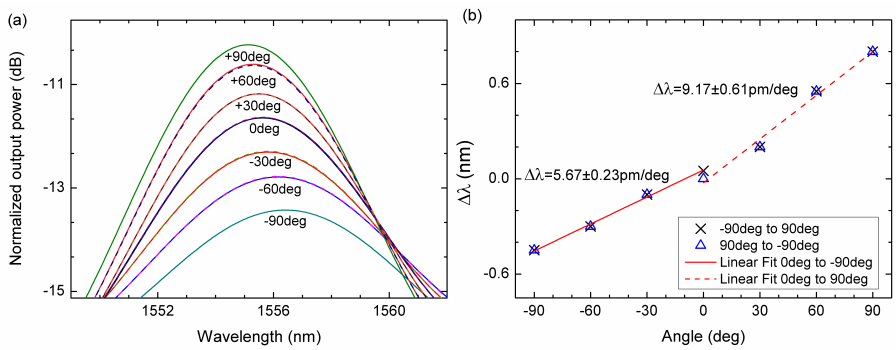

FIGURE 4.17. (a) Evolution of the low-frequency interferogram with angle, and (b) characterization of the wavelength shift with curvature.

Likewise, the high-frequency spectral interferogram presented the same behavior (see Figure 4.18), in this case with sensitivities of -2.17 pm/deg and -7.83 pm/deg in the ranges of 0 to -90 deg and o to 90 deg, respectively.

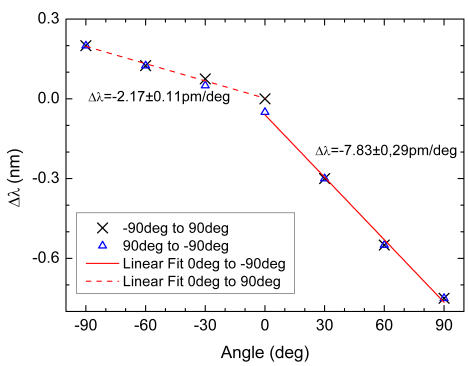

FIGURE 4.18. Characterization of the wavelength shift of the high-frequency interferogram with curvature.

Due to the linear behavior of the sensor response in each angular zone, it was possible to configure the sensing head for simultaneous measurement of bend

angle and temperature. For this purpose we used the characterization in the range from 0 to 90 deg which presented a higher sensitivity to angle variations. The wavelength variation (in pm) of the high and low frequency interferograms can be expressed as:

$$\Delta\lambda_{Low-freq} = 9.17 \cdot \Delta\alpha - 6.01 \cdot \Delta T \quad (4.6)$$

$$\Delta\lambda_{High-freq} = -7.83 \cdot \Delta\alpha + 25.3 \cdot \Delta T \quad (4.7)$$

This way the angle and temperature can be calculated by:

$$\begin{bmatrix}\Delta\alpha \\ \Delta T\end{bmatrix} = \frac{1}{184.95} \cdot \begin{bmatrix}25.3 & 6.01 \\ 7.83 & 9.17\end{bmatrix} \begin{bmatrix}\Delta\lambda_{Low-freq} \\ \Delta\lambda_{High-freq}\end{bmatrix} \quad (4.8)$$

Applying the same approach considered for the simultaneous measurement of strain and temperature, the resolution was evaluated resulting in values of $\delta\alpha$ = 1.69 deg and δT = 0.92 °C, for curvature and strain respectively.

4.4. CONCLUSIONS

This chapter has provided a review of the work carried out related to transducers based on microstructured optical fibers. Three sensors with different behaviors have been presented. In this section the MOF unusual features, in comparison with standard fibers, have been exploited.

In the first MOF sensor a configuration for an interferometric fiber optic strain sensor has been presented and experimentally demonstrated. The sensing head has been achieved by using a Hi-Bi MOF in-reflection. An experimental characterization of this sensing head was made using an optical backscatter reflectometer, which is in accordance with the presented theoretical simulations. Using a more cost-effective setup, strain variations can be accurately retrieved. The in-reflection sensing head presents a sensitivity of 7.96 dB/mε to strain induced variations. Due to the demonstrated strain sensitivity, this interferometric sensing head is a very attractive solution for applications such as strain measurement in hazard environments and health monitoring of complex structures.

These results have been published in [10, 11].

The second sensor which has been presented is a strain fiber optic sensor based on multimode interferences. The sensing head has been accomplished by using a suspended core MOF in transmission. A characterization study of the influence of the length of the sensor and the applied strain in the sensitivity of the system has been carried out. This study shows that the sensitivity increases with the separation of the stages and also shows an optimal sensor length of 5 mm and 75 mm with the higher sensitivities, for a 0.5 m stage separation of -2.42 pm/με and -2.40 pm/με respectively. For this sensor length values a temperature characterization has been also carried out, showing that the best length sensor option is 5 mm, that is practically insensitive to temperature variations, whereas the 75 mm sensor has a sensitivity of 5.93 pm/°C. Also the insensitivity of system to the curvature effect for bending radii higher than 0.25 m has been demonstrated.

These results have been published in [12].

Finally, a simultaneous temperature-strain fiber optic sensor based on the combination of the characteristics of two interferograms with distinct frequency fringe patterns has been presented. The sensing head has been accomplished by using a three hole suspended core MOF operated in transmission. Each interferometric pattern presents different response to strain and temperature, allowing the simultaneous measurement of both parameters. Through a low-pass frequency filtering of the detected spectrum, the wavelength displacement of each interferogram can be measured allowing the discrimination of temperature and strain with resolutions of 0.45°C and 4.02 με, respectively. Furthermore, the sensor has been tested for angle measurements, demonstrating that a sensitivity of 9.17 pm/deg in the 0 to 90 deg range is possible. In this regard, results have been presented indicating the feasibility of simultaneous measurement of bend angles and temperature with resolutions of ±1.69 deg and ±0.92°C, respectively.

These results have been published in [13,14]

4.5. REFERENCES

[1] J. M. López-Higuera, L. R. Cobo, A. Q. Incera and A. Cobo, "Fiber optic sensors in structural health monitoring," *J. Lightwave Technol.*, Vol. 29, Iss. 4, pp. 587-608, 2011.

[2] H. N. Li, D. S. Li and G.B. Song, "Recent applications of fiber optic sensors to health monitoring in civil engineering," *Eng. Struct.*, Vol. 26, Iss. 11, pp. 1647-1657, 2004.

[3] W. Qian, C. L. Zhao, X. Dong and W. Jin, "Intensity measurement based temperature-independent strain sensor using a highly birefringent photonic crystal fiber loop mirror," *Opt. Commun.,* Vol. 283, Iss. 24, pp. 5250-5254, 2010.

[4] A. M. R. Pinto, O. Frazão, J. L. Santos, M. Lopez-Amo, J. Kobelke and K. Schuster, "Interrogation of a suspended-core Fabry-Perot temperature sensor through a dual wavelength Raman fiber laser," *J. Lightwave Technol.,* Vol. 28, Iss. 21, pp. 3149-3155, 2010.

[5] B. Dong, J. Hao, C. Y. Liaw, B. Lin and S. C. Tjin, "Simultaneous strain and temperature measurement using a compact photonic crystal fiber intermodal interferometer and a fiber Bragg grating," *Appl. Opt.,* Vol. 49, Iss. 32, pp. 6232-6235, 2010.

[6] T. Li, X. Dong, C. C. Chan, L. Hu and W. Qian, "Simultaneous strain and temperature measurement based on a photonic crystal fiber modal-interference interacting with a long period fiber grating," *Opt. Commun.,* Vol. 285, Iss. 24, pp. 4874-4877, 2012.

[7] R. A. Perez-Herrera, R. M. André, S. F. Silva, M. Becker, K. Schuster, J. Kobelke, M. Lopez-Amo, J. L. Santos and O. Frazao, "Simultaneous measurement of strain and temperature based on clover microstructured fiber loop mirror," in *Proceedings of SPIE 8421,* 22nd International Conference on Optical Fiber Sensors (OFS-22), 84216W, 2012 .

[8] R. M. André, M. B. Marques, P. Roy and O. Frazão, "Fiber loop mirror using a small core microstructured fiber for strain and temperature discrimination," *IEEE Photonics Technology Letters,* Vol. 22, Iss. 15, pp. 1120-1122, 2010.

[9] W. Jin, W. C. Michie, G. Thursby, M. Konstantaki and B. Culshaw, "Simultaneous measurement of strain and temperature: Error analysis," *Optical Engineering,* Vol. 36, Iss. 2, pp. 598-609, 1997.

[10] S. Rota-Rodrigo, M. Bravo, A. M. R. Pinto and M. Lopez-Amo, "High-sensitivity PCF sensing head for strain measurement," in *Proceedings of SPIE 8421,* 22nd International Conference on Optical Fiber Sensors (OFS-22), 842136, 2012 .

[11] S. Rota-Rodrigo, A. M. Pinto, M. Bravo and M. Lopez-Amo, "An in-reflection strain sensing head based on a Hi-Bi photonic crystal fiber." *Sensors,* Vol. 13, Iss. 7, pp. 8095-8102, 2013.

[12] S. Rota-Rodrigo, M. Lopez-Amo, J. Kobelke, K. Schuster, J. L. Santos and O. Frazão, "Control of the strain sensitivity using a suspended core photonic crystal fiber sensing head," in *Proceedings of SPIE* 9157, 23nd International Conference on Optical Fiber Sensors (OFS-23), 91571Y, 2014 .

[13] S. Rota-Rodrigo, M. Lopez-Amo, J. Kobelke, K. Schuster, J. L. Santos and O. Frazão, " Simultaneous strain and temperature measure based on a single suspended core photonic crystal fiber," in *Proceedings of SPIE* 9157, 23nd International Conference on Optical Fiber Sensors (OFS-23), 915721, 2014 .

[14] S. Rota-Rodrigo, M. Lopez-Amo, J. Kobelke, K. Schuster, J. L. Santos and O. Frazão, "Multimodal interferometer based on a suspended core fiber for simultaneous measurement of physical parameters," *IEEE Journal of Lightwave Technology,* DOI: 10.1109/JLT.2014.2375896, on-line version, 2014.

CHAPTER V

OPTICAL FIBER SENSORS SYSTEMS

upna Universidad Pública de Navarra Nafarroako Unibertsitate Publikoa

CHAPTER V

INTRODUCTION

Throughout chapters 3 and 4, different fiber lasers and transducers have been presented. The aim of this chapter is to combine both types of structures, in order to obtain an optical fiber sensor system. Throughout this chapter, different configurations of fiber sensor systems are presented, showing their main properties such as stability, sensitivity, output power and OSNR. Moreover, other features like multiplexing, scalability or remote monitoring, are taken into account.

Section 5.1 shows two ultra-long range fiber Bragg grating sensor interrogation systems. In the first approach four FBGs are located 200 km away from the monitoring station and a signal to noise ratio of 20 dB is obtained. The second improved version is able to detect the four multiplexed FBGs placed 250 km away, offering a signal to noise ratio of 6–8 dB. Both systems are based on a wavelength swept laser to scan the reflection spectra of the FBGs, and they are composed of two identical-length optical paths: the first one aims to launch the amplified laser signal by means of Raman amplification, and the other one is employed to guide the reflected signals to the reception system.

Section 5.2 presents a fiber laser sensor system for temperature measurements. This system is based on the detection in the electrical domain of the resulting beat signal of two different SLM laser lines, which are generated by an EDFRL. The SLM operation is achieved by using PSFBGs with ultra-narrow bandwidths. Two Independent cavities for the reference signal and sensor signal generation are used to avoid the wavelength competition and to improve the stability. Also, this configura-

tion allows the control of the temperature operation point of the system by adjusting the temperature in the reference side.

Section 5.3 shows a 50 Km remote and switchable fiber optic sensing system based on an EDFRL. The system allows the integration of different interrogation methods based on the detection of wavelength or amplitude variations of the laser. This integration is carried out by sequentially activating different ring cavities through an optical switch. With this scheme, the maximum gain zone of the erbium doped fiber amplifier can be used to increase the distance of the sensor system. Also, experimental demonstrations of a bending intensity sensor and a FBG based strain sensor, for high and low-strain measurements respectively, are presented.

Section 5.4 presents a multi wavelength EDFRL system for sensing applications based on MUX/DMUX and fiber Bragg gratings. The FBGs actuate as wavelength selection method and at the same time, as sensors. Four-wavelength laser emissions are obtained simultaneously. The utilization of this new laser for temperature sensor applications and also its applicability for remote sensing has been probed.

Section 5.5 shows a new method for increasing simultaneously the sensitivity and interrogation stability of fiber-optic intensity sensors. The fiber laser sensor system is based on a double-coupler ring resonator. On the one side, the attenuation sensitivity of the sensor is enhanced by placing it inside a ring resonator. On the other side, the stability of the interrogation method is widely improved by creating an external lasing ring resonator with matched spectral response. The combination of the wavelength selective response of the ring resonator and optical amplification is used to create different fiber lasers. This section also presents four practical cases for displacement measurements through a bending sensor, where three of them are based on an EDFRL configuration and the other one in a random laser configuration.

Finally section 5.6 summarizes the chapter's main conclusions.

5.1. REMOTE 250KM FBG SENSOR

As it has been seen in section 2.4.2, remote sensing is particularly appealing for applications such structural health monitoring [1, 2], tsunami detection [3, 4] and geodynamical monitoring [5]. Also, in Table 2.4 it has been presented the state of the art of remote sensing systems. The longest network length up to 2011 was of 230 Km, as it was demonstrated in [6]. The aim of this section is the development of the longest remote sensing system, with all the active elements allocated at the monitoring station.

Description of the remote sensing system

The basic design of the 200 and 250 km ultra-long fiber Bragg grating sensor systems is schematically depicted in Figure 5.1.

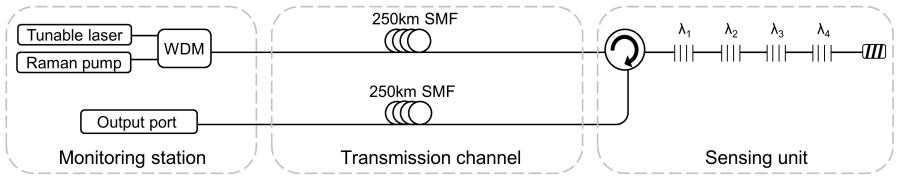

FIGURE 5.1. Schematic depiction of the ultra-long fiber Bragg grating sensor system.

As it is shown in Figure 5.1 the system was divided into three essential sections. The sensors unit was composed of four multiplexed FBG sensors and a circulator which redirected the reflected signals towards the output port. The FBGs were disposed in a serial configuration and located within the Raman-amplified wavelength band. Their central wavelengths were $\lambda 1 = 1{,}555.24$ nm, $\lambda 2 = 1{,}549.82$ nm, $\lambda 3 = 1{,}546.88$ nm and $\lambda 4 = 1{,}552.40$ nm, each one showing a bandwidth of 0.19 nm, 0.16 nm, 0.19 nm and 0.24 nm and a reflectivity of 98.9%, 98.3%, 99% and 99.8% respectively. Initially, this serial configuration might seem an obstacle to achieve power equalization for the channels, however, in this scheme it was not a problem, because the system was not based on a long distance laser structure. In those systems [7], the mode competition has a crucial influence when all the channels must lase at the same time. In our proposed system, the channels equalization depended on both the non-uniform shape of the Raman profile and the insertion loss of the FBGs located in front of the sensor interrogated in each moment.

As far as the monitoring station is concerned, it included a wavelength division multiplexer which combined the signal which came from the tunable laser and the Raman pump. The fiber Raman laser emitting at 1445 nm was deployed to generate distributed Raman amplification in the system. On the other hand, and also in the monitoring head, two different tunable lasers were utilized depending on the length of the sensor system. When the network reached 200 km, a tunable laser (ANDO AQ8201-13) with a bandwidth of 100 MHz was used to sweep the whole span comprised of the FBGs. However, when the FBGs were located at a distance of 250 km from the monitoring station some nonlinear effects appeared. Namely, stimulated Brillouin scattering arose with the adverse effect that this entailed. A detailed analysis of this issue is presented in the next section. Consequently, a tunable laser with a wider bandwidth was deployed to cope with these impairments. The tunable laser was based on a previously studied and published scheme [8]. The basic design of the laser, which included a tunable FBG in order to acquire the tuning capability, is depicted in Figure 5.2 The tunable FBG had a bandwidth of 0.6 nm and offered an extinction ratio of 65 dB. It was able to sweep the whole span comprised of the FBGs.

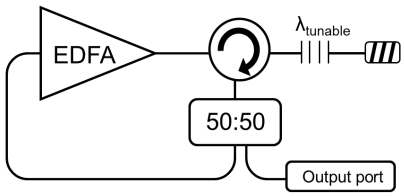

FIGURE 5.2. Basic design of the tunable laser.

On the other hand, the monitoring station also included the detection system, which for this experiment was a commercial OSA (Advantest Q8384). Finally, the transmission channel consisted of two identical-length optical paths. The first one intended to launch the amplified laser signal by means of discrete Raman amplification and the other one was employed to guide the reflection signal to the reception system, avoiding the Rayleigh backscattering.

The operation mode of the remote sensing system was the simplest one. To interrogate the remote fiber Bragg gratings sensors, the tunable laser made a wavelength sweep of the whole band where the FBGs were located, avoiding the utilization of modulated signals, as in [6]. We also demonstrated the benefits of avoiding the utilization of high coherence length lasers, as employed in other remote systems with Rayleigh scattering limitations [9, 10].

Remote sensing (200 km) FBG interrogation system

For the first system, we examined the interrogation of the sensor unit, composed by four FBGs located 200 km away from the monitoring station. Figure 5.3 shows the reflected signal when optical powers of 0.72 W from the Raman pump laser and 10.68 dBm from the tunable laser were launched into the system. This figure collects (superposes) the individual measurements carried out when the laser wavelength was tuned into each FBG reflection peak wavelength. From Figure 5.3 we can draw some conclusions as follows: firstly, the OSNR from the remotely multiplexed four FBGs varied from 20 dBm, in the worst case, to 22 dBm in the best one.

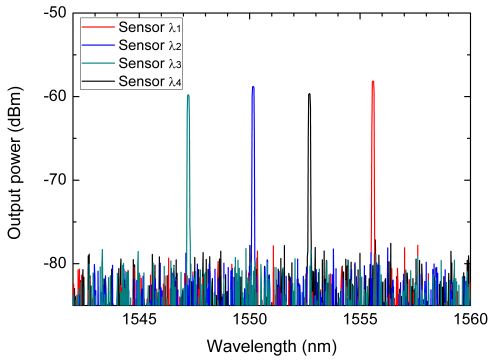

FIGURE 5.3. Spectrum of the reflected signal from the four remotely multiplexed FBGs for $P_{pum\text{-}Raman}$=0.72 W, $P_{tunable\text{-}laser}$=10.68 dBm and $OSA_{resolution}$= 0.1 nm.

As discussed before, the OSNRs are determined by the non-uniform shape of the Raman gain profile. Figure 5.4 shows this spectrum when the transmission channel was 200 km long. It reveals that even if the Raman gain profile was not completely uniform, the wavelength bandwidth where the FBGs were located had 1 dB of maximum deviation. As a result, the OSNR maximum variation was 2 dB between the best and the worst case. Secondly, the remote system was a low noise configuration because it coped with the two principal dominating sources of noise of a fiber Raman amplifier. The ASE generated by spontaneous Raman scattering was addressed by the FBGs, since they only reflect the Bragg wavelength. Furthermore, the multipath interference (MPI) noise mainly produced by Rayleigh backscattering did not play a crucial role because the reflected signal travelled through a different optical path than the launched by the tunable laser and the distributed Raman amplification.

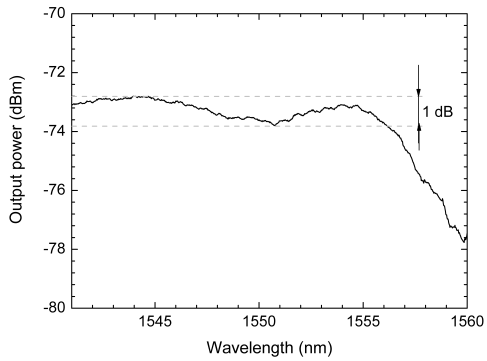

FIGURE 5.4. Amplified spontaneous emission at 200 km for a $P_{pum\text{-}Raman}$=0.85 W.

The proposed remote sensing system was a low noise configuration wherein the background noise was hidden by the noise imposed by the OSA. This great signal to noise ratio encouraged to increase the number of sensors to be multiplexed or to try to reach further distances. The ability to multiplex several sensors is not only relevant from a conceptual point of view, but it is also important for practical reasons considering that it allows, in general, a reduction in the cabling and cost of the sensing system [11].

Remote sensing (250 km) FBG interrogation system

The first attempt to reach 250 km used the same system. It was obvious that a higher amount of Raman pump power was necessary since the amount of loss to compensate with the distributed Raman amplification was also higher than in the previous system. To this end, the Raman pump power was increased, but unsurprisingly Brillouin scattering arose, which hampered the signal amplification, as in many fiber communication systems [12]. Figure 5.5 shows the spectrum of the tunable laser after 250 km length of SMF; it illustrates the progression of the Stokes lines: the higher the pump power was, the greater the spectrum broadening and the Stokes lines power were.

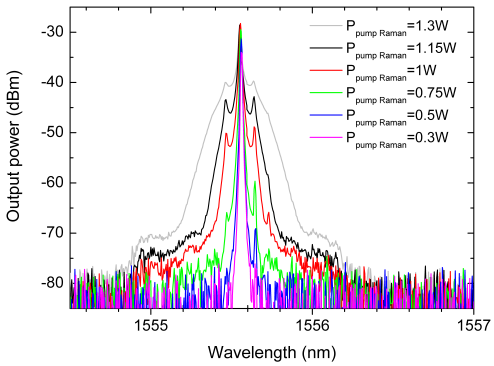

FIGURE 5.5. Spectrum of the tunable laser after 250 km length transmission for a $P_{tunable\text{-}laser}$=10.68 dBm and $OSA_{resolution}$= 0.01 nm.

For conventional fibers, the threshold pump power for this process is few mW, however, the impairments start when the amplitude of the scattered wave is comparable to the signal power. The biggest problem appears in this kind of situations when the backscattered light experiences gain from the forward-propagating signal which leads to depletion of the signal power. In consequence, there was a practical limitation of the maximum possible gain, as shown in Figure 5.6.

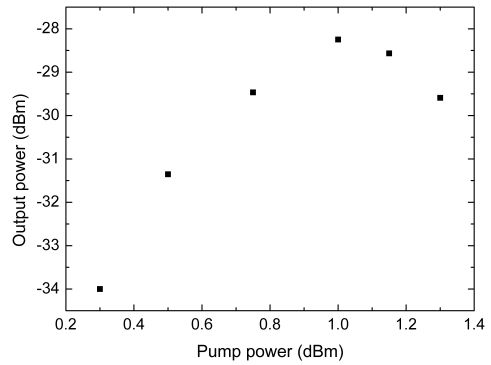

FIGURE 5.6. Evolution of laser power vs. Raman pump laser.

For lasers with linewidths $\Delta\lambda$ much larger than 20 MHz, SBS gain is inversely proportional to $\Delta\lambda$ [13]. Thus, for this 250 km length span, we developed a tunable laser, as it is shown in Figure 5.2, with a wider bandwidth to reduce the problems caused by SBS. Our selected tunable laser bandwidth was 0.6 nm, and it launched 11 dBm with and extinction ratio of 65 dB. Figure 5.7 shows the spectrum of the reflected signal from the four FBG located 250 km away from the monitoring station. The optical sig-

nal to noise ratio was 6 dB in the worst case and 8 dB in the best one. To the best of our knowledge, this ultra-long range FBG sensor system is the longest reported system to interrogate a FBG. It is also worth noticing that the system is able to multiplex FBG sensors.

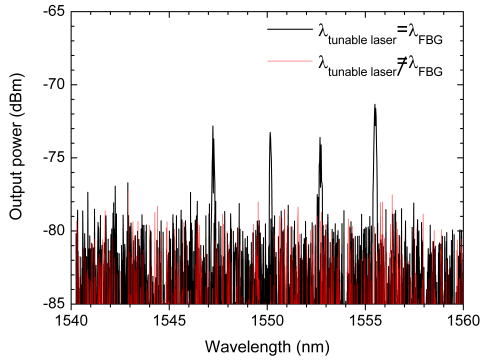

FIGURE 5.7. Spectrum of the reflected signal from the remotely multiplexed four FBG. $P_{pum\text{-}Raman}$=1.3W, $P_{tunable\text{-}laser}$=11dBm and $OSA_{resolution}$= 0.1nm.

In order to assess the sensing capability of our system, the FBG centered at 1555 nm was located in a climatic chamber and heated up. Figure 5.8 illustrated the FBG linear behavior versus the temperature which resulted in a sensitivity of 9.4 pm/°C.

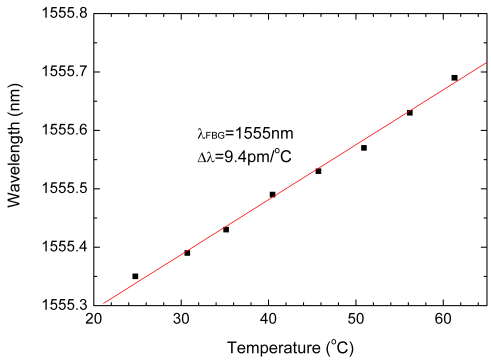

FIGURE 5.8. Wavelength shift of the heated up FBG.

As mentioned previously, the proposed system was restricted by the noise level imposed by the detection scheme. In our set-up, in order to reduce this level we had used the OSA option sweep high sensitivity. This measurement option reduced the

noise level averaging, thus the background noise decreased and the OSNR increased meaningfully. Thus, the measured OSNRs improved from 20 to 18 dB for the best and worst case, as Figure 5.9 shows.

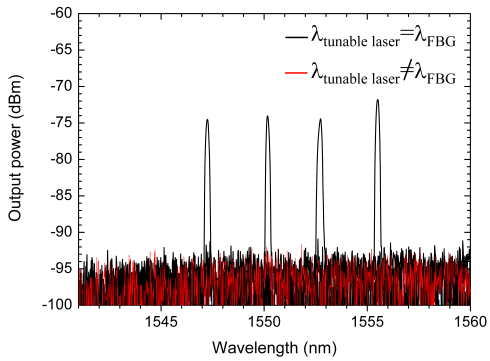

FIGURE 5.9. Spectrum of the reflected signal from the four FBG using the OSA sweep option of high sensitivity. $P_{pum\text{-}Raman}$=1.3 W, $P_{tunable\text{-}laser}$=11 dBm and $OSA_{resolution}$= 0.1 nm.

5.2 SWITCHABLE ERBIUM DOPED FIBER RING LASER SYSTEM FOR TEMPERATURE SENSORS MULTIPLEXING

In this section a switchable optical fiber laser system for multiplexing temperature sensors is presented. The sensor system is based on the electrical detection of the beat of two EDFRL emission lines in single longitudinal mode operation. The SLM behavior is achieved by using PSFBGs with ultra-narrow BW, as in the EDFRL presented in section 3.1.2. As it has been mentioned earlier, EDFAs present a homogeneous broadening. This fact could be a problem in a sensor system based on the beating of two close SLM emission lines. Therefore, in order to reduce the output power competition and to improve the stability, independent rings for each EDFRL have been employed for the reference and the sensor. Also, the independent EDFRL configuration allows extending the temperature measurement range by using a temperature control reference.

Description of the laser sensor system

Figure 5.10 shows the experimental setup of the proposed temperature-sensor system, which was based on the electrical domain detection of the mixing of two

single-longitudinal mode erbium-doped fiber-ring laser emission lines. The wavelength selection of both emission lines obtained from our EDFRL (reference line and sensors lasing signal), was carried out using a combination of FBGs and PSFBGs. The FBG was located in-reflection using a circulator and its purpose was the coarse wavelength selection. The FBGs were centered at 1550 nm, measured at room temperature (24ºC), having a reflectivity close to 90% and a corresponding FWHM of 0.12 nm. The PSFBG acted as a narrow transmission filter with a FWHM less than 6 pm.

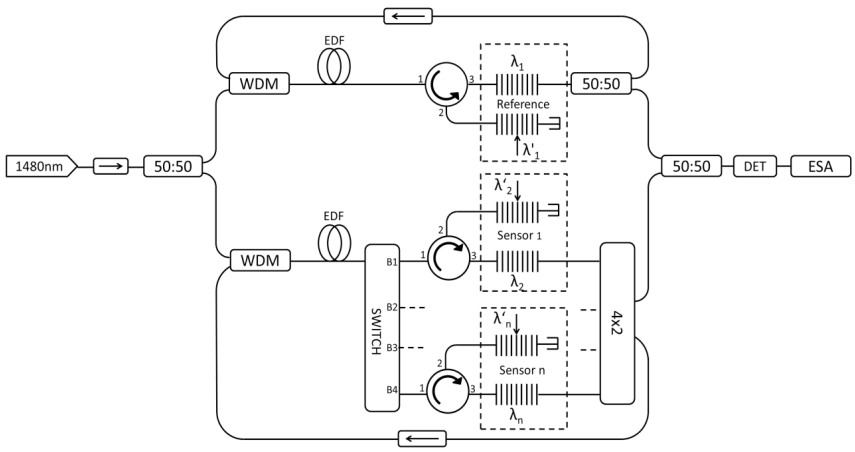

FIGURE 5.10. Experimental setup of the proposed switchable EDFRL system for temperature sensors multiplexing, where λi and λi' are the FBGs and the PSFBGs, respectively.

Based on [14], any phase shift can be obtained by changing the sampling period of a Sampled Fiber Bragg Grating (SFBG) [15].For this application the PSFBGs were written into a standard telecommunication optical fiber using the phase mask technique illuminated with a continuous laser emitting at 244 nm. The sampling effect was generated by opening and closing the laser shutter at preset locations. The total length of the PSFBGs was $L \approx 24$ mm with a sampling period of $P=1.5$ mm. An increment in the sampling period P with a scale factor of $F=1.5$ located in the center of the grating creates an equivalent pi-phase shift in the first order of the SFBG. The obtained spectrum of the phase-shifted SFBG is detailed in the Figure 5.11.

The utilized gain medium into the laser consisted of two EDFs of 7 m, one for the reference EDFRL and the other for the lasing sensor arm. These EDFs were pumped with the same laser at 1480 nm trough the 50:50 optical coupler, with a pump power of

200 mw. The selection of each sensor was made by an optical switch (HP 86061C) with a maximum switching time of 370 ms. The four outputs of the switch were connected to the sensing elements that consisted of couples of FBG and PSFBG. A 4x2 coupler collected the signal from the operational branch of the switch. The isolator ensured the unidirectional operation of each EDFRL and therefore, avoiding the spatial hole-burning effect.

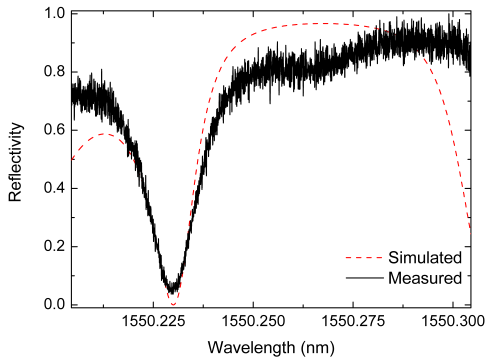

FIGURE 5.11. Simulated and measured reflection spectra for the phase shift of the SFBG first order.

The signals from the selected sensor and the reference were mixed by a 50:50 coupler and their outputs were converted to the electrical domain by the photodetector (HP 11982A) that showed a BW of 20 GHz. An electrical spectrum analyzer with 1 KHz of resolution (HP 8592L) was used to retrieve the output signal.

For the sensor characterization, a Peltier unit having a thermo electrical cooler (TEC) was used. Figure 5.12 shows the disposition of the FBG and PSFBG on the Peltier. Each couple of FBG and PSFBG experienced the same temperature change and therefore the same variation at their wavelengths. A conducting paste was used to ensure the uniform distribution of the temperature.

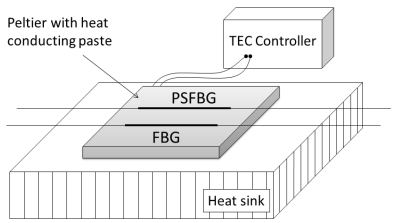

FIGURE 5.12. Schematic representation of the experimental setup for the sensors temperature test.

Experimental results

Figure 5.13 (a) shows the optical spectrum at 24ºC measured at a high-resolution Brillouin optical spectrum analyzer (BOSA-C Aragon Photonics) with a resolution of 0.08 pm. The wavelengths correspond to the reference EDFRL and the EDFRL of sensor 1. Both lasing signals operated in single longitudinal mode regime. Figure 5.13 (b) displays the electrical spectra of the beaten of these signals demonstrating the SLM behavior of both EDFRL. The peak at 11.9 GHz corresponds to the spacing between both lasers.

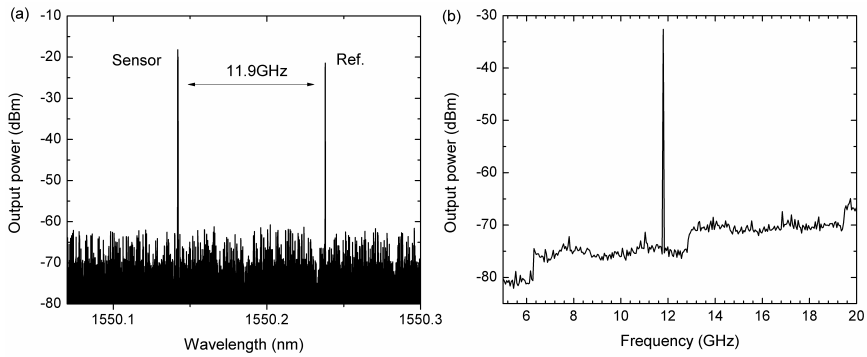

FIGURE 5.13. (a) Optical output spectrum at 24ºC measured at BOSA and (b) electrical output spectrum at 24ºC measured at ESA.

In order to determine the response of the sensor with temperature variations and its instability, a series of measurements for sensor 1, ranging from 19ºC to 30ºC with steps of 1 ºC were carried out. The reference arm operated at room temperature (24 ºC). Each measurement step consisted of a period of 10 minutes with captures every minute (Figure 5.14 (a)). The frequency instability was lower than 200 MHz, value that as can be seen below did not affect significantly the linearity of the sensor. The global instability was due to the TEC instability in combination with the thermal insulation tolerance of the characterization setup that can easily cause fluctuations of 0.1ºC. Figure 5.14 (b) shows the beat frequency dependence with the temperature, measured by using a time averaging technique. High sensitivity of 1.55 GHz/ºC with a coefficient of determination of R^2=0.9993 was obtained, being these values better than the obtained in [16], that were 1.30 GHz/ºC with a linearity of 0.9662 or in [17] 1.47 GHz/ºC with R^2=0.9935.

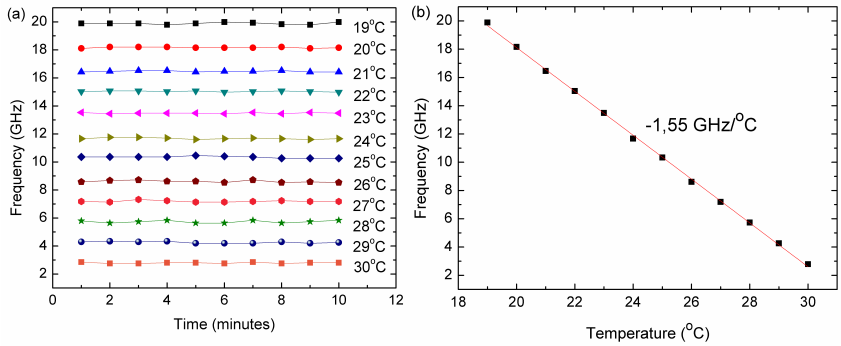

FIGURE 5.14. (a) Beat frequency dependence with time at different temperatures. (b) Average beat frequency shift dependence with temperature.

Considering that all the FBGs and PSFBGs were written in the same fiber and with the same process, all of them have the same behavior with the temperature (1.55 GHz/°C) resulting in an absolute equation for the measured temperature:

$$T(°C) = -\frac{Freq(GHz) - 49.12}{1.55} + (T_{ref} - 24) \qquad (5.1)$$

By controlling the reference temperature (*Tref*) with a Peltier system, we can displace the temperature operation point of the system maintaining the BW of the detector. Figure 5.15 shows the theoretical range of an application where different reference temperatures were employed to improve the dynamic range. This is an important advantage in comparison with other sensors systems [16, 17] wherein the temperature range is limited by the BW of the detector.

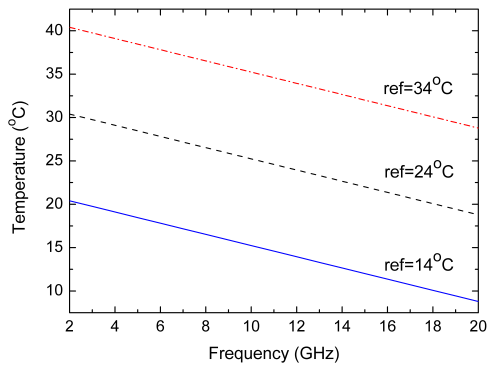

FIGURE 5.15. Theoretical beat frequency shift dependence with temperature for different reference temperatures.

The transient switching response of the sensors was also studied. This switching time is defined as the time delay between the moment in which one sensor is turned off and the other has a stabilized output. For the measurement we employed a photo-detector (Thorlabs PDA400) and an oscilloscope (Agilent 54622A). Figure 5.16 shows the switching measured time from B1 to B4 output (solid line) and from B4 to B1 output (dotted line). For both the switching time were less than 250 ms.

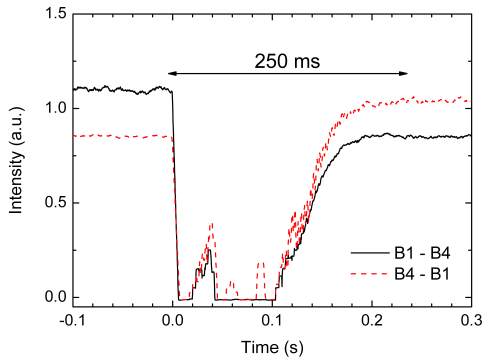

FIGURE 5.16. Switching time from B1 to B4 output (solid line) and from B4 to B1 output (dotted line).

5.3 SWITCHABLE FIBER OPTIC LASER SYSTEM FOR HIGH AND LOW-STRAIN FIBER OPTIC SENSORS REMOTE MULTIPLEXING

As it has been mentioned before, remote sensing has received a high attention during last years as a useful tool for monitoring the optical sensors from a central station located tens kilometers away from the field, especially in structural health monitoring [18, 19]. One of the main parameters to be measured in these remote sensing systems is strain. Depending on the application, low and medium strain measurements are not enough and high strain measurements are needed [20]. The aim of the system presented below, is to convert an EDFRL in a sensor system that allows a 50 km remote monitoring, and also the integration of different kind of sensors into the network.

Description of the laser sensor system

The proposed remote sensing system was based on an EDFRL with different rings selected by a switch. The gain medium was an EDFA (Photonetics FIBERAMP-BT 17).

This configuration allowed the integration of different interrogation methods based on the detection of wavelength or amplitude variations of the laser. As mentioned above, in this work is presented the multiplexing of a bending intensity sensor and a wavelength strain sensor for high and low-strain measurements respectively. Figure 5.17 shows the experimental setup of the remote sensing system.

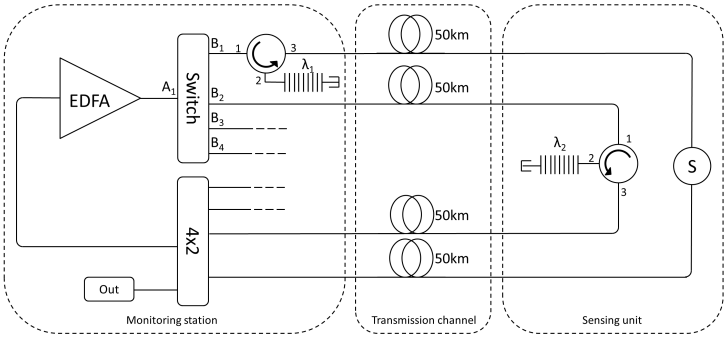

FIGURE 5.17. Experimental setup configuration for the EDFRL remote sensing system.

The high-strain EDFRL sensor corresponded to the B1 switch output port. This sensor was based on intensity variations of the laser induced by applying strain to a bending sensor. The wavelength selection was made by an FBG in reflection located at the monitoring station. The FBG was centered at λ1=1531.66 nm with a corresponding FWHM of 0.120 nm and a reflectivity above 90%. The sensing unit was allocated at 50 Km from the monitoring station and the transmission channel was a cable that includes 4 SMFs. In real applications, the cost of the system does not increase significantly if several SMFs are used inside the fiber optic cable instead of using only one. The sensing head was made by 20 turns of a SMF around a coil of 38 mm of diameter. The coil was covered by a rubber tube in order to ensure a uniform response under deformation. The sensor was placed between two anchors, one of them fixed and the other one movable, by using a micrometric step-motor (Figure 5.18).

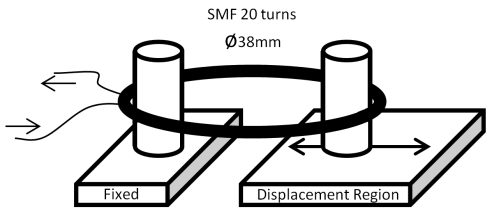

FIGURE 5.18. Schematic of the high-strain bending intensity sensor.

The low-strain EDFRL sensor was interrogated using the B2 switch output port. This sensor was made with an in-reflection FBG located at the sensing unit at 50 Km from the monitoring station. When selected, this FBG generates the central lasing wavelength of the EDFRL. The FBG was centered at $\lambda 2$=1530.61 nm with a corresponding FWHM of 0.125 nm and a reflectivity above 90%. This sensor was based on wavelength variations of the laser induced by applying strain to the FBG.

A 2x4 switch with a maximum switching time of 370 ms (HP 86061C) and a 4x2 coupler were used to select and recombine the different EDFRL sensor signals respectively. The half of the signal was extracted by the coupler to the output and the other half was redirected to the EDFA. The output was connected to an OSA (HP-70952B) with a resolution of 0.1 nm.

Experimental results

Firstly, the high-strain sensor was analyzed by selecting the B1 switch output port. In this case an EDFRL at $\lambda 1$ was generated. The amplitude of this lasing wavelength depended on the bending sensor attenuation caused by the strain applied. In order to determinate their response with strain variations, a series of measurements from 0 to 182 mili-strain with steps of 0.13 mili-strain was carried out. Figure 5.19 (a) shows the measured spectra at OSA for the initial position and for the higher strain of 182 mili-strain. The minimum OSNR corresponded to this last position with a value of 46 dB. This obtained OSNR was better than the results from other previously published remote sensors systems [21, 22].

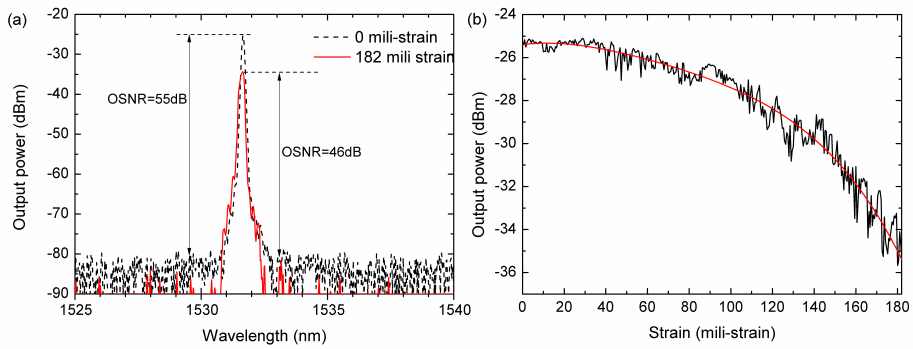

FIGURE 5.19. (a) Output spectra of the high-strain sensor for different strain values and, (b) output power evolution with the strain.

Figure 5.19 (b) presents the dependence of the output power with stain. That dependence was adjusted by a four degree polynomial curve. The curve slope was determined by the number of sensor turns. We used 20 turns in order to reduce the cladding-modes coupling by curvature effects and to increase the resolution [23].

The next step was to carry out the characterization of the low-strain sensor by selecting the B2 switch output port. In this case, the change of the EDFRL wavelength, produced by the strain applied to the FBG, was the parameter to be measured. Figure 5.20 (a) shows the spectrum of four different strain values with an OSNR of 55 dB for all of them that, again better than the obtained in other published sensors systems.

In order to characterize the sensor with strain, a series of measurements within a range of 3750 με and steps of 5 με were performed. Figure 5.20 (b) presents a high linear FBG response against strain with a sensitivity of 0.97 pm/με.

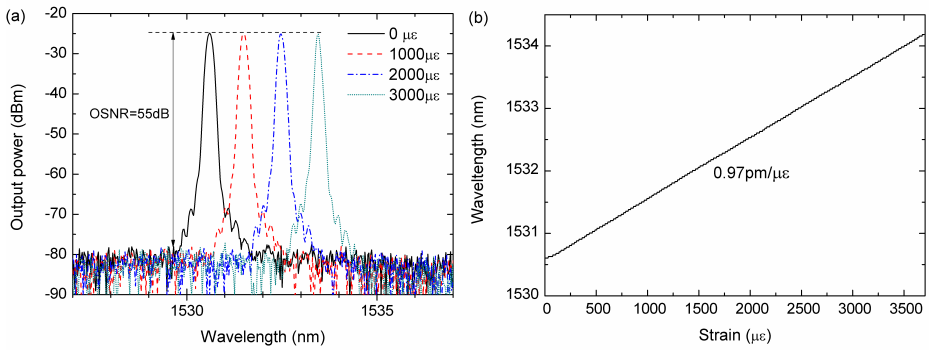

FIGURE 5.20. (a) Output spectra of the low-strain sensor for different strain values and, (b) output wavelength evolution with the strain (b).

Finally the transient switching response of the sensors was also studied. For the measurements we employed a photo-detector (Thorlabs PDA400) and an oscilloscope (Agilent 54622A). Figure 5.21 shows the switching time measured time for B1 to B2 output (solid line) and for B2 to B1 output (dotted line). For both the switching time were less than 250 ms.

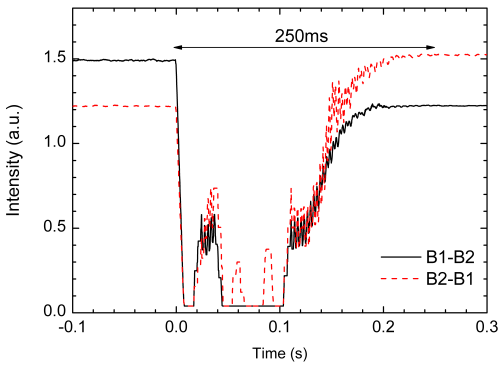

FIGURE 5.21. Switching time from B1 to B2 output (solid line) and from B2 to B1 output (dotted line).

5.4 MULTI-WAVELENGTH FIBER LASER IN SINGLE-LONGITUDINAL MODE OPERATION BASED ON DWDMS FOR SENSING APPLICATIONS

In section 3.1.3 an EDFRL based on the combination of MUX/DMUX with a Sagnac interferometer has been demonstrated. The idea presented in this section is to transform that EDFRL into a laser sensor system. This process is now carried out by changing the Sagnac interferometer by an array of FBGs, which actuate as wavelength selection element. To achieve it, a MUX/DMUX is used. The FBGs act as sensor elements.

Description of the laser sensor system

The experimental setup of the proposed MEDFRL sensor system is shown in Figure 5.22. This set-up consisted of a ring, in which 5 meters of fiber highly doped with erbium (Er-30 by Liekki, with an absorption of 10.8 dB/m at λ=978 nm) was used as gain medium. A 95% optical coupler was used to complete the ring laser. This coupler was used for inserting a 980 nm pump source inside the ring and also for enabling the extraction of 5% of the laser output power from the ring and redirecting it to the OSA (Advantest Q8384).

Inside this fiber ring laser there was also a 200GHz dense WDM multiplexer and demultiplexer with 4 channels, which was used to filter the out-of-band ASE noise generated by the EDFA. This filtering also improved the amplification efficiency and gave a flat spectral response. The ITU channels selected by this DWDM were C31, C35, C41

and C47 corresponding to the wavelength values of 1552.52, 1549.32, 1544.53 and 1539.77 nm, respectively. Four fiber Bragg gratings, centered at these channels, were used in this topology. Specifically, these FBGs had the Bragg wavelengths of 1552.33 nm, 1549.6 nm, 1544.38 nm and 1539.9 nm with a corresponding FWHM of 0.24 nm, 0.21 nm, 0.28 nm and 0.2 nm, respectively. One of the major problems in MEDFRL is their channels equalization. Because of this, an optical variable attenuator was placed at each wavelength output of the DMUX.

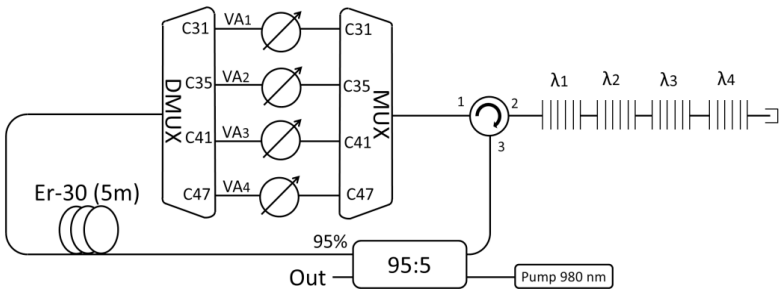

FIGURE 5.22. Proposed single-longitudinal-mode four-wavelength fiber laser for sensors applications.

One of the advantages of this MUX/DMUX structure, in comparison with typical inline filtering, is the ease of the individual control of the loss of each channel by including these variable attenuators between the MUX and the DMUX. Because of that, and due to the low loss of this kind of devices, we could easily increase the number of wavelengths of the laser by replacing the MUX/DMUX configuration for another with more channels.

It is worth to notice that this topology allowed an individual equalization of the reflected FBGs signals despite of being connected in a serial configuration. In this topology, after being multiplexed, the FBGs reflected signals were inserted into the ring by using an optical circulator obtaining a serial topology. This configuration ensured the unidirectional operation inside the ring and therefore, the SHB effect was avoided. In addition to this, all the free terminations were immersed in refractive-index-matching gel to avoid undesired reflections.

Experimental results

The output spectrum of the MEDFRL measured at the OSA for a 108.2 mW pump power is shown in Figure 5.23 (a). As shown in this figure, four lasing channels were

obtained. The power of each of the four output channels was around -10 dBm with an OSNR higher than 55 dB. Several previous studies show that these values were reasonably good for most sensor applications [24].

As it was seen in section 2.3.3.2, in ring fiber laser configurations multiple longitudinal modes are supported by the cavity. However, as reported previously [25], under some specific conditions, such as in the case of similar pumping levels, SLM operation of the laser can be achieved. The single-longitudinal mode lasing was verified in two different ways. The first one was carried out by using a BOSA, with a resolution of 0.08 pm. Its spectral resolution had a lower value than the mode spacing between the longitudinal modes of the ring, given by:

$$\Delta\lambda = \frac{\lambda^2}{n \cdot L} \qquad (5.2)$$

where n is the refractive index of the fiber, L is the ring length and λ is the central mode wavelength. Taking into account that: n=1.476, and L=12.5 m for the worst case, that was the FBG located at the end of the serial topology, the mode spacing between the longitudinal modes was about 0.13 pm. As a consequence, we can verify the SLM operation condition by using this BOSA. Figure 5.23 (b) illustrates this SLM lasing behavior.

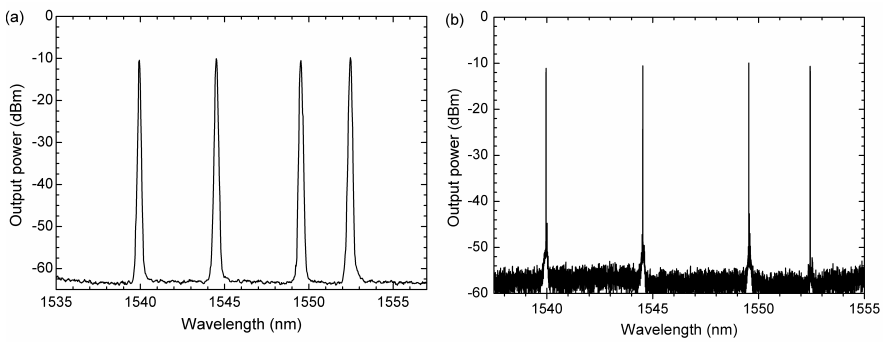

FIGURE 5.23. Output spectrum response of the MEDFRL (a)measured at OSA and (b) measured at BOSA.

The second verification was done by heterodyne detection of the output signal. In this method each laser line was combined with the output of a tunable laser source with a linewidth of 100 kHz. In this way, the beating signal was observed after a photo-

detector by means of an ESA, whose resolution bandwidth can be as good as 1 Hz. Figure 5.24 shows the output optical spectrum measured by the ESA for the channel 47 with a SLM operation. Similar results were obtained for the other three channels.

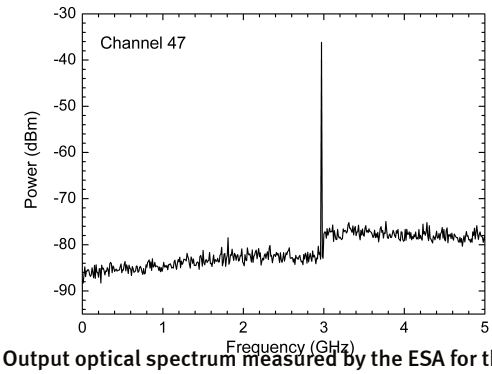

FIGURE 5.24. Output optical spectrum measured by the ESA for the channel 47.

To determine the emission lines band width, a series of measurements using the self-heterodyne method presented in section 2.3.4, was carried out. Figure 5.25 shows the spectrum at ESA with a resolution of 1 kHz for channel 35. This spectrum presented a Gaussian shape. Because of this, the spectrum was square root times the laser bandwidth. Therefore, the BW at channel 35 was 5.83 kHz. The rest of the measured values were, 5.58 kHz, 5.33 kHz and 8.13 kHz, corresponding with the channels 47, 41 and 31, respectively.

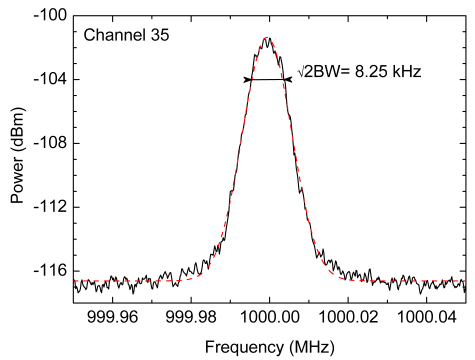

FIGURE 5.25. Spectrum of emission line measured at ESA with the self-heterodyne detection method for channel 35.

The utilization of this new laser for sensor multiplexing was carried out using the FBGs as temperature sensors. The temperature response of the sensors was tested by heating them on a climatic chamber one by one in the range of 23.5°C to 80°C. Figure 5.26 illustrates the center wavelength shift for the laser emission located at 1544.5 nm. This laser presented a clear linear behavior, and a temperature sensitivity of about 9 pm/°C was measured. Similar results were obtained for the other three temperature sensors. Taking into consideration this temperature sensitivity and the flat spectral response of the 200 GHz DWDM used in this work, a temperature range of about 150°C can be measured. Depending on the center wavelength emission of the FBGs used for this configuration, different temperature values could be measured.

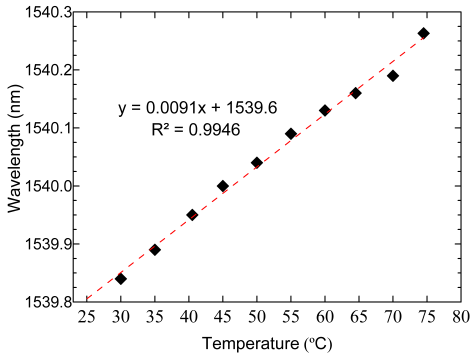

FIGURE 5.26. Wavelength shift as a function of temperature change.

In order to investigate the applicability of this proposed system for remote sensing applications, a SMF fiber reel was located between the circulator and the FBGs to simulate a network with 4 sensors located at 10 km. As can be observed in Figure 5.27 the power obtained from each of the output channels in this case was around -15 dBm and these four lasing wavelengths showed an OSNRs about 47 dB.

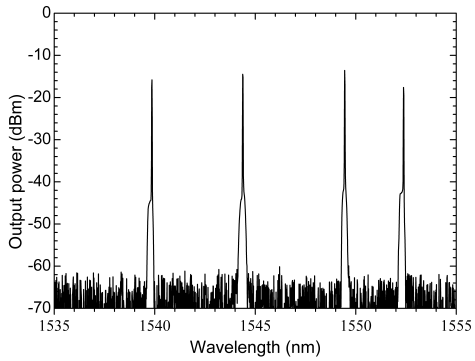

FIGURE 5.27. Output spectrum response of the MEDFRL with the sensors located at 10 km of distance, measured at OSA.

5.5 COMPOUND LASING FIBER OPTIC RING RESONATORS FOR SENSOR SENSITIVITY ENHANCEMENT

Throughout this chapter, different laser sensor systems for sensors multiplexing and remote monitoring have been presented. This section is focus on designing a laser sensor system based on fiber optical ring resonators (FORRs), in order to increase simultaneously the sensitivity and interrogation stability of a fiber optic intensity sensor.

5.5.1. DOUBLE COUPLER FORR CHARACTERIZATION

Firstly, in this section we performed a theoretical and experimental study of the ring resonator in which the sensor was based.

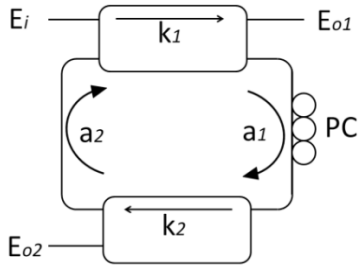

FIGURE 5.28. Compound fiber-based ring resonator.

The FORR structure used in this system used two couplers forming a compound resonator. The upper coupler provided a sensitive response to the losses in the ring. The lower coupler showed a complementary response to the upper one as shown below.

Considering the structure depicted in Figure 5.28, E_{o1} and E_{o2}, are the transmitted and reflected signals of the FORR, respectively, and will be given by;

$$E_{o1} = E_i \frac{k_1 \, exp\left(\frac{iwnL}{c}\right) - k_2 a_1 a_2}{exp\left(\frac{iwnL}{c}\right) - k_1 k_2 a_1 a_2} \qquad (5.3)$$

$$E_{o2} = (E_i - E_{o1})(1 - k_2) a_1 \qquad (5.4)$$

Where, E_i is the input signal, K_i and a_i, are the coupling ratios and the attenuations in the resonator, respectively, and L the total length of the ring.

As it is visible, the response of the ring is periodic in frequency, with resonant peaks spaced by a quantity c/nL. These resonances manifest as spectral dips in the power transmission response of E_{o1}. Under resonant conditions, the recirculation of power in the cavity is maximized, and the photon lifetime in the cavity grows significantly. In these resonant conditions, the sensitivity to small absorption/attenuation changes in the ring can be maximized, a fact that has been often used in spectroscopic measurements, as in cavity ring-down spectroscopy systems. However, it has been not often been used to enhance the sensitivity of conventional fiber-optic intensity sensors. The main reason is that it requires the interrogation of the spectral dip in the center of the resonance, which, as it will be seen later, requires precise and stable wavelength scanning lasers. We can now turn our attention to how much can the sensitivity be improved in this kind of setup in comparison with the direct readout of the intensity sensor. To evaluate this, we need to obtain the power transmission coefficient of the ring in the center of the dip, which can be written as:

$$T = \frac{|k_1 - k_2 a_1 a_2|^2}{|1 - k_1 k_2 a_1 a_2|^2} \qquad (5.5)$$

The sensitivity to absorption or losses in the resonator can be evaluated by computing dT/da_i. The resulting expression is:

$$\frac{dT}{da_i} \propto |1 - k_1 k_2 a_1 a_2|^{-3} \qquad (5.6)$$

As it can be seen, higher values of k result in higher values of sensitivity. The sensitivity of the system is higher as we approach higher Q factors (as k_i and a_i approach 1). However this also leads to more challenging interrogation systems as the operation of the cavity becomes more and more narrowband. Hence a proper trade-off has to be found in these values. An initial study of the spectral response of the structure was carried out using 90% couplers ($k_1 = k_2 = 0.9$). The remaining values of the experimental setup were $L = 2.14$ m and, $a_1 = a_2 = 0.05$ dB due to the splices between the couplers. To optimize the system response, a polarization control was included.

For the resonator characterization, a tunable laser source (Santec TLS-210) and a photo-detector (New Focus 1811) in combination with an oscilloscope (Agilent 54622A) were used as input and output, respectively. Figure 5.29 shows the comparison of the experimental and theoretical simulation results.

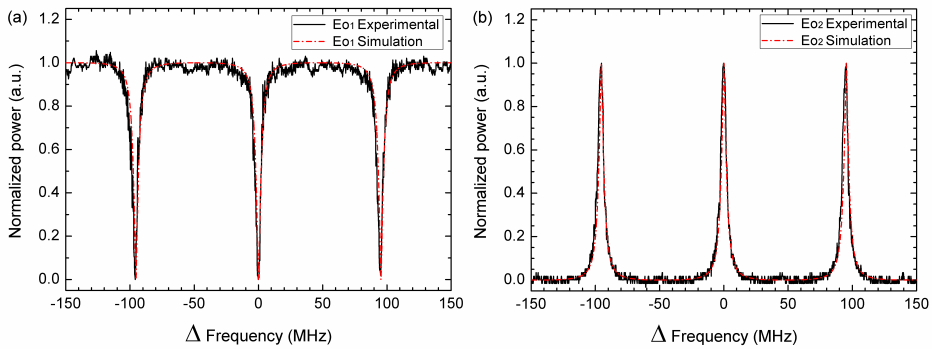

FIGURE 5.29. Experimental and simulated normalized spectra of the resonator for Eo1 (a), and Eo2 (b).

As might be expected, the resonator spectra showed resonances with a periodicity given by c/nL. In this case, the peaks separation was about 95 MHz, which was in good agreement with the expected value for $L = 2.14$ m.

5.5.2. INTERROGATION METHOD

Once the ring resonator response was characterized, the next step was to determine an interrogation method to measure the loss introduced by a sensor element (S) inside the ring.

The first configuration selected to carry out the characterization of the sensing ring consisted of the use of a tunable laser source (TLS Agilent 81600B) as light source.

The laser was operated at 1550 nm, with a linewidth of 100 KHz and an instability of ±1 pm along 24 hours. As it is shown in Figure 5.30, a power meter (Ando Aq2140) was used for the detection.

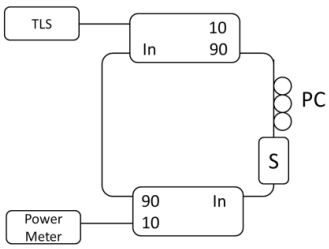

FIG. 5.30 Experimental setup of the TLS interrogation method.

In order to characterize the reliability of this configuration, a power instability measurement was carried out without attenuation (*S*=0dB). The measurement was done along 30 minutes, taking a sample each 10 seconds. Figure 5.31 shows the high instability behavior that made this interrogation method unsuitable for the vast majority of intensity sensor applications. The problem of this configuration was due to the transfer function instability of the ring in combination with the TLS wavelength instability. The separation of peaks in the transfer function was very narrow, so small TLS wavelength variations cause a substantial change of the detected output power.

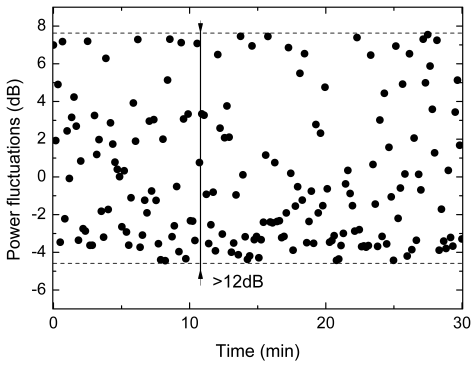

FIGURE 5.31. Output power fluctuations of the TLS interrogation method.

The proposed solution was the use of the E_{02} output of the ring as a seed, for generating a fiber ring laser. This way the structure itself behaved as the interrogator of the sensor. Any ambient variation leading to changes in the transmitted signal is immediately manifested in the reflected response. Hence, the "self-interrogation" of the structure seemed a very convenient way to improve the stability of the measurement method. The actual configuration used is shown in Figure 5.32. The gain medium was an EDFA (EFA-P21 from MPB Technologies). For the laser wavelength selection, a filter at 1533.9 nm with a BW of 0.1 nm was used. Note that the lasing cavity in Figure 5.32 was much longer than the FORR cavity, so effectively the spectral response of the obtained laser turns out to be approximately that of E_{02}.

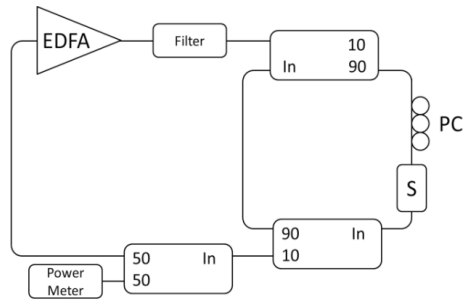

FIGURE 5.32 Experimental setup of the EDFRL interrogation method.

As in the previous setup, an instability characterization was carried out with the sensor tuned at o dB attenuation, obtaining, as shown in Figure 5.33, an instability lower than 0.1 dB.

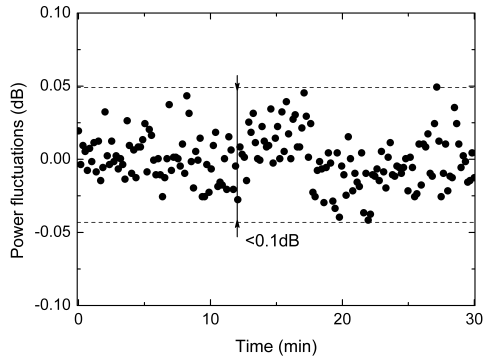

FIGURE 5.33. Output power fluctuations of the EDFRL interrogation method.

Taking into account the results obtained, the selected method for the sensor interrogation was this erbium doped fiber laser.

5.5.3 EDFRL SYSTEM CHARACTERIZATION

Once the interrogation method was chosen, the next step was the characterization of the system through the use of a variable attenuator, simulating an intensity sensor element. For this purpose a voltage controlled VA was used in order to increase the precision and the resolution of the characterization.

Figure 5.34 shows the proposed schematic in which there are two positions, A and B, where the sensor can be located. Placing alternatively the sensor in these two positions we can compare the behavior of a sensor inside the ring (B) and outside it (A). Furthermore, by disconnecting the internal FORR (dash line in Figure 5.34) the sensor can be compared with a simple ring configuration. The proposed system showed strong improvements in sensitivity compared to the open-loop response of the sensor and also in comparison with the conventional lasing ring resonator (see Figure 5.35). A series of measurements varying the applied voltage of the VA from 0 to 4 V with steps of 10 mV were carried out.

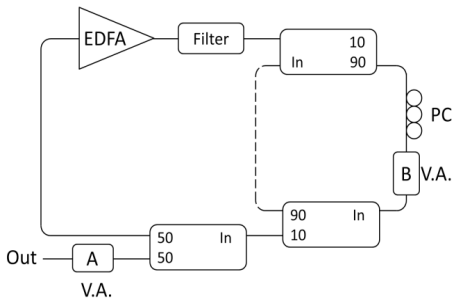

FIGURE 5.34. Experimental setup of the EDFRL sensor system.

As can be seen in Figure 5.35, when the VA was located inside the ring, the dynamic range of the system can be increased up to 15 dB. The attenuation operation range was defined from 0 dB (0 V) to 7.5 dB (3.25 V), where the loss of the cavity finally prevents the laser emission.

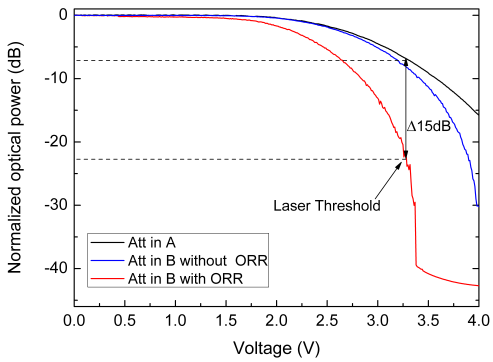

FIGURE 5.35. Output power response against the voltage applied to VA located in position A (dash), position B (continuous) and position B without FORR (dash-dotted).

Also a study of the output power instability following the VA attenuation inside the ring was performed. The system was tested for 11 different voltage values of the VA and each measurement was carried out along 30 minutes, using an acquisition time of 10 seconds.

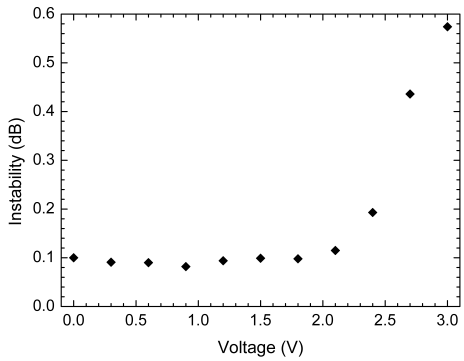

FIGURE 5.36 Output power instability of the structure against the voltage applied to VA.

The obtained results, Figure 5.36, showed an instability close to 0.1 dB for the whole VA range up to 2.1 V. From this value onwards, the instability increased up to a maximum of 0.6 dB, when a voltage of 3 V was applied to the attenuator. This was again justified by the close operation of the system to the laser threshold.

As stated before, the sensitivity of the system is higher for higher k values (see eq. 5.6). In order to confirm this, an experimental study for k_1=0.5 and k_1=0.9 coupling ratios, (recirculating inside the ring the 50% and 90% of the optical power, respectively), was carried out. Figure 5.37 shows that in both cases the achieved output power of the lasing system were similar, but with the higher coupling ratio (k_1=0.9) the sensitivity increased, as expected from the previous theoretical arguments.

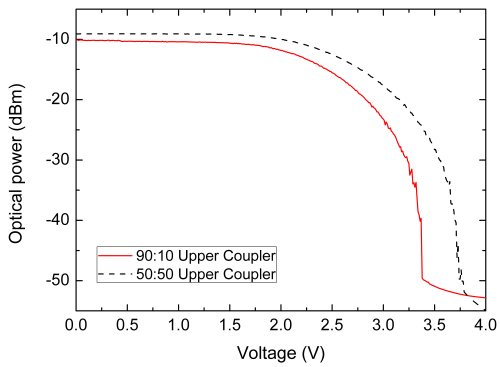

FIGURE 5.37. Output power response against the voltage applied to a VA for two different coupling ratios of the upper coupler.

5.5.4 EDFRL DISPLACEMENT SENSOR SYSTEM

In this section a practical case for displacement measurements based on a bending sensor was investigated. It is known that the sensors based on bending an optical fiber have a non-linear response due to the cladding-modes coupling effect [23]. Therefore, three different spectral configurations of our EDFRL sensor system were studied in order to determine the best option for this kind of sensors.

The experimental setup for the EDFRL sensor system is shown in Figure 5.38. The difference of each configuration consisted on the different filters used; no filter for a wide-band interrogation, a filter with a BW=0.1 nm for achieving a multimode laser interrogation and the combination of this filter with a PSFBG to obtain a single-longitudinal mode interrogation, corresponding with sections 5.5.4 A, 5.5.4 B and 5.5.4 C respectively.

The gain medium was again the previously utilized EDFA (EFA-P21) and the output power detection was made through a power meter (AQ2140).

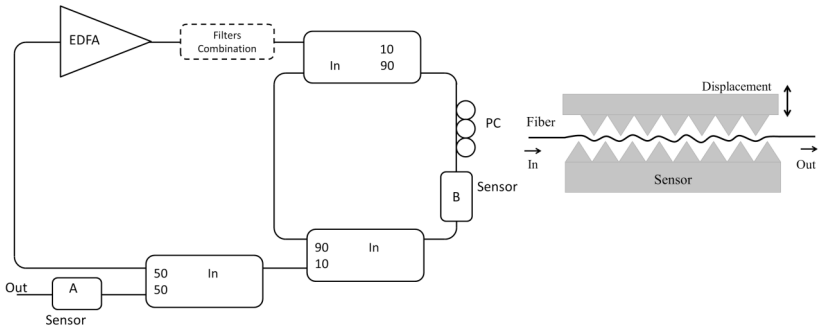

FIGURE 5.38 Experimental setup of EDFRLs for the displacement sensor interrogation system and, schematic of the displacement sensor based on bending.

The characterization of each scheme was conducted through a precision mechanic attenuator based on stress-inducing plates, similar to the one used in [26]. All measurements were carried out in the same way, ranging from 0 to 1000 μm with a step of 4.27 μm. Before each measurement, the polarization was optimized using the PC.

In the sub-sections below, we present the experimental results for each configuration, in each case analyzing the performance in terms of the next different parameters: maximum output power, measurement range, dynamic range increase, instability and cladding-modes coupling behavior. The dynamic range increment was in all cases measured at 400 μm as this value corresponded to the sensor with the minimum displacement range. The instability was also measured at 400 μm along 30 minutes, taking a sample each 10 seconds.

A. Wideband Ring-Based System

In the first case, no additional filtering inside the ring laser was used, so the interrogation method was based on a wideband laser. Figure 5.39 shows the measured results for the sensor at positions A and B.

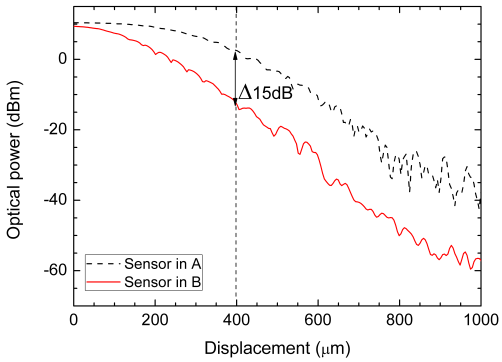

FIGURE 5.39 Output power response versus the displacement applied to the sensor, when located in position A (dotted) and B (continuous).

As seen above, when the sensor was located inside the ring, a dynamic range increment of 15 dB at 400 μm was achieved. This configuration allowed to measure up to 1000 μm.

The cladding modes coupling effect generated a ripple on the sensor response. In order to quantify this effect the output power response was fitted up to 400 μm by a second-order polynomial. The ripple was quantified trough the coefficient of determination (R^2), which is defined as the square of the sample correlation coefficient between the measured values and their predicted values [27]. For the wide band ring based system a R^2 of 0.99711 and an instability of 0.21 dB were measured.

B. Multi-Longitudinal Mode Fiber Ring Laser-Based System

In this case, a multimode EDFRL was created. Figure 5.40 shows the optical spectrum of the laser and the filter transmission (inset) measured with a high resolution (0.08 pm) optical spectrum analyzer.

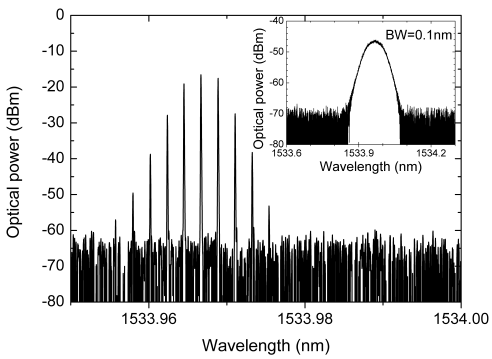

FIGURE 5.40 Optical spectrum of the multi longitudinal mode EDFRL and the filter transmission (inset) measured with a BOSA.

The characterization, Figure 5.41, shows the same sensitivity increment at 400 μm, as in the previous configuration. Also a low cladding-modes coupling effect was appreciated. As in the previous case, a fit up to 400 μm was carried out showing a R^2 of 0.99775.

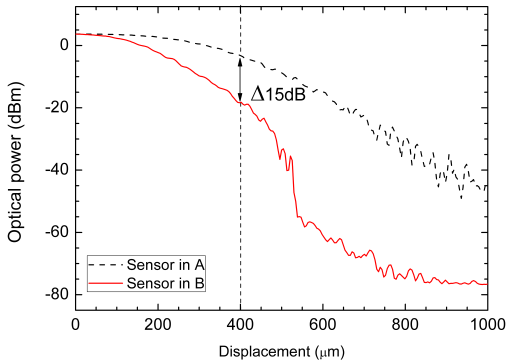

FIGURE 5.41 Output power response depending on the sensor displacement in position A (dotted) and B (continuous).

Because this configuration was operating as an EDFRL, there was an attenuation threshold from which the laser condition was not satisfied, reducing the sensor range to 530 μm. Also, the system presented an instability of 0.34 dB.

C. Single Longitudinal-Mode Fiber Ring Laser-Based System

In order to achieve a single longitudinal mode operation EDFRL, a PSFBG was added to the configuration. Figure 5.42 shows the optical spectra of the SLM laser and the PSFBG transmission (inset) measured with BOSA.

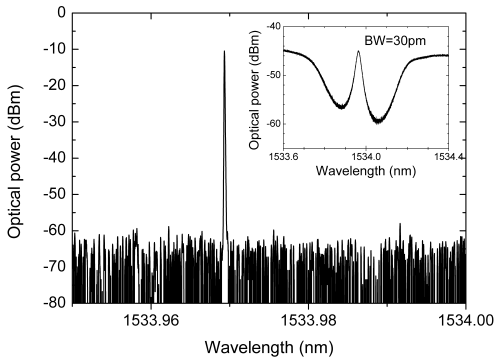

FIGURE 5.42 Optical spectrum of the single longitudinal mode EDFRL and the filter transmission (inset) measured with a BOSA.

Figure 5.43 shows that in this case there was a dynamic range increment of 18 dB at 400 μm in comparison with the 15 dB achieved in sections 5.5.4 A and 5.5.4 B. However, since all the power was concentrated in a single longitudinal mode, the cladding-modes coupling effect was enhanced, showing a R^2 of 0.98326 (lower than the previous cases). The sensor range was reduced to 400 μm and the maximum output power was less than -3 dBm. In this case the instability was increased up to 1.48 dB. The high wavelength sensitivity of the PSBG to temperature variations in combination with the filter provoked this increment of the instability.

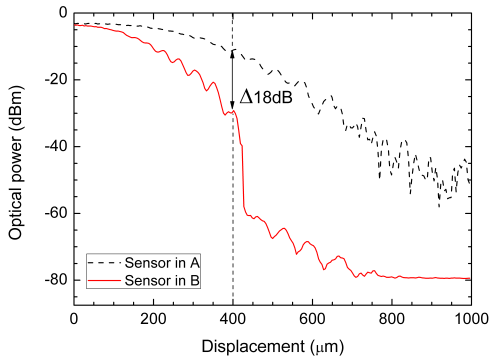

FIGURE 5.43 Output power response depending on the sensor displacement measured at position A (dotted) and at position B (continuous).

5.5.5 RANDOM LASER DISPLACEMENT SENSOR SYSTEM

Finally, a configuration based on a random laser was investigated (Figuer 5.44). EDFRL lasers studied above combine in their transfer function the longitudinal modes coming from the ring resonator with the corresponding to the external ring used to connect the EDFA to the FORR. Random fiber lasers have some interesting properties, such as their high bandwidth and modeless behavior [28]. In order to check their suitability for FORR measurements, we developed a configuration that used a 2.4 Km dispersion compensating fiber pumped with a Raman laser (RLD-3-1445 from IPG Laser) at 1445 nm with an output power of 1 W, as Raman gain medium. Due to the Rayleigh backscattering, the fiber acted not only as gain medium but also as a randomly distributed mirror. A 3-port circulator was utilized to connect the previous sensor structure with the random laser.

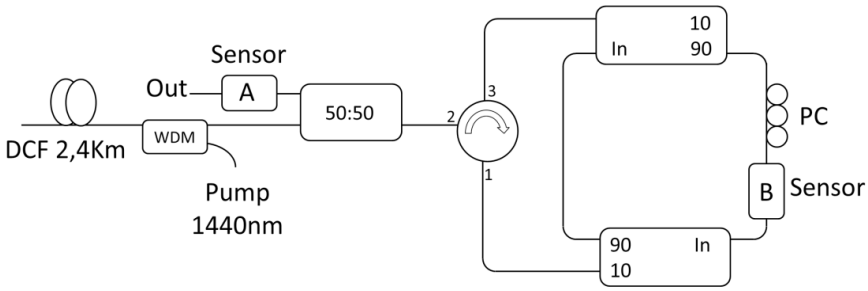

FIGURE 5.44. Experimental setup of the micro-bending random fiber laser sensor system.

The measurement process was the same as the one used in the previous sections. Figure 5.45 shows the characterization of the sensor located at position A and B of the schematic. In this case a sensitivity increment of 10 dB at 400 μm, a displacement range close to 800 μm, an output power of 5 dBm and, an instability of 0.04 dB were reached. In the figure it is also shown that the cladding-modes coupling effect was reduced, with a R^2 of 0.99646.

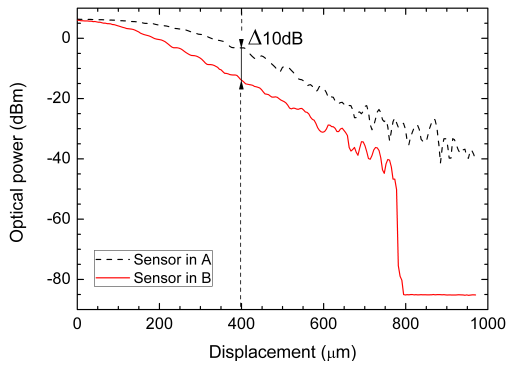

FIGURE 5.45 Output power response depending on the sensor displacement in positions A (dotted) and B (continuous).

5.5.6 COMPARISON OF THE DEVELOPED DISPLACEMENT SENSOR SYSTEMS

To summarize the analysis carried out with the different configurations for the displacement sensor system, a table with the studied parameters of each configuration is presented (Table 5.1).

	NO-FILTER	FILTER 0.1NM	FILTER 0.1NM + PSBG	RANDOM
Sensor Range (μm)	1000	530	410	780
P_{max} (dBm)	9.5	3.7	-3.5	6
Dynamic Range Inc. @ 400μm (dB)	15	15	18	10
R^2 of the Fit up to 400 μm	0.99711	0.99775	0.98326	0.99646
Instability @ 400 μm (dB)	0.21	0.34	1.48	0.04

TABLE 5.1 Critical parameters comparison of the different sensor configurations.

For this kind of sensors, the cladding-modes coupling is a critical point since it could cause errors in the measurements. Because of that, the system based on the 0.1 nm filter in combination with the PSFBG appears clearly as the worst option with the lower R^2.

On the other hand the non-filtered and 0.1 nm filtered systems show comparable dynamic range increments and instabilities, and also the lowest dependence to the cladding-modes coupling so, for medium displacement ranges, these options can be considered the best configurations for our micro-bending sensor system. However, the use of the filter allows us to select and lock the wavelength emission of the laser, which is an important issue if several rings were to be multiplexed.

5.6 CONCLUSIONS

This chapter has provided a review of the work carried out related to optical fiber sensor systems.

In the first part of the chapter, two ultra-long range FBG sensor interrogation systems have been experimentally demonstrated. Both systems are based on a wavelength sweep laser to interrogate the multiplexed FBGs. The systems are composed by two optical paths of identical lengths. The first one launches the amplified laser signal by means of Raman amplification. The other one is employed to guide the reflection

signal up to the reception system avoiding the Rayleigh backscattering. In the first approach the four FBGs have been located 200 km away from the monitoring station, and a signal to noise ratio of 20 dB is reached. An optimized version of the system is able to detect the FBGs placed at 250 km, with an OSNR of 6–8dB (18–20 dB using averaging methods). Thus, it is the longest range FBG multiplexing sensor system, with all active elements in the header, reported to date.

These results have been published in [29].

The second proposed system consists of a switchable EDFRL system for temperature sensors multiplexing. The system is based on the electrical domain detection of the beat of two laser lines operating in single-longitudinal mode regime. The SLM operation is achieved using PSFBGs with ultra-narrow bandwidths. Independent cavities for the generation of the reference signal and the sensor signal were used to avoid the wavelength competition and to improve the stability. The measurements show a high sensitivity of 1.55 GHz/°C and a high linearity. The inclusion of a temperature control in the reference signal allows the control of the temperature operating point of the system, maintaining a constant receptor band-width.

These results have originated the publication in reference [30].

The third one presents a 50 Km switchable EDFRL system for remote multiplexing of sensors. This system allows the integration of different interrogation methods, based on wavelength or amplitude detection. This integration is sequentially carried out through an optical switch that also allows the use of close FBG wavelengths for all the sensors. Using this technique, no gain competition among different wavelengths occurs, as happens in multiwavelength lasers. Therefore, the utilized wavelength can be always the corresponding to the higher gain of the optical amplifier, in order to optimize the achieved distance of the system. A bending intensity sensor for high strain measurements and a FBG based low-strain sensor have been successfully tested.

These results have originated the publication in reference [31].

Next, a novel multi-wavelength ring laser configuration for sensing applications by means of a DWDM and four FBGs has been proposed and experimentally demonstrated. In this work, four single-longitudinal mode wavelength laser emissions are obtained simultaneously, showing an OSNR higher than 55 dB. Emission lines showing bandwidths as good as 5.3 kHz have been measured by using a self-heterodyne method. Finally, the sensor system has been tested for temperature sensor applications showing a sensitivity of 9 pm/°C, and also for remote sensing applications.

These results have originated the publications in references [32,33].

Finally, a new fiber laser system for enhancing fiber-optic intensity sensor measurements, based on a resonant ring cavity has been presented. The main advantage of this method is its ability to increase the dynamic range of an intensity sensor up to 15 dB, while keeping good stability values. The solution is based on the use of a compound lasing fiber-optic ring resonator, in which the intensity sensor is inserted. Because the reflected function of the ring-resonator is used to generate the EDFRL, the lasing system is perfectly matched to work as a "self-interrogator" of the sensor. The resulting system shows an enhanced sensitivity and high stability, showing an output power instability lower than 0.1 dB. The proposed interrogation system is particularly suited for any kind of transmissive intensity sensors and only requires two active elements, an EDFA as gain medium and an optical power meter acting as detector. In addition, the concept has been tested for the development of displacement sensors based on fiber optic bending. A study of different topologies, 3 based on an EDFRL with different filters and another one based on a random fiber laser, were carried out. As a result of this study it was concluded that laser configurations without additional filtering or using a filter of 0.1 nm, showed the best results with a dynamic range increment higher than 15 dB, and a comparatively low cladding-modes coupling effect.

These results have originated the publications in references [34,35].

5.7 REFERENCES

[1] E. Mehrani, A. Ayoub and A. Ayoub, "Evaluation of fiber optic sensors for remote health monitoring of bridge structures," *Materials and Structures/ Materiaux Et Constructions,* Vol. 42, Iss. 2, pp. 183-199, 2009.

[2] Y. J. Rao, Z. L. Ran and R. R. Chen, "Long-distance fiber Bragg grating sensor system with a high optical signal-to-noise ratio based on a tunable fiber ring laser configuration," *Opt. Lett.,* Vol. 31, Iss. 18, pp. 2684-2686, 2006.

[3] A. S. Guru Prasad, S. Asokan and R. Tatavarti, "Detection of tsunami wave generation and propagation using fiber Bragg grating sensors," in *Proceedings of IEEE Sensors*, 5398388,pp. 1278-1281, 2009.

[4] H. Nakstad and J. T. Kringlebotn, "Realisation of a full-scale fibre optic ocean bottom seismic system," in *Proceedings of SPIE 7004,* 19th International Conference on Optical Fibre Sensors (OFS-19), 700436, 2008 .

[5] P. Ferraro and G. De Natale, "On the possible use of optical fiber Bragg gratings as strain sensors for geodynamical monitoring," *Optics and Lasers in Engineering,* Vol. 37, Iss. 2-3, pp. 115-130, 2002.

[6] T. Saitoh, K. Nakamura, Y. Takahashi, H. Iida, Y. Iki and K. Miyagi, "Ultra-long-distance (230 km) FBG sensor system," in *Proceedings of SPIE 7004,* 19th International Conference on Optical Fibre Sensors (OFS-19), 70046C, 2008 .

[7] M. Fernandez-Vallejo, S. Díaz, R. A. Perez-Herrera, D. Passaro, S. Selleri, M. A. Quintela, J. M. L. Higuera and M. Lopez-Amo, "Resilient long-distance sensor system using a multiwavelength Raman laser," *Measurement Science and Technology,* Vol. 21, Iss. 9, 2010.

[8] R. A. Pérez-Herrera, M. A. Quintela, M. Fernández-Vallejo, A. Quintela, M. López-Amo and J. M. López-Higuera, "Stability comparison of two ring resonator structures for multiwavelength fiber lasers using highly doped er-fibers," *J. Lightwave Technol.,* Vol. 27, Iss. 14, pp. 2563-2569, 2009.

[9] M. J. Marrone, A. D. Kersey, C. A. Villarruel, C. K. Kirkendall and A. Dandridge, "Elimination of coherent Rayleigh backscatter induced noise in fibre Michelson interferometers," *Electron. Lett.,* Vol. 28, Iss. 19, pp. 1803-1804, 1992.

[10] G. A. Cranch, A. Dandridge and C. K. Kirkendall, "Suppression of double Rayleigh scattering-induced excess noise in remotely interrogated fiber-optic interferometric sensors," *IEEE Photonics Technology Letters,* Vol. 15, Iss. 11, pp. 1582-1584, 2003.

[11] J. M. López-Higuera,"*Handbook of Optical Fiber Sensing Technology,"* J.M. López-Higuera, Ed. John Wiley & Sons, 2002.

[12] R. B. Jenkins, R. M. Sova and R. I. Joseph, "Steady-state noise analysis of spontaneous and stimulated Brillouin scattering in optical fibers," *J. Lightwave Technol.,* Vol. 25, Iss. 3, pp. 763-770, 2007.

[13] A. R. Chraplyvy, "Limitations on lightwave communications imposed by optical-fiber nonlinearities," *J. Lightwave Technol.,* Vol. 8, Iss. 10, pp. 1548-1557, 1990.

[14] Y. Dai, X. Chen, D. Jiang, S. Xie and C. Fan, "Equivalent phase shift in a fiber Bragg grating achieved by changing the sampling period," *IEEE Photonics Technology Letters,* Vol. 16, Iss. 10, pp. 2284-2286, 2004.

[15] B. J. Eggleton, P. A. Krug, L. Poladian and F. Ouellette, "Long periodic superstructure Bragg gratings in optical fibres," *Electron. Lett.,* Vol. 30, Iss. 19, pp. 1620-1622, 1994.

[16] H. Ahmad, A. A. Latif, M. Z. Zulkifli, N. A. Awang and S. W. Harun, "Temperature sensing using frequency beating technique from single-longitudinal mode fiber laser," *IEEE Sensors Journal,* Vol. 12, Iss. 7, pp. 2496-2500, 2012.

[17] Y. Dai, Q. Sun, J. Zhang, J. Wo and D. Liu, "Tunable dual-wavelength double-ring fiber laser and its application in highly sensitive temperature sensing," in *Conference on Lasers and Electro-Optics (CLEO 2012),* paper JW2A.75, 2012, .

[18] B. Culshaw and A. Kersey, "Fiber-optic sensing: A historical perspective," *J. Lightwave Technol.,* Vol. 26, Iss. 9, pp. 1064-1078, 2008.

[19] J. M. López-Higuera, L. R. Cobo, A. Q. Incera and A. Cobo, "Fiber optic sensors in structural health monitoring," *J. Lightwave Technol.,* Vol. 29, Iss. 4, pp. 587-608, 2011.

[20] M. Bravo, J. Sáenz, M. Bravo-Navas and M. Lopez-Amo, "Concrete beam bending test monitorization using a high strain fiber optic sensor," *J. Lightwave Technol.,* Vol. 30, Iss. 8, pp. 1085-1089, 2012.

[21] M. Fernandez-Vallejo and M. Lopez-Amo, "Optical fiber networks for remote fiber optic sensors," *Sensors,* Vol. 12, Iss. 4, pp. 3929-3951, 2012.

[22] M. C. Shih, C. L. Ko and C. Y. Yang, "Dynamic strain monitoring by wavelength locking between two fiber Bragg gratings fiber sensing system," *Optics and Lasers in Engineering,* Vol. 46, Iss. 7, pp. 546-549, 2008.

[23] M. Bravo and M. López-Amo, "Remote-time division multiplexing of bending sensors using a broadband light source," *Journal of Sensors,* Vol. 2012, Article ID: 154586, 2012.

[24] S. Diaz, S. Abad and M. Lopez-Amo, "Fiber-optic sensor active networking with distributed erbium-doped fiber and Raman amplification," *Laser and Photonics Reviews,* Vol. 2, Iss. 6, pp. 480-497, 2008.

[25] M. A. Quintela, R. A. Perez-Herrera, I. Canales, M. Fernández-Vallejo, M. Lopez-Amo and J. M. López-Higuera, "Stabilization of dual-wavelength erbium-doped fiber ring lasers by single-mode operation," *IEEE Photonics Technology Letters,* Vol. 22, Iss. 6, pp. 368-370, 2010.

[26] M. Bravo, A. M. R. Pinto, M. Lopez-Amo, J. Kobelke and K. Schuster, "High precision micro-displacement fiber sensor through a suspended-core Sagnac interferometer," *Opt. Lett.,* Vol. 37, Iss. 2, pp. 202-204, 2012.

[27] L. T. Skovgaard, "Applied regression analysis". 3rd edn. N. R. Draper and H. Smith, Wiley, New York, 1998.

[28] M. Bravo, M. Fernandez-Vallejo and M. Lopez-Amo, "Internal modulation of a random fiber laser," *Opt. Lett.,* Vol. 38, Iss. 9, pp. 1542-1544, 2013.

[29] M. Fernandez-Vallejo, S. Rota-Rodrigo and M. Lopez-Amo, "Remote (250 km) fiber Bragg grating multiplexing system," *Sensors,* Vol. 11, Iss. 9, pp. 8711-8720, 2011.

[30] S. Rota-Rodrigo, L. Rodriguez-Cobo, M. A. Quintela, J. M. Lopez-Higuera and M. Lopez-Amo, "A switchable erbium doped fiber ring laser system for temperature sensors multiplexing," *IEEE Sensors Journal,* Vol. 13, Iss. 6, pp. 2279-2283, 2013.

[31] S. Rota-Rodrigo, L. Rodríguez-Cobo, M. A. Quintela, J. M. López-Higuera and M. López-Amo, "Switchable fiber optic laser system for high and low-strain fiber optic sensors remote multiplexing," in *Proceedings of SPIE 8794,* Fifth European Workshop on Optical Fibre Sensors (EWOFS 2013), 87943U, 2013.

[32] D. Leandro, R.A. Pérez-Herrera, S. Rota-Rodrigo and M. López-Amo, "Multi-wavelength fiber laser in single-longitudinal mode operation based on DWDMs for sensing applications," VIII Iberoamerican Conference on Optics and XI Latinamerican Meeting on Optics, Lasers and Applications (RIAO/OPTILAS 2013), RIA100-506, 2013.

[33] D. Leandro, R.A. Pérez-Herrera, S. Rota-Rodrigo and M. López-Amo, "Laser monomodo multilínea utilizando DWDMs para sensores de fibra óptica," VIII Reunión Española de Optoelectrónica, 2013.

[34] S.Rota-Rodrigo, M. González-Herráez and M. López-Amo, "Compound lasing fiber optic ring resonators for sensing," *Proceedings of SPIE 9157*, 23rd International Conference on Optical Fibre Sensors (OFS-23), postdeadline 9157D7, 2014.

[35] S.Rota-Rodrigo, M. González-Herráez and M. López-Amo, "Compound lasing fiber optic ring resonators for sensor sensitivity enhancement," *IEE Journal of Lightwave Technology,* DOI:10.1109/JLT.2014.2387428, online version, 2014.

CHAPTER VI

CONCLUSIONS AND OPEN RESEARCH LINES

upna Universidad Pública de Navarra Nafarroako Unibertsitate Publikoa

CHAPTER VI

6.1. CONCLUSIONS

Optical fiber technology as well as its rapidly evolution, has attracted the scientific community attention to develop lasers, fiber optic transducers and sensor networks. In this regard, the appearance in the last decades of commercial devices such as optical amplifiers, semiconductor high power lasers and others, has contributed to the rise of this technology. In this framework, a contribution to the improvement of the main parameters of fiber lasers and sensors has been presented in this PhD. work, taking into account their main merits and addressing their principal challenges.

With regard to the new contributions of this thesis, chapter 3 has been devoted to the development of different configurations of fiber lasers. The aim of this chapter has been to contribute to the improvement of the fiber lasers´ main parameters such as OSNR and output power stability. Single longitudinal mode operation with narrow emission lines bandwidths has been also pursued. The multiwavelength operation and the independent control of the loss of each emission line have been also taken into account.

The first section of chapter 3 presents four new configurations of multiwavelength erbium-doped fiber ring lasers. Different methods for the selection of the emission lines have been used such as FBGs, FBGs in combination with PSFBGs, Add-Drops and MUX-DMUX devices. The output power obtained for the EDFRL varies in the range of -10 dBm to 0 dBm. On the other hand, OSNR higher than 65dB for three of the presented lasers and higher than 55dB for the last one, have been achieved. Also, single longitudinal mode operation has been experimentally demonstrated for three of the EDFRL proposed, achieving emission bandwidths of a few kilohertz. Finally, low instabilities close to 1 dB for the SLM EDFRLs, one of them lower than 0.4 dB, have been retrieved.

The second part of this chapter has been dedicated to the development of a single-longitudinal mode linear cavity laser. The system uses a narrow filtering technique based on the spectral overlapping of two uniform FBGs in order to achieve the SLM regime. This laser presents features such as a short length of 58 mm, an OSNR of 55 dB and an instability lower than 1 dB with a linewidth of 5 KHz. Moreover, the system can be tuned by controlling its temperature or strain, maintaining the SLM condition in whole the tuning range.

The last section of chapter 3 has been dedicated to random distributed feedback lasers. A configuration for sub-gigahertz line-width for the first time in a RDFB laser has been proposed and experimentally demonstrated. This configuration is based on a narrow filtering technique achieved by using a combination of FBGs with PSFBGs. A study of the evolution of the linewidth depending on parameters such as the output coupling factor and the pump power has been carried out. Next, this configuration has been extended to develop a multiwavelength laser with four narrow emission lines (linewidths between 5 to 9 pm) and instabilities lower than 0.07 dB. These instability results are substantially better than the achieved with the EDFLs based on ring and linear cavities. This is due to the absence of longitudinal modes in a random cavity, in combination with an inhomogeneous gain medium. Finally, to conclude this chapter, a comparative study between a random, a ring and a hybrid ring-random cavity has been performed. From this study, it can be concluded that the combination of both kind of reflectors, ring and random, has a positive effect on the threshold power, but a negative impact on the output power and slope efficiency in comparison with the pure ring cavity. Because this study has been carried out only for one emission line, all schemes shows a low instability. However the worst case corresponds to the hybrid ring-random cavity. Finally, it has been demonstrated that the random fiber laser is able to adapt their cavity to any internal modulation frequency, in contrast with ring fiber laser or hybrid ring-random fiber lasers, whose repetition rate is constrained by the length of the cavity.

Chapter 4 is fully dedicated to the development of transducers based on microstructured optical fibers for sensor systems. The main goal of this chapter has been to exploit MOF's features in comparison with standard fibers. MOFs present a low Young modulus which provides high sensitivities to strain. Also, a suitable design of their refractive index profile allows the fabrication of high-birefringence (Hi-Bi) MOFs for polarimetric sensors. Finally, Hi-Bi MOFs fabricated with a single material, present low temperature dependence. Based on these characteristics, three different MOF sensor systems have been developed and experimentally demonstrated in this chapter.

In the first MOF sensor, a configuration for an interferometric fiber optic strain sensor has been developed. The sensing head has been achieved by using a Hi-Bi MOF placed in an in-reflection configuration. An experimental characterization of this sensing head has been performed using an optical backscatter reflectometer. The achieved measurements have agreed with the presented theoretical simulations. Moreover, a cost-effective setup for the same transducer by using a laser for the interrogation has been presented. The in-reflection sensing head shows a sensitivity of 7.96 dB/mε to strain induced variations, and a negligible response to temperature because of its single material fabrication.

The second developed sensor has been a strain fiber optic sensor based on multimode interferences. The sensing head has been built by using a suspended core MOF arranged in a transmissive configuration. An experimental study about influence of the sensing head and stage separation lengths in the sensitivity of the system has been carried out. This study shows that the sensitivity increases with the separation of the stages, due to low Young modulus of the MOF. Sensitivities up to -2.42 pm/με have been achieved.

The last MOF transducer has been developed for simultaneous measurements of two physical parameters. The sensor is based on the combination of the characteristics of two interferograms with distinct frequency fringe patterns. These patterns are generated by using a three holes suspended core MOF operated in transmission. Each interferometric pattern presents different response to strain, temperature and curvature. Through a low-pass frequency filtering of the detected spectrum, the wavelength displacements of each interferogram are measured. This process allows the discrimination of temperature and strain with resolutions of 0.45°C and 4.02 με respectively , and bend angles and temperature with resolutions of 1.69 deg and 0.92°C, respectively.

Chapter 5 presents different optical fiber sensor systems which have been designed to contribute to different topics such as remote monitoring, multiplexing, integration of different kind of transducers, instability and sensitivity enhancement.

The first sensor systems have been developed in order to demonstrate the feasibility of remote multiplexing systems for distances higher than 200 km. Two remote 200 Km and 250 Km sensor systems have been experimentally demonstrated. Both systems, designed to use a minimum number of optical components at the monitoring station, are based on a wavelength sweep laser suitable to interrogate four multiplexed FBGs. Each system uses two optical paths of identical lengths. The first path launches an amplified laser signal by using Raman amplification and the other one is employed to guide back the reflected signal to the detector of the monitoring station, minimizing the effect of Rayleigh backscattering. With this configuration the system is able to detect four FBGs placed at 250 Km with an OSNR ranging from 6 to 8 dB. Thus, it is the longest range FBG sensor system, with all active elements in the header, reported to date that includes fiber sensor multiplexing capability.

Afterward, a fiber laser sensor system for temperature measurements is presented. This system is based on the detection in the electrical domain of the resulting beat signal of two different SLM laser lines, which are generated by an EDFRL. The SLM operation is achieved by using PSFBGs with ultra-narrow bandwidths. Independent cavities for the generation of the reference signal and the sensor signal were used in order to avoid the wavelength competition and to improve the stability. The measurements show a high sensitivity of 1.55 GHz/ºC and a high linearity. The inclusion of a temperature control in the reference signal allows the control of the temperature operating point of the system, maintaining a constant receptor band-width.

The third sensor system presented in chapter 5, has been a 50 Km switchable EDFRL system for sensors remote multiplexing. This system allows the integration of different interrogation methods, based on wavelength or amplitude detection. This integration has been sequentially carried out through an optical switch that also allows the use of closer FBG wavelengths for all the sensors. Using this technique, no gain competition among different wavelengths occurs, as happens in multiwavelength lasers. Therefore, the utilized wavelength can be always the corresponding to the higher gain of the optical amplifier, in order to optimize the achieved distance of the system. A bending intensity sensor for high strain measurements and a FBG based low-strain sensor have been successfully tested.

Afterwards, a novel multi-wavelength ring laser configuration for sensing applications by means of a DWDM and four FBGs has been proposed and experimentally demonstrated. In this experiment, four single-longitudinal mode wavelength laser emissions have been obtained simultaneously, showing an OSNR higher than 55 dB. Emission lines showing bandwidths as good as 5.3 kHz have been

achieved. The sensor system has been tested for temperature sensor applications showing a sensitivity of 9 pm/°C, and also for remote sensing applications.

The last part of chapter 5 has been dedicated to present a new fiber laser system for enhancing fiber-optic intensity sensor measurements, based on a resonant ring cavity. The main advantage of this method is its ability to increase the dynamic range of an intensity sensor up to 15 dB, while keeping good stability values. The solution is based on the use of a compound lasing fiber-optic ring resonator, within which the intensity sensor has been inserted. Because the reflected transfer function of the ring-resonator is used to generate the EDFRL, the lasing system is perfectly matched to work as a "self-interrogator" of the sensor. The resulting system shows an enhanced sensitivity and high stability, showing an output power instability lower than 0.1 dB. The proposed interrogation system is particularly well suited for any kind of transmissive intensity sensors and only requires two active elements, an EDFA as gain medium and an optical power meter acting as detector. In addition, the concept has been tested for the development of displacement sensors based on fiber optic bending. A study of different topologies (3 based on an EDFRL with different filters and another one based on a random fiber laser), has been carried out, achieving a dynamic range increment higher than 15 dB in the best case.

6.2 CONCLUSIONES

Desde la irrupción de la fibra óptica en las telecomunicaciones, han surgido multitud de desarrollos basados en sus propiedades. Así, en las últimas décadas, la rápida evolución de los sistemas basados en fibra óptica, así como la aparición en el mercado de dispositivos como amplificadores ópticos, láseres de semiconductor de alta potencia, y otros elementos, ha hecho avanzar considerablemente la investigación en este campo. Además de la utilización de la fibra óptica en telecomunicaciones, han surgido nuevas aplicaciones, generando nuevas familias de dispositivos. Dos de ellas, particularmente interesantes, son los láseres de fibra óptica y los sensores de fibra óptica. Ambas familias pueden combinarse de manera que sensores y redes de sensores de fibra óptica pueden interrogarse por medio de láseres de fibra óptica. En este marco de investigación se centra esta tesis, donde se han desarrollado estructuras avanzadas de fibra óptica para láseres y sensores. El objetivo ha sido mejorar las propiedades de los láseres de fibra, sensores y sus sistemas de monitorización, así como abordar los diferentes problemas que éstos presentan actualmente.

El capítulo 3 se ha dedicado al desarrollo de diferentes configuraciones de láseres de fibra diferenciados por el tipo de cavidad utilizado, pudiéndose diferenciar entre: láseres en anillo, láseres de cavidad lineal y finalmente, láseres basados en espejos distribuidos o "random". El desarrollo de los láseres se ha realizado teniendo como objetivo la mejora de sus parámetros fundamentales como la relación señal a ruido óptica (OSNR), su potencia de salida así como su estabilidad, el número de líneas de emisión y su anchura espectral. También se han tenido en cuenta propiedades como la operación en un único modo longitudinal, y la posibilidad de controlar de forma independiente la amplitud de cada línea de emisión del láser.

En la primera sección del tercer capítulo de esta tesis se presentan cuatro nuevas configuraciones de láseres en anillo multilínea basados en fibra dopada con erbio (EDFRL). Cada una de ellas utiliza diferentes métodos de filtrado para seleccionar las longitudes de onda de emisión. Inicialmente, mediante redes de difracción Bragg (FBGs), solas o en combinación con redes Bragg con cambio de fase (PSFBGs). A continuación, mediante Add-Drops, y por último, mediante una combinación de multiplexores-demultiplexores (MUX-DMUX). Con estas configuraciones se han obtenido láseres de fibra con potencias de salida en el rango de -10 dBm a 0 dBm; con un OSNR mayor de 65 dB para tres de ellos y de 55 dB para el otro. También se ha demostrado la condición de un único modo longitudinal de emisión (SLM) para tres de los láseres propuestos, con anchos de banda de emisión de unos pocos kilohercios. Finalmente, la inestabilidad de los láseres desarrollados se ha conseguido reducir hasta 1 dB; e incluso hasta 0.4 dB en uno de los casos.

La segunda parte de este capítulo se ha dedicado al desarrollo de un láser de cavidad lineal que opera en un único modo longitudinal. El método para conseguirlo se ha basado en una técnica de filtrado estrecho mediante la superposición espectral de dos FBGs. Este láser presenta propiedades como su reducida longitud de 58 mm, un OSNR de 55 dB, una inestabilidad menor de 1 dB. Además opera en SLM con una anchura de línea de 5 KHz. También permite su sintonización mediante temperatura o estiramiento, manteniendo la condición SLM en el rango de sintonización.

La última sección del capítulo 3 se ha dedicado al estudio y desarrollo de láseres de cavidad distribuida mediante dispersión Rayleigh (random). En este sentido se ha presentado por primera vez una configuración laser RDFB con líneas de emisión por debajo del gigahercio. Esta configuración se ha basado en una técnica de filtrado estrecho mediante la combinación de FBGs con PSFBGs. Se ha realizado un estudio sobre la evolución de la anchura de la línea de emisión del

láser en función del factor de acoplo utilizado en la salida del láser, así como en función de la potencia del bombeo Raman utilizado. A continuación, se ha extendido esta configuración para conseguir un láser con 4 líneas de emisión con anchuras que han ido desde 5 pm hasta 9 pm, e inestabilidades menores de 0.07 dB. La reducida inestabilidad del láser es debida a la ausencia de modos longitudinales de los láseres basados en cavidades random, y presenta una mejora considerable en comparación con los láseres de fibra dopada con erbio basados en cavidades lineales y en anillo. Finalmente, para concluir el capítulo, se ha llevado a cabo un estudio comparativo entre un láser de cavidad random, otro en anillo y también con una combinación de ambos. De este estudio se puede concluir que la combinación de ambas cavidades tiene un efecto positivo a la hora de alcanzar el punto de condición laser. Sin embargo presenta una menor potencia de salida, así como la peor inestabilidad de los tres casos estudiados. Dado que los láseres comparados solo presentan una única línea de emisión y el medio de ganancia es inhomogéneo, la inestabilidad es muy reducida en todos los casos, siendo el peor de ellos el de la cavidad combinada de anillo y random. En este estudio también se ha demostrado que la cavidad random se puede modular independientemente de la frecuencia de modulación aplicada, lo cual es una de las grandes ventajas que presenta frente a la cavidad en anillo y la combinación de ambas. En estas últimas, las frecuencias a las que se puede modular están marcadas por las resonancias y por lo tanto por la longitud del láser.

El capítulo 4 se ha centrado en el desarrollo de transductores basados en fibra óptica micro-estructurada (MOF). El objetivo principal ha sido explotar las ventajas que presentan este tipo de fibras en comparación con las fibras estándar. Las fibras MOFs presentan un menor módulo de Young que proporciona a los transductores basados en estas fibras una mayor sensibilidad ante el estiramiento. Por otro lado, las numerosas opciones de diseño de la sección transversal de las MOFs permite la fabricación de fibras altamente birrefringentes (Hi-Bi) para el desarrollo de sensores polarimétricos. Finalmente, las Hi-Bi MOF presentan una baja sensibilidad a los cambios de temperatura debido a que generalmente son fabricadas de un único material. A lo largo de este capítulo se han presentado tres sistemas sensores basados en las propiedades arriba descritas.

El primer sistema está basado en un sensor polarimétrico en reflexión para la monitorización de estiramiento. Su diseño se ha realizado mediante una fibra micro-estructurada altamente birrefringente. El sistema se ha caracterizado experimentalmente mediante un analizador óptico de la dispersión espacial reflejada (Optical Backscattering Reflectometer, OBR) cuyos resultados concuerdan con el análisis teórico del sensor. Después de este análisis, se ha realizado un diseño con un mayor coste-eficiencia mediante la utilización de un láser para la

interrogación del sensor, consiguiendo una sensibilidad de 7.96 dB/mε y una respuesta a temperatura despreciable ya que la MOF está compuesta de un único material.

El segundo sensor desarrollado se basa en la interferencia generada en la transición entre fibras monomodo-multimodo-monomodo, para la medida de estiramiento. Para ello se ha utilizado una MOF de núcleo suspendido. Se ha realizado un estudio para caracterizar la influencia de la longitud del sensor, así como de la longitud entre los puntos de fijación del mismo, en la sensibilidad del sensor. Este estudio ha demostrado que la sensibilidad aumenta al incrementar la separación entre los puntos de fijación debido al menor módulo de Young en comparación con la fibra estándar. Con este sensor se ha obtenido una sensibilidad máxima de -2.42 pm/με.

El último transductor está basado en una fibra MOF con núcleo suspendido y asimétrico, y ha sido desarrollado para la medida simultánea de diferentes magnitudes físicas. El sensor está basado en dos patrones de interferencia generados por la birrefringencia de la fibra y por la transición monomodo-multimodo-monomodo, los cuales presentan diferentes sensibilidades ante estiramiento, temperatura y curvatura. La discriminación se ha realizado mediante el filtrado a través de software de las componentes frecuenciales. Con este sistema se ha medido temperatura y estiramiento con resoluciones de 0.45°C y 4.02 με respectivamente, y también de ángulo y temperatura, con resoluciones de 1.69 grados en posición angular y 0.92°C respectivamente.

En el capítulo 5 se han presentado diferentes sistemas sensores de fibra óptica, centrando su desarrollo en aspectos como la monitorización remota, la multiplexación e integración de diferentes tipos de transductores basados en fibra óptica, y finalmente la mejora de parámetros como estabilidad y sensibilidad de los mismos.

En el primer sistema sensor desarrollado se ha puesto especial interés en los aspectos de monitorización remota y multiplexación de sensores, consiguiendo demostrar experimentalmente dos sistemas a 200 Km y 250 km capaces de monitorizar 4 FBGs que actúan como sensores. Ambos sistemas están basados en la interrogación mediante el barrido en longitud de onda de un láser, el cual es amplificado mediante ganancia Raman. Cada sistema está formado por dos fibras estándar de idéntica longitud, la primera utilizada para enviar la señal de interrogación y conseguir la amplificación por medio del efecto Raman, y la segunda utilizada para conducir la señal modulada por los sensores hasta la cabecera, evitando así el ruido Rayleigh producido en la primera fibra. Con esta configuración se ha conseguido detectar 4 FBGs situados a una distancia de 250

Km con un OSNR entre 6 y 8 dB, lo cual supone el sistema de monitorización remota sin amplificación intermedia y con multiplexación de sensores de mayor alcance realizado hasta la fecha.

Seguidamente, se ha presentado un sistema para la monitorización de temperatura, basado en la detección en el dominio eléctrico del batido de dos líneas laser SLM, generadas por un EDFRL. Cada una de las líneas, correspondientes a la señales de referencia y del sensor, se generan mediante la utilización de PSFBGs, y mediante cavidades independientes. Con esta configuración se evita la competencia en ganancia entre ambas líneas, y por lo tanto se mejora la estabilidad del sistema. Los resultados obtenidos muestran una respuesta lineal con una alta sensibilidad de 1.55 GHz/°C. Además, incluyendo un control de temperatura en la señal de referencia, se puede ajustar el punto de operación en temperatura del sistema, manteniendo el ancho de banda del receptor constante.

El tercer sistema desarrollado se centra en la integración de diferentes tipos de sensores basados en la detección de variaciones en amplitud y longitud de onda. Este sistema se ha basado en un láser en anillo con una longitud total de 100 km, lo que permite interrogar sensores a una distancia de 50 km. La integración de los diferentes sensores se ha llevado a cabo mediante un conmutador óptico, por lo que se ha podido utilizar la misma longitud de onda para los diferentes sensores. Este es un punto importante, ya que de esta forma se puede utilizar la zona de máxima ganancia del amplificador y a su vez se evita la competencia entre líneas de emisión. Se han demostrado experimentalmente tanto un sensor de curvatura basado en intensidad como un sensor de deformación basado en los cambios de longitud de onda de un FBG.

Seguidamente, se ha presentado un sistema sensor basado en un láser multilínea. El láser presenta cuatro longitudes de onda seleccionadas mediante FBGs. En este apartado se ha demostrado que el láser opera en un único modo longitudinal, con anchos de línea hasta de 5.3 KHz y con un OSNR mayor de 55 dB, requisitos importantes para aplicaciones de monitorización. También se ha realizado una prueba para monitorización de temperatura consiguiendo una sensibilidad de 9 pm/°C.

Finalmente, la última parte del capítulo 5 se ha dedicado al desarrollo de un nuevo sistema que es capaz de aumentar la sensibilidad así como la estabilidad de un sensor de intensidad, basado en una configuración de anillos resonantes. La principal ventaja de este sistema es que consigue aumentar el rango dinámico de un sensor de intensidad en más de 15 dB, manteniendo buenos niveles de estabilidad en la potencia medida. El sensor se ha introducido dentro del anillo resonante. La salida de este anillo se ha utilizado como semilla para

la generación de un láser que actúa como interrogador del propio sensor. Esta disposición hace que el láser este enganchado a las variaciones de la cavidad, reduciendo considerablemente las inestabilidades presentes en sistemas que usan interrogación externa. Otra ventaja de este sistema es que sólo precisa un amplificador óptico y un detector de potencia como dispositivos activos del sistema. El sistema presentado permite utilizar cualquier tipo de sensor en transmisión basado en intensidad. Para analizar sus prestaciones, se ha probado el sistema para un sensor de desplazamiento basado en curvaturas. Para ello se ha realizado el estudio para tres topologías basadas en EDFRL con diferentes filtros; y otro basado en una configuración random, mostrando incrementos del rango dinámico de hasta 15 dB.

6.3 OPEN RESEARCH LINES

Once the conclusions have been exposed, some open research lines should be considered as continuity of the research lines which has been carried out in this PhD. work. Due to the variety of optical fiber systems that have been developed, three main research lines can be differentiated: optical fiber lasers, fiber transducers and finally, optical fiber sensor systems.

Fiber lasers

Regarding to optical fiber lasers, there are many parameters that could be improved such as OSNR, output power, efficiency and stability. Therefore, this research line presents many possibilities and could be further investigated in order to enhance fiber laser´s behavior. Also, as has been presented in this PhD. work, there are different ways to achieve a SLM laser, concretely one based on the equalization of the emission lines with similar output powers. This phenomena has not been clearly explained so far, thus, an in depth study of these SLM lasers should be interesting.

On the other hand, Random DFB fiber lasers have been growing up in interest due to their main property of been a modeless cavity. The development of this kind of structures could be very interesting for sensing and also for communications. In this last case, and as it has been demonstrated, RDFB lasers can be internally modulated at any frequency. Therefore another open research line would be focused on the development of multiwavelength and modulated RDFB lasers, and the study of their parameters related to optical communications requirements.

Finally, the use of SLM fiber lasers not only for communications or sensor interrogation, but also for other fields such as the generation of radiofrequency sig-

nals by beating their emission lines, could be another interesting line for future research works.

Microstructured optical fiber transducers

As it has been demonstrated, the use of microstructured optical fiber as transducers can increase the sensor sensitivity, and also can reduce its sensitivity to undesired parameters. Moreover, MOF transducers allow the monitoring of simultaneous measurements. These features in combination with the development of new techniques and the rapidly evolution in the fabrication process, reinforce the convenience of research in these MOF transducers. In this PhD. Work, temperature, strain and curvature have been measured with MOFs, however a deep study for measuring magnitudes such as humidity, gases and pressure among others, would be highly interesting. In this regard, the use of new equipments such as the OBR and a precision splicing machine could contribute to facilitate this research line. Also, the use of specific software for simulating the MOF fields could contribute not only to compare the experimental results with simulations, but also to the development of precise MOF designs for specific applications.

Optical fiber sensor systems

In reference to the sensor systems two open research lines can be differentiated. The first is related to the remote monitoring, being their main goals the increasing of both, the distance of the remote sensor with all active elements in the header, and the number of multiplexed sensors of the network. On the other hand, the development of techniques such as the ORR system for enhancing the sensors sensitivity, presented in this PhD. work, is another line to be considered for future research.

APPENDIX

APPENDIX

LIST OF PUBLICATIONS RELATED TO THE THESIS

APPENDIX

1. PAPERS IN INTERNATIONAL JOURNALS

[1] M. Fernandez-Vallejo, **S. Rota-Rodrigo** and M. Lopez-Amo, "Remote (250 km) fiber Bragg grating multiplexing system," *Sensors,* Vol. 11, Iss. 9, pp. 8711-8720, 2011.

[2] **S. Rota-Rodrigo**, R. A. Perez-Herrera, M. Fernandez-Vallejo and M. López-Amo, "Low noise dual-wavelength erbium fiber laser in single-longitudinal-mode operation," *Appl. Phy. B,* Vol. 106, Iss. 3, pp. 563-567, 2012.

[3] **S. Rota-Rodrigo**, R. A. Perez-Herrera, I. Ibañez, A. M. R. Pinto, M. Fernandez-Vallejo and M. Lopez-Amo, "Multiwavelength fiber ring laser based on optical add-drop multiplexers and a photonic crystal fiber Sagnac interferometer," *Opt. Laser Technol.,* Vol. 48, pp. 72-74, 2013.

[4] **S. Rota-Rodrigo**, I. Ibañez and M. López-Amo, "Multi-wavelength fiber laser in single-longitudinal mode operation using a photonic crystal fiber Sagnac interferometer," *Appl. Phy. B,* Vol. 110, Iss. 3, pp. 303-308, 2013.

[5] **S. Rota-Rodrigo**, A. M. Pinto, M. Bravo and M. Lopez-Amo, "An in-reflection strain sensing head based on a Hi-Bi photonic crystal fiber." *Sensors,* Vol. 13, Iss. 7, pp. 8095-8102, 2013.

[6] **S. Rota-Rodrigo**, L. Rodriguez-Cobo, M. A. Quintela, J. M. Lopez-Higuera and M. Lopez-Amo, "A switchable erbium doped fiber ring laser system for temperature sensors multiplexing," *IEEE Sensors Journal,* Vol. 13, No. 6, pp. 2279-2283, 2013.

[7] L. Rodriguez-Cobo, M. A. Quintela, **S. Rota-Rodrigo**, M. López-Amo and J. M. López-Higuera, "Single-longitudinal mode laser structure based on a very narrow filtering technique," *Optics Express,* Vol. 21, Iss. 8, pp. 10289-10294, 2013.

[8] **S. Rota-Rodrigo**, L. Rodriguez-Cobo, M. A. Quintela, J. M. Lopez-Higuera and M. Lopez-Amo, "Dual-wavelength single-longitudinal mode fiber laser using phase-shift bragg gratings," *IEEE Journal on Selected Topics in Quantum Electronics,* Vol. 20, Iss. 5, pp- 161-165, 2014.

[9] M. Fernandez-Vallejo, **S. Rota-Rodrigo** and M. Lopez-Amo, "Comparative study of ring and random cavities for fiber lasers," *Appl. Opt.,* Vol. 53, Iss. 16, pp. 3501-3507, 2014.

[10] **S. Rota-Rodrigo**, M. Lopez-Amo, J. Kobelke, K. Schuster, J. L. Santos and O. Frazão, "Multimodal interferometer based on a suspended core fiber for simultaneous measurement of physical parameters," *IEEE Journal of Lightwave Technology,* DOI: 10.1109/JLT.2014.2375896, on-line version, 2014.

[11] **S. Rota-Rodrigo**, M. González-Herráez and M. Lopez-Amo, "Compound lasing fiber optic ring resontators for sensor sensivity enhancement," *IEEE Journal of Lightwave Technology,* DOI:10.1109/JLT.2014.2387428, online version, 2014.

2. INTERNATIONAL CONFERENCES

[1] **S. Rota-Rodrigo**, M. Bravo, A. M. R. Pinto and M. Lopez-Amo, "High-sensitivity PCF sensing head for strain measurement," *Proceedings of the SPIE 8421,* 22nd International Conference on Optical Fibre Sensors (OFS-22), 842136, 2012.

[2] **S. Rota-Rodrigo**, L. Rodríguez-Cobo, M. A. Quintela, J. M. López-Higuera and M. López-Amo, "Switchable fiber optic laser system for high and low-strain fiber optic sensors remote multiplexing," *Proceedings of SPIE 8794,* 5th European Workshop on Optical Fibre Sensors (EWOFS-2013), 87943U, 2013 .

[3] D. Leandro, R.A. Pérez-Herrera, **S. Rota-Rodrigo** and M. López-Amo, "Multiwavelength fiber laser in single-longitudinal mode operation based on DWDMs for sensing applications," VIII Iberoamerican Conference on Optics and XI Latinamerican Meeting on Optics, Lasers and Applications (RIAO/OPTILAS 2013), RIA100-506, 2013.

[4] **S. Rota-Rodrigo**, M. Lopez-Amo, J. Kobelke, K. Schuster, J. L. Santos and O. Frazão, "Control of the strain sensitivity using a suspended core photonic crystal fiber sensing head," *Proceedings of SPIE 9157,* 23rd International Conference on Optical Fibre Sensors (OFS-23), 91571Y, 2014.

[5] **S. Rota-Rodrigo**, M. Lopez-Amo, J. Kobelke, K. Schuster, J. L. Santos and O. Frazão, "Simultaneous strain and temperature measure based on a single suspended core photonic crystal fiber," *Proceedings of SPIE 9157,* 23rd International Conference on Optical Fibre Sensors (OFS-23), 915721, 2014.

[6] **S. Rota-Rodrigo**, M. González-Herráez and M. López-Amo, "Compound lasing fiber optic ring resonators for sensing," *Proceedings of SPIE 9157*, 23rd Interna-

tional Conference on Optical Fibre Sensors (OFS-23), postdeadline 9157D7, 2014.

[7] **S. Rota-Rodrigo**, M. González-Herráez and M. López-Amo, "Fiber laser sensor system based on a random mirror and a compound ring resonator for displacement measurements," 24rd International Conference on Optical Fibre Sensors (OFS-24), 2015, accepted.

[8] **S. Rota-Rodrigo**, R.A. Pérez-Herrera, A. López-Aldaba, M. Bravo, M.C. López-Bautista, O. Esteban and M. López-Amo, " Nanowire humidity Optical sensor system based on fast Fourier transform technique," 24rd International Conference on Optical Fibre Sensors (OFS-24), 2015, acepted.

3. NATIONAL CONFERENCES

[1] D. Leandro, R.A. Pérez-Herrera, **S. Rota-Rodrigo** and M. López-Amo, "Laser monomodo multilínea utilizando DWDMs para sensores de fibra óptica," VIII Reunión Española de Optoelectrónica, 2013.

[2] **S. Rota-Rodrigo**, R.A. Pérez-Herrera, A. López-Aldaba, M. Bravo, M.C. López-Bautista, O. Esteban and M. López-Amo, " Sensor de humedad basado en microhilo de fibra óptica y detección mediante Transformada de Fourier," IX Reunión Española de Optoelectrónica, 2015.

4. PAPERS UNDER REVIEW

[1] D. Leandro, **S. Rota-Rodrigo,** D. Ardanaz and M. López-Amo, "Narrow-linewidth multi-wavelength random distributed feedback laser," *IEEE Journal of Lightwave Technology,* under revision.